Geoscience BC

Geoscience BC Report 2018-01

Summary of Activities 2017:

Minerals and Mining

GEOSCIENCE BC SUMMARY OF ACTIVITIES 2017: MINERALS AND MINING

Geoscience BC Report 2018-1

This publication is also available, free of charge, as colour digital files in Adobe Acrobat® PDF format from the Geoscience BC website: http://www.geosciencebc.com/s/SummaryofActivities.asp.

Every reasonable effort is made to ensure the accuracy of the information contained in this report, but Geoscience BC does not assume any liability for errors that may occur. Source references are included in the report and the user should verify critical information.

When using information from this publication in other publications or presentations, due acknowledgment should be given to Geoscience BC. The recommended reference is included on the title page of each paper. The complete volume should be referenced as follows:

Geoscience BC (2018): Geoscience BC Summary of Activities 2017: Minerals and Mining; Geoscience BC, Report 2018-1, 112 p.

Summary of Activities: Minerals and Mining (Geoscience BC)
Annual publication

ISSN 2561-4584 (Print)
ISSN 2561-4592 (Online)

Geoscience BC
1101–750 West Pender Street
Vancouver, British Columbia V6C 2T7
Canada

Cover photos and credits (clockwise from top left): 1) QUEST project area, central BC (O. Peterson, 2007); **2)** Search Phase III geophysical survey helicopter, northern BC (B. Madu, 2017); **3)** Quartz vein breccia, central BC (M. Allan, 2016); **4)** Roadcut basal-till sampling site, QUEST-South project, south-central BC (W. Jackaman, 2009); **5)** Endako mine, central BC (W. Jackaman, 2008); **6)** Project map, northern BC (R. Whiten, 2015); **7)** View over Groundbirch area, northeastern BC (S. Morgan, 2016; **8)** Sample recovery of sediment pulps from archive storage, Ottawa ON (W. Jackaman, 2008); **9)** Basal-till sampling, TREK project, central BC (B. Madu, 2016).

Foreword

Geoscience BC is pleased to once again present results from our ongoing projects in our annual *Summary of Activities* publication. For the past 10 years, we have published the results from our minerals and energy projects together in one volume. This year we have decided to publish the 'Minerals and Mining' and 'Energy' papers in two separate volumes. This volume, *Summary of Activities 2017: Minerals and Mining*, contains 11 papers from Geoscience BC–funded projects and 2017 scholarship winners. A second volume, *Summary of Activities 2017: Energy*, contains 10 papers on projects in northeastern British Columbia (BC). Both volumes are also available for download from our website.

Summary of Activities 2017: Minerals and Mining

The first two papers in this volume provide updates on the Search project, which started in 2015. Madu and Ballantyne provide an overview of the Search Phase III airborne magnetic and radiometric survey in the Toodoggone region, the first time Geoscience BC has flown a terrain-contouring survey. Rahimi et al. continue to work in the Search Phase I area near Smithers and, in this volume, their work using ASTER data to identify potential alteration zones is highlighted.

Two papers detail ongoing work in northwestern BC. Arne et al. provide preliminary results on a regional assessment of stream-sediment geochemical data collected as part of the Regional Geochemical Survey program and modernized by Geoscience BC's multiyear reanalysis program. McLeish et al. provide an update on their work examining the nature and origin of the Brucejack deposit.

Southeastern BC continues to be a focus for Geoscience BC. Höy has continued mapping in the Penticton area and, in this volume, introduces his current work in the Greenwood map area (NTS 082E/02). Rioseco and Pattison present preliminary observations on the mineralogically rich interface between the Purcell Anticlinorium and Kootenay Arc.

This past year also saw Geoscience BC taking on new types of projects as part of its growth beyond an early-stage mineral exploration focus. Simister et al. present an introduction to the first genomic study supported by Geoscience BC. Their work aims to develop microbial-community fingerprinting as an exploration tool. Similarly, Mackay et al. summarize the near-final results of the first coal project supported by Geoscience BC, an innovative project using a water-based Roben Jig to clean coal samples prior to analysis of their coking potential.

Three student papers also introduce research topics new to Geoscience BC. Kumar et al. examine rare-earth elements in coal, and Volden et al. examine selenium in the residual produced from biologically treated mine-impacted waters. Finally, Vanderzee et al. introduce research assessing the stabilization of ultramafic mine tailings and reduction of greenhouse gas emissions.

Geoscience BC Minerals and Mining Publications 2017

In addition to the two *Summary of Activities* volumes, Geoscience BC releases interim and final products from our projects as Geoscience BC reports. All Geoscience BC data and reports can be accessed through our website. Geoscience BC released the following minerals and mining reports in 2017:

- 19 technical papers in the *Geoscience BC Summary of Activities 2016* volume (the volume also includes energy papers)
- **Basal Till Potential Maps for the Anahim Lake (NTS 093C/06), Satah Mountain (NTS 093C/07), Downtown Creek (NTS 093C/10), Christensen Creek (NTS 093C/11), Carnlick Creek (NTS 093C/14), Kushya River (NTS 093C/15) Map Areas, British Columbia,** by D. Sacco, H. Arnold, T. Ferbey and W. Jackaman (Geoscience BC Report 2017-02 and British Columbia Geological Survey Open Files 2017-02 to 2017-07)
- **Search Project Phase II: 2016 Airborne Magnetic Survey,** by Sander Geophysics Ltd. (Geoscience BC Report 2017-03)
- **2016 Regional Geochemical Survey Sample Reanalysis Project,** by W. Jackaman (Geoscience BC Report 2017-04)
- **Bedrock Geology, TREK Project Area, Northern Interior Plateau, Central British Columbia (parts of NTS 093B, C, F, and G),** by J.J. Angen, M. Rahimi, C.J.R. Hart, E. Westberg, J.M. Logan and R. Kim (Geoscience BC Map 2017-06-01 and MDRU Map 12-2017)

- **Aeromagnetic Correlation with Bedrock Geology, TREK Project Area, Northern Interior Plateau, Central British Columbia (parts of NTS 093B, C, F, and G),** by J.J. Angen, M. Rahimi, C.J.R. Hart, E. Westberg, J.M. Logan and R. Kim (Geoscience BC Map 2017-06-02 and MDRU Map 13-2017)
- **Constraints on the Metallogeny and Geochronology of the Bridge River Gold District and Associated Intrusions, Southwestern British Columbia (NTS 092J/15),** by C.J.R. Hart and R.J. Goldfarb (Geoscience BC Report 2017-08)
- **Paleomagnetic Evidence for Extreme Block Faulting East of the Rocky Mountain Trench near Kimberley, BC,** by P.W. Ransom, T. Day and R.J. Enkin (Geoscience BC Report 2017-09)
- **Geology of the Christian Valley Map Sheet (NTS 082E/10),** by T. Höy (Geoscience BC Map 2017-10-01)
- **Halogens and Other Volatile Compounds in Surface Sample Media as Indicators of Mineralization, Part 1: Lara VMS Deposit, Vancouver Island, BC (NTS 092B/13),** by D.R. Heberlein, C.E. Dunn and S. Rice (Geoscience BC Report 2017-11)
- **Halogens and Other Volatile Compounds in Surface Sample Media as Indicators of Mineralization, Part 2: Mount Washington Epithermal Au-Cu-Ag Prospect, Vancouver Island, BC (NTS 092F/14),** by D.R. Heberlein, C.E. Dunn and S. Rice (Geoscience BC Report 2017-11)
- **Rapid, Field-Based Hydrogeochemical-Survey Analysis and Assessment of Seasonal Variation Using a Field-Portable Photometer and Voltammeter, Marmot Lake NTS Area, South-Central British Columbia (NTS 093B/13),** by R. Yehia, D.R. Heberlein and R.E. Lett (Geoscience BC Report 2017-13)
- **TREK Project Area Gravity Compilation, Enhancement Filtering and Structure Detection,** by A.J. Buckingham, D.P. Core, C.J.R. Hart and S. Jenkins (Geoscience BC Report 2017-14)
- **Orogenic Gold Mineralization of the Eastern Cordilleran Gold Belt, British Columbia: Structural Ore Controls in the Cariboo (093A/H), Cassiar (104P) and Sheep Creek (082F) Mining Districts**, by M.M. Allan, D.A. Rhys and C.J.R. Hart (Geoscience BC Report 2017-15)

All releases of Geoscience BC reports and data are announced through our website and e-mail list. If you are interested in receiving information regarding these reports and other Geoscience BC news, please contact info@geosciencebc.com. Most final reports and data can be viewed through our Earth Science Viewer at http://www.geosciencebc.com/s/WebMaps.asp.

Acknowledgments

Geoscience BC would like to thank all authors and reviewers of the *Summary of Activities: Minerals and Mining* papers for their contributions to this volume. RnD Technical is also acknowledged for their work in editing and assembling the volume. As well, Geoscience BC would like to thank the Province of British Columbia and our project funding partners for their ongoing support of public geoscience and express appreciation for the leaders and volunteers in British Columbia's mineral exploration, mining and energy sectors who support our organization through their guidance, use and recognition of the information that we collect and distribute.

Christa Pellett
Project Co-ordinator
Geoscience BC
www.geosciencebc.com

Contents

Search Project: Phase III Activities in North-Central British Columbia (Phase III, Covering NTS 094C, D, E, F, 093M, N)

B.E. Madu, Geoscience BC, Vancouver, BC, madu@geosciencebc.com

T. Ballantyne, in3D Geoscience, Vancouver, BC

Madu, B.E. and Ballantyne, T. (2018): Search project: Phase III activities in north-central British Columbia (Phase III, covering NTS 094C, D, E, F, 093M, N); *in* Geoscience BC Summary of Activities 2017: Minerals and Mining, Geoscience BC, Report 2018-1, p. 1–6.

Introduction

The Search project was conceived by Geoscience BC's Minerals Technical Advisory Committee to generate regional magnetic data and complementary earth science for prospective mineral-exploration areas of the province. The exploration sector will use this new information to focus or renew its efforts in discovering and developing opportunities within the province. First Nations, communities and governments will also benefit from new earth science because it will help them make more informed resource-management decisions and will highlight economic opportunities.

The name 'Search' was selected as it contains the word 'arch', a reference to the program's initial focus on the Skeena arch—a paleotopographic high whose erosion created the sediments found in the Bowser and Nechako basins (Tipper and Richards, 1976). Today, this arch bridges the gap between the Stikine and Quesnel geological terranes.

The Search project is, in part, a generation of airborne geophysical surveys with a line spacing of 250 m that creates opportunities for geological interpretations at a property scale. The large scale of the surveys can also support the development of refined tectonic frameworks. Other Geoscience BC projects with similar-style surveys are the TREK, Northern Vancouver Island, QUEST-Northwest and Jennings River (partnership with Natural Resources Canada) projects (Figure 1).

The Search project in 2017 departed from plans by surveying an area farther to the north than was forecasted for the year (Madu, 2017). This change was proposed by Geoscience BC's Technical Advisory Committee to stimulate exploration interest in an area where the organization had never before conducted an airborne survey (i.e., north of the original QUEST survey). The project boundary was designed to complement the joint BC Geological Survey–Geological Survey of Canada Toodoggone survey completed in 2003 (Shives et al., 2004).

The approximate centre of the survey area is located 250 km north of Fort St. James, 225 km northwest of Mackenzie, 200 km northeast of Smithers and 325 km west of Fort St. John (Figure 2). Closer to the survey are the communities of Fort Ware (known locally as 'Kwadacha'), Tsay Key Dene and Takla Landing, where many of the region's indigenous residents live.

As the survey area is remote and the terrain rugged, a budget of $1.7 million was identified for this year's program. Significant support of $250 000 from the Northern Development Initiative Trust allowed the survey to expand to the north and include the proposed Kemess underground mine (Figure 3), located within the Peace River Regional District (MINFILE 094E 021; BC Geological Survey, 2017). The extension will provide valuable new data on this important mining camp for explorers to interrogate in their regional programs (for background on the Kemess camp, see Rebagliati et al., 1995).

In addition to the proposed mine area, the survey flew the greater 'camp', where encouraging potential is being recognized in areas such as the Kemess East project (AuRico, 2017; MINFILE 094E 315). The survey also overflew several significant projects, such as the Kliyul, Lorraine and Sustut (Figure 3; MINFILE 094D 023, 094D 113, 093N 002, 094D 063).

Regional Geology

The regional geology of the survey and surrounding area is unique, since it is here that two of British Columbia's (BC's) metal-endowed geological terranes, the Quesnel and Stikine, come into contact (Figure 3; Monger et al., 1991; Nelson et al., 2013). The majority of the province's operating copper-molybdenum-gold mines are located within these terranes. The Quesnel terrane is at its northernmost extent in the survey area, while the Stikine terrane is at its easternmost extent. These terranes are separated by the regional-scale Pinchi-Ingenika-Finlay fault system, which traverses the approximate centre of the survey area in a north to northwest orientation. A section of the Cache

This publication is also available, free of charge, as colour digital files in Adobe Acrobat® PDF format from the Geoscience BC website: http://www.geosciencebc.com/s/SummaryofActivities.asp.

Figure 1. Location of other Geoscience BC airborne geophysical surveys with 250 m line spacing include the Search Phases I and II, TREK, Northern Vancouver Island, QUEST-Northwest and Jennings River (with Natural Resources Canada) projects. Blue outline, Search Phase III survey area; red outlines, coverage of previous airborne geophysical surveys conducted or funded by Geoscience BC.

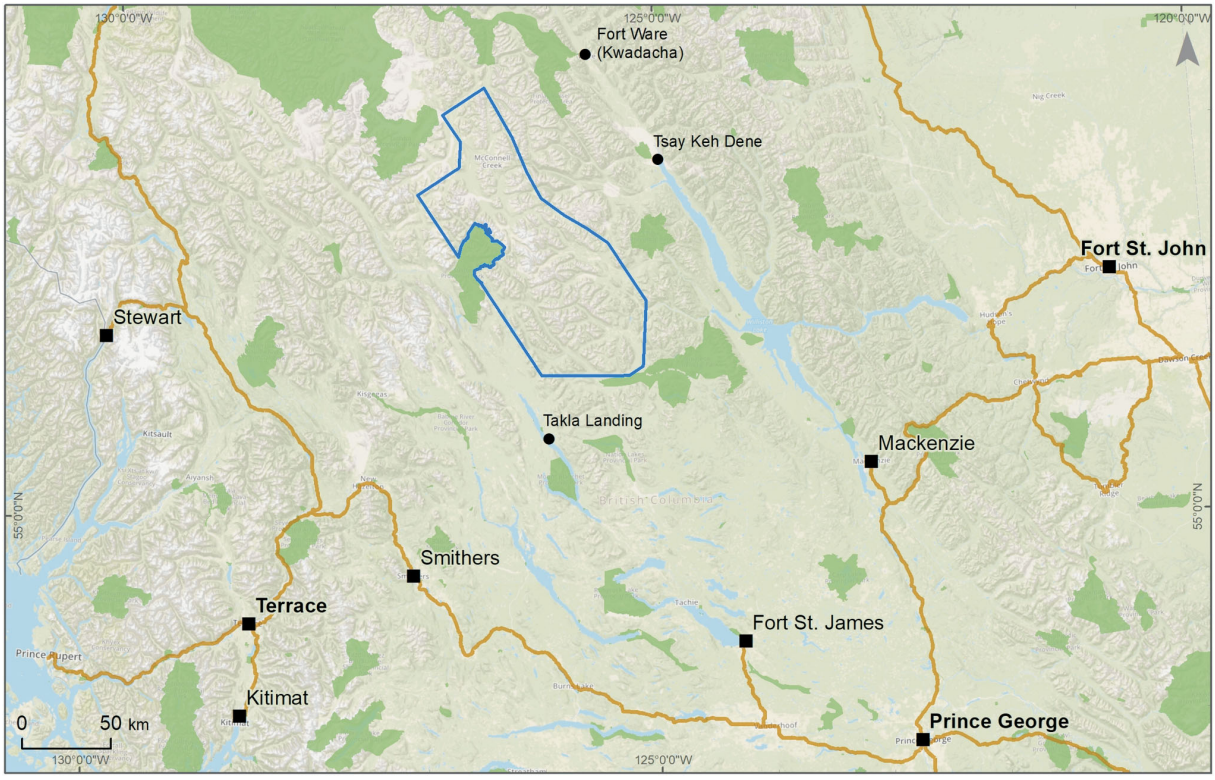

Figure 2. Location of the Search Phase III project in relation to communities of north-central British Columbia. Blue outline, Search Phase III survey area.

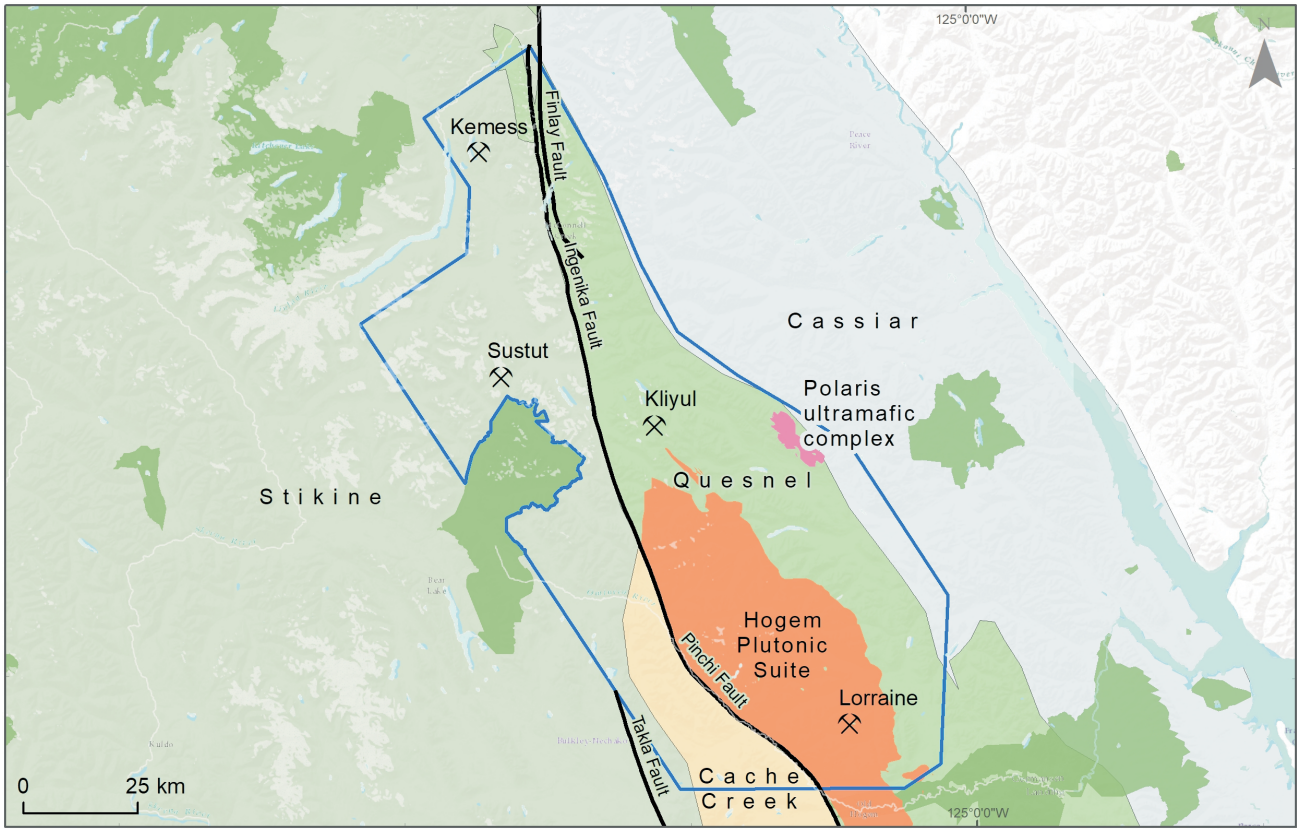

Figure 3. Regional tectonic setting surrounding the Search Phase III survey area, showing the contact between the Quesnel and Stikine terranes, and the locations of the Hogem Plutonic Suite and Polaris ultramafic complex.

Creek terrane is found in the southwestern portion of the survey area.

The Hogem Plutonic Suite is a regional-scale igneous body that intrudes the Quesnel terrane and is bounded on the west by the Pinchi-Ingenika fault (Garnet, 1978). It has been subdivided into three phases based on age and composition. Phase I is oldest (212–176 Ma), calcalkaline in composition and reportedly poorly mineralized. Phase II is dated at 182–162 Ma, alkaline in composition and of significant interest to explorers where its syenitic rocks and related potassium-feldspar alteration are spatially associated with numerous copper occurrences (e.g., Duckling Creek syenite). Phase III, the youngest, is dated at 126–108 Ma, calcalkaline in composition and spatially associated with copper and molybdenum mineralization. Although there is already a considerable amount of knowledge concerning the Hogem Plutonic Suite, new insights will be gained from the Search Phase III survey that should stimulate explorers to challenge current assumptions of mineral potential and test new ideas. In particular, the collection of radiometric data over the survey area may provide new discrimination of the batholith's phases, including the alteration signatures that are key in identifying areas with higher mineral potential.

The Stikine terrane is host to the Kemess mine camp at the northern end of the survey. South of this camp are portions of the Stikine terrane that are currently less explored and, at the time of writing, several MINFILE occurrences were untenured. The western survey boundary is roughly defined by the mapped transition from Stikine terrane to Upper Cretaceous Sustut Group.

The eastern survey boundary is roughly defined by the mapped boundary between the Quesnel and Cassiar terranes. Rocks of the Cassiar terrane were not targeted by the survey, but those of the Polaris ultramafic complex were included.

Terrain Contouring versus Preplanned Drape-Surface Surveying

The Search Phase III survey was the first time that Geoscience BC solicited proposals allowing for the option of either an 80 m clearance terrain-contouring survey or a preplanned drape-surface survey. This was undertaken in response to airborne-survey service providers suggesting that the higher quality of terrain-contouring survey data should be considered against the higher cost of acquisition.

Geoscience BC chose a terrain-contouring survey because of the benefit it would bring to both the magnetic-radiometric data and the end user. The lower and more consistent survey height above ground allows for increased data amplitude and improved resolution of near-surface complex

sources. Surveys conducted along higher preplanned drape surfaces risk complex or multiple-source responses coalescing into apparent single responses or poorly defined source responses due to excessive ground clearance. Preplanned drape surveys in rugged terrain can yield data that are highly attenuated in valleys due to the necessity of designing a flight surface within a specific aircraft's climb and descent limitations. Radiometric data benefit from terrain contouring by having less reliance on elevation-related data-attenuation corrections, as well as a reduction in data that are nulled because the maximum allowable effective height for spectrometer count-rate confidence was exceeded. A boom-mounted horizontal-magnetic-gradient system fixed to the aircraft was chosen over a towed-bird configuration. The anticipated benefits were better terrain contouring, increased spectrometer signal amplitude and pilot safety. Helicopter terrain-contour surveys result in increased cost and survey duration relative to the more common fixed-wing preplanned drape surveys. However, the extra cost results in superior data for both magnetic and radiometric surveys. An example of the various survey flight surfaces over rugged topography is shown in Figure 4. The red profile is actual survey height above Shuttle Radar Topography Mission (SRTM) topography, whereas the blue profiles are 2-D preplanned drape surfaces of 6% (fixed-wing aircraft) and 40% (helicopter) calculated using the Geological Survey of Canada's Drape DTM 2.0 software.

Geophysical Program

Search Phase III field activities began in early July 2017 after a contract was awarded to Ontario-based CGG Canada Services Ltd. The contract was to fly an estimated 42 286 line-km using two helicopters fitted with the proprietary Midas horizontal-gradient multisensor package for magnetic surveying (Figure 5) and acquire data at a nominal 80 m terrain-contouring height. Main flight lines trended 054° at 250 m intervals and tie lines trended 234° at 2500 m intervals. The survey also collected radiometric data as a secondary priority: flights were optimized for magnetic-data collection and not altered where radiometric data were expected to be compromised (e.g., rain-saturated ground). Quality assurance and control for the program data was provided by in3D Geoscience Inc.

Pilots followed operating procedures for wildlife observations and were authorized to deviate flight patterns to mitigate negative effects. A temporary program cessation in mid-September to accommodate the seasonal activities of an outfitting operator delayed program completion by nearly a month. Two base camps were established, at the Kemess mine and the Osilinka logging camp, with remote fuelling depots in additional locations.

Results of the 9600 km^2 survey are scheduled for release at AME RoundUp 2018 in map and digital format through the Geoscience BC website, and as an interactive map layer on the organization's Earth Science Viewer. The Earth Science Viewer allows a broad client base to immediately interact with Geoscience BC's data alongside other public information, such as current mineral tenures and the BC Geological Survey's geological, MINFILE and ARIS data.

Porphyry Integration Project

Geoscience BC has supported the creation of two geoexploration atlases, for the Endako (Devine et al., 2015) and Mount Polley mines (Rees et al., 2014), and two more are in preparation, for the Mount Milligan mine and the Duckling Creek syenite. These atlases are compendiums of datasets (e.g., geology, geochemistry and geophysics) plotted at deposit and camp scales in a single document. These 'coffee table–style' atlases are reference books for the deposits or camps, intended as teaching aids for relevant mineral-deposit models and for exploration courses.

Production of the Duckling Creek atlas awaits magnetic and radiometric data from this survey for areas where the Duckling Creek syenite is known to exist. Once the data

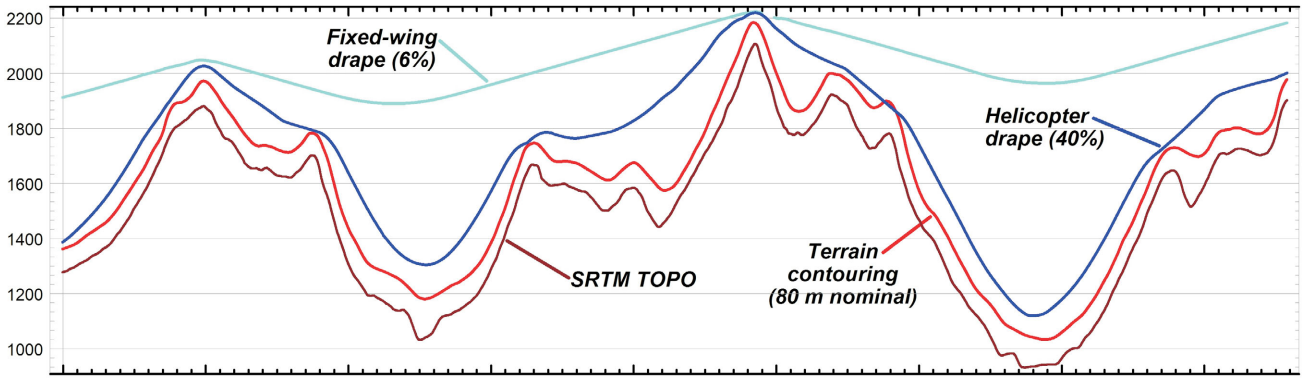

Figure 4. Example of improved airborne survey height above rugged topography using terrain contouring (red line) compared to the more common 2-D preplanned drape surveys: fixed-wing drape surface using 6% slope (light blue) and a hypothetical helicopter 40% drape surface (dark blue). The 2-D drape surfaces were calculated using the Geological Survey of Canada's Drape DTM 2.0 software. Note that the vertical axis is exaggerated. All survey heights are relative to Shuttle Radar Topography Mission topography (SRTM TOPO).

Figure 5. One of two helicopters used in flying the Search Phase III survey. The aircraft were fitted with booms to collect magnetic data using the proprietary Midas horizontal-gradient system of CGG Canada Services Ltd. Radiometric data were collected utilizing a Radiation Solutions Inc. RS-500 digital airborne gamma-ray spectrometer.

have been incorporated into the atlas, it is expected to be released in 2018.

Summary

The Search project is a multiyear project for Geoscience BC that is focused on generating regional magnetic-survey data and complementary earth science for prospective mineral areas of the province. In 2017, the project included an airborne survey covering 9600 km^2. Data from the survey will be made available through both Geoscience BC's website and on its web mapping application—the Earth Science Viewer.

Explorers will have access to new high-quality data from which they can both generate property-level targets for exploration and, since the survey is regional in scale, understand their projects in a broader context. Researchers will be able to develop new regional-scale frameworks to understand the geological history of the region and identify metallogenic trends and opportunities. Land-use planners, governments and First Nations will have modern data from which resource-management or economic-development opportunities can be identified.

Acknowledgments

This paper benefited from a constructive review by C. Salas, Geoscience BC.

References

AuRico (2017): AuRico Metals announces positive preliminary economic assessment for Kemess East gold-copper project; AuRico Metals Inc., press release, May 29, 2017, URL <http://s2.q4cdn.com/215682844/files/doc_news/2017/2017-05-29-AMI-Kemess-East-PEA-FINAL.pdf> [October 2017].

BC Geological Survey (2017): MINFILE, British Columbia mineral deposit database; BC Ministry of Energy, Mines and Petroleum Resources, BC Geological Survey, URL <http://www.minfile.ca> [October 2017].

Devine, F.A.M., Pond, M., Heberlein, D.R., Kowalczyk, P. and Kilby, W. (2015): A geo-exploration atlas of the Endako porphyry molybdenum district; Geoscience BC, Report 2015-08, 44 p., URL <http://www.geosciencebc.com/s/Report2015-08.asp> [November 2017].

Garnett, J.A. (1978): Geology and mineral occurrences of the southern Hogem batholith; BC Ministry of Energy, Mines and Petroleum Resources, Bulletin 70, 75 p.

Madu, B.E. (2017): Search project: Phase II activities in west-central British Columbia (phases I and II, covering NTS 093E, F, G, K, L, M, N, 103I); *in* Geoscience BC Summary of Activities 2016, Geoscience BC, Report 2017-1, p. 91–94. URL <http://www.geosciencebc.com/i/pdf/SummaryofActivities2016/SoA2016_volume.pdf> [November 2017].

Monger, J.W.H., Wheeler, J.O., Tipper, H.W., Gabrielse, H., Harms, T. and Struik, L.C. (1991): Upper Devonian to Middle Jurassic assemblages; Chapter 8 *in* Geology of the Cordilleran Orogen in Canada, H. Gabrielse and C.J. Yorath (ed.), Geological Survey of Canada, Geology of Canada, no. 4, p. 281–327.

Nelson, J.L., Colpron, M. and Israel, S. (2013): The Cordilleran of British Columbia, Yukon and Alaska: tectonics and metallogeny; *in* Tectonic, Metallogeny, and Discovery: The North American Cordillera and Similar Accretionary Settings, M. Colpron, T. Bissig, B.G. Rusk and J.F.H. Thompson (ed.), Society of Economic Geologists, Special Publication 17, p. 53–109.

Rebagliati, C.M., Bowen, B.K., Copeland, D.J. and Niosi, D.W.A. (1995): Kemess South and Kemess North porphyry gold-copper deposits, northern British Columbia; *in* Porphyry Deposits of the Northwestern Cordillera of North America, T.G. Schroeter (ed.), Canadian Institute of Mining, Metallurgy and Petroleum, Special Volume 46, p. 377–396.

Rees, C., Gillstrom, G., Ferreira, L., Bjornson, L. and Taylor, C. (2014): Geology of the Mount Polley intrusive complex; Geoscience BC, Report 2014-08. URL <http://www.geosciencebc.com/s/Report2014-08.asp> [November 2017].

Shives, R.B.K., Carson, J.M., Ford, K.L., Holman, P.B. and Diakow, L. (2004): Helicopter-borne gamma ray spectrometric and magnetic total field geophysical survey, Toodoggone area, British Columbia; BC Ministry of Energy, Mines and Petroleum Resources, BC Geological Survey, Open File 2004-08 and Geological Survey of Canada, Open Files 4606–4613.

Tipper, H.W. and Richards, T.A. (1976): Jurassic stratigraphy and history of north-central British Columbia; Geological Survey of Canada, Bulletin 270, 73 p.

Application of ASTER Data to Identify Potential Alteration Zones on Microwave Ridge, Northeastern Search Project Area, West-Central British Columbia (part of NTS 093L)

M. Rahimi, Mineral Deposit Research Unit (MDRU), The University of British Columbia, Vancouver, BC, mrahimi@eoas.ubc.ca

J.J. Angen, MDRU, The University of British Columbia, Vancouver, BC

C.J.R. Hart, MDRU, The University of British Columbia, Vancouver, BC

Rahimi, M., Angen, J.J. and Hart, C.J.R. (2018). Application of ASTER data to identify potential alteration zones on Microwave ridge, northeastern Search project area, west-central British Columbia (part of NTS 093L); *in* Geoscience BC Summary of Activities 2017: Minerals and Mining, Geoscience BC, Report 2018-1, p. 7–22.

Introduction

Geoscience BC's Search project (Phase I) area is located between the towns of Smithers and Terrace, British Columbia (BC), and encompasses the western Skeena arch tectonic domain across the Stikine terrane (Figure 1a). This is a highly prospective region that hosts more than 220 metallic mineral occurrences, including abundant vein-type Cu-(Ag-Au) deposits, six of which have historically been mined by hand (e.g., Copper Queen mine, refer to Stock MINFILE 093L 085, BC Geological Survey, 2017). Among the Cu-(Ag-Au) occurrences are numerous examples that are classified as conforming to the volcanic-hosted redbed-copper mineral-deposit model, and others that are assigned to a variety of intrusion-related and subvolcanic mineral-deposit models. There are 54 mineral occurrences that are ambiguously classified as both, despite their mutually exclusive genetic origins.

Distinguishing between these mineral-occurrence types has value for explorers since intrusion-related occurrences are a potential indicator for significant styles of mineralization such as porphyry copper systems, whereas redbed-copper occurrences are not. Methods to potentially discriminate between these two deposit types include gaining a better understanding of their geological setting and identifying the nature of the alteration footprints, which are different for these two mineralization styles. Volcanic-hosted redbed-copper occurrences are typically stratabound and are associated with minimal alteration (Lefebure and Church, 1996), whereas intrusion-related copper veins crosscut stratigraphy, are associated with intrusions and the veins typically have significant sericite-clay– and/or chlorite–alteration zones (Lefebure, 1996) that can be zoned around a central core.

This publication is also available, free of charge, as colour digital files in Adobe Acrobat® PDF format from the Geoscience BC website: http://www.geosciencebc.com/s/SummaryofActivities.asp.

Satellite-acquired infrared spectral data are a valuable source of remotely sensed information that can identify alteration mineralogy that formed from interactions between the hostrock and hot hydrothermal fluids, which may also form metallic mineral deposits. Many alteration minerals (or groups of alteration minerals) have characteristic or diagnostic absorption features that can be remotely detected in infrared spectral data. Advanced Spaceborne Thermal Emission and Reflection Radiometer (ASTER) spectral data, in particular, can be utilized to remotely map the distribution of specific minerals that form different types of alteration potentially related to mineralizing processes. Such remote-sensing technologies have been widely and successfully used for lithological and alteration-mineral mapping as a contribution to mineral exploration efforts (Watts and Harris, 2005; Azizi et al., 2010; Rajendran et al., 2012; Van Ruitenbeek et al., 2012).

Microwave ridge is an informal name given to a northwest-trending ridge in the central portion of the Skeena arch, approximately 15 km southwest of Hudson Bay Mountain, west of the town of Smithers (Figure 1a). This area hosts three ambiguously assigned Cu-(Ag-Au) occurrences and was chosen to test the effectiveness of alteration mapping using ASTER data in distinguishing between intrusion-related and volcanic-hosted redbed-copper types of mineral occurrences. Microwave ridge is an ideal location due to the relatively simple geology of this area, such that variations in spectral responses are likely the product of hydrothermal alteration, and not simply caused by the underlying lithology.

Geological Setting

Regional Geology

The Skeena arch is an east-northeast-trending geomorphological belt that transects the Stikine terrane in central BC. It is underlain by Mississippian through Neogene rocks that record the transition from island-arc magmatism and re-

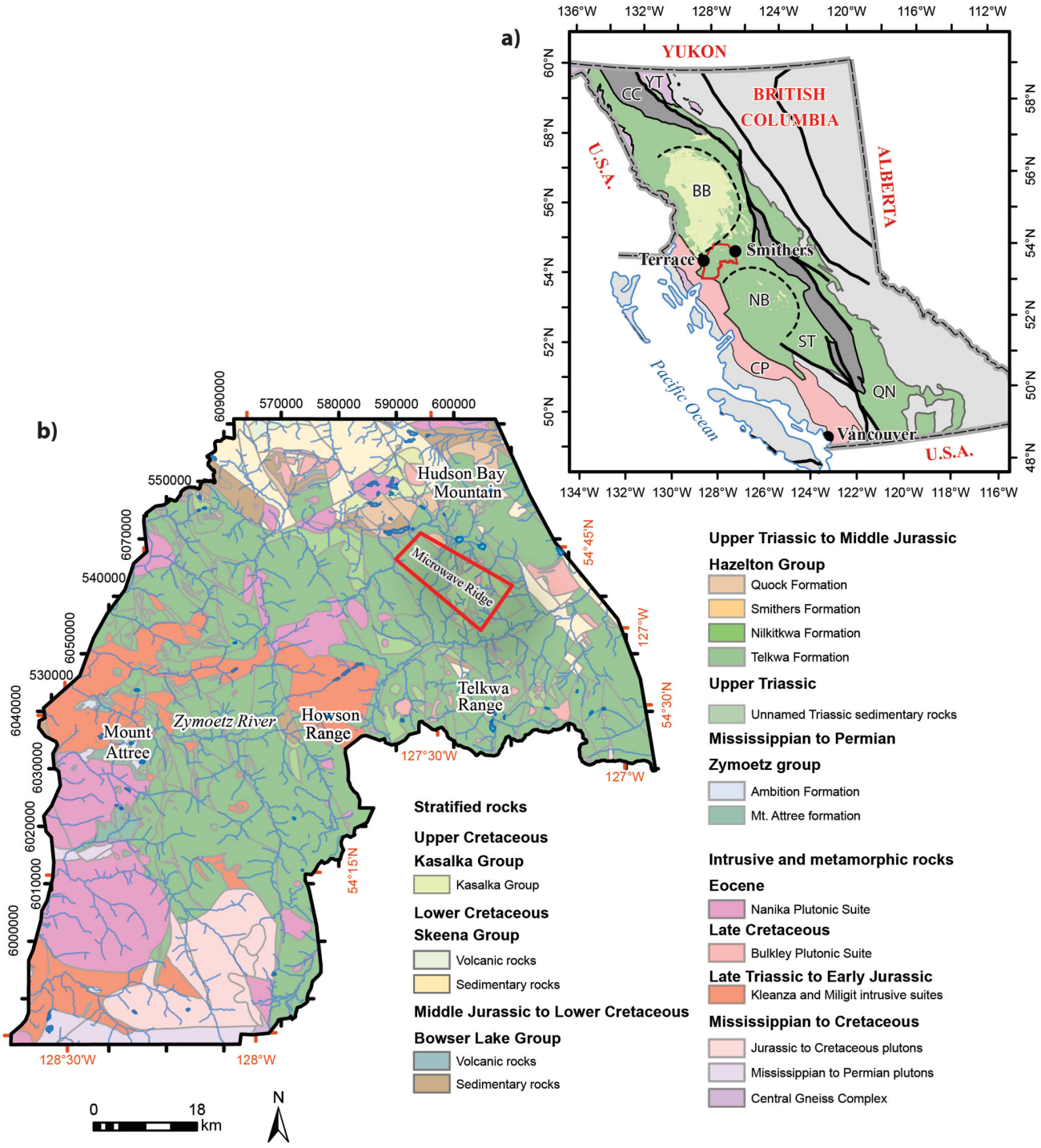

Figure 1. Search project in west-central British Columbia: **a)** location of the area of interest within the context of selected terranes and tectonic elements in British Columbia, including the Cache Creek (CC), Quesnel (QN), Stikine (ST) and Yukon-Tanana (YT) terranes, Coast Plutonic Complex (CP), Bowser Basin (BB) and Nechako Basin (NB)—the Skeena arch corresponds to the region between the Bowser and Nechako basins (terranes modified after Colpron and Nelson, 2011; strata deposited in the Bowser and Nechako basins modified after Cui et al., 2015); **b)** simplified geology of the area of interest, with the outline of the Microwave ridge study area in red (distribution of rock units modified after Cui et al., 2015). Place name with the generic in lower case is unofficial.

lated sedimentation of the Stikine terrane to post-accretionary continental-margin–arc magmatism and sedimentation of the overlap assemblages. The oldest rocks are primitive-arc volcanic rocks of the Mississippian to Permian Mt. Attree formation, which form isolated exposures in the western Search project area (Figure 1b; Nelson et al., 2008). They are overlain by Permian limestone of the Ambition Formation and an unnamed Middle Triassic unit of thin-bedded chert and argillite (Nelson et al., 2006). Mississippian to Permian intrusions in the southwestern corner of the Search project area occur with younger intrusions and metamorphic rocks that make up the Coast Plutonic Complex (Figure 1a).

The most widely exposed rock unit is the uppermost Upper Triassic to Lower Jurassic Telkwa Formation of the Hazelton Group. At the latitude of the Skeena arch, the Telkwa Formation has been subdivided into the western Howson subaerial facies, the central Babine shelf facies and the eastern Kotsine submarine facies (Tipper and Richards, 1976a). The Search project area is mostly within the Howson facies, named after the Howson Range (Figure 1b). The transition easterly from the Howson to the Babine facies is marked by increasing proportions of sedimentary rocks. The Kleanza intrusive suite is the plutonic equivalent of the Telkwa Formation (Nelson, 2017). Slightly older Late Triassic intrusive rocks in the Howson Range are herein called the Miligit intrusive suite (Figure 1). The proportion of sedimentary rocks also increases upsection within the Hazelton Group. The Telkwa Formation is conformably and locally gradationally overlain by mixed sedimentary and volcanic strata of the Nilkitkwa Formation (Pliensbachian to Toarcian; Tipper and Richards, 1976a). The Nilkitkwa Formation includes the Red Tuff Member: a sequence of well-bedded, brick red, crystal-lithic Toarcian tuff, with minor basalt and rhyolite that are (nearly) indistinguishable from the red tuffs in the upper Telkwa Formation (Tipper and Richards, 1976a). The Nilkitkwa Formation is overlain by tuffaceous sandstone of the Smithers Formation (Toarcian to Bathonian) and tuffaceous mudstone of the Quock Formation (Bajocian to Callovian; Gagnon et al., 2012).

The Hazelton Group is gradationally overlain by siliciclastic rocks of the Bowser Lake Group (Figure 1b). The uppermost distinguishable tuff bed within a sequence of deep marine sedimentary rocks marks the boundary between these two groups along the southern margin of the Bowser Basin (Evenchick et al., 2010). Middle Jurassic to Lower Cretaceous sedimentary rocks of the Bowser Lake Group are rare across most of the Skeena arch, which supports it being interpreted as a topographic highland that formed the southern boundary of the Bowser Basin and the northern boundary of the Nechako Basin at that time (Tipper and Richards, 1976a). In the central Skeena arch, the Bowser Lake Group is absent and Lower to Upper Cretaceous sedimentary and volcanic rocks of the Skeena Group unconformably overlie the Telkwa Formation (Figure 1b; Palsgrove and Bustin, 1991). The Upper Cretaceous Kasalka Group volcanic rocks locally overlie the Skeena Group (Figure 1b).

The Late Cretaceous Bulkley and Eocene Nanika plutonic suites are widespread across the Skeena arch (Figure 1b). They typically occur as small stocks, dikes and sills of diorite to monzogranite. The majority of mineralization within the Skeena arch is associated with these Late Cretaceous and Eocene intrusions (MacIntyre, 2006).

Microwave Ridge Geology

Microwave ridge is underlain by a series of moderately northeast- to southeast-dipping homoclinal panels of Telkwa Formation volcanic rocks that are separated by northwest-trending faults with minimal displacement (Figure 2). The Telkwa Formation in this area includes a lower unit of andesitic lapilli tuff, aphyric basalt and rhyolite lenses; a middle tuffaceous sedimentary unit; and an upper unit of quartz-bearing dacitic tuff. The stratified rocks are cut by isolated intrusions that are interpreted as belonging to the Bulkley Plutonic Suite (Figure 2).

Lower Telkwa Formation Andesitic Tuff Unit

The lower Telkwa Formation on Microwave ridge includes fine-grained basalt flows, andesitic to dacitic lapilli tuff and ash tuff, rhyolite lenses and minor interbedded sedimentary rocks. Basalt flows are typically aphyric, fine grained and dark grey, with purple and maroon pumiceous flow-top breccias (Figure 3a). They locally contain chlorite- or calcite-filled amygdules and well-developed Liesegang rings. Zeolite- and epidote-cemented flow-top breccias were reported by MacIntyre et al. (1989b). Basalt flows are 2–10 m thick and are not laterally continuous. They are interpreted to fill paleotopographic depressions and/or scoured lava-flow channels. Lapilli-tuff beds are maroon to brick red, with fragments of plagioclase-phyric andesite, cream-coloured rhyolite and dark grey basalt, as well as up to 15% plagioclase-crystal fragments. One lapilli-tuff bed at the top of this sequence includes 3% quartz-crystal fragments. Individual tuff beds vary from 10 cm to 5 m in thickness and are laterally continuous.

Middle Telkwa Formation Sedimentary Unit

A lens of epiclastic conglomerate, siltstone, calcareous tuff and limestone bisects Microwave ridge and overlies the quartz-bearing lapilli tuff described above (Figure 2). Conglomerate beds contain well-rounded cobbles to boulders of volcanic rock units similar to the underlying lower Telkwa Formation within a coarse sand matrix (Figure 3b). Carbonate-rich sandstone and tuff beds weather recessively (Figure 3b). Fine- to coarse-grained epiclastic sandstone occurs in planar beds 5–10 cm thick, some of which fine up-

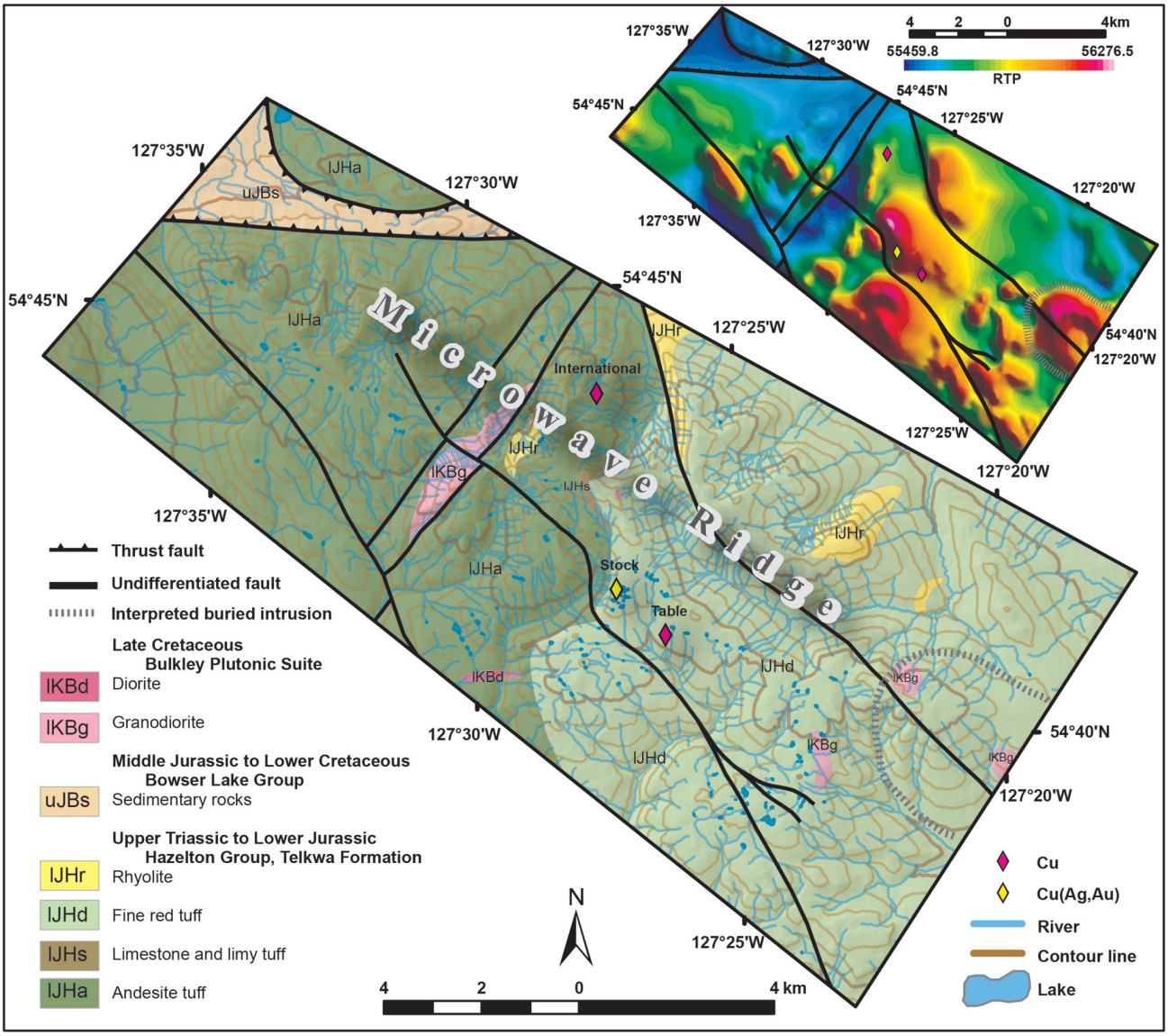

Figure 2. New geological interpretation for Microwave ridge, west-central British Columbia, integrated from previous geological mapping (Tipper and Richards, 1976b; MacIntyre et al., 1989a), aerial photographs, new aeromagnetic data and ground truthing. Inset is reduced-to-pole aeromagnetic data for the Microwave ridge area (modified after Precision GeoSurveys Inc., 2016).

ward into maroon mudstone. MacIntyre et al. (1989b) reported pure limestone as a component of this sedimentary sequence.

MacIntyre et al. (1989b) interpreted this lens as part of the Nilkitkwa Formation. Desjardins et al. (1990) interpreted a similar fossiliferous sedimentary sequence in the Thautil River map area to the south as a component of the Telkwa Formation. Stanley and McRoberts (1993) studied a Sinemurian reef in the Thautil River map area, which they assigned to the Nilkitkwa Formation, yet also acknowledged that other workers consider it to be part of the Telkwa Formation. New, preliminary U-Pb zircon analyses of samples bracketing the sedimentary sequence on Microwave ridge yield overlapping ages of 197.5 ±2.6 Ma and 201.5 ±1.5 Ma. The Nilkitkwa Formation, as originally described, is dominantly black mudstone, with abundant Pliensbachian fossils in the base of the unit as well as restricted Toarcian volcanic rocks (Tipper and Richards, 1976a). These shallow-marine sedimentary rocks are interbedded with Hettangian to Sinemurian volcanic rocks, which indicates that they are not part of the Nilkitkwa Formation but are rather a sedimentary inlier of the Telkwa Formation. Tipper and Richards (1976a) reported isolated marine sedimentary rocks, including limestone interbedded with subaerial volcanic rocks, at the transition zone between the Howson and Babine facies of the Telkwa Formation.

Upper Telkwa Formation Dacitic Tuff Unit

The upper Telkwa Formation is dominated by brick red dacitic lapilli, crystal and ash tuff, with minor rhyolite,

sandstone and siltstone. Dacitic tuff beds vary from 5 cm to 5 m in thickness and are normally graded. Lapilli-tuff components contain maroon and purple, aphanitic to sparsely plagioclase-phyric lapilli, rare beige rhyolitic lapilli, up to 3% quartz-crystal fragments and 5–10% feldspar-crystal fragments in fine red-ash groundmass. Some beds contain accretionary lapilli (Figure 3c). This section includes interbedded sandstone and siltstone. The upper contact of the Telkwa Formation is not exposed in this area.

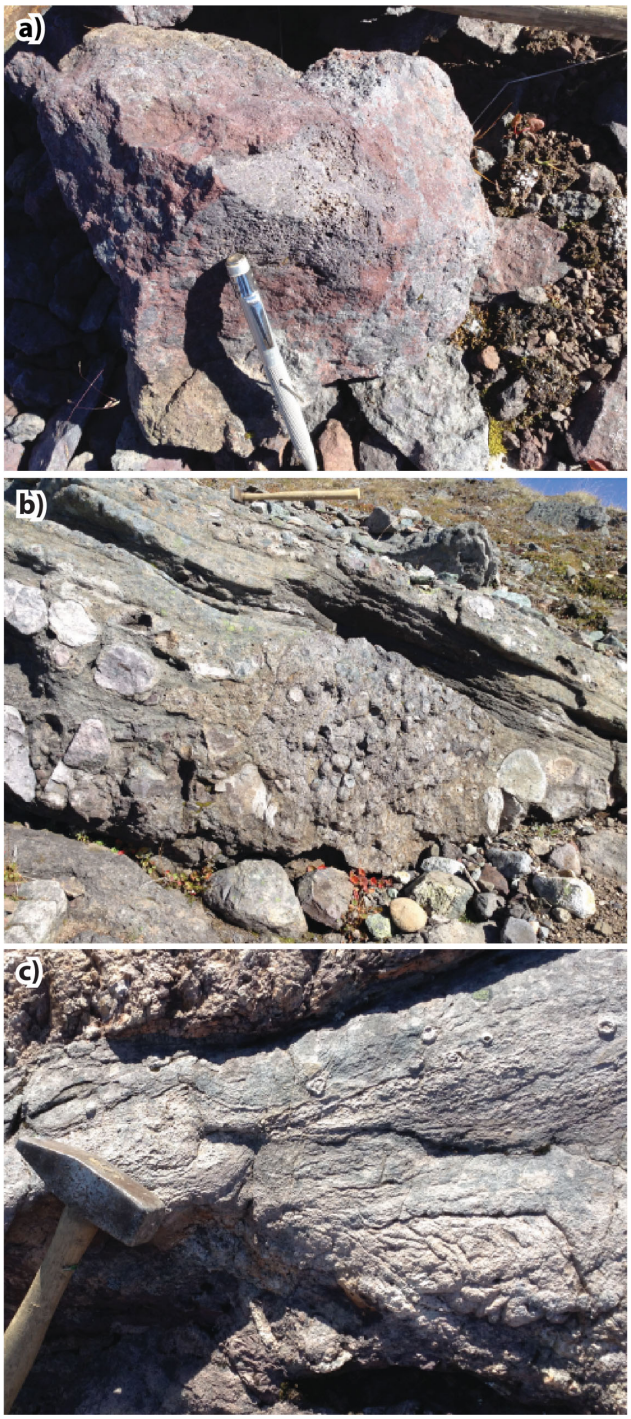

Figure 3. Characteristic rock units of the Telkwa Formation on Microwave ridge, west-central British Columbia: **a)** pumiceous breccia in Telkwa Formation basalt; **b)** Telkwa sedimentary unit, with conglomerate and recessively weathering limy epiclastic sandstone; **c)** Telkwa Formation red dacite tuff, with accretionary lapilli.

Telkwa Formation Rhyolite

Rhyolite lenses up to 2 km wide and 1 km thick occur within the lower and upper volcanic units on Microwave ridge (MacIntyre et al., 1989b). They include flow-banded and spherulitic flow domes, which locally intrude older volcanic rocks, but also occur as concordant lapilli-tuff accumulations. These centres of rhyolite contain trace to 2% pyrite and typically lack quartz phenocrysts. Some fine-grained felsic exposures were previously interpreted as Cretaceous or Eocene felsite intrusions (Tipper and Richards, 1976b; MacIntyre et al., 1989a). The presence of rhyolite lapilli fragments within red-tuff beds indicates that at least some of the rhyolite belongs to the Telkwa Formation. Where Telkwa Formation rhyolite flow domes and breccias occur elsewhere in the Search project area, they have low magnetic susceptibilities (average of 0.2×10^{-3} SI based on data collected by the authors) in contrast to the much younger Bulkley and Nanika felsic intrusive suites (see below). Felsic intrusions mapped as 'felsite' on Microwave ridge by Tipper and Richards (1976b) and MacIntyre et al. (1989a) lack corresponding high aeromagnetic anomalies and are therefore tentatively interpreted as Telkwa Formation rhyolite and not younger intrusions.

Bowser Lake Group

In the valley north of Microwave ridge, there is a domain of low magnetic response (Figure 2 inset). This corresponds to an area that is interpreted to be underlain by Bowser Lake Group sedimentary rocks (Tipper and Richards, 1976b). Where the Bowser Lake Group is exposed farther west, it includes well-bedded sandstone, siltstone and minor granule conglomerate with Callovian shallow-marine fossils (Tipper and Richards, 1976a). This domain is in fault contact with the Telkwa Formation to the north and south (Figure 2).

Bulkley (or Nanika) Plutonic Suite

Isolated exposures of quartz-feldspar porphyry and diorite on Microwave ridge were assigned previously to the Bulkley (or Nanika) Plutonic Suite (Tipper and Richards, 1976b; MacIntyre et al., 1989a). The Bulkley Plutonic Suite in the Search project area typically consists of quartz-phyric diorite to granodiorite, and the Nanika Plutonic Suite intrusions are typically porphyritic monzogranite to diorite. Both plutonic suites contain magnetite that results in typically high average magnetic susceptibilities (combined average of 7.7×10^{-3} SI, based on data collected by the authors). As noted by Angen et al. (2017), these units typically correspond to regions of high aeromagnetic response. Both units are also associated with significant mineralization in the Skeena arch (MacIntyre, 2006).

Two previously mapped exposures of quartz-feldspar–phyric granodiorite (Tipper and Richards, 1976b; MacIntyre et al., 1989a) at the southeastern end of Microwave ridge are within a ~3 km long ovoid-shaped aeromagnetic high that likely indicates a buried magnetite-bearing intrusion (Figure 2). A pronounced northeast-trending aeromagnetic high bisects Microwave ridge and corresponds to two parallel faults that were mapped by Tipper and Richards (1976b; Figure 2 inset). This aeromagnetic high corresponds to resistant, light grey, massive rocks that are exposed between well-bedded maroon volcanic rocks to the northwest and southeast, as observed in aerial photographs. These light grey rocks are interpreted as a probable magnetite-bearing granodiorite dike. All of the magnetic intrusive rocks that are exposed on Microwave ridge are tentatively assigned to the Bulkley Plutonic Suite.

Structure of Microwave Ridge

Numerous northwest-trending faults, identifiable from minor linear topographic depressions, are visible in aerial photos. Most faults are minor and only a few hundred metres long with no significant impact on the geology. A few are more continuous and separate structural domains that have internally consistent bedding orientations (Figure 2).

A thrust fault juxtaposes the Telkwa Formation on Microwave ridge on top of sedimentary rocks of the Bowser Lake Group (Tipper and Richards, 1976b). A top-to-the-north displacement component is inferred, since the footwall exposures are some of the southernmost exposures of Bowser Basin rocks (Tipper and Richards, 1976a). The age of the thrust is uncertain but must be younger than Callovian, based on the age of the rocks in the footwall. Fault movement is likely coeval with the Early Cretaceous or younger northeast-trending folds and northwest-vergent thrust faults that are documented elsewhere in the Skeena arch (Angen et al., 2017).

ASTER Spectral Data

The Advanced Spaceborne Thermal Emission and Reflection Radiometer (Jet Propulsion Laboratory, 2017) is a multispectral imager. The imager was launched on the panel of the National Aeronautics and Space Administration (NASA) Terra spacecraft in December 1999 (Kalinowski and Oliver, 2004). The most important feature of ASTER images, in comparison with other multispectral images, is that ASTER covers a wide spectral zone with 14 bands from the visible to the thermal infrared. The ASTER images provide high spatial, spectral and radiometric resolution compared to other images used in the earth sciences, such as Landsat 7 ETM+ and Landsat 8 (OLI). The wavelength range of 2–2.5 micrometres (µm) is the most suitable part of the spectrum for identifying hydroxyl-bearing minerals, carbonates and iron oxides, which have a significant absorption feature in this range; all of these mineral groups include important products of hydrothermal alteration. This wavelength range is mostly covered by a single band (band 7) in Landsat 7 ETM+ and Landsat 8, whereas it is divided into five bands in ASTER data; therefore, ASTER data allows for better distinction between these minerals of interest. Data acquired using ASTER include visible- and near-infrared (VNIR) radiation recorded in three spectral bands (0.52–0.86 µm, 15 m spatial resolution); shortwave-infrared (SWIR) radiation, in six spectral bands (1.6–2.43 µm, 30 m spatial resolution); and thermal-infrared (TIR) radiation, in five bands (8.12–11.65 µm, 90 m resolution). Each ASTER scene covers an area of 60 by 60 km. New AST L1T images in hierarchical data format are freely downloadable from NASA or the United States Geological Survey (USGS) ASTER archive (United States Geological Survey, 2017).

Pre-Processing

Geometric and radiometric corrections have been carried out by NASA/USGS on the original AST L1A images to produce AST L1T. These calibrations and corrections include radiometric calibration, geometric processing, and corrections for the SWIR crosstalk. Also, scene registration corrections for SWIR and TIR are applied to SWIR for parallax errors as a result of spatial locations of the bands. To get the best images of the area of interest by converting radiance to reflectance on the ground, an atmospheric correction algorithm was applied on the NASA datasets. In this project, the internal average relative reflectance algorithm was used to calibrate the image.

A variety of masking techniques were applied in order to reduce image spectral variability (Mather, 1999) to that which is related to the exposed bedrock surface. The normalized difference vegetation index was used to mask the vegetation. Dark-object subtractions were applied to the images to mask the dark pixels in shadows, based on their digital number (DN) values. For ice and snow, target DN values were determined using false-colour composites. This method helps to keep the areas that have light and scattered snow coverage in the datasets. Since scenes with less than 10% cloud coverage were initially obtained, the area with cloud coverage was very limited; however, these areas were also removed from the cloud mask final result.

Processing

To obtain the most reliable results, three ASTER scenes with considerable overlap were processed (Table 1). The methods of band ratio (BR), relative absorption band depth (RBD), least squares fit (LS-Fit), linear spectral unmixing (LSU) and matched filtering (MF) were applied individually in conjunction with each pre-processed scene to detect specific alteration minerals, including epidote, chlorite, calcite, muscovite, kaolinite and alunite, as well as iron-ox-

Table 1. ASTER scenes utilized to identify potential alteration on Microwave ridge in west-central British Columbia.

Granule ID	Centre Latitude	Centre Longitude	Acquisition date	Acquisition time	Sun azimuth
AST_L1T_00308142001194937_20150501182409_113892	54°47'18.24"N	127°06'57.96"W	14/08/2001	49:37.7	164.139311
AST_L1T_00302172001200556_20150414212851_118220	54°58'00.84"N	127°40'42.96"W	17/02/2001	05:56.4	169.94084
AST_L1T_00309042006194746_20150516010940_107577	54°40'38.64"N	127°53'05.28"W	04/09/2006	47:46.3	165.567025

ide and ferric iron-bearing minerals. A summary of the steps of ASTER-image processing from data to output is shown on Figure 4.

Band Ratio (BR) Method

Band ratio is one of the basic methods used for image processing; each pixel in the image has a specific DN for each band. In the BR technique, a ratio of two DN values is calculated for each pixel to generate a new set of DN values. This method reduces the effect of illumination variability, based on the interpretation that radiance across the entire spectrum will be proportional to illumination: a region in direct sunlight will have much greater radiance than a region in shadow but the ratio of any given two bands should be similar if the surface material is the same (Husdal, 1999). The DN value of a single band is highly dependent on illumination, whereas pixels representing the same material will return similar ratios, significantly reducing the effect of topography (Sabins, 1997). The BR technique applied to ASTER imagery has been widely used in alteration mapping (Hewson et. al., 2001; Bierwirth, 2002; Rowan et. al., 2003; Mars and Rowan, 2006; Palomera, 2015; Commonwealth Scientific and Industrial Research Organisation, 2017).

Relative Absorption Band Depth (RBD) Method

The RBD technique is used to represent the spectral contrast of a specific absorption feature and has been broadly used for geology and alteration mapping (Rowen and Mars, 2003). The method works based on the maximum and minimum values around an absorption feature. As with the BR technique, this method reduces the effect of topography (Crowley et al., 1989). In this technique, first the appropriate absorption feature is selected for a given material of interest. Then bands near the shoulder and the minimum of the absorption feature are selected, and the algorithm is applied to the data (Van der Meer et. al., 2008). The sum of the reflectance values at the shoulder of the targeted spectral band(s) is divided by the sum of reflectance values at the minimum (Crowley et al., 1989; Ramachandran et al., 2010). The result includes a set of pixels that have a range of DN values related to the potential presence of a certain mineral; therefore to map the most likely areas, mask-threshold values should be applied to the results of RBD analysis.

Least Squares Fitting (LS-Fit) Method

The LS-Fitting method is based on band simulation and assumes that the bands used as input values are performing as the variables of a linear expression. In this method, a predicted band that includes the spectral characteristics of target minerals is selected. The algorithm calculates the output value from this band (Asadi Haroni and Lavafan, 2007). Then a set of bands are selected to put in the model as predictor bands. By applying correlation coefficients on predictor bands, a model prediction-band value is calculated that can be compared with the predicted-band value.

The results of the method include a model prediction band and a residual band. The residual band actually represents the difference between the prediction band and the predicted band in the form of an image for the target material. In the hypothetical case where a pixel represents exactly the material of interest, the model prediction-band value, based on predictor bands, will be equal to the real predicted-band value and the residual will be zero. Since the pixels are not pure, they may have a lower response than the expected amount for the target material in the predicted band. This method is a knowledge-based method and the predicted and predictor bands are selected based on expert knowledge of mineralogical assemblages expected to occur in the area of interest.

Linear Spectral Unmixing (LSU) Method

The LSU method is a supervised classification technique that defines relative abundances of minerals using their spectral characteristics. Pixels in the ASTER images are not pure and the value of each pixel is based on a mixture of the spectral characteristics of different minerals. In this approach, the unmixing coefficients are detected by minimizing the sum of the squares of the errors (Shimabukuro and Smith, 1991). Depending on the complexity of the scene, as well as the number and the wavelengths of the bands used, different numbers of end members contribute to the model (Tseng, 2000).

The results of LSU provide a series of single-band images for each target mineral. The reference spectra for this study

were selected from the USGS spectral library, based on the geological knowledge of the area of interest, and include spectra of kaolinite, alunite, muscovite, calcite, epidote, chlorite, jarosite, hematite, goethite and limonite. The USGS spectra were resampled to the number of ASTER bands selected for this analysis (Figure 5). Selected pixel spectra taken from each ASTER granule are processed using the new spectral library.

Matched Filtering (MF) Method

The MF method is also a supervised classification technique. The model achieves a partial unmixing of spectra; therefore it is not essential to find the spectra of all end members in the image. The method filters the image to define the best matches of the selected spectra for the target minerals by detecting the abundance of defined end members. In this technique, the known end member is processed and the result of the responses is maximized, then the unknown composite of the dataset is predicted using the results from the processing of the known end member. The method increases the possibility of obtaining an accurate analysis. The result of this process includes a set of images, each corresponding to a specific mineral. The brightest pixels in this image represent the highest probability of the presence of a specific mineral in the target spatial dataset (Boardman et al., 1995).

Results and Discussion

A natural-colour composite of ASTER bands 2, 3 and 1 (RGB) for the area of interest emphasizes the contrast between bedrock exposure and vegetation coverage (Fig-

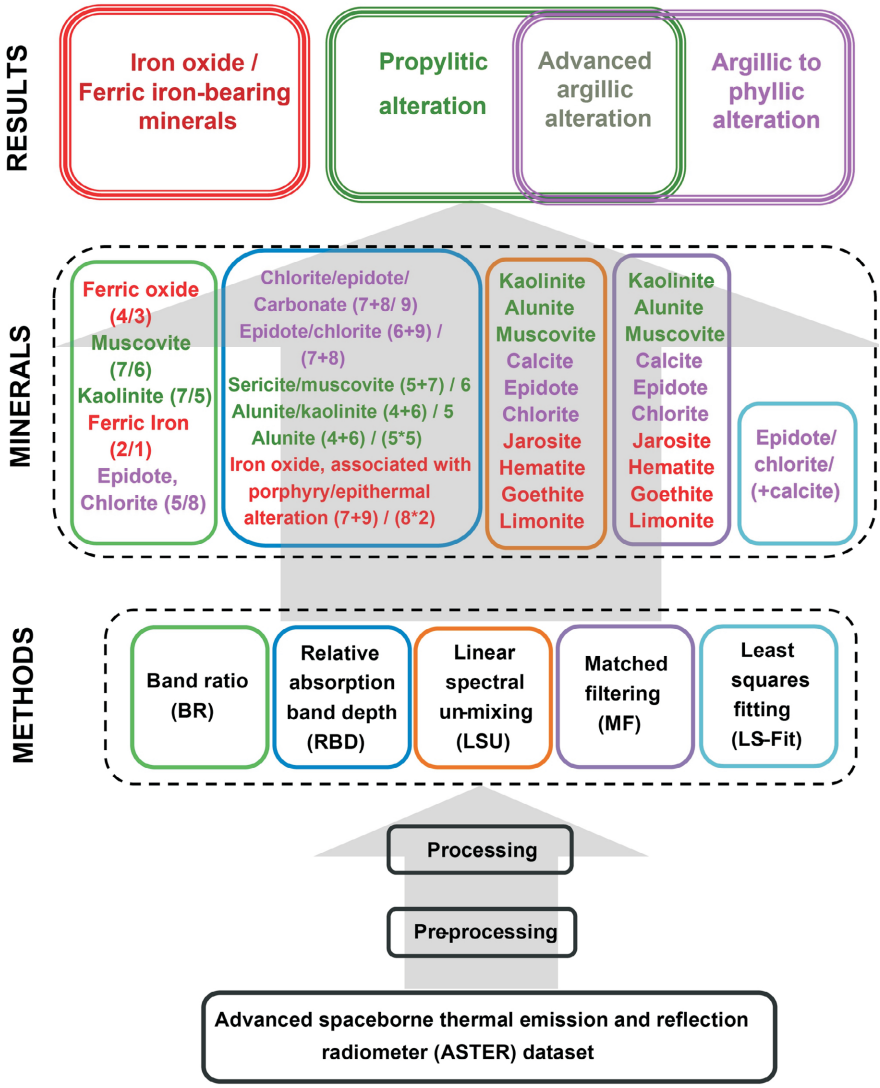

Figure 4. Processing workflow for ASTER data, showing the methods used to generate intermediate maps for specified minerals or groups of minerals. The numbers in the mineral row indicate the ASTER bands used in calculations. The coloured text in the mineral row indicates the intermediate maps that were used to generate the corresponding final output maps in the results row.

ure 6a). The results of BR and RBD are raster images with multiple DN values. The DN values are acquired by applying the proper thresholds and reflecting the proportional amounts of the targeted minerals interpreted to be within a given pixel. Clustered high DN values are considered to be probable alteration zones. These intermediate maps were merged with other results to generate the maps discussed below.

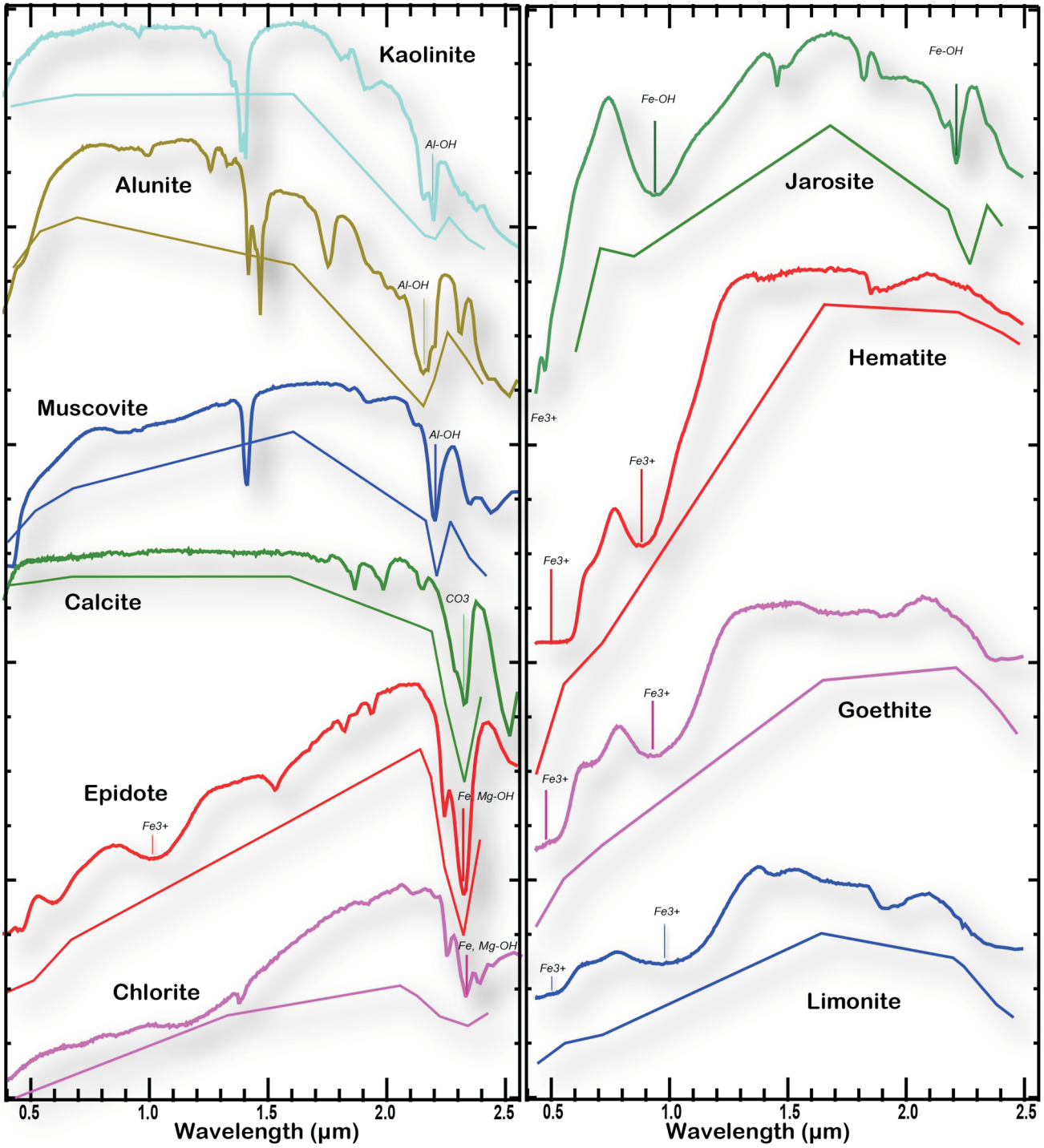

Figure 5. Comparison between laboratory spectra of kaolinite, alunite, muscovite, calcite, epidote, chlorite, jarosite, hematite, goethite and limonite, and their equivalents, resampled to ASTER bands. The upper line for each mineral is the laboratory spectra and the lower line is the resampled equivalent. Calcite has a prominent 2.33 μm CO_3 absorption feature; limonite has a broad 0.66–1.165 μm Fe^{3+} absorption feature; kaolinite, muscovite and alunite have Al-OH absorption features at 2.165, 2.20 and 2.20 μm, respectively; and epidote and chlorite have an Fe-Mg-OH absorption feature at 2.32 μm (modified after Clark et al., 1993; Ramachandran et al., 2010; Beiranvand Pour and Hashim, 2014).

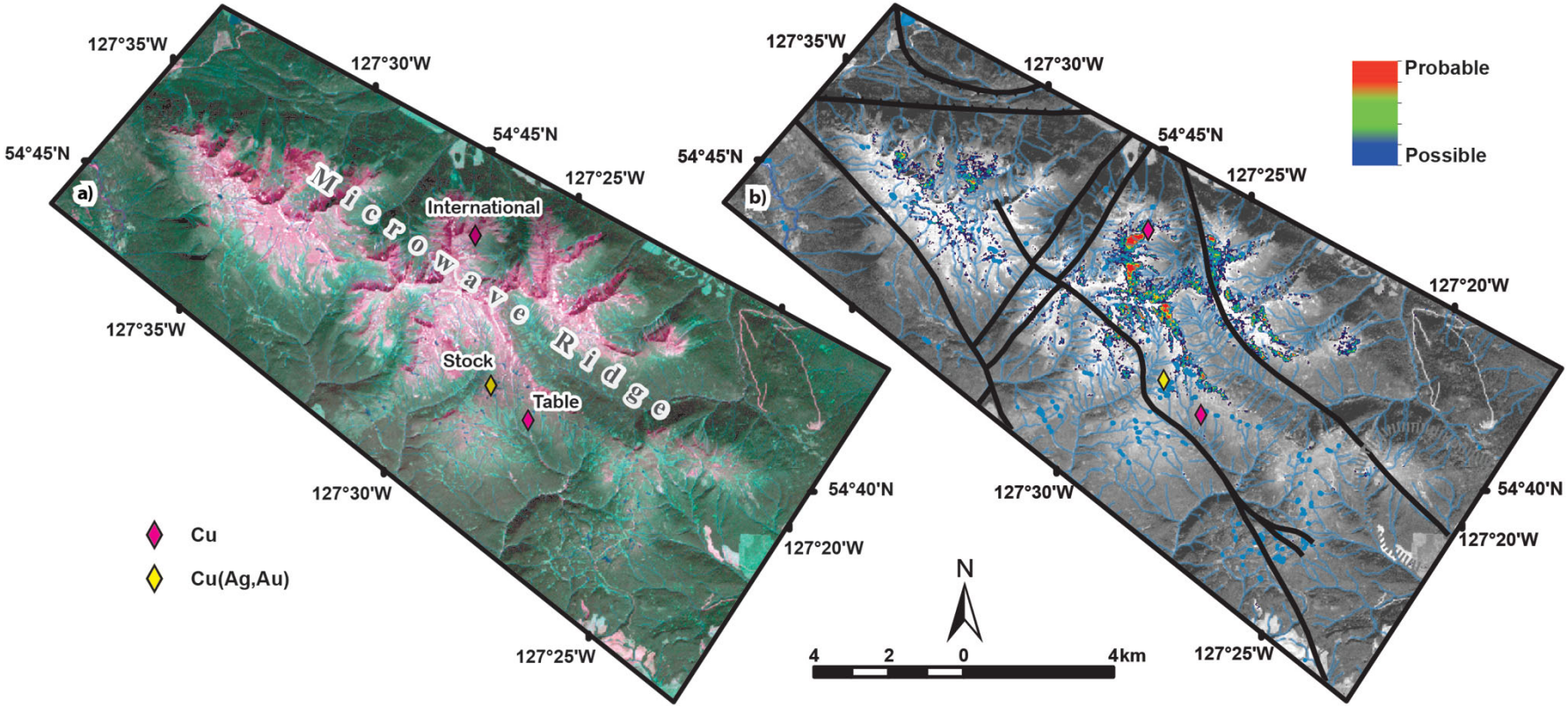

Figure 6. Results of processing ASTER data from Microwave ridge in west-central British Columbia for epidote and chlorite (±calcite): **a)** ASTER natural-colour composite using bands 2, 3 and 1 (RGB) emphasizes the contrast between bedrock and vegetation; **b)** pseudo-colour image generated by the LS-Fitting method displays the results for epidote, chlorite and possibly calcite minerals; red represents the highest concentration, whereas dark blue represents the lowest concentration for pixels where these minerals were detected.

The intensity of absorption at band 8 is presented in Figure 6b. This absorption feature is characteristic of Mg-OH–bearing minerals such as epidote and chlorite, which are a significant component of propylitic alteration. Band 8 is also sensitive to carbonate minerals, which are also present in propylitic alteration zones. A combination of BR, RBD and LS-Fit processing has been applied to detect these minerals. There is a low-intensity response across much of the exposed bedrock on Microwave ridge that likely reflects background chlorite, epidote and carbonate, which occur in small amounts throughout the Telkwa Formation (Figure 6b). By filtering out everything except the highly anomalous responses, three distinct potential alteration zones and a few minor outliers stand out (Figure 7a), the southernmost of these three possible alteration zones is centred on a region previously-mapped as granodiorite (Tipper and Richards, 1976b). It is possible that the two, more northerly alteration zones of anomalous response correspond to either unmapped or unexposed granodiorite, with corresponding hydrothermal alteration zones.

Absorption at 2.22–2.24 μm (band 6) is characteristic of Al-OH–bearing minerals including, kaolinite, alunite and sericite (muscovite), which may reflect argillic (kaolinite), advanced argillic- (alunite) or phyllic- (sericite) alteration mineral assemblages. A combination of BR, RBD, LSU and MF processing has been applied to detect these minerals. Regions where ASTER data indicate potentially anomalous concentrations of these minerals are presented along with the Mg-OH data in Figure 7a. This processing has identified many widely distributed zones of potential kaolinite, alunite and/or sericite. Clay minerals produced from the weathering of feldspar typically contain Al-OH, therefore interpretation of the Al-OH results must be done with caution since these identified zones may simply reflect weathering. However, it is notable that the three potential propylitic-alteration zones identified above are apparently flanked by zones of Al-OH–bearing minerals.

A combination of BR, RBD, LSU and MF techniques was applied to detect iron-oxide and ferric iron-bearing minerals, such as hematite, goethite and jarosite (Figure 8a–d). There appears to be a correlation between interpreted iron-oxide and ferric iron-bearing minerals and northwest-trending faults, which may indicate structurally controlled hydrothermal alteration. This is particularly evident around the fault closest to the Table and Stock prospects (Figure 8a). Structurally controlled ferric iron-oxide alteration could be the product of low-temperature hydrothermal fluids associated with volcanic-hosted redbed-copper mineralization (Lefebure and Ray, 1998). The three overlapping zones identified in Figure 7a also correspond to possible Fe-oxide and ferric iron-bearing alteration zones (Figure 7b).

Understanding the distribution of rock units is critical to adequately interpreting the results of ASTER processing. The unaltered rock units on Microwave ridge are not likely to yield significantly different responses for any of the selected processing methods. Therefore, the identified zones are interpreted to reflect potential zones of alteration rather than simply differences in rock type.

The results of ASTER processing suggest the presence of three potential zones of overlapping Mg-OH–bearing ±carbonate minerals, Al-OH–bearing minerals and iron oxides. One of these overlapping zones corresponds to a location previously mapped as Bulkley Plutonic Suite granodiorite. It is possible that the other two correspond to alteration related to Bulkley granodiorite that is either unrecognized or blind. The International (MINFILE 093L 086) occurrence is located along the margin of the northernmost alteration zone. The showing consists of minor disseminated chalcopyrite and fractures lined with malachite within amygdaloidal basalt; on its own, this minor copper showing may be of little interest (Robertson, 1917). The hydrothermal fluid responsible for these overlapping zones of alteration may be related to the Bulkley Plutonic Suite intrusion(s) with potential for other, more significant styles of mineralization nearby.

The noted lack of alteration identified through ASTER processing in the immediate vicinity of the Stock (MINFILE 093L 085) and Table (MINFILE 093L 084) occurrences, combined with iron-oxide–dominated alteration along associated northwest-trending minor faults, suggest that these occurrences formed from relatively low-temperature hydrothermal fluids. This is likely consistent with either a volcanic-hosted redbed-copper style of mineralization, or potentially a cool and distal expression of an intrusion-related hydrothermal fluid, as opposed to a proximal higher temperature intrusion-related hydrothermal fluid. Either way, these occurrences are poorer indicators of nearby intrusion-related mineralization.

Conclusion

The Microwave ridge area is a dominantly east-dipping structural panel that exposes a section through the Telkwa Formation that is cut by small, Late Cretaceous (or Eocene) intrusions. A calcareous epiclastic sedimentary horizon that had previously been assigned to the Nilkitkwa Formation is reinterpreted as a local sedimentary inlier within the dominantly volcanic Telkwa Formation. Rhyolite lenses within the sequence are interpreted as isolated Telkwa Formation rhyolitic eruptive centres. They are distinguished from porphyritic Late Cretaceous or Eocene intrusions, in part, by their lack of aeromagnetic response.

Processing of ASTER data has identified three potential zones of overlapping kaolinite+alunite+sericite, epidote+

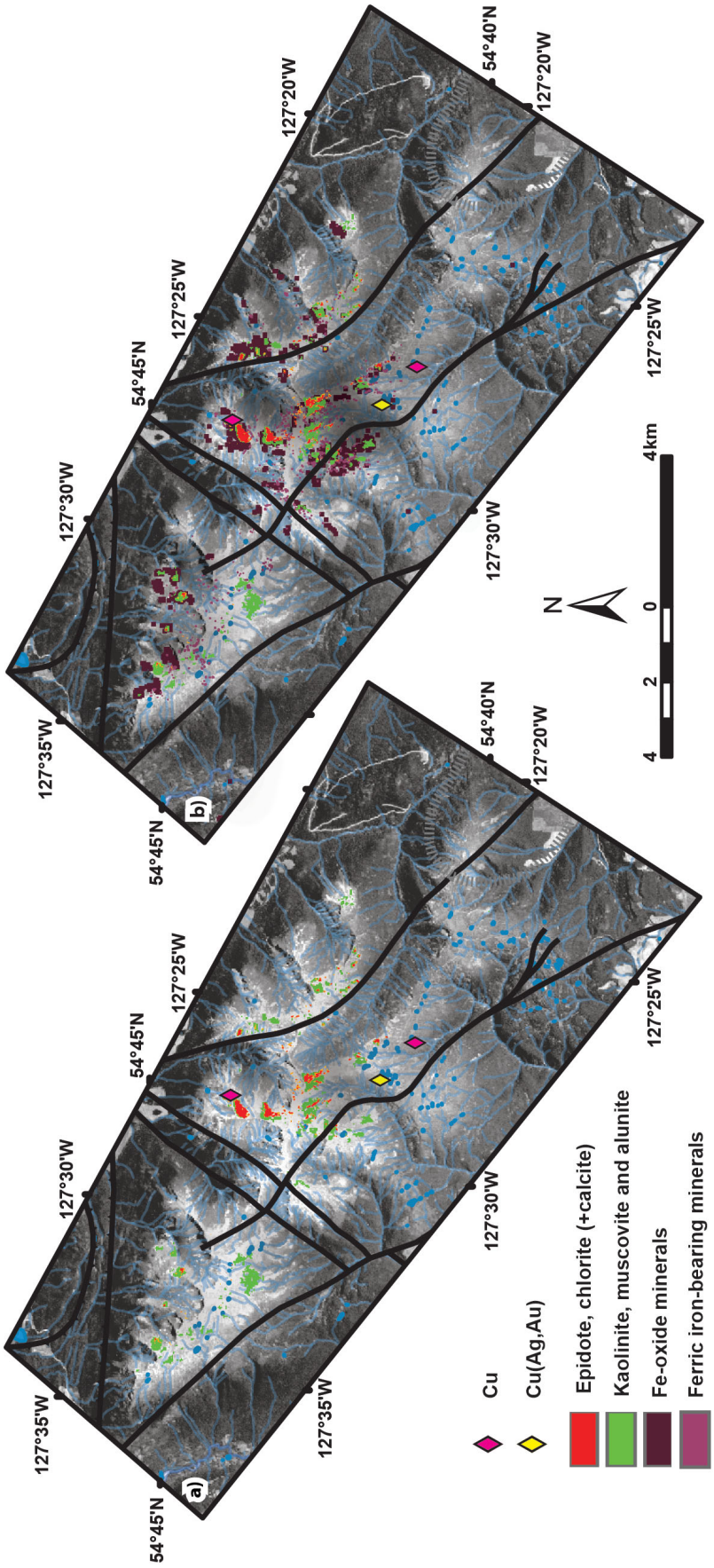

Figure 7. Zones of strongest response for the mineral groupings investigated at Microwave ridge in west-central British Columbia: **a)** the highest responses for epidote and chlorite (±calcite) are plotted in red, along with kaolinite, muscovite and alunite in green; **b)** the highest responses for Fe-oxide zones are plotted in purple, along with ferric iron-bearing zones (including ferric oxides) in pink, overlain on the responses plotted in Figure 7a.

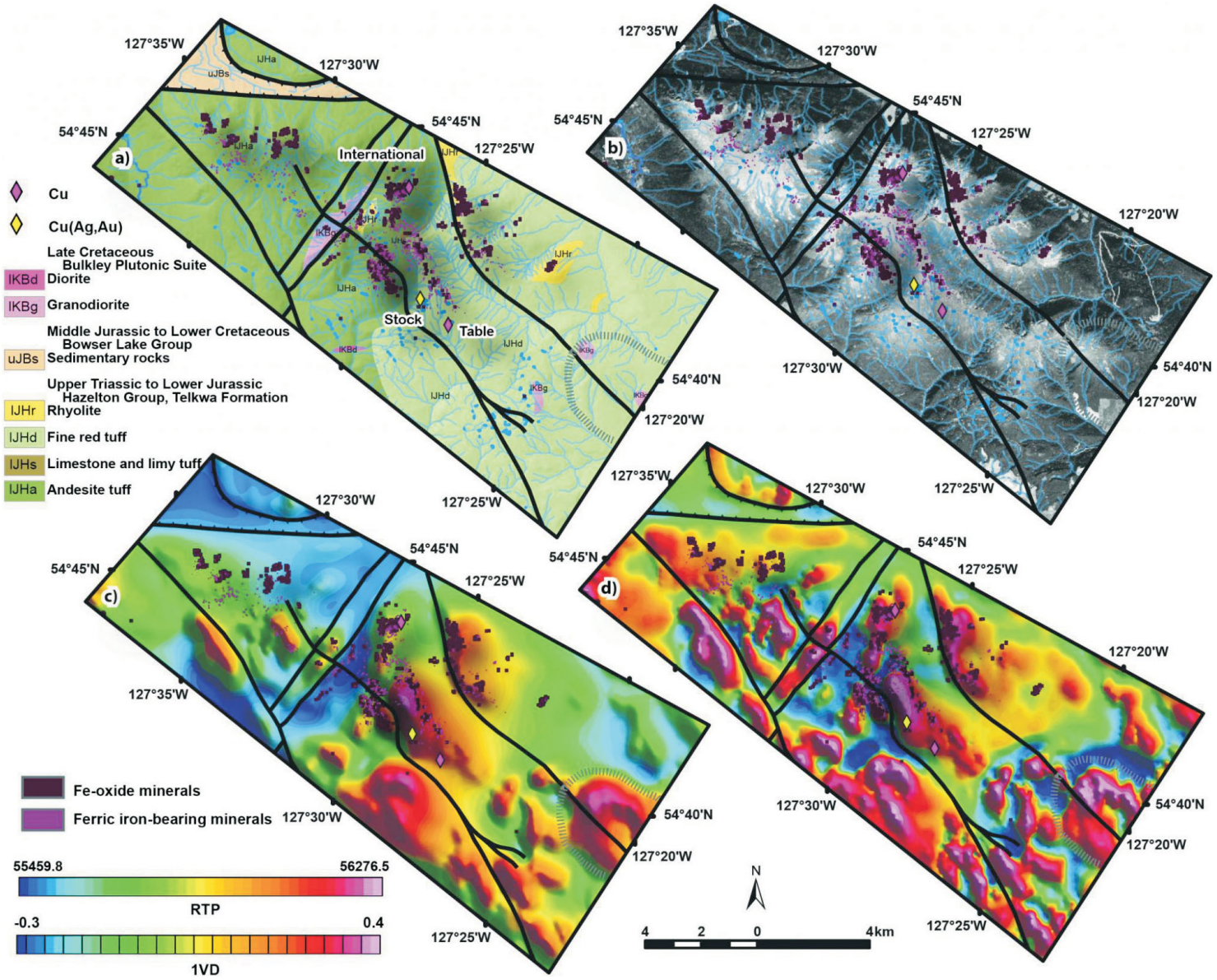

Figure 8: Zones of Fe-oxide (purple) and ferric iron-bearing (pink) minerals in the Microwave ridge area, west-central British Columbia, that were detected through BD, RBD, LSU and MF processing of ASTER data: **a)** interpreted Fe-oxide–altered pixels overlain on bedrock geology map of the Microwave ridge area; **b)** interpreted Fe-oxide–altered pixels overlain on band 1 ASTER data; **c)** results overlain on RTP total-field aeromagnetic data; **d)** results overlain on first vertical-derivative (1VD) aeromagnetic data.

chlorite±calcite and Fe-oxide alteration. One of these zones corresponds to a region mapped as porphyritic granodiorite. It is speculated that the other two areas may similarly represent porphyritic granodiorite.

The three MINFILE occurrences on Microwave ridge include Cu-(Ag-Au) mineralization within the Telkwa Formation. The Stock (MINFILE 093L 085) and Table (MINFILE 093L 084) occurrences, on the southern slope of the ridge, lack a strong spectral response in their immediate vicinity despite good bedrock exposure. They occur along one of a series of northwest-trending minor faults. The northwesterly extension of the closest mapped fault corresponds with a clustered zone of possible iron-oxide and ferric iron-bearing minerals, flanked by Al-OH–bearing minerals, as indicated by ASTER processing. It is possible that the alteration is zoned away from a potential causative intrusion. The International (MINFILE 093L 086) occurrence, in contrast, is adjacent to one of the interpreted alteration zones and therefore may be proximal to a causative intrusion.

Acknowledgments

This manuscript benefited greatly from a thorough review by A. Fonseca. Excellent assistance for the field component of this investigation was provided by G. Lesage. Discussions with T. Richards provided valuable insight into the geology of the Skeena arch.

References

Angen, J.J., Nelson, J.L., Rahimi, M. and Hart, C.J.R. (2017): Mapping in the Tatsi and Zymo ridge areas of west-central British Columbia: implications for the origin and history of the Skeena Arch; *in* Geological Fieldwork 2016, BC Ministry of Energy, Mines and Petroleum Resources, BC Geological Survey, Paper 2017-1, p. 35–48.

Asadi Haroni, H. and Lavafan, A. (2007): Integrated analysis of ASTER and Landsat ETM data to map exploration targeting in the Muteh gold-mining area, Iran; *in* 5th International Symposium on Spatial Data Quality, XXXVI-2/C43, no. 5, Actas, June 13-15, 2007, Enschede, Netherlands, URL <http://www.isprs.org/proceedings/XXXVI/2-C43/Poster session/ASADI.pdf> [October 2017].

Azizi, H., Tarverdi, M.A. and Akbarpour, A. (2010): Extraction of hydrothermal alterations from ASTER SWIR data from east Zanjan, northern Iran; Advances in Space Research, v. 46, p. 99–109. doi:10.1016/j.asr.2010.03.014

BC Geological Survey (2017): MINFILE BC mineral deposits database; BC Ministry of Energy, Mines and Petroleum Resources, BC Geological Survey, URL <http://minfile.ca> [November 2017].

Beiranvand Pour, A. and Hashim, M. (2014): ASTER, ALI and Hyperion sensors data for lithological mapping and ore minerals exploration; Springer plus 2014, 19 p. doi:10.1186/2193-1801-3-130. URL: <http://www.springerplus.com/content/3/1/130> [October 2017].

Bierwirth, P.N. (2002): Evaluation of Aster satellite data for geological applications; consultancy report to Geoscience Australia, 50 p.

Boardman, J. W., Kruse, F. A. and Green, R. O. (1995): Mapping target signatures via partial unmixing of AVIRIS data; *in* Summaries of the Fifth JPL Airborne Earth Science Workshop, January 23-26, 1995, Pasadena, California, JPL Publication 95-1, v. 1, p. 23–26.

Clark, R.N., Swayze, G.A., Gallagher, A., King, T.V.V. and Calvin, W.M. (1993): The U.S. Geological Survey, Digital Spectral Library: Version 1: 0.2 to 3.0 microns; United States Geological Survey, Open File Report 9-592, 1340 p.

Colpron, M. and Nelson, J.L. (2011): A digital atlas of terranes for the northern Cordillera; accessed online from the Yukon Geological Survey, URL <http://www.geology.gov.yk.ca> [November, 2017].

Commonwealth Scientific and Industrial Research Organisation (2017): Mineral discovery and exploration; Commonwealth Scientific and Industrial Research Organisation website, URL <https://www.csiro.au/en/Research/Mining-manufacturing/Mineral-discovery-and-exploration> [November 2017].

Crowley, J. K., Brickey, W.D. and Rowan, C.L. (1989): Airborne imaging spectrometer data of the Ruby Mountains, Montana: mineral discrimination using relative absorption band-depth images; Remote Sensing of Environment, v. 29, p. 121–134.

Cui, Y., Miller, D., Nixon, G. and Nelson, J. (2015): British Columbia digital geology; BC Ministry of Energy, Mines and Petroleum Resources, BC Geological Survey, Open File 2015-2.

Desjardins, P., MacIntyre, D.G., Hunt, J., Lyons, L. and Pattenden, S. (1990): Geology of the Thautil River map area (93L/6); *in* Geological Fieldwork 1989, BC Ministry of Energy, Mines and Petroleum Resources, BC Geological Survey, Paper 1993-1, p. 91–99.

Evenchick, C.A., Poulton, T.P. and McNicoll, V.J. (2010): Nature and significance of the diachronous contact between the Hazelton and Bowser Lake groups (Jurassic), north-central British Columbia; Bulletin of Canadian Petroleum Geology, v. 58, p. 235–267.

Gagnon, J.F., Barresi, T., Waldron, J.F., Nelson, J.L., Poulton, T.P. and Cordey, F. (2012): Stratigraphy of the Upper Hazelton Group and the Jurassic evolution of the Stikine terrane, British Columbia; Canadian Journal of Earth Sciences, v. 49, p. 1027–1052.

Hewson, R.D., Cudahy, T.J. and Huntington, J.F. (2001). Geological and alteration mapping at Mt. Fitton, South Australia, using ASTER satellite-borne data; IEEE Transactions in Geoscience and Remote Sensing, p. 724–726.

Husdal, J. (1999): ERDAS Practical exercises website; University of Leicester, Leicester, United Kingdom, URL <https://erdas.wordpress.com/> [November 2017].

Jet Propulsion Laboratory (2017): Advanced Spaceborne Thermal Emission and Reflection Radiometer (ASTER); online information, URL<https://asterweb.jpl.nasa.gov/> [October 2017].

Kalinowski, A. and Oliver, S. (2004): ASTER Mineral Index Processing Manual; Remote Sensing Applications, Geoscience Australia, internal report, 39 p.

Lefebure, D.V. (1996): Cu+/-Ag quartz veins; *in* Selected British Columbia Mineral Deposit Profiles, Volume 2 – Metallic

Deposits; D.V. Lefebure and T. Hõy (ed.), BC Ministry of Employment and Investment, Open File 1996-13, p. 71–74.

Lefebure, D.V. and Church, B.N. (1996): Volcanic redbed Cu; *in* Selected British Columbia Mineral Deposit Profiles, Volume 2 – Metallic Deposits; D.V. Lefebure and T. Hõy (ed.), BC Ministry of Employment and Investment, Open File 1996-13, p. 5–7.

Lefebure, D.V. and Ray, G.E. (1998): Unconventional metal deposits in volcanic arcs; *in* Metallogeny of Volcanic Arcs, BC Geological Survey Branch, Short Course Notes, Open File 1998-8, Section I.

Mars, J.C. and Rowan L.C. (2006): Regional mapping of phyllic- and argillic-altered rocks in the Zagros magmatic arc, Iran, using Advanced Spaceborne Thermal Emission and Reflection Radiometer (ASTER) data and logical operator algorithms; Geosphere, v. 2, p. 161–186. doi:10.1130/GES00044.1

MacIntyre, D.G. (2006): Geology and mineral deposits of the Skeena Arch, west-central British Columbia: a Geoscience BC digital data compilation project; *in* Geological Fieldwork 2005, BC Ministry of Energy, Mines and Petroleum Resources, BC Geological Survey, Paper 2006-1, p. 303–312.

MacIntyre, D., Desjardins, P., Tercier, P. and Koo, J. (1989a): Geology of the Telkwa River Area, NTS 093L/11; BC Ministry of Energy, Mines and Petroleum Resources, BC Geological Survey, Open File 1989-16, 1:50 000 scale, URL <http://www.empr.gov.bc.ca/Mining/Geoscience/PublicationsCatalogue/OpenFiles/1989/Pages/1989-16.aspx> [November 2017].

MacIntyre, D.G., Desjardins, P. and Tercier, P. (1989b): Jurassic stratigraphic relationships in the Babine and Telkwa Ranges (93L/10, 11, 14, 15); *in* Geological Fieldwork 1989, BC Ministry of Energy, Mines and Petroleum Resources, BC Geological Survey, Paper 1989-1, p. 195–208.

Mather, P. (1999): Computer Processing of Remotely-Sensed Images: An Introduction; 2nd edition, John Wiley and Sons, 306 p.

Nelson, J. (2017): Composite pericratonic basement of west-central Stikinia and its influence on Jurassic magma conduits: examples from the Terrace-Ecstall and Anyox areas; *in* Geological Fieldwork 2016, BC Ministry of Energy, Mines and Petroleum Resources, BC Geological Survey, Paper 2017-1, p. 61–82.

Nelson, J.L., Barresi, T., Knight, E. and Boudreau, N. (2006): Geology and mineral potential of the Usk map area (103I/09) near Terrace, British Columbia; *in* Geological Fieldwork 2005, BC Ministry of Energy, Mines and Petroleum Resources, BC Geological Survey, Paper 2006-1, Report 2006-1, p. 117–134.

Nelson, J.L., Kyba, J., McKeown, M. and Angen, J.J. (2008): Terrace regional mapping project, Year 3: contributions to stratigraphic, structural and exploration concepts, Zymoetz River to Kitimat River, east-central British Columbia; *in* Geological Fieldwork 2007, BC Ministry of Energy, Mines and Petroleum Resources, BC Geological Survey, Paper 2008-1, p. 159–174.

Palomera, R.P.A. (2015): Spectral prospectivity mapping of Deseado Massif, Argentina: deciphering the geochemistry and mineralogy of a low to intermediate sulphidation epithermal system; University of Twente, Enschede, Netherlands, 220 p. doi:10.3990/1.9789036539067

Palsgrove, R.J. and Bustin, R.M. (1991): Stratigraphy, sedimentology and coal quality of the lower Skeena Group, Telkwa coalfield, central British Columbia (NTS 093L/11); BC Ministry of Energy, Mines and Petroleum Resources, BC Geological Survey, Paper 1991-2, 68 p.

Precision GeoSurveys Inc. (2016): Airborne Magnetic Survey, Search Project; Geoscience BC, Report 2016-02, 62 p.

Rajendran, S., Al-Khirbasha, S., Pracejusa, B., Nasira, S., Al-Abria, A.H., Kusky, T.M. and Ghulam, A. (2012). ASTER detection of chromite bearing mineralized zones in Semail Ophiolite Massifs of the northern Oman Mountains: exploration strategy; Ore Geology Reviews, v. 44, p. 121–135.

Ramachandran, B., Justice, C.O. and Abrams, M.J., editors (2010): Land Remote Sensing and Global Environment Change: NASA's Earth Observing System and the Science of ASTER and MODIS; Springer Verlag, New York, New York, 873 p. doi:10.1007/978-1-4419-6749-7

Robertson, W. F. (1917): Copper Queen; *in* Minister of Mines, Annual Report 1917, BC Ministry of Energy, Mines and Petroleum Resources, p. 119–120.

Rowan, L.C. and Mars, J.C. (2003). Lithologic mapping in the Mountain Pass, California area using Advanced Spaceborne Thermal Emission and Reflection Radiometer (ASTER) data; Remote Sensing of Environment, v. 84, no. 3, p. 350–366.

Rowan, L.C., Hook, S.J., Abrams, M.J. and Mars, J.C. (2003): Mapping hydrothermally altered rocks at Cuprite, Nevada, using the Advanced Spaceborne Thermal Emission and Reflection Radiometer (ASTER), a new satellite-imaging system; Economic Geology, v. 98, p. 1019–1027.

Sabins, F.F. (1997): Remote Sensing: Principles and Interpretation; 3rd edition, W.H. Freeman and Company, New York, New York, 494 p.

Shimabukuro, Y. E. and Smith, J. A. (1991): The least-squares mixing models to generate fraction images derived from remote sensing multispectral data; IEEE Transactions on Geoscience and Remote Sensing, v. 29, no. 1, p. 16–20.

Stanley, G. D. and McRoberts, C. A. (1993): A coral reef in the Telkwa Range, British Columbia: the earliest Jurassic example; Canadian Journal of Earth Sciences, v. 30, p. 819–831, URL <http://www.nrcresearchpress.com/doi/abs/10.1139/e93-068#.WfoZZHZxmM8> [November 2017].

Tipper, H.W. and Richards, T.A. (1976a): Jurassic stratigraphy and history of north-central British Columbia; Geological Survey of Canada, Bulletin 270, 73 p.

Tipper, H.W. and Richards, T.A. (1976b): Smithers map-area; Geological Survey of Canada, Open File 351, 1:253 440 scale.

Tseng, Y.H. (2000): Spectral unmixing for the classification of hyperspectral image; International Archives of Photogrammetry and Remote Sensing, v. XXXIII, Part B7.

United States Geological Survey (2017): Advanced Spaceborne Thermal Emission and Reflection Radiometer (ASTER); Global Visualization Viewer; United States Geological Survey, URL <https://glovis.usgs.gov/> [October 2017].

Van der Meer, F., Van der Werff, H., Van der Meijde, M., Van Ruitenbeek, F., Hecker, C. and de Jong, S. (2008): Object extraction and attribution from hydrospectral images; Chapter 15 *in* Advances in Photogrammetry, Remote Sensing and Spatial Information Sciences, Z. Li, J. Chen and E. Baltsavias (ed.), XXIst Congress of the International Society for

Photogrammetry and Remote Sensing, July 3–11, 2008, Beijing, China, congress book, p. 205–212.

Van Ruitenbeek, F.J.A., Cudahy, T.J., Van der Meer, F.D. and Hale M. (2012): Characterization of the hydrothermal systems associated with Archean VMS-mineralization at Panorama, Western Australia, using hyperspectral, geochemical and geothermometric data; Ore Geology Reviews, v. 45, p. 33–46.

Watts, D.R. and Harris, N.B.W. (2005): Mapping granite and gneiss in domes along the North Himalayan antiform with ASTER SWIR band ratios; Geological Society of America Bulletin, v. 117, no. 7/8, p. 879–886.

Integrated Assessment of Regional Stream-Sediment Geochemistry for Metallic Deposits in Northwestern British Columbia (Parts of NTS 093, 094, 103, 104)

D.C. Arne, CSA Global, Vancouver, BC, dennis.arne@csaglobal.com

R. Mackie, CSA Global, Vancouver, BC

C. Pennimpede, CSA Global, Vancouver, BC

E. Grunsky, CSA Global, Vancouver, BC

Arne, D.C., Mackie, R., Pennimpede, C. and Grunsky, E. (2018): Integrated assessment of regional stream-sediment geochemistry for metallic deposits in northwestern British Columbia (parts of NTS 093, 094, 103, 104); *in* Geoscience BC Summary of Activities 2017: Minerals and Mining, Geoscience BC, Report 2018-1, p. 23–30.

Introduction

Regional stream-sediment geochemistry is important to mineral exploration companies, governments and First Nations communities because it helps inform mineral exploration potential in suitable geographical terranes. From 2002 to 2017, Geoscience BC undertook projects involving the reanalysis of archived stream-sediment sample material by inductively coupled plasma–mass spectrometry (ICP-MS) and inductively coupled plasma–atomic emission spectrometry (ICP-AES), increasing the number of elements reported and lowering detection limits compared to historical analytical methods. These improvements allow for a more rigorous assessment of the variation in sediment composition and the filtering of effects related to lithological controls and secondary scavenging, which can mask signals related to metallic metal deposits. Some of these new data covering southern and central British Columbia (BC) have been evaluated using catchment basin analysis and a variety of multivariate statistical approaches (e.g., Arne and Bluemel, 2011; Arne and Brown, 2015); however, data from much of northern BC have not yet been assessed.

Several factors should be considered when interpreting regional stream-sediment geochemical data, including the effects of dilution in catchment basins of differing sizes; the influence of variable bedrock types on geochemical background values; the potential effects of scavenging metals onto secondary Fe and Mn oxides or organic matter; as well as the influence of streamwater pH and Eh, which control the solubilities of most metals (e.g., Hawkes, 1976; Bonham-Carter and Goodfellow, 1986; Carranza, 2009; Arne and Brown, 2015; Mackie et al., 2015). A major conclusion from previous studies is the importance of bedrock geology as a control on stream-sediment geochemistry, although this will depend to a certain extent on the elements under consideration. For example, when using conventional aqua-regia digestion, elevated Cu values would be expected in catchment basins draining areas dominated by basalt, making it difficult to distinguish elevated background from slightly elevated Cu values associated with sulphide mineralization. Black shales are also often elevated in a variety of metals, including those commonly used for geochemical targeting of mineral deposits. Their extent may be poorly mapped and/or their influence on stream-sediment composition may be disproportionate to their surface expression. The effects of scavenging by secondary Fe or Mn oxides or organics will vary by geographical setting. Streamwater pH is largely bedrock controlled but will influence the distribution of important commodity pathfinder elements such as Zn, As, Sb, Cu and Hg. Using the newly available multi-element geochemistry in conjunction with catchment information, the influence of these effects can be assessed and filtered for more accurate exploration targeting using commodity and pathfinder elements.

This project is a regional assessment of stream-sediment geochemical data from various Geoscience BC reanalysis programs encompassing parts of twenty 1:250 000 scale NTS map areas, as shown in Figure 1. The limits of the project were generally based on the following criteria:

- areas where samples have been reanalyzed by ICP-MS
- areas with an absence of regionally extensive Quaternary cover
- areas with a lack of previous geochemical interpretations of stream-sediment data
- areas with a high degree of interest from mineral exploration companies

The areas covered by the Spatsizi Plateau Wilderness Provincial Park and the Tatlatui Provincial Park have also been excluded from this study. The study area was further constrained to include only regions underlain by the Stikine, Quesnel and Cache Creek terranes. This geological filter was applied because the fringing terranes to the east and

This publication is also available, free of charge, as colour digital files in Adobe Acrobat® PDF format from the Geoscience BC website: http://www.geosciencebc.com/s/SummaryofActivities.asp.

west will have distinctly different lithological background values for many elements, which could limit the ability to 'isolate' geochemical signals associated with mineralization within the targeted terranes. The adjacent terranes are also not significant hosts for base- or precious-metal mineralization and thus are of less immediate exploration interest.

Geological Setting and Mineral Deposits

The study area covers much of the northwestern Stikine terrane of central and northern BC (Figure 1), including important regions of mineral exploration and development. The Stikine terrane is part of the Intermontane Belt, which stretches through BC, Yukon and into Alaska (Colpron et al., 2006). It comprises a north- to northwest-trending allochthonous belt of dominantly Devonian to Jurassic sedimentary and volcanic rocks intruded by coeval Late Devonian, Triassic and Jurassic plutonic rocks (Gunning et al., 2006). Paleozoic volcanic and sedimentary rocks of the Stikine terrane include calcalkaline to tholeiitic sequences largely dominated by basalt, marine limestone and lime mudstone. Volcanism and continued deposition of marine sediments continued through the Mesozoic until the mid-Cretaceous, following a break during the late Permian. The Stikine terrane was accreted to the adjacent Cache Creek and Quesnel terranes by the Middle Jurassic, followed by the deposition of Middle Jurassic to Early Cretaceous fluvial to marine clastic sediments that lie unconformably over the Stikine terrane in the Bowser and Sustut basins (Ricketts et al., 1992). Marine sedimentation and subaerial volcanism resumed in the Late Cretaceous or Paleogene and Neogene.

Parts of the study area have previously been included in Geoscience BC projects that have focused on well-mineralized areas of the Stikine and Quesnel terranes (Figure 1). The informally named 'Golden Triangle', stretching from south of the Red Mountain Au-Ag deposit to the Red Chris Cu-Au mine, was included in the QUEST-Northwest project. This area contains volcanic-hosted massive sulphide (VHMS) deposits at Granduc and Eskay Creek, as well as porphyry Cu-Au and epithermal Au-Ag deposits such as Brucejack and KSM. The QUEST-Northwest project to the north of the Golden Triangle also encompassed the Thorn Au-Ag and Tulsequah Chief VHMS deposits. An area centred on the town of Smithers formed the basis of the QUEST-West project that includes porphyry Cu-Au and Mo deposits, including Endako. Porphyry Cu-Au deposits in the western portion of the original QUEST project area are also included within the study area. The northern portion of the TREK project area, which contains epithermal Au-Ag deposits such as Blackwater, occurs in the southeast corner of the study area. The majority of known mineral deposits in the study area are of magmatic hydrothermal origin, associated mainly with calcalkaline to alkaline Triassic and Jurassic intrusive rocks, and to a lesser extent with Late Cretaceous–Paleogene calcalkaline intrusive rocks in the central and southern Stikine terrane (Nelson et al., 2013). The main deposit types that are the focus of the current investigation, therefore, are porphyry Cu-Ag-Au, epithermal Au-Ag and, less commonly, VHMS Zn-Cu-Ag-Au. Skarn deposits in the study area will also have a similar geochemical signature.

Methodology

Data Compilation and Conditioning

The data assembly for this project built on a previous compilation of historical regional geochemical data conducted by the BC Geological Survey (BCGS; Rukhlov and Naziri, 2015). This compilation was updated to include all the ICP-MS data generated through the various recent Geoscience BC projects. A summary of NTS map areas and public reports is provided in the form of a matrix in Table 1. Note that the reanalysis data were supplied from two separate laboratories. The bulk of the reanalyses were undertaken at Bureau Veritas Minerals (formerly Acme Analytical Laboratories Ltd.; Vancouver, BC), whereas reanalyses of samples from part of NTS map area 093F were undertaken by Eco-Tech Laboratories Ltd. (Kamloops, BC) in 2009. In addition, the reanalyses span 2002 to 2017, a period of 15 years. The use of two laboratories and the time span involved raises the possibility that some levelling of data to account for systematic variations within the compiled dataset may be required.

Table 1. Summary of NTS map areas in the study area and data sources.

NTS map area	Report: Jackaman (2008a)	Jackaman (2008b)	Jackaman (2012)	Jackaman (2011)	Jackaman (2009a)	Jackaman (2009b)	Friske et al. (2003)	Jackaman (2017)
093E					x			x
093F					x	x		
093K						x	x	
093L					x			
093M					x			
093N	x							
094C				x				
094D				x				
094E				x				
103I		x						
103J		x						
103O								x
103P								x
104A				x				
104B				x				
104F, G				x				
104H				x				
104I				x				
104J				x				
104K			x					

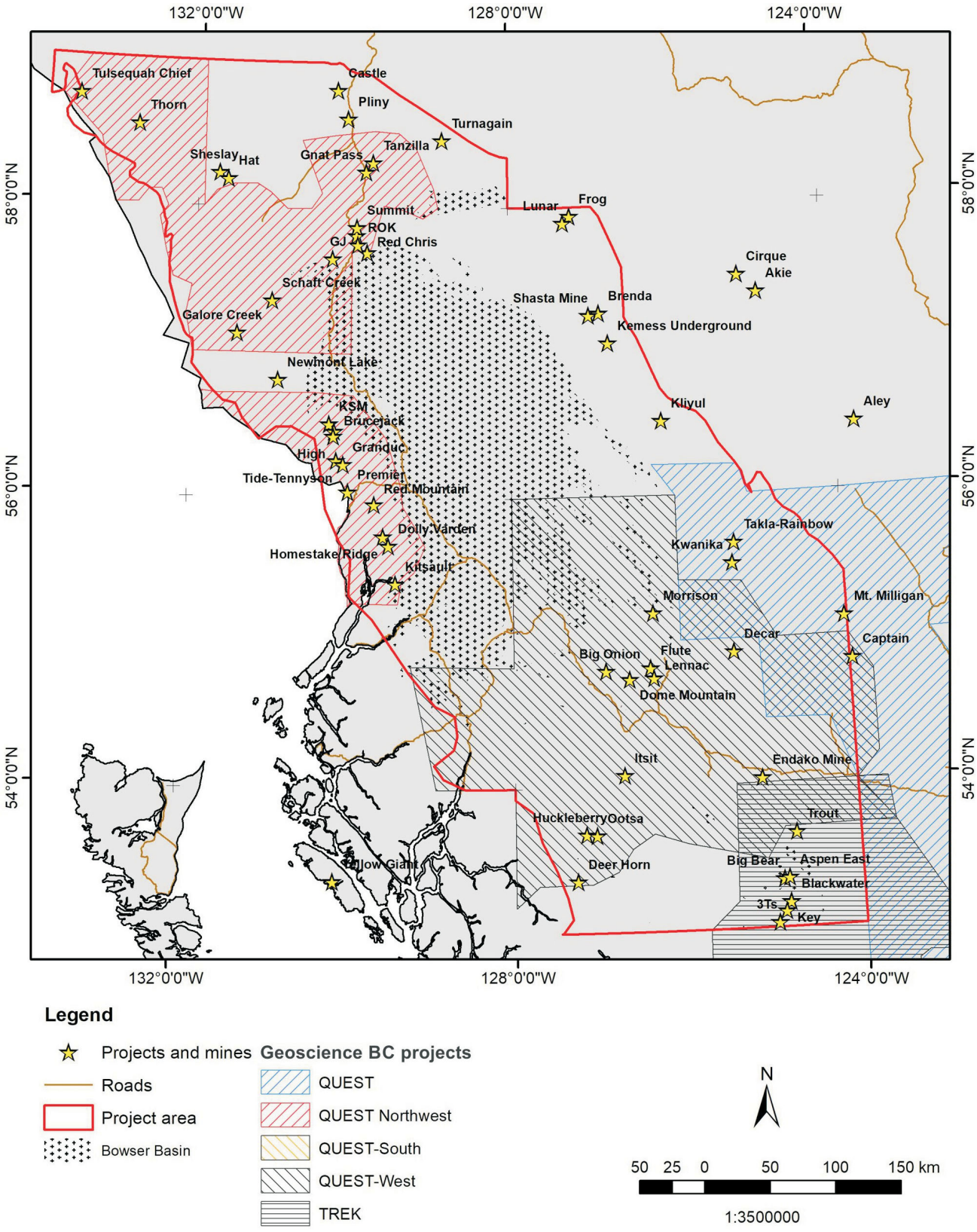

Figure 1. Location of study area, showing the areas covered by previous Geoscience BC initiatives, the locations of major mineral deposits and the area of bedrock covered by Bowser Basin sedimentary rocks that postdate some periods of mineralization.

An assessment of the database indicates that 36 elements have concentrations typically greater than the lower limits of detection while providing maximum spatial coverage. These include Au, Ag, Al, As, Ba, Bi, Ca, Cd, Co, Cr, Cu, Fe, Ga, Hg, K, La, Mg, Mn, Mo, Na, Ni, P, Pb, S, Sb, Sc, Se, Sr, Te, Th, Ti, Tl, U, V, W and Zr. This process resulted in the selection of 14 877 samples, excluding quality-control samples but including those collected within the Bowser Basin, most of which will be excluded from catchment basin analysis. Data for values below the lower limits of detection were computed by the method of nearest neighbour replacement estimates. The adjusted data were then used for subsequent multivariate statistical analyses. Multivariate analyses of data for these elements, including principal and independent component analysis following a centred-log ratio transformation to remove the effects of closure (Aitchison, 1986), are consistent with a dominant spatial control that can be related to regional lithological and mineral deposit trends for most elements. Commodity and pathfinder elements show a general spatial correlation with major mineral deposits and districts. Raw-element and principal-component gridded maps show no abrupt variations that might be related to map area and/or survey boundaries, indicating that interpretation of the geochemical data can proceed without the necessity of levelling the data for analytical batch effects.

Sampling and Analysis

The original regional geochemical survey (RGS) stream-sediment samples were generally collected from first- and second-order streams under Canada's National Geochemical Reconnaissance (NGR) program at an approximate density of one sample per every 13 km^2 in BC (e.g., Friske et al., 2003). The samples were sieved to –80 mesh (<177 μm) prior to analysis, originally using either aqua-regia digestion followed by atomic absorption spectroscopy (AAS), instrumental neutron activation analysis (INAA) or, for Au only, lead-collection fire assay. Splits of the original sieved sample material were archived in Ottawa, Ontario at the Geological Survey of Canada (GSC). This material was sampled for reanalysis using a dilute aqua-regia digestion (1 HCl:1 HNO_3:1 H_2O) at Bureau Veritas or standard aqua-regia digestion at Eco-Tech Laboratories and analysis by combined ICP-MS and ICP-AES. The original quality-control samples (field duplicates, blind or pulp duplicates and reference materials) were also sampled for reanalysis.

As demonstrated by Arne and Bluemel (2011), Arne and MacFarlane (2014) and Arne and Brown (2015), the precision of the original RGS Au data is poor, even when using up to 10 g of sample material. The original data, however, are superior to Au analysis of the archived material by ICP-MS using a 0.25–0.5 g sample aliquot (Mackie et al., 2017; this paper). For this reason, the original Au data have been used for the present compilation. Duplicate Au analyses have been averaged where available.

Data Quality

Quality-control data from the relevant Geoscience BC reanalysis projects have been provided by W. Jackaman (pers. comm., 2017). Data from a total of 1379 field duplicate pairs, 1394 pulp (blind) duplicate pairs, 1476 RGS reference materials and 2350 laboratory reference materials have been assessed for Au, As, Cu and Mo. These elements are representative of the types of mineral deposits found in the region of most interest (porphyry Cu-Mo, epithermal Au-Ag and VHMS Cu-Zn). Descriptions could not be obtained for all the reference materials submitted with the original stream-sediment batches, although data from them can still be assessed in terms of data consistency. The same reference materials were also not used throughout the original sampling programs, so it is difficult to assess continuity beyond a 10 year period, and is only possible for the Red Dog RGS reference material.

As expected, the precision and accuracy of the Au data are poor (Figure 2a, b), but improve for As, Cu and Mo. Neither the Acme DS7 (Acme Analytical Laboratories' in-house reference material; Natural Resources Canada, 2017) or Red Dog reference materials were designed for accurate and precise Au analyses, although they do demonstrate the amount of variability that might be observed in actual stream-sediment samples sieved to <177 μm. The control limits shown for the Red Dog reference material in Figure 2 were calculated from long-term averages, excluding outliers (R. Lett, pers. comm., 2017), and there are clearly numerous outliers that can be explained by inhomogeneity of the material and a nuggety distribution of Au particles in the reference material.

The accuracy of the Cu and As data is variable in Acme DS7 and Red Dog reference materials, respectively, but this is not surprising given that the reanalysis of the stream-sediment samples was completed between 2002 and 2017 (Figure 2c, d). Clear breaks in data for the reference materials occur where there is a break in the time sequence of the analyses; however, slight differences in the aqua-regia digestions used between labs, as well as variations over time at Bureau Veritas, are not considered to be significant for the interpretation of the data, although the Au ICP-MS data must be treated with caution.

Another important data-quality consideration is the reliability of original sample location information. The generation of catchment basins for individual samples uses modern 1:20 000 terrain resource information management (TRIM) topographical and hydrological data (Cui et al., 2009). Samples must, therefore, be accurately located within the modern topographical framework to ensure the correct catchment basin is allocated to each sample. In most

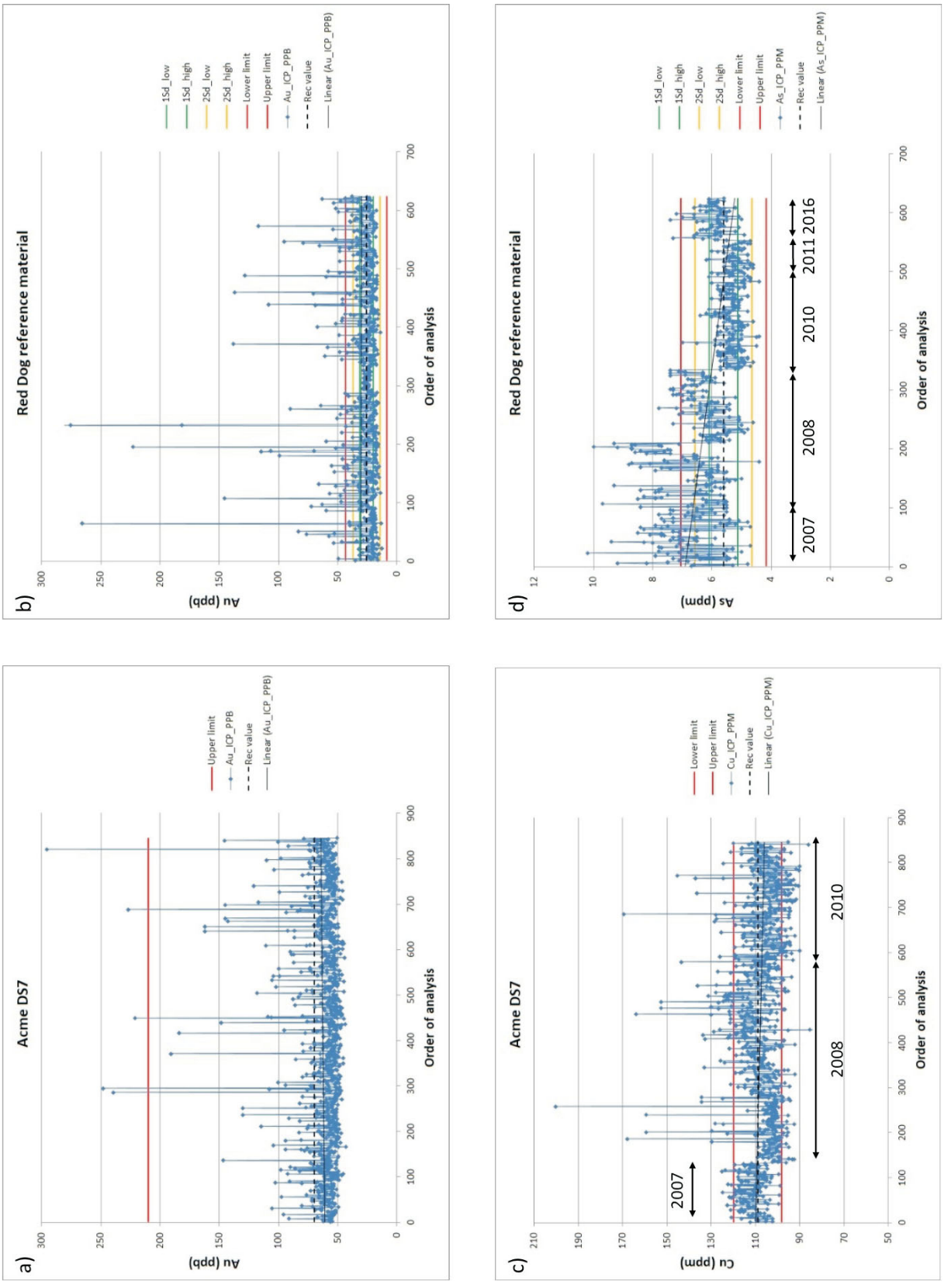

Figure 2. Summary of dilute aqua-regia inductively coupled plasma–mass spectrometry (ICP-MS) analyses of internal laboratory (Acme DS7) and RGS survey (Red Dog) reference materials: **a)** analysis of Acme DS7 for Au, **b)** analysis of Red Dog for Au, **c)** analysis of Acme DS7 for Cu and **d)** analysis of Red Dog for As. Analytical values (y-axis) are plotted in chronological order (x-axis).

cases, sample locations were manually marked onto 1:10 000 to 1:25 000 scale topographic map sheets and then the UTM grid reference locations measured off the map sheets in either NAD27 or NAD83 datums. In some cases, locations were recorded on sketch maps. In addition to the uncertainties associated with identifying sample locations prior to the availability of GPS receivers, the locations of streams have sometimes either physically shifted or vary by comparison to more precise topographical data. The result is that sample locations often do not plot on the correct drainage, and validation or correction of the locations is required (Cui, 2010). This process can be time consuming as not all location errors can be rectified using automated procedures within a GIS.

An example of a typical location validation issue is presented in Figure 3. In all three instances shown on this figure, sample points (shown by grey dots) plot up to 1 km from the locations plotted by hand using red circles shown on the georeferenced original sample location map. Samples 1391 and 1390 are good examples of a common location error that would be partially fixed by using a 'snap to' tool in a GIS, although the location for sample 1390 could potentially snap to the wrong stream given its distance from the correct tributary. Sample 1388 is an example of a considerable plotting error that required a significant move to its correct sample point location based on the original map. Validated, or corrected, sample locations (shown by pink dots) are the preferred sample locations based on the original sample location map.

Preliminary Results

Analysis of the distribution of raw elements shows a strong spatial association of commodity and pathfinder elements such as Au, Ag, Cu, Mo, Sb, Bi, Hg and Pb with areas of known mineral deposits. These elements also define loadings on the main principal components that account for nearly 60% of the variation within the dataset. It is unusual to see such a strong influence of commodity and pathfinder elements in the main principal components from a regional dataset; this bodes well for defining anomalous catchment

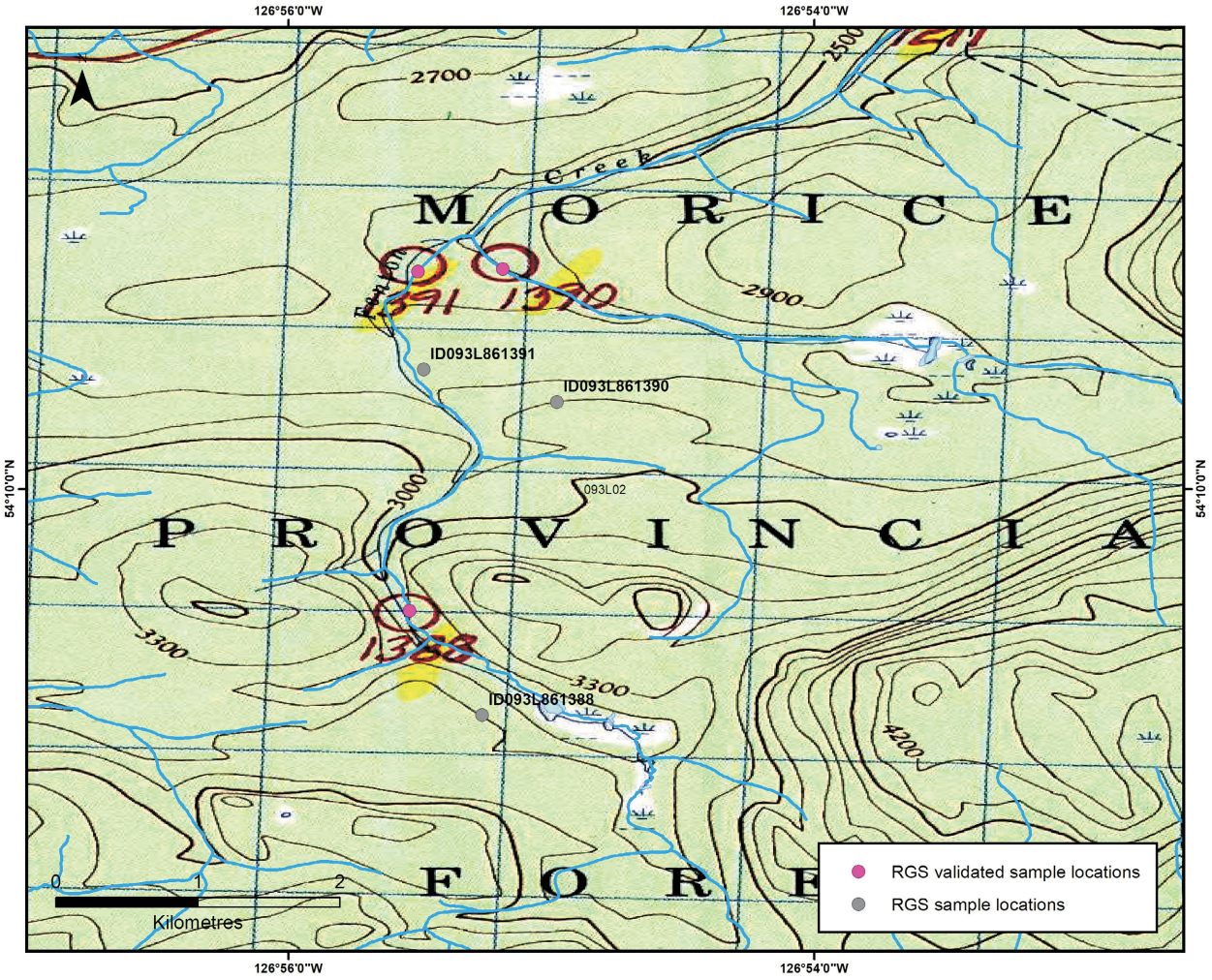

Figure 3. Example of regional geochemical survey (RGS) sample location validation problem (grey dots show the original sample location, red circles show the sampling locations marked on the original hard-copy map by the sampler and pink dots show the validated location).

basins with minimal processing of the data. Samples derived from sedimentary rocks of the Bowser Basin have a distinct geochemical signature defined largely by elements with a mafic affiliation (Co, Mg, Sc, Ni, Cr), as well as being elevated in elements that are often enriched in black shales (Cd, Sb, Ag, As, Se, Hg, Zn, Te). Triassic magmatic belts and batholiths of the Coast Plutonic Complex are characterized by elements having a felsic affinity (U, Bi, La, Mo, K).

Conclusions and Future Work

This project highlights the value of new ICP-MS geochemical data by assessing areas of known hydrothermal magmatic mineralization in the northern Stikine terrane in a single data compilation. Work remaining to be completed in this project includes validation and/or correction of sample locations prior to the generation of catchment basins by the BCGS for samples outside of the Bowser Basin. Catchment area and bedrock geology will be defined for each sample for comparison with inferred geology based on multi-element signatures for the main bedrock types. Geochemical data from individual samples will be levelled for the effects of variable bedrock geology in individual catchment basins. This will be followed by the generation of a series of exploration targeting catchment map products using a weighted sums modelling approach (Garrett and Grunsky, 2001) to optimize the geochemical fingerprint for different mineral deposit types using known mineral deposits and occurrences. These new products will identify specific basin catchments containing geochemical signatures consistent with the presence of mineralization, and thus provide new exploration targets for further investigation.

Acknowledgments

The authors thank Geoscience BC for funding to undertake this project. N. Reynolds of CSA Global is thanked for undertaking a peer review of this report.

References

Aitchison, J. (1986): The Statistical Analysis of Compositional Data; Chapman and Hall, New York, 416 p.

Arne, D.C. and Bluemel, E.B. (2011): Catchment analysis and interpretation of stream sediment data from QUEST South, British Columbia; Geoscience BC, Report 2011-5, 25 p., URL <http://www.geosciencebc.com/s/2011-05.asp> [October 2017].

Arne, D.C. and Brown, O. (2015): Catchment analysis applied to the interpretation of new stream sediment data from northern Vancouver Island, Canada (NTS 102I and 92L); Geoscience BC, Report 2015-4, 41 p., URL <http://www.geosciencebc.com/s/Report2015-04.asp> [October 2017].

Arne, D. and MacFarlane, B. (2014): Reproducibility of gold analyses in stream sediment samples from the White Gold District and Dawson Range, Yukon Territory, Canada; Explore, no. 164, p. 1–10.

Bonham-Carter, G.F and Goodfellow, W.D. (1986): Background corrections to stream geochemical data using digitized drainage and geological maps: application to Selwyn Basin, Yukon and Northwest Territories; Journal of Geochemical Exploration, v. 25, p. 139–55.

Carranza, E.J.M. (2009): Catchment analysis of stream sediment anomalies; *in* Geochemical Anomaly and Mineral Prospectivity Mapping in GIS, E.J.M. Carranza (ed.), Handbook of Exploration and Environmental Geochemistry, Elsevier Science, The Netherlands, v. 11, p. 115–144.

Colpron, M., Nelson, J.L. and Murphy, D.C. (2006): A tectonostratigraphic framework for the pericratonic terranes of the northern Canadian Cordillera; *in* Paleozoic Evolution and Metallogeny of Pericratonic Terranes at the Ancient Pacific Margin of North America Canadian and Alaskan Cordillera, M. Colpron and J. Nelson (ed.), Geological Association of Canada Special Paper 45, p. 1–23.

Cui, Y. (2010): Regional geochemical survey: validation and refitting of stream sample locations; *in* Geological Fieldwork 2010, BC Ministry of Energy, Mines and Petroleum Resources, BC Geological Survey, Paper 2011-1, p. 169–179, URL <http://www.empr.gov.bc.ca/Mining/Geoscience/PublicationsCatalogue/Fieldwork/Documents/2010/12_Cui_2010_hr.pdf> [October 2017].

Cui, Y., Eckstrand, H. and Lett, R.E. (2009): Regional geochemical survey: delineation of catchment basins for sample sites in British Columbia; *in* Geological Fieldwork 2008, BC Ministry of Energy, Mines and Petroleum Resources, BC Geological Survey, Paper 2009-1, p. 231–238, URL <http://www.empr.gov.bc.ca/Mining/Geoscience/PublicationsCatalogue/Fieldwork/Documents/2008/19_Cui.pdf> [October 2017].

Friske, P.W.B., Jackaman, W., Lett, R.E.W. and McCurdy, M.W. (2003): Regional stream sediment and water data, Fort Fraser, British Columbia; Geological Survey of Canada, Open File 1766, CD-ROM, doi:10.4095/214447

Garrett, R.G. and Grunsky, E.C. (2001): Weighted sums – knowledge based empirical indices for use in exploration geochemistry; Geochemistry: Exploration, Environment, Analysis, v. 1, p. 135–141.

Gunning, M.H., Hodder, R.W. and Nelson, J.L. (2006): Contrasting volcanic styles and their tectonic implications for the Paleozoic Stikine assemblage, western Stikine terrane, northwestern British Columbia; *in* Paleozoic Evolution and Metallogeny of Pericratonic Terranes at the Ancient Pacific Margin of North America Canadian and Alaskan Cordillera, M. Colpron and J. Nelson (ed.), Geological Association of Canada, Special Paper 45, p. 201–227.

Hawkes, H.E. (1976): The downstream dilution of stream sediment anomalies; Journal of Geochemical Exploration, v. 6, p. 345–358.

Jackaman, W. (2008a): QUEST Project sample reanalysis (NTS 93A, 93B, 93H, 93G, 93N); Geoscience BC, Report 2008-3, URL <http://www.geosciencebc.com/s/2008-03.asp> [November 2017].

Jackaman, W. (2008b): Regional stream sediment and water geochemical data: Terrace & Prince Rupert (NTS 103I & 103J), British Columbia; Geoscience BC, Report 2008-11, URL <http://www.geosciencebc.com/s/2008-11.asp> [November 2017].

Jackaman, W. (2009a): QUEST-West Project sample reanalysis (NTS 93E, 93F, 93L, 93M); Geoscience BC, Report 2009-5,

URL <http://www.geosciencebc.com/s/2009-05.asp> [November 2017].

Jackaman, W. (2009b): Regional drainage sediment and water geochemical data, central British Columbia (parts of NTS 93E, F, G, J, K, L, M, N & O); Geoscience BC Report 2009-11, URL <http://www.geosciencebc.com/s/2009-11.asp> [November 2017].

Jackaman, W. (2011): Northern BC sample reanalysis project (NTS 94C, 94D, 94E, 94L, 94M, 104B, 104G, 104I, 104O, 104P); Geoscience BC, Report 2011-02, URL <http://www.geosciencebc.com/s/2011-02.asp> [November 2017].

Jackaman, W. (2012): QUEST-Northwest sample reanalysis (ICP-MS) (NTS 104K); Geoscience BC, Report 2012-05, URL <http://www.geosciencebc.com/s/Report2012-05.asp> [November 2017].

Jackaman, W. (2017): 2016 RGS sample reanalysis project (parts of NTS 082G, 082J, 092N, 093E, 093H, 103O, 103P and 104N); Geoscience BC, Report 2017-04, URL <http://www.geosciencebc.com/s/Report2017-04.asp> [November 2017].

Mackie, R.A., Arne, D.C. and Brown, O. (2015): Enhanced interpretation of regional stream sediment geochemistry from Yukon: catchment basin analysis and weighted sums modelling; Yukon Geological Survey, Open File 2015-10, 9 p., URL <http://data.geology.gov.yk.ca/Reference/69462> [November 2017].

Mackie, R.A., Arne, D.C. and Pennimpede, C. (2017): Assessment of Yukon regional stream sediment catchment basin and geochemical data quality; Yukon Geological Survey, Open File 2017-4, 36 p., URL <http://data.geology.gov.yk.ca/Reference/79430> [October 2017].

Natural Resources Canada (2017): Control reference metadata: Acme DS7; Natural Resources Canada, URL <http://geochem.nrcan.gc.ca/cdogs/content/cr_/cr_00165_e.htm> [November 2017].

Nelson, J.L., Colpron, M. and Israel, S. (2013): The cordillera of British Columbia, Yukon and Alaska: tectonics and metallogeny; *in* Tectonic, Metallogeny, and Discovery: The North American Cordillera and Similar Accretionary Settings, M. Colpron, T. Bissig, B.G. Rusk and J.F.H. Thompson (ed.), Society of Economic Geology, Special Publication 17, p. 53–109.

Ricketts, B.D., Evenchick, C.A., Anderson, R.G. and Murphy, D.C. (1992): Bowser Basin, northern British Columbia: constraints on the timing of subsidence and Stikine terrane-North American terrane interactions; Geology, v. 20, p. 1119–1122.

Rukhlov, A. and Naziri, M. (2015): Regional geochemical survey database 2015; BC Geological Survey, BC Ministry of Energy, Mines and Petroleum Resources, Geofile 2015-3, URL <http://www.empr.gov.bc.ca/Mining/Geoscience/PublicationsCatalogue/GeoFiles/Pages/GF2015-3.aspx> [November 2017].

Nature and Origin of the Brucejack High-Grade Epithermal Gold Deposit, Northwestern British Columbia (NTS 104B): 2017 Update

D.F. McLeish, Department of Earth and Planetary Sciences, McGill University, Montréal, QC, duncan.mcleish@mail.mcgill.ca

A.E. Williams-Jones, Department of Earth and Planetary Sciences, McGill University, Montréal, QC

W.S. Board, Pretium Resources Inc., Vancouver, BC

J.R. Clark, Department of Earth and Planetary Sciences, McGill University, Montréal, QC

McLeish, D.F., Williams-Jones, A.E., Board, W.S. and Clark, J.R. (2018): Nature and origin of the Brucejack high-grade epithermal gold deposit, northwestern British Columbia (NTS 104B): 2017 update; *in* Geoscience BC Summary of Activities 2017: Minerals and Mining, Geoscience BC, Report 2018-1, p. 31–40.

Introduction

The Brucejack Au-Ag deposit of Pretium Resources Inc. (MINFILE 104B 193 and 104B 199; BC Geological Survey, 2017) is a recently discovered, large and exceptionally high grade (up to 41 000 g/ton Au), intermediate- or possibly low-sulphidation, epithermal deposit located in the Stewart–Eskay Creek mining district of northwestern British Columbia (BC). With commissioning completed in May of 2017 and commercial production achieved two months later, the deposit is host to Canada's newest Au mine. This project is taking advantage of the unparalleled opportunity offered by the extensive preproduction exploration and mine-development workings at Brucejack to study the genesis and evolution of high-grade epithermal Au deposits and, in particular, investigate 1) the chemical (including isotopic) characteristics of its ores and associated hydrothermal alteration; 2) the general mechanisms responsible for high-grade Au transport at temperatures characteristic of the epithermal realm; 3) the physicochemical conditions controlling Au deposition during the different stages of mineralization; and 4) the genetic relationship with spatially associated porphyry systems (if any). Ultimately, the aim of the project is to address the fundamental question of whether the large, high-grade Brucejack resource can be explained using a simple solubility model.

This paper provides an update on the study and presents findings made since the initial project overview was published last year (McLeish et al., 2017). Specific attention is given to recent advances in understanding the different styles of Au mineralization in the deposit, including the recent discovery of invisible Au mineralization in arsenian pyrite, as well as progress made in other areas of ore- and alteration-mineral chemistry. The problem of low-temperature Au solubility in hydrothermal fluids, a major motivation for this project, is discussed at length in the McLeish et al. (2017) paper and is not repeated here; the interested reader is referred to the 'Introduction' section of that paper for more information. The regional and property geology descriptions and the deposit mineralization overview are repeated from McLeish et al. (2017), with minor updates to deposit geochronological and lithostratigraphic data.

This publication is also available, free of charge, as colour digital files in Adobe Acrobat® PDF format from the Geoscience BC website: http://www.geosciencebc.com/s/SummaryofActivities.asp.

Regional Geology

The Brucejack deposit is situated in the northwestern Stikine terrane (Figures 1, 2), a paleo–island arc system akin to that of the modern-day Philippine archipelago (Marsden and Thorkelson, 1992). The Stikine terrane formed as an intraoceanic island arc in the mid-Paleozoic and was accreted to the western continental margin of Laurentia in the Middle to Late Jurassic (Monger et al., 1991; Anderson, 1993). Volcano-sedimentary rocks of the Late Triassic Stuhini Group and Early Jurassic Hazelton Group dominate the stratigraphy of the Stikine terrane. Two distinct episodes of magmatism in the Late Triassic and in the Early Jurassic (229–221 Ma and 195–175 Ma, respectively; Macdonald et al., 1996) affected the Stuhini-Hazelton succession, which was deformed during Middle to Late Jurassic accretion and later Cretaceous compressional tectonism (Greig and Brown, 1990; Alldrick, 1993). Porphyry magmatism is known to have spanned the interval ca. 220–186 Ma on a terrane scale (Logan and Mihalynuk, 2014); however, within the Stewart–Eskay Creek district, U-Pb ages for porphyry intrusions are generally limited to the ca. 197–193 Ma range (Kirkham and Margolis, 1995).

Brucejack Property Geology

Five zones of mineralization have been explored in detail at Brucejack (West, Valley of the Kings, Bridge, Gossan Hill and Shore zones; Figure 3), all of which are hosted within hornblende- and/or feldspar-phyric volcanic flows, lapilli

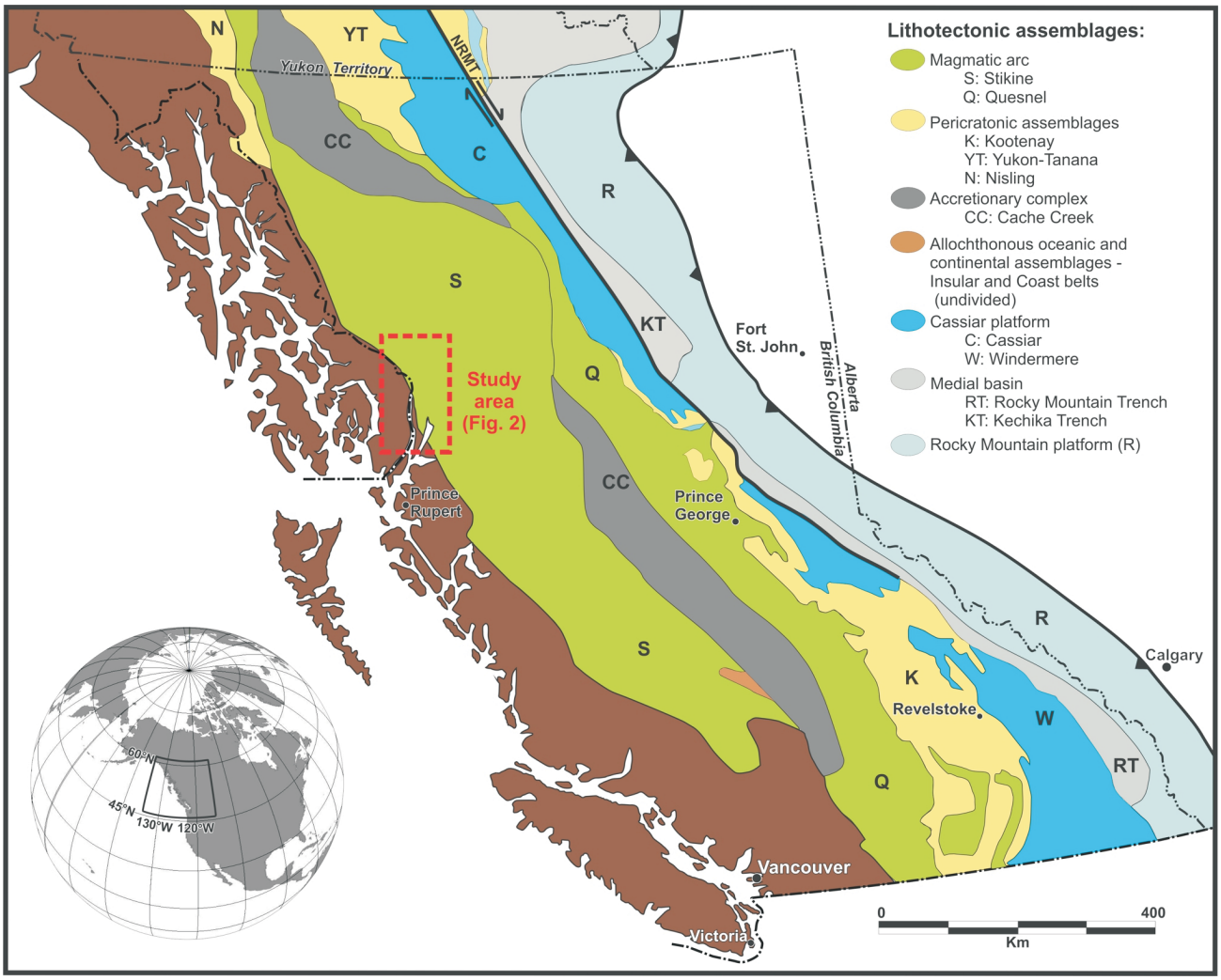

Figure 1: Location of the study area in reference to the major lithotectonic subdivisions of the Canadian Cordillera (modified after McLeish [2013] with lithotectonic boundaries from Johnston [2008]). Abbreviation: NRMT, Northern Rocky Mountain Trench (fault).

tuff, locally derived pyroclastic and volcanic conglomerate, and volcanic sandstone, siltstone and mudstone of the lowermost Hazelton Group, proximal to the regional-scale unconformity between the Stuhini and Hazelton groups (Board and McNaughton, 2013). To the immediate west and northwest of these zones, monzonitic, syenitic and granitic rocks of the Mitchell suite intruded volcaniclastic rocks of the Stuhini and Hazelton groups; these intrusions are closely associated with porphyry-style Cu-Au-Mo mineralization on the adjacent Kerr-Sulphurets-Mitchell and Snowfield properties (Kirkham and Margolis, 1995). Uranium-lead zircon ages from various phases of these intrusions suggest that the porphyry-style mineralization was emplaced at 197–190 Ma (Bridge, 1993; Margolis, 1993; Macdonald et al., 1996; Febbo et al., 2015). Large areas of hydrothermal alteration affected and surround the intrusive complexes of the Mitchell suite. These consist of 1) early potassic alteration closely associated with porphyry Cu and Au mineralization; 2) locally overprinting propylitic and chlorite-sericite alteration; and 3) widespread and well-developed, late quartz-sericite-pyrite alteration that pervasively overprinted earlier alteration and extends distally into the surrounding hostrocks of the Stuhini and Hazelton groups (Ghaffari et al., 2012).

Deposit Mineralization

Within the Valley of the Kings zone (VOK; Figure 3), Au mineralization is hosted by extensive, predominantly subvertical, quartz-carbonate-sulphide vein stockworks and subordinate vein breccias. Five stages of veins have been recognized in the VOK: 1) discontinuous pyrite-stringer veins containing carbonate and quartz (Vn_0); 2) electrum-bearing quartz–carbonate±sericite sheeted, stockwork and brecciated veins (Vn_{1a}, Vn_{1b} and Vn_{1c}, respectively); 3) Zn–Pb±Cu sulphide veins containing Ag sulphosalts and electrum (Vn_2); 4) carbonate±quartz veins containing abundant orange-coloured, Mn-bearing calcite, and electrum (Vn_3); 5) postmineralization, Cretaceous, orogenic quartz±carbonate shear veins with rare, remobilized pyrite,

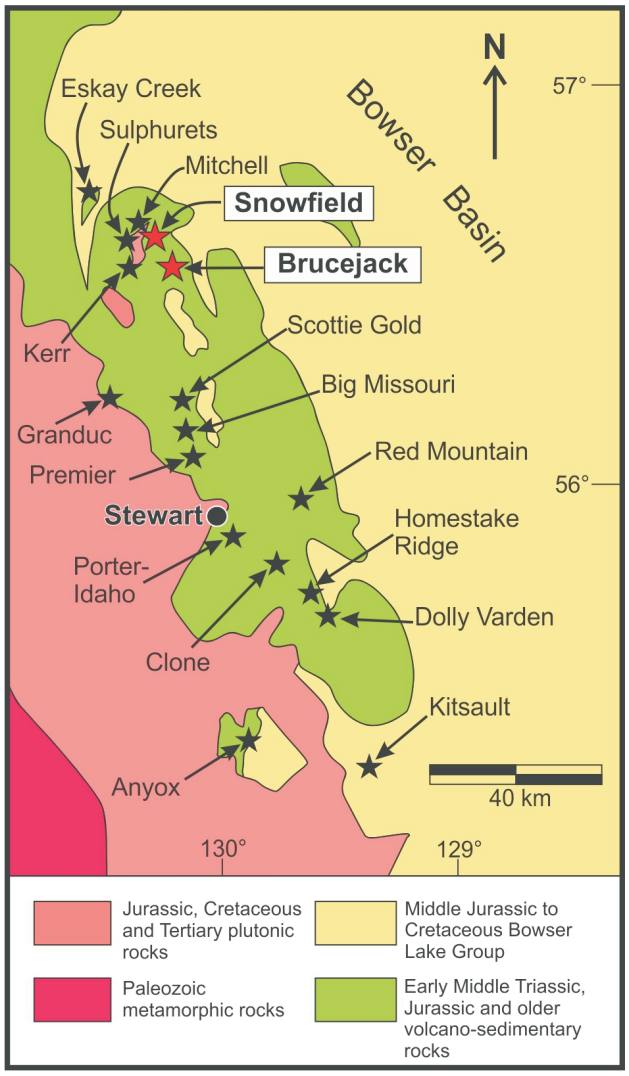

Figure 2: Major porphyry, epithermal and volcanogenic massive-sulphide deposits of the Stewart–Eskay Creek district (modified after Ghaffari et al., 2012), with the locations of the Brucejack and Snowfield properties highlighted.

electrum and base-metal sulphides in thrust-related shear bands (Vn_{4a}, Vn_{4b}) and subhorizontal, barren, white quartz tension-gash veins with adjacent chlorite alteration (Vn_{4c}; classification modified after Tombe et al., 2014). The Vn_0, $Vn_{1a\text{-}c}$, Vn_2 and Vn_3 veins are largely undeformed to weakly deformed, except within localized strain zones where they are moderately to strongly deformed. Evidence from cross-cutting relationships paired with recent, unpublished, hostrock U-Pb zircon determinations have constrained the age of $Vn_{1a\text{-}c}$, Vn_2 and Vn_3 vein formation to ca. 184–183 Ma (Board, pers. comm., 2017). Variably developed but generally intense quartz-sericite-pyrite alteration occurs throughout the deposit but is strongest proximal to the Brucejack fault and the unconformity between the Stuhini and Hazelton groups, which suggests that these structures may have acted as important fluid conduits during hydrothermal alteration and mineralization. Preliminary paleotemperature vectors derived from alteration, mineralization and vein textures suggest a down-temperature thermal gradient toward the east (up stratigraphy) and away from the Snowfield and Kerr-Sulphurets-Mitchell higher temperature porphyry centres, located northwest of the deposit (Board, 2014).

Preliminary Mineral Chemistry

Pyrite

Following the discovery of widespread, oscillatory zoned arsenian pyrite during the initial petrography study (McLeish et al., 2017), pyrite from all mineralization-stage vein types (Vn_{1s}, Vn_2 and Vn_3) was analyzed using electron microprobe analyzer–wavelength dispersive spectroscopy (EMPA-WDS). The goal of these analyses was to determine if the arsenian pyrite hosts any invisible Au mineralization, either as submicroscopic (<0.1 µm) crystal inclusions or as Au atoms structurally bound in the pyrite lattice (i.e., in solid solution), as has been found in other epithermal deposits (e.g., Reich et al., 2005). Two representative arsenian-pyrite–bearing thin sections from each vein class were chosen for study based on the nature of the oscillatory zoned arsenian pyrite, which was determined by backscattered-electron (BSE) imaging.

The EMPA-WDS analyses of pyrite were performed at the joint University of Ottawa–Canadian Museum of Nature MicroAnalysis Laboratory using a JEOL 8230 SuperProbe with five X-ray wavelength-dispersive spectrometers. Pyrite grains from 18 thin sections were quantitatively analyzed for As (Lα), Au (Lα), Cu (Kα), Fe (Kα), and S (Kα) using the following synthetic and natural standards: Au80Ag20 alloy (Au), cubanite (Cu), GaAs alloy (As) and pyrite (Fe and S). Microbeam analyses were performed using a beam energy of 20 keV, a 40° takeoff angle, a 2 µm beam diameter and a 200 nA beam current. Minimum detection limits of 150 ppm and 100 ppm Au were achieved using these operating conditions with 100 and 200 second counting times, respectively.

Results from BSE imaging and EMPA-WDS analyses show oscillatory zoned arsenian pyrite contains localized occurrences of high-grade Au mineralization (150–1920 ppm Au; Figure 4). Many of the pyrite grains analyzed contain electrum-filled fractures that clearly crosscut the As-bearing oscillatory zones (Figure 4a, b), indicating that pyrite-hosted invisible Au mineralization predates electrum-stage mineralization. Furthermore, phyllically altered wallrocks in the VOK host oscillatory zoned pyrite similar to that documented in all three mineralization-stage vein types (cf. Figure 5, grains S430136a and U585EX315). This suggests that the vein-hosted pyrite may be inherited from the wallrocks. Pre-electrum deformation of pyrite is also locally evident in the form of microfractures offsetting

arsenian growth zones in the intermediate sections of grains (Figure 4c).

In order to better understand the distribution of Au and other trace elements in VOK pyrite, laser-ablation inductively coupled plasma–mass spectrometry (LA-ICP-MS) maps of pyrite were prepared. Although destructive and having less spatial resolution than the EMPA-WDS method, LA-ICP-MS has the advantage of being able to provide multi-element data rapidly for an entire mineral grain. Twenty-eight pyrite grains with oscillatory, As-rich growth zones were selected for LA-ICP-MS mapping. All grains chosen were hosted completely within, or were immediately adjacent to, Vn_1 or Vn_3 veins.

Sixteen grains were successfully mapped using a Resonetics RESOlution M-50 ArF excimer laser (193 nm) coupled to an Agilent 7900x ICP-MS at the Laboratoire des Matériaux Terrestres of the l'Université du Québec à Chicoutimi. The concentrations of ^{27}Al, ^{29}Si, ^{33}S, ^{34}S, ^{44}Ca, ^{47}Ti, ^{51}V, ^{53}Cr, ^{55}Mn, ^{57}Fe, ^{59}Co, ^{60}Ni, ^{61}Ni, ^{63}Cu, ^{65}Cu, ^{66}Zn, ^{72}Ge, ^{74}Ge, ^{75}As, ^{77}Se, ^{82}Se, ^{95}Mo, ^{96}Mo, ^{109}Ag, ^{111}Cd, ^{113}In, ^{115}In, ^{118}Sn, ^{121}Sb, ^{125}Te, ^{128}Te, ^{137}Ba, ^{182}W, ^{184}W, ^{197}Au, ^{200}Hg, ^{202}Hg, ^{203}Tl, ^{204}Pb, ^{205}Tl, ^{206}Pb, ^{207}Pb, ^{208}Pb and ^{209}Bi were measured. Element-distribution maps (Figure 5) were made by performing a series of line scans across each grain with a beam size of 11–19 µm and a stage speed of 10–20 µm/s. A laser fluence of 13 J/cm^2 with a repetition rate of

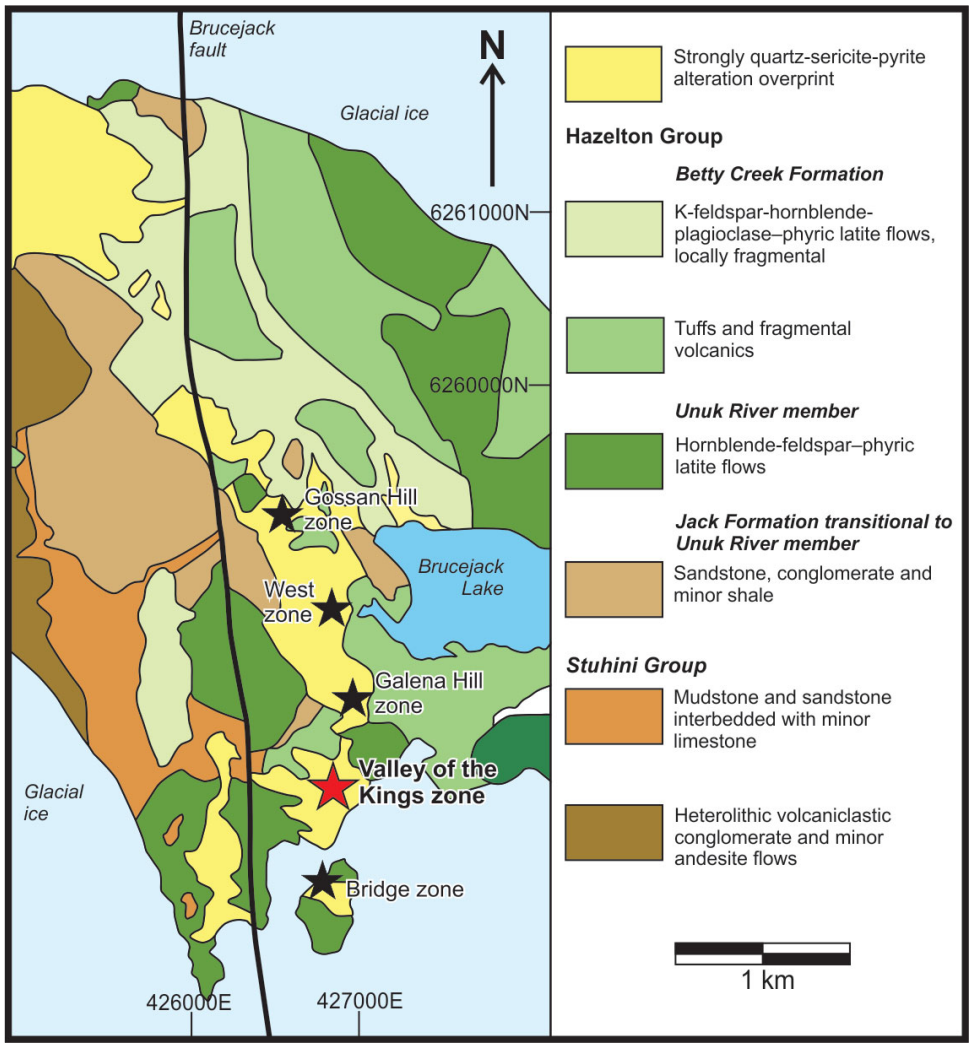

Figure 3: Geology of the Brucejack deposit area (modified after Tombe [2015] with revised stratigraphic nomenclature from Nelson and Kyba [2014]), showing five main zones of mineralization that are hosted within a moderately to strongly sericite-quartz-pyrite–altered sequence of hornblende- and/or feldspar-phyric volcanic flows, lapilli tuffs, locally derived pyroclastic and volcanic conglomerate, and volcanic sandstone, siltstone and mudstone of the lowermost Hazelton Group. All zones are proximal to a regional-scale unconformity between the Stuhini and Hazelton groups. Area covered by this figure is approximately the size of Brucejack star on Figure 1.

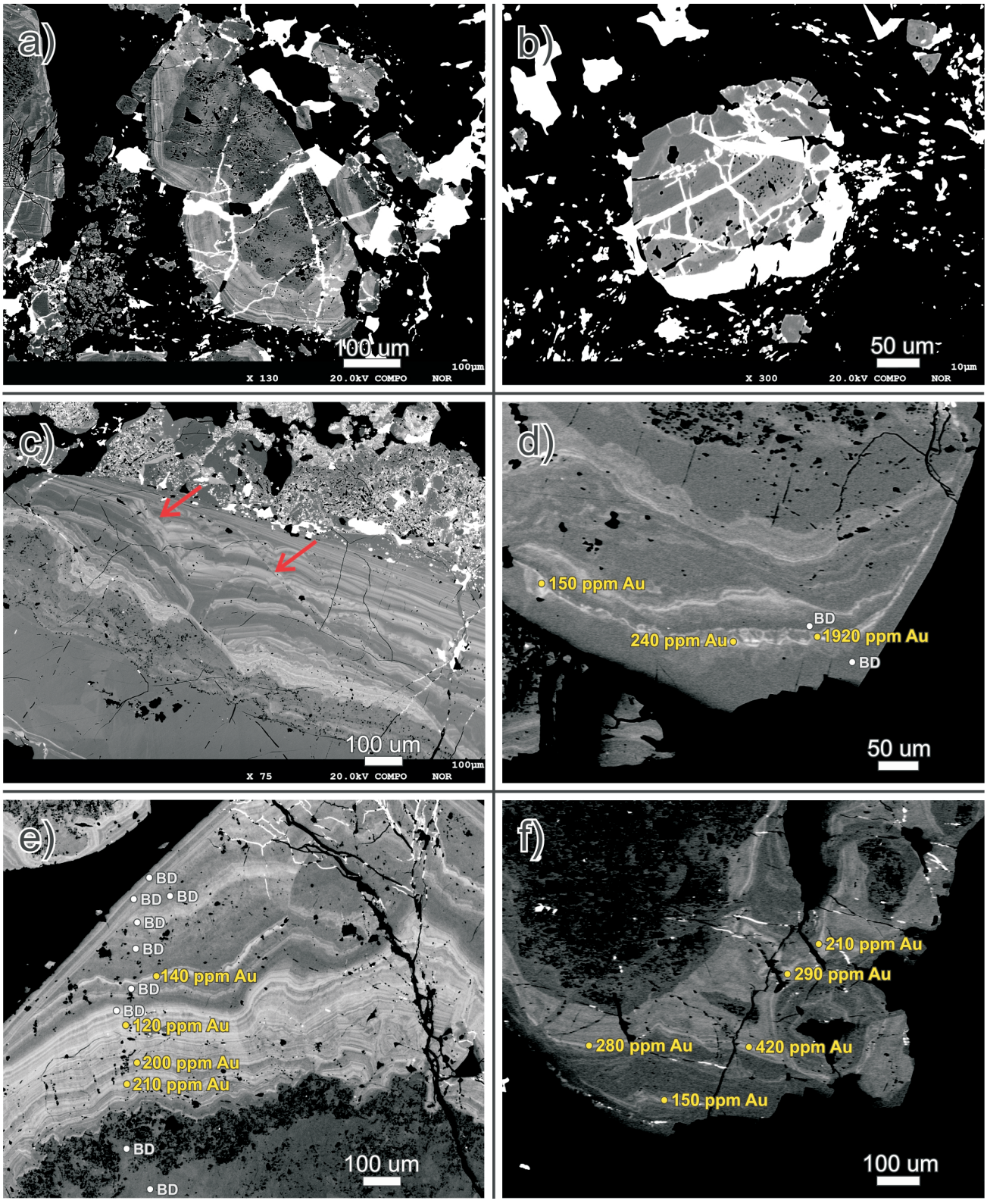

Figure 4: Backscattered-electron (BSE) images of pyrite and electrum from ore-stage quartz-carbonate veins at the Brucejack deposit: **a) and b)** electrum (brightest mineral) crosscuts oscillatory zoned arsenian pyrite (As-rich bands of pyrite are lighter coloured and surround an As-poor pyrite core); **c)** pre-electrum deformation of the arsenian pyrite is manifested by several groups of microfractures (red arrows) in the pyrite, which offset intermediate arsenian pyrite bands but do not propagate into the outermost pyrite growth zones; **d)**, **e)** and **f)** EMPA-WDS spot analyses of pyrite indicate significant Au concentrations in irregularly shaped, intermediate, arsenian growth zones (yellow dots), whereas As-poor cores and outer growth zones all have Au concentrations below detection limit (grey dots labelled 'BD'; i.e., <100 ppm Au).

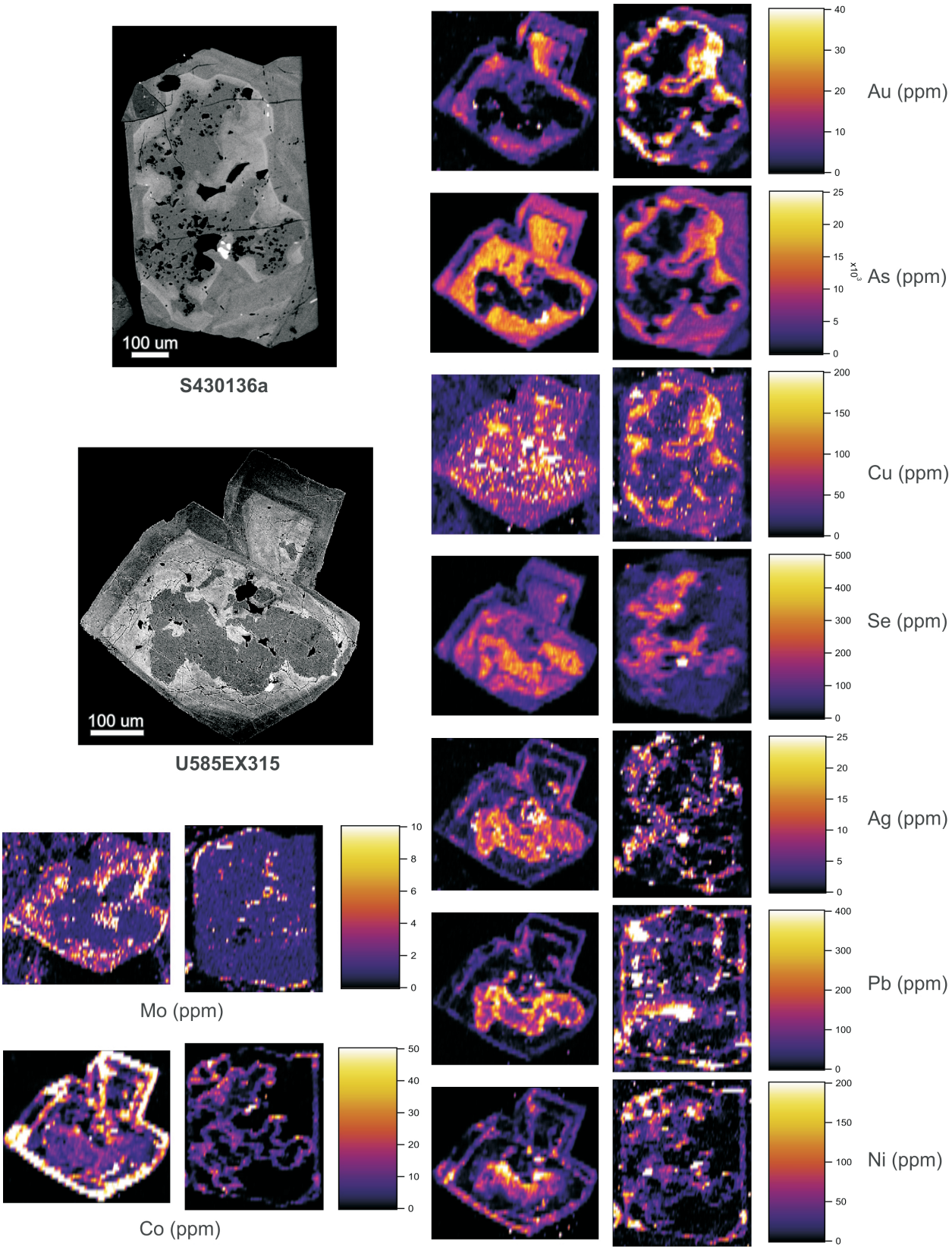

Figure 5: Laser-ablation inductively coupled plasma–mass spectrometry (LA-ICP-MS) elemental maps of pyrite from the Valley of the Kings zone at the Brucejack deposit, shown in reference to the grain before ablation (BSE images at top left). The upper BSE image is of a pyrite grain from a sample containing ore-stage (Vn_1) vein-hosted pyrite (sample S430136a). The lower BSE image is of a pyrite grain from a sample containing medium- to coarse-grained, wallrock-hosted pyrite located marginal to a Vn_1 vein (~1 cm away from the vein margin; sample U585EX315). See text for discussion.

15 Hz was used for all line scans. The following certified standards were used for external calibration: JB-MSS5, a synthetic FeS crystal, containing 50–70 ppm of most chalcophile elements, supplied by J. Brenan of Dalhousie University; MASS-1, a ZnCuFeS pressed-powder pellet doped with 50–70 ppm of Ag, As, Bi, Pb, Re, Sb, Se, Sn and Te, supplied by the United States Geological Survey (USGS); Laflamme Po727, a synthetic FeS crystal doped with 40 ppm of platinum-group elements and Au, supplied by Memorial University; and GSE-1G, a synthetic glass doped with 300–600 ppm Ba, Cr, Ge, La, Mn, Ni, Re, Si, Sr, Ti, V, W and Yb, supplied by the USGS. The standard JB-MSS5 was also used as a secondary reference material for intrastandard quality control. The maps were generated in the software package Iolite using the time-resolved composition of each element; they are semiquantitative and indicate the relative concentration of each element.

Preliminary results from LA-ICP-MS mapping of characteristic VOK vein-hosted, and wallrock-hosted vein-marginal, pyrite are presented in Figure 5. These grains generally display similar trace-element distribution patterns, with several elements being strongly zoned. The elements Se, Sb, Ni, Pb, Ag, and Bi are strongly focused in grain cores, whereas As, Au, and Cu are enriched in irregularly shaped intermediate growth zones; Mo also appears weakly concentrated in these intermediate zones, as well as in U585EX315. With the exception of weak anomalies of Ni, Tl and Co defining narrow, regular (cubic) growth zones, the outer grain-rim areas beyond the irregularly shaped intermediate growth zones do not usually display trace-element zonation.

Electrum

Initial EMPA-WDS analyses of electrum from the different mineralized VOK vein stages and substages identified an apparently regular and systematic variation in the Au:Ag ratio of the mineral with vein type. A significant number (n = 24) of new samples have been analyzed since this finding was first published (McLeish et al., 2017). They show that the variation in electrum chemistry between vein types initially documented holds true across the VOK. New samples were collected from each vein type, based on the nature and abundance of electrum mineralization present. Specific emphasis was placed on selecting samples from the Vn_2-type veins, which were not analyzed during the initial study.

A large number of EMPA-WDS analyses of electrum were performed at the McGill University Electron Microprobe Laboratory and the joint University of Ottawa–Canadian Museum of Nature MicroAnalysis Laboratory, using JEOL 8900 and JEOL 8230 SuperProbe instruments, respectively. Both instruments are equipped with five X-ray wavelength-dispersive spectrometers and, with limited exceptions, identical operating conditions were used at both facilities. Electrum grains were quantitatively analyzed for Ag (Lα), Au (Mα), Hg (Lα in Montréal; Mβ in Ottawa) and Te (Lβ) using the following synthetic and natural standards: Au60Ag40 alloy (Au and Ag), cinnabar (Hg) and native Te (Te in Montréal; Sb_2Te_3 in Ottawa). Microbeam analyses were performed using a beam energy of 20 keV, a 40° takeoff angle, a 5 µm beam diameter and a 30 nA beam current (40 nA current in Ottawa). Duplicate EMPA-WDS spot tests were done on selected electrum grains at both facilities and no significant difference in results was observed.

Gold and silver results from the EMPA-WDS analyses of electrum are shown, together with those from McLeish et al. (2017), in Figure 6. The Au:Ag ratio of the electrum appears to vary considerably with vein type, and no significant variation in the Au:Ag ratio of electrum was observed within individual samples. Analyses were taken across electrum grains (rim-core-rim) for both quartz-carbonate-matrix–hosted and pyrite-inclusion–hosted electrum, with no obvious Au:Ag differences observed. No Te was detected in the electrum; trace levels of mercury (<1.4 wt. %) were found in electrum samples with a high Ag content (40–60 wt. %) from Vn_2 veins. The regular, systematic variation in the Au:Ag ratio of the electrum with vein type was confirmed, with some overlap observed between vein types. Two Vn_2 samples in which electrum occurs in textural equilibrium with galena and sphalerite (SU-312 and SU-580) yielded Au values significantly lower than in Vn_2 veins where no textural equilibrium was observed between electrum and base-metal sulphide mineralization. Initial three-dimensional modelling of the electrum chemistry results show that there is no significant spatial control on electrum chemistry.

Summary and Future Work

The petrographic and mineral chemistry results presented here indicate that the Brucejack deposit was formed from multiple, possibly long-lived mineralizing events, which likely originated from at least two chemically and temporally distinct hydrothermal systems. The finding of high-grade invisible Au mineralization in As-rich growth zones of pyrite crosscut by electrum demonstrates that a significant Au mineralization event predated the hydrothermal activity responsible for the three generations of epithermal quartz-carbonate-electrum veins (Vn_1-Vn_3). Furthermore, evidence of pre-electrum, post–auriferous-pyrite deformation indicates that the pyrite-hosted Au and electrum mineralization were separated by a deformation event of presently unknown extent.

Preliminary petrographic observations suggest that the older, invisible Au–hosting pyrite within the ore-stage veins of the VOK was likely inherited from the adjacent phyllically altered wallrocks. If the phyllic alteration af-

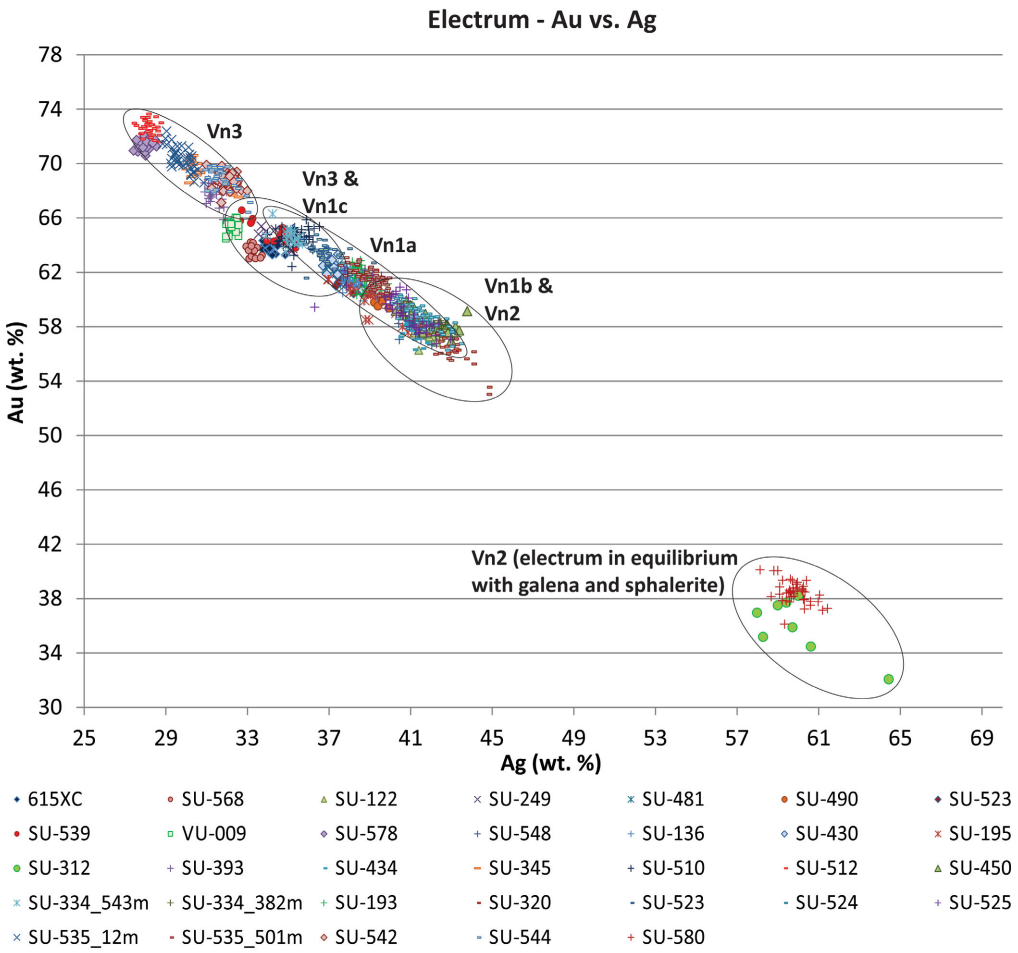

Figure 6: Gold and silver concentrations in electrum from the Valley of the Kings zone at the Brucejack deposit, based on EMPA-WDS analyses. See text for discussion.

fecting the VOK wallrocks is genetically related to the broader phyllic-alteration halo surrounding the older Kerr-Sulphurets-Mitchell and Snowfield porphyry deposits, as has been suggested from regional mapping (e.g., Nelson and Kyba, 2014), the invisible pyrite-hosted Au mineralization identified here may be the product of an approximately 8–10 m.y. older, magmatic-hydrothermal mineralizing event. The implications of such a genetic model, if correct, are potentially profound considering the widespread nature and strength of pyrite alteration/mineralization in phyllically altered country rocks of the VOK. For example, this model would suggest that 1) the electrum-hosting epithermal veining alone is not sufficient to account for the 8.7 million ounce Au reserve at Brucejack; and 2) the broad swath of phyllically altered country rocks in the vicinity of the VOK have the potential to, on their own, host possibly significant refractory Au mineralization.

Mineral chemistry and petrographic investigations will continue, and the fluid-inclusion and thermodynamic-modelling work described in the initial *Summary of Activities* paper (McLeish et al., 2017) will begin, in order to further test hypotheses advanced in that paper and to look for other insights into the origin and physicochemical evolution of the deposit. A major thrust of the research during the coming year will be to determine the reason for the extraordinarily high Au concentrations in the Brucejack deposit. To this end, work will build on the observations of Harrichhausen (2016) and Harrichhausen et al. (2016) of Au-Ag nanoparticles in relict amorphous silica–hosted electrum dendrites at Brucejack, by conducting a comprehensive high-resolution (nano-scale) transmitted electron microscopic (TEM) examination of electrum in the deposit. If it can be demonstrated that much of the electrum was initially nanoparticulate, this could eliminate the dependence on simple solubility and point to colloidal processes (mechanical transport) as a potentially important means of Au hyperenrichment (cf. Williams-Jones et al., 2009).

Acknowledgments

Major funding for this project is being provided by the Natural Sciences and Engineering Research Council of Canada

(NSERC) and Pretium Resources Inc. The authors thank O. Vasyukova for providing a careful and constructive review of this paper. The lead author also thanks Geoscience BC and the Society of Economic Geologists (SEG) for their financial support through the Geoscience BC Scholarship and SEG Student Research Grant programs, respectively. Lastly, the authors gratefully acknowledge the logistical and accommodation support generously provided by Pretium during the summer field season.

References

Alldrick, D.J. (1993): Geology and metallogeny of the Stewart mining camp, northwestern British Columbia; BC Ministry of Energy, Mines and Petroleum Resources, BC Geological Survey, Bulletin 85, 105 p.

Anderson, R.G. (1993): A Mesozoic stratigraphic and plutonic framework for northwestern Stikinia (Iskut River area), northwestern British Columbia, Canada; *in* Mesozoic Paleogeography of the Western United States, II, G.C. Dunne and K.A. McDougall (ed.), Society of Economic Paleontologists and Mineralogists, Pacific Section, Los Angeles, California, p. 477–494.

BC Geological Survey (2017): MINFILE BC mineral deposits database; BC Ministry of Energy, Mines and Petroleum Resources, BC Geological Survey, URL <http://minfile.ca/> [November 2017].

Board, W.S. (2014): Brucejack geology summary; Pretium Resources Inc., URL <http://s1.q4cdn.com/222336918/files/doc_downloads/geology/2013429_Geology_for_website_APRIL2013_WSB.pdf> [November 2016].

Board, W.S. and McNaughton, K.C. (2013): The Brucejack high-grade gold project, northwest British Columbia, Canada; *in* Proceedings of NewGenGold Conference, November 26–27, 2013, Perth, Australia, p. 177–191.

Bridge, D.J. (1993): The deformed Early Jurassic Kerr copper-gold porphyry deposit, Sulphurets gold camp, northwestern British Columbia; M.Sc. thesis, The University of British Columbia, Vancouver, BC, 303 p.

Febbo, G.E., Kennedy, L.A., Savell, M., Creaser, R.A. and Friedman, R.M. (2015): Geology of the Mitchell Au-Cu-Ag-Mo porphyry deposit, northwestern British Columbia, Canada; *in* Geological Fieldwork 2014, BC Ministry of Energy, Mines and Petroleum Resources, BC Geological Survey, Paper 2015-1, p. 59–86.

Ghaffari, H., Huang, J, Hafez, S.A., Pelletier, P., Armstrong, T., Brown, F.H., Vallat, C.J., Newcomen, H.W., Weatherly, H., Wilchek, L. and Mokos, P. (2012): Technical report and updated preliminary economic assessment of the Brucejack project; NI 43-101 report by Tetra Tech, Wardrop, Rescan, PE Mining, Geospark and AMC Mining, 327 p.

Greig, C.J. and Brown, D.A. (1990): Geology of the Stikine River–Yehiniko Lake area, northwestern British Columbia; Geological Association of Canada–Mineralogical Association of Canada, Joint Annual Meeting, Program with Abstracts, v. 15, p. A51.

Harrichhausen, N.J. (2016): Role of colloidal transport in the formation of high-grade gold veins at Brucejack, British Columbia; Ph.D. thesis, McGill University, Montréal, Quebec, 123 p.

Harrichhausen, N.J., Rowe, C.D., Board, W.S. and Greig, C.J. (2016): Relationship between amorphous silica and precious metals in quartz veins: examples from Brucejack, British Columbia and Dixie Valley, Nevada; Association for Mineral Exploration (AME) Roundup, conference poster, URL <http://www.geosciencebc.com/i/pdf/Roundup2016/2016%20poster_Harrichhausen.pdf> [November 2016].

Johnston, S.T. (2008): The Cordilleran ribbon continent of North America; Annual Review of Earth and Planetary Sciences, v. 36, p. 495–530.

Kirkham, R.V. and Margolis, J. (1995): Overview of the Sulphurets area, northwestern British Columbia; *in* Porphyry Deposits of the Northwestern Cordillera of North America, T.G. Schroeter (ed.), Canadian Institute of Mining, Metallurgy and Petroleum, Special Volume 46, p. 473–508.

Logan, J.M. and Mihalynuk, M.G. (2014): Tectonic controls on Early Mesozoic paired alkaline porphyry deposit belts (Cu-Au ± Ag-Pt-Pd-Mo) within the Canadian Cordillera; Economic Geology, v. 109, p. 827–858.

Macdonald, A.J., Lewis, P.D., Thompson, J.F.H., Nadaraju, G., Bartsch, R., Bridge, D.J., Rhys, D.A., Roth, T., Kaip, A., Godwin, C.I. and Sinclair, A.J. (1996): Metallogeny of an Early to Middle Jurassic arc, Iskut River area, northwestern British Columbia; Economic Geology, v. 91, p. 1098–1114.

Margolis, J. (1993): Geology and intrusion related copper-gold mineralization, Sulphurets, British Columbia: Ph.D. thesis, University of Oregon, Eugene, Oregon, 289 p.

Marsden, H. and Thorkelson, D.J. (1992): Geology of the Hazelton Volcanic Belt in British Columbia: implications for the Early to Middle Jurassic evolution of Stikinia; Tectonics, v. 11, p. 1266–1287.

McLeish, D.F. (2013): Structure, stratigraphy, and U-Pb zircon-titanite geochronology of the Aley carbonatite complex, northeast British Columbia: evidence for Antler-aged orogenesis in the Foreland Belt of the Canadian Cordillera; M.Sc. thesis, University of Victoria, Victoria, BC.

McLeish, D.F., Williams-Jones, A.E. and Board, W.S. (2017): Nature and origin of the Brucejack high-grade epithermal gold deposit, northwestern British Columbia (NTS 104B); *in* Geoscience BC Summary of Activities 2016, Geoscience BC, Report 2017-1, p. 223–231, URL <http://www.geosciencebc.com/i/pdf/SummaryofActivities2016/SoA2016_McLeish.pdf> [October 2017].

Monger, J.W.H., Wheeler, J.O., Tipper, H.W., Gabrielse, H., Harms, T., Struik, L.C., Campbell, R.B., Dodds, C.J., Gehrels, G.E. and O'brien, J. (1991): Upper Devonian to Middle Jurassic assemblages; Chapter 8 *in* Geology of the Cordilleran Orogen in Canada, H. Gabrielse and C.J. Yorath (ed.), Geological Survey of Canada, Geology of Canada, No. 4, p. 281–328.

Nelson, J. and Kyba, J. (2014): Structural and stratigraphic control of porphyry and related mineralization in the Treaty Glacier–KSM–Brucejack–Stewart trend of western Stikinia; *in* Geological Fieldwork 2013, BC Ministry of Energy, Mines and Petroleum Resources, BC Geological Survey, Paper 2014-1, p. 111–140.

Reich, M., Kesler, S.E., Utsunomiya, S., Palenik, C.S., Chryssoulis, S.L. and Ewing, R.C. (2005): Solubility of gold in arsenian pyrite; Geochimica et Cosmochimica Acta, v. 69, p. 2781–2796.

Tombe, S.P. (2015): Tectonomagmatic setting of the Sulphurets Cu-Au porphyry-epithermal district, northwestern British

Columbia. M.Sc. thesis; University of Alberta, Edmonton, AB, 178 p.

Tombe, S.P., Greig, C.J., Board, W.S., Richards, J.P., Friedman, R.M. and Creaser, R.A. (2014): The Brucejack porphyry-related epithermal Au deposit, northwestern British Columbia; PDAC-CMIC-SEG Canada Student Minerals Colloquium, conference abstracts; URL <http://cmic-footprints.ca/smc/files/2014/Tombe_2014SMC_British%20Columbia_Porphyry_Gold%20Silver%20Brucejack.pdf> [November 2016].

Williams-Jones, A.E., Bowell, R.J. and Migdisov, A.A. (2009): Gold in solution; Elements, v. 5, p. 281–287. doi:10.2113/gselements.5.5.281

Geology of the Greenwood Map Area (NTS 082E/02), Boundary District, Southern British Columbia

T. Höy, consultant, Sooke, BC, thoy@shaw.ca

Höy, T. (2018): Geology of the Greenwood map area (NTS 082E/02), Boundary district, southern British Columbia; *in* Geoscience BC Summary of Activities 2017: Minerals and Mining, Geoscience BC, Report 2018-1, p. 41–46.

Introduction

Geological mapping and compilation of the Greenwood map area in the Boundary district of southern British Columbia (BC) is a continuation of work completed in the eastern half of the Penticton map area (NTS 082E). Five 1:50 000 NTS maps have been published, as shown in Figure 1, and the Greenwood map (NTS 082E/02) will be released in 2018. The project is focused mainly on the potential and controls of Paleogene and older base- and precious-metal mineralization. Compilation of the eastern part of the Penticton map area, including correlation of all units and a standardized nomenclature, will also be completed in 2018. The project includes radiometric dating of intrusive and volcanic rocks throughout the area, done in conjunction with The University of British Columbia, that will better constrain magmatic and coeval mineral and tectonic events.

Geological Setting

The location and geological setting of the Greenwood map area is shown in Figure 1. The exhumed Grand Forks complex occurs immediately to the east, bounded by the extensional Kettle River and Granby faults. The northern extension of the Toroda graben occurs in the western part of the area (Tempelman-Kluit, 1989). The grabens, bounded by high-angle normal faults that record a complex history of extension throughout the Paleogene, are filled by a thick succession of dominantly alkalic volcanic rocks of the Penticton Group, in part as remnants of more extensive volcanism and in part controlled by marginal growth faults. Large exposures of dominantly syenite of the middle Eocene Coryell intrusions occur to the north and extend into the northeastern part of the Greenwood map area.

The distribution of base- and precious-metal mineralization in the Penticton map area, and farther east to the Slocan camp, is controlled in part by the north-trending extensional faults that bound the core complexes. These faults expose higher structural levels in their hangingwall, an environment more conducive to mineralization as seen in the Franklin mining camp, but also locally may cause deposition of Eocene-age mineralization as in the Slocan camp (Höy, 2013).

Local Geology

A simplified geological map of the Greenwood area is shown in Figure 2, in large part modified from regional mapping by Little (1983), Fyles (1990) and Massey (2007a), as well as more detailed mapping in the Greenwood mining camp by Church (1986). Mapping this past field season concentrated north and east of the work by Fyles (1990) and Massey (2007a), mainly in an attempt to tie together lithological units and structures across map boundaries and to bridge geological mapping to the north in the Almond Mountain map area (NTS 082E/07; Höy and Jackaman, 2016) with that of Little (1983). As well, an attempt is being made to more closely constrain the age of intrusive and volcanic rocks by radiometric dating, which is being done at The University of British Columbia.

The oldest layered rocks within the area, the Knob Hill Group, have been described in considerable detail by Fyles (1990). Massey (2006) informally changed the name to the Knob Hill complex, a term that is retained in this paper as it reflects the inclusion of intrusive units with layered volcanic and sedimentary rocks. The complex is poorly dated: a single macrofossil of Carboniferous or Permian age was reported by Little (1983) but Late Devonian conodonts were obtained from the same limestone bed by Orchard (1993). Exposures of gabbro, referred to as the 'Old Diorite' by Church (1986) intrude the complex south and east of Greenwood (Figure 2) and serpentinites in the complex form tectonically emplaced lenticular bodies along thrust faults (Fyles, 1990; Massey, 2007b). Several areas of paragneiss (Pkgn) are included with the Knob Hill complex, a correlation that was supported by Church (1986), Fyles (1990) and Massey (2007a).

The Attwood Group comprises mainly deformed metasedimentary rocks that have yielded macrofossils and conodonts of Mississippian to Permian age (Little, 1983; Church, 1986; Orchard, 1993). Their relationship to the Knob Hill complex is not known because there are no recognized stratigraphic contacts between the units. Massey (2007b) suggested that the Paleozoic rocks south of Rock

This publication is also available, free of charge, as colour digital files in Adobe Acrobat® PDF format from the Geoscience BC website: http://www.geosciencebc.com/s/SummaryofActivities.asp.

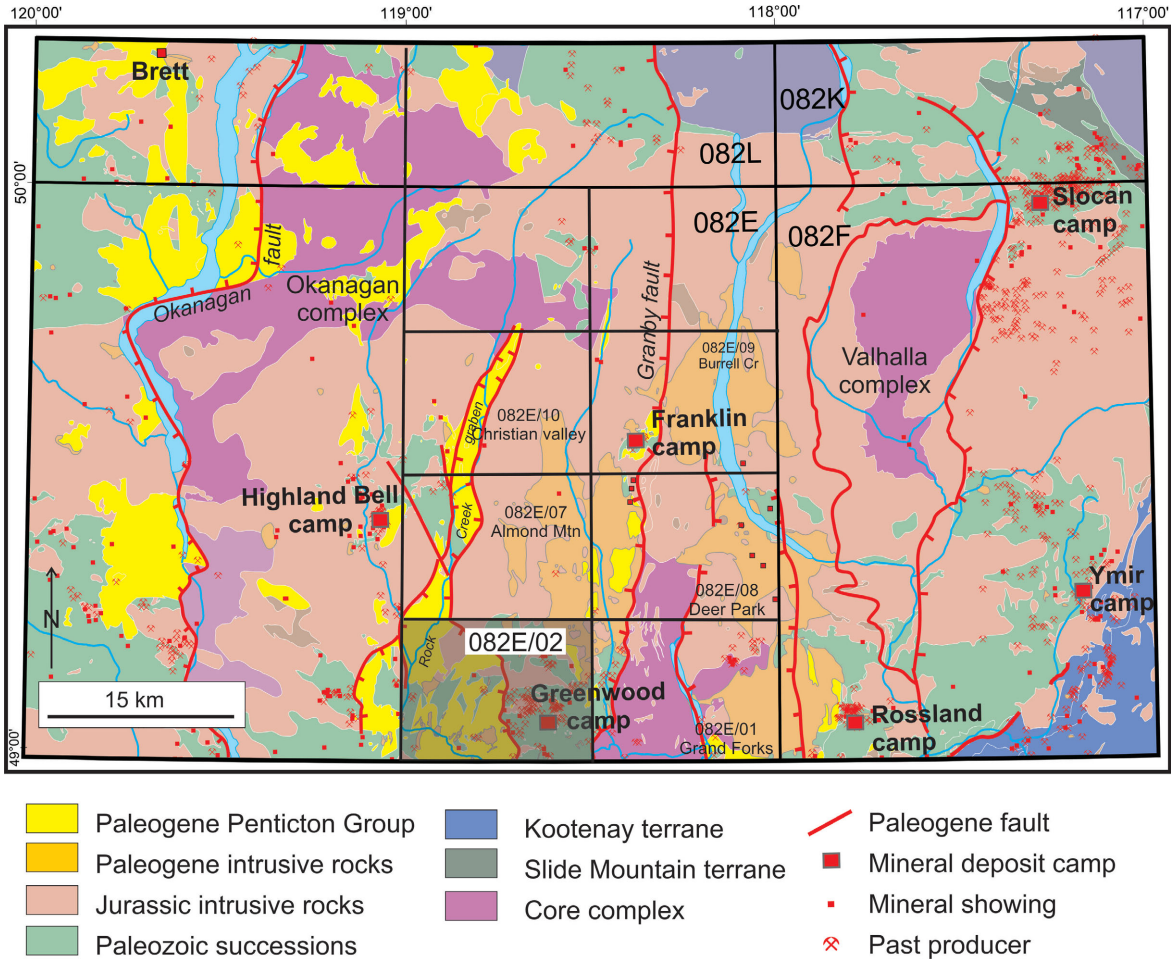

Figure 1. Location of the Greenwood map area (NTS 082E/02), southern British Columbia, showing major tectonic elements and locations of recently published 1:50 000 maps (Höy and Jackaman, 2005, 2010, 2013, 2016, 2017): Grand Forks (082E/01), Almond Mountain (082E/07), Deer Park (082E/08), Burrell Creek (082E/09) and Christian Valley (082E/10).

Creek should be referred to as the Anarchist schist, after the original mapping by Daly (1912) and Cairnes (1940). As noted by Massey (op. cit.), they are lithologically similar to the Knob Hill complex, but more argillaceous and complexly deformed. Massey also suggested that similarly deformed rocks farther east in the Greenwood area, referred to as the Knob Hill Group by Fyles (1990), should be included as Anarchist schist. Until more definitive work is done on these Paleozoic rocks, the term Knob Hill complex for these more eastern exposures is preferred (Figure 2).

The Middle to Late Triassic Brooklyn Formation unconformably overlies the Attwood Formation and Knob Hill complex in the central and eastern part of the area. Three main rock types are recognized (Fyles, 1990): chert breccia or 'sharpstone conglomerate'; limestone; and volcanic greenstone, pyroclastic breccia and subvolcanic microbreccia.

The Penticton Group (Church, 1973) is exposed in downdropped blocks throughout the western part of the area, in the southern extension of the Rock Creek graben and northern extension of the Toroda graben in Washington State. A basal unit comprising mainly sandstone and conglomerate, the Kettle River Formation, is overlain by mainly alkalic volcanic rocks of the middle Eocene Marron Formation.

Relatively fresh, massive granodiorite intrusion dominates the northern part of the Greenwood map area and occurs as scattered stocks throughout the remainder of the area. They are included in the Middle Jurassic–Cretaceous Nelson plutonic complex (Little, 1983; Fyles, 1990) due to their lithological similarity with Jurassic plutons to the east, and to a 179.9 ±3.8 Ma U-Pb zircon date on the Greenwood pluton (Massey et al., 2010). Farther north, leucocratic, medium- to coarse-grained granite, the Valhalla intrusion (Little, 1983) or Okanagan batholith (Tempelman-Kluit, 1989) intrudes the granodiorite. It has not been dated within the map area (Figure 2), but several granitic exposures to the north in the Almond Mountain and Christian Valley map areas (NTS 082E/07, 10; Höy, 2016; Höy and DeFields, 2017) have recently been dated by both Ar/Ar and U-Pb zircon geochronology (J. Gabites and R. Friedman, Geochronology Laboratory, The University of British Colum-

bia) as Paleocene. Syenite, part of the middle Eocene Coryell batholith, is exposed in the northeastern part of the Greenwood map area and in small isolated stocks and dikes throughout the area (Figure 2).

Structures in the Greenwood area are dominated by a series of pre-Paleogene, north-dipping thrusts that are commonly marked by lenses of serpentinite (Fyles, 1990; Massey, 2007b). These are overprinted by low- to high-angle normal or extensional faults. In the western part of the area, these late faults bound the structural basins that contain the thick accumulations of Penticton Group sediments and volcanics.

Mineral deposits in the area are described in detail by Peatfield (1978) and Church (1986) and numerous industry

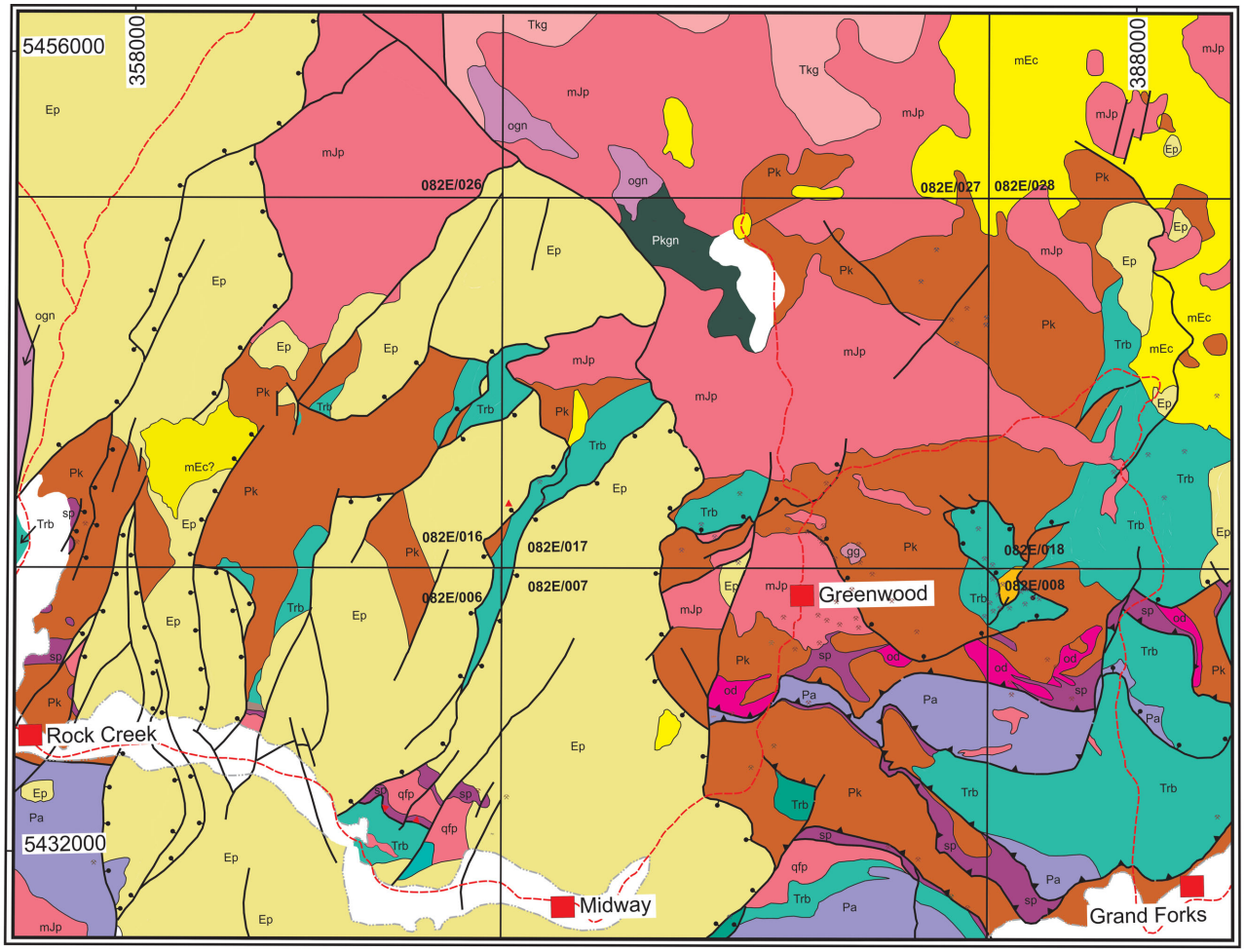

Cenozoic
Quaternary
Alluvium, sand, gravel
Eocene
mEc Coryell alkalic intrusions
Ep Penticton Group
Paleogene, (Cretaceous)?
TKg granite, granodiorite
Mesozoic
Jurassic (?)
mJp granodiorite, granite
Triassic
qfp quartz-feldspar porphyry
Trb Brooklyn Formation
Paleozoic
Late Devonian–Permian (?)
Pk Knob Hill complex
gg Greenwood pluton
sp serpentine, ultramafics
Age unknown (Paleozoic)
Pkgn Knob Hill? paragneiss
Pa Attwood group
Ogn orthogneiss, (paragneiss)

Symbols
highway
town
geological contact
fault
thrust
normal fault
extensive overburden
past producing mine
age date
U-Pb zircon
K-Ar, Ar/Ar
4 km

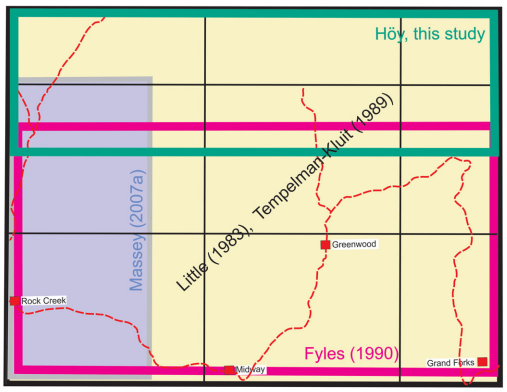

Figure 2. Simplified geology of the 1:50 000 scale Greenwood map area (NTS 082E/02), showing locations of past producers. Inset shows the data sources and approximate area of 2017 field mapping (this study).

assessment reports describe recent exploration (e.g., Caron, 2007; Dufresne, 2012). This information is summarized in the BC MINFILE database (BC Geological Survey, 2017), which lists 169 occurrences or deposits throughout the Greenwood map area, including 79 past producers, which are shown in Figure 2.

Summary

A 1:50 000 scale geological map of the Greenwood map area, including 2017 mapping and a compilation of previous work will be released in 2018. As well, a regional compilation map of the east half of the Penticton map area, including the recently published 1:50 000 Geoscience BC maps to the north and east (Figure 1), will be updated and released in 2018. Isotopic dating of intrusive and volcanic units, currently in progress in the Geochronology Laboratory at The University of British Columbia, will help constrain ages of magmatic events, structures and related mineralization and help define models for known mineralization throughout the Greenwood map area.

Acknowledgments

Geoscience BC is gratefully acknowledged for financial support of this study. G.M. DeFields is thanked for assistance in the field and W. Jackaman for preparing base maps. The manuscript was reviewed by G.E. Ray, W. Jackaman and Geoscience BC. RnD Technical edited the manuscript.

References

BC Geological Survey (2017): MINFILE BC mineral deposits database; BC Ministry of Energy, Mines and Petroleum Resources, URL <http://minfile.ca> [November 2017].

Caron, L.J. (2007): 2007 work program, geology, soil and rock geochemistry, grid work, geophysics and trenching on the Phoenix and Bluebell properties; BC Ministry of Energy, Mines and Petroleum Resources, Assessment Report 29 626, 205 p., URL <http://aris.empr.gov.bc.ca/search.asp?mode=repsum&rep_no=29626> [November 2017].

Church, B.N. (1973): Geology of the White Lake basin; BC Ministry of Energy, Mines and Petroleum Resources, BC Geological Survey, Bulletin 61, 120 p., URL <http://www.empr.gov.bc.ca/Mining/Geoscience/Publications Catalogue/BulletinInformation/BulletinsAfter1940/Pages/Bulletin61.aspx> [November 2017].

Church, B.N. (1986): Geological setting and mineralization in the Mount Attwood-Phoenix area of the Greenwood camp; BC Ministry of Energy, Mines and Petroleum Resources, BC Geological Survey, Paper 1986-2, 70 p., URL <http://www.empr.gov.bc.ca/Mining/Geoscience/PublicationsCatalogue/Papers/Pages/1986-2.aspx> [November 2017].

Cairnes, C.E. (1940): Kettle River, west half, Similkameen and Osoyoos districts, British Columbia; Geological Survey of Canada, Map 538A, scale 1:253 440, doi:10.4095/106916

Daly, R.A. (1912): Geology of the North American Cordillera at the forty-ninth parallel; Geological Survey of Canada, Memoir 38, 17 maps at 1:63 360 scale, doi:10.4095/100513

Dufresne, M.B. (2012): Assessment report for Grizzly Discoveries Inc. Greenwood property; BC Ministry of Energy, Mines and Petroleum Resources, Assessment Report 32 649, 5560 p., URL <http://aris.empr.gov.bc.ca/search.asp?mode=repsum&rep_no=32649> [November 2017].

Fyles, J.T. (1990): Geology of the Greenwood-Grand Forks area, British Columbia; BC Ministry of Energy, Mines and Petroleum Resources, BC Geological Survey, Open File 1990-25, 25 p., URL <http://www.empr.gov.bc.ca/Mining/GeoscienceCatalogue/OpenFiles/1990/Pages/1990-25.aspx> [November 2017].

Höy, T. (2013): Burrell Creek map area: setting of the Franklin mining camp, southeastern British Columbia; *in* Geoscience BC Summary of Activities 2012, Geoscience BC, Report 2013-1, p. 91–101, URL <http://www.geosciencebc.com/i/pdf/SummaryofActivities2012/SoA2012_Hoy.pdf> [October 2017].

Höy, T. (2016): Geology of the Kettle River area, Almond Mountain project, southern British Columbia; *in* Geoscience BC Summary of Activities 2015, Geoscience BC, Report 2016-1, p. 23–34, URL <http://www.geosciencebc.com/i/pdf/SummaryofActivities2015/SoA2015_Hoy.pdf> [October 2017].

Höy, T. and DeFields, G.M. (2017): Geology of the northern extension of the Rock Creek graben, Christian Valley map area, south-central British Columbia (NTS082E/10); *in* Geoscience BC Summary of Activities 2016, Geoscience BC, Report 2017-1, p. 245–256, URL <http://www.geosciencebc.com/i/pdf/SummaryofActivities2016/SoA2016_Hoy.pdf> [October 2017].

Hoy, T. and Jackaman, W. (2005): Geology of the Grand Forks map sheet, British Columbia (NTS 082E/01); BC Ministry of Energy, Mines and Petroleum Resources, Geoscience Map 2005-2, scale 1:50 000, URL <http://www.empr.gov.bc.ca/Mining/Geoscience/PublicationsCatalogue/Maps/GeoscienceMaps/Documents/GM2005-02_GrandForks.pdf> [November 2017].

Höy, T. and Jackaman, W. (2010): Geology of the Deer Park map sheet (NTS 82E/08); Geoscience BC, Map 2010-7-1, scale 1:50 000, URL <http://www.geosciencebc.com/i/project_data/GBC_Report2013-07/GBC_Map2013-07-1_Burrell.pdf> [November 2017].

Höy, T. and Jackaman, W. (2013): Geology of the Burrell Creek map sheet (NTS 82E/09); Geoscience BC, Map 2013-07-1, scale 1:50 000.

Höy, T. and Jackaman, W. (2016): Geology of the Almond Mountain map sheet (NTS 082E/07); Geoscience BC, Map 2016-08, 1 sheet, 1:50 000 scale, URL <http://www.geosciencebc.com/s/Report2016-08.asp> [October 2017].

Höy, T. and Jackaman, W. (2017): Geology of the Christian Valley map sheet (NTS 82E/10); Geoscience BC, Map 2017-10, scale 1:50 000, URL <http://www.geosciencebc.com/i/project_data/GBCReport2017-10/GBC_Map2017-10_CV.pdf> [November 2017].

Little, H.W. (1983): Geology of the Greenwood map-area, British Columbia; Geological Survey of Canada, Paper 79-25, 37 p., doi:10.4095/119503

Massey, N. (2006): Boundary project: reassessment of Paleozoic rock units of the Greenwood area (NTS 082E/02), southern BC; *in* Geological Fieldwork 2005, BC Ministry of Energy, Mines and Petroleum Resources, BC Geological Survey, Paper 2006-1, p. 99–107, URL <http://www.empr.gov.bc.ca/Mining/Geoscience/PublicationsCatalogue/Fieldwork/Documents/2005/Paper10.pdf> [November 2017].

Massey, N. (2007a): Geology and mineral deposits of the Rock Creek area, British Columbia; BC Ministry of Energy, Mines and Petroleum Resources, BC Geological Survey, Open File 2007-7, 1 map at 1:25 000, URL <http://www.empr.gov.bc.ca/Mining/Geoscience/PublicationsCatalogue/OpenFiles/2007/Pages/2007-7.aspx> [November 2017].

Massey, N. (2007b): Boundary project: Rock Creek area (NTS 082E/02W, 03E), southern British Columbia; *in* Geological Fieldwork 2006, BC Ministry of Energy, Mines and Petroleum Resources, BC Geological Survey, Paper 2007-1, p. 117–128, URL <http://www.empr.gov.bc.ca/Mining/Geoscience/PublicationsCatalogue/Fieldwork/Documents/2006/12-Massey.pdf> [November 2017].

Massey, N., Gabites, J.E., Mortensen, J.K. and Ullrich, T.D. (2010): Boundary project: geochronology and geochemistry of Jurassic and Eocene intrusions, southern British Columbia (NTS 082E); *in* Geological Fieldwork 2009, BC Ministry of Energy, Mines and Petroleum Resources, BC Geological Survey, Paper 2009-1, p. 127–142, URL <http://www.empr.gov.bc.ca/Mining/Geoscience/PublicationsCatalogue/Fieldwork/Documents/2009/11_Massey_2009.pdf> [November 2017].

Orchard, M.J. (1993): Report on conodonts and other microfossils, Penticton (082E); Geological Survey of Canada, Open File 1993-19.

Peatfield, G.R. (1978): Geological history and metallogeny of the "Boundary District", southern British Columbia and northern Washington; Ph.D. thesis, Queen's University, 80 p.

Tempelman-Kluit, D.J. (1989): Geology, Penticton, west of sixth meridian, British Columbia; Geological Survey of Canada, Map 1736A, scale 1:250 000, doi:10.4095/127379

Preliminary Investigations of the Metamorphic and Thermochronological Interface between the Purcell Anticlinorium and the Kootenay Arc, Southeastern British Columbia (NTS 082F, G)

N.A. Rioseco, Department of Geoscience, University of Calgary, Calgary, AB, nicole.rioseco@ucalgary.ca

D.R.M. Pattison, Department of Geoscience, University of Calgary, Calgary, AB

Rioseco, N.A. and Pattison, D.R.M. (2018): Preliminary investigations of the metamorphic and thermochronological interface between the Purcell Anticlinorium and the Kootenay Arc, southeastern British Columbia (NTS 082F, G); *in* Geoscience BC Summary of Activities 2017: Minerals and Mining, Geoscience BC, Report 2018-1, p. 47–56.

Introduction

The mineralogically rich East Kootenay region encompasses the interface between two major Cordilleran tectonic domains, the Purcell Anticlinorium and the Kootenay Arc. This project is a regional study that seeks to 1) elucidate the nature of differences in metamorphism, structure and cooling history between these two domains; and 2) draw potential links between the tectonic significance of these differences and the mineralization that occurs within the region.

Regional Geology

The study area (Figure 1) includes the region between Creston, Crawford Bay and Kimberley in southeastern British Columbia (BC). The rocks under investigation occur east of the Eocene Purcell Trench fault, an east-side-down extensional normal fault. The eastern portion of this domain is occupied by the Purcell Anticlinorium, a regional-scale, northwest-trending and northwest-plunging anticlinal structure that is cored by Mesoproterozoic rocks of the Belt-Purcell Supergroup. This tectonic domain transitions westward into deformed and metamorphosed Neoproterozoic through Paleozoic pericratonic rocks and accreted island-arc rocks of the Kootenay Arc. Mesozoic deformation and metamorphism within the Kootenay Arc are attributed to Cordilleran orogenic processes spanning the Early Jurassic through the Eocene. The Purcell Anticlinorium is also a Cordilleran structure but preserves, within its core, some of the oldest rock exposures in the Cordillera, as well as evidence for Precambrian deformation and metamorphic events.

The Belt-Purcell Supergroup comprises rift-related clastic rocks and synsedimentary Moyie Sills that are interpreted to have been deposited in an intracratonic rift basin between 1500 and 1350 Ma (Price, 1964; Harrison, 1972; Höy, 1989). The lowermost unit, the Aldridge Formation, comprises predominantly turbiditic deposits and is host to a suite of 1468 Ma dioritic to gabbroic sills, known as the Moyie Sills (Höy, 1989). Belt Purcell strata are unconformably overlain by the Neoproterozoic Windermere Supergroup, exposed on the flanks of the Purcell Anticlinorium. On the west flank of the Purcell Anticlinorium, the Windermere Supergroup occurs in the interface with the Kootenay Arc (Warren, 1997). Farther to the west, within the Kootenay Arc, the Windermere Supergroup is overlain by pericratonic and coarse clastic and carbonate Paleozoic rocks (Bond et al., 1985; Warren, 1997; Colpron et al., 2002).

In addition to this stratigraphic change, the transition between the Purcell Anticlinorium and the Kootenay Arc is marked by a prominent change in structural style, metamorphism, and magmatism. The Purcell Anticlinorium was affected by three cryptic, Proterozoic orogenic events, the ca. 1350–1300 Ma East Kootenay orogeny, a ca. 1050 Ma Grenville-age event and the ca. 900–800 Ma Goat River orogeny (Leech, 1962; McMechan and Price, 1982; McFarlane and Pattison, 2000; McFarlane, 2015). Despite its ancient history, the regional-scale anticlinal structure of the Purcell Anticlinorium is attributed to Mesozoic Cordilleran orogenesis (Price, 1964). The Purcell Anticlinorium is of relatively low metamorphic grade, comprising the chlorite and biotite subzones of the greenschist facies (Leech, 1962; Read et al., 1991). There are rare occurrences of garnet-bearing rocks in the core of its southern part, within rocks of the Aldridge Formation on Mount Olson and Mount Mahon, near the town of Yahk, BC (Read et al., 1991). The garnet-bearing rocks have one of two explanations: they are either domains of locally elevated metamorphic grade, as in the Matthew Creek metamorphic zone (McFarlane and Pattison, 2000); or domains of unusual bulk composition favourable for garnet development, as in the area near the St. Eugene mine (Pattison and Seitz, 2012). The Kootenay Arc is an arcuate belt of rocks that have been ductilely deformed, metamorphosed and intruded in several pulses between 180 and 50 Ma (Archibald et al., 1983, 1984; Klepacki, 1985; Leclair et al., 1993; Moynihan and Pattison, 2013; Webster and Pattison, 2017).

This publication is also available, free of charge, as colour digital files in Adobe Acrobat® PDF format from the Geoscience BC website: http://www.geosciencebc.com/s/SummaryofActivities.asp.

Regional metamorphic grade in the Kootenay Arc ranges from greenschist to amphibolite facies. The higher grade domains are broadly attributed to Barrovian (kyanite-sillimanite–type) metamorphism that locally reaches sillimanite+potassium-feldspar grade (Leclair, 1982; Moynihan and Pattison, 2013; Webster and Pattison, 2017).

The prominent change in deformation styles and metamorphism between the Purcell Anticlinorium and the Kootenay Arc is complemented by a westward decrease in K-Ar and Ar/Ar cooling ages in hornblende and micas (Figure 2). Hunt (1962) and McMechan and Price (1982) reported many K-Ar ages in the range 1084–600 Ma that are indicative of Mesoproterozoic and Neoproterozoic exhumation of the core and eastern flank of the Purcell Anticlinorium. In contrast, metamorphic rocks in the Kootenay Arc, whose protoliths include rocks of the Belt-Purcell and Windermere supergroups, yield K-Ar and Ar/Ar ages in the range of 90–45 Ma, indicating much younger, Mesozoic and Cenozoic, exhumation (Figure 2; Archibald et al., 1983, 1984; Webster and Pattison, 2017).

Project Goals

The objective of this project is to elucidate the nature and tectonic significance of the transition in structural style, metamorphism and cooling history between the Purcell Anticlinorium and the Kootenay Arc. A comparison of

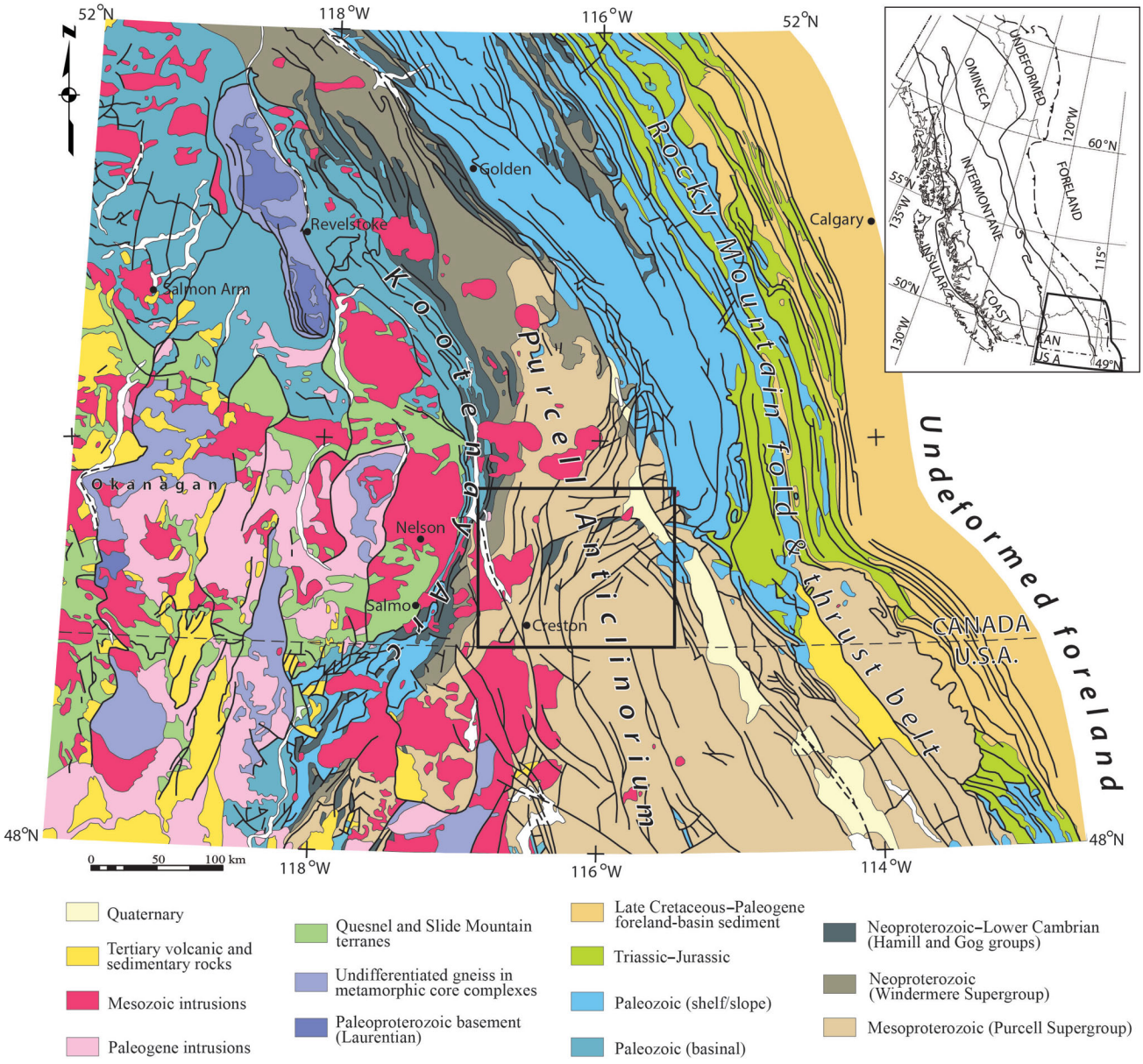

Figure 1. Regional geology of the southeastern Canadian Cordillera in southeastern British Columbia. Study area indicated by black outline. Map modified from Webster and Pattison (2017), originally after Wheeler and McFeely (1991).

structural styles across the Purcell Anticlinorium and into the transition zone with the Kootenay Arc will be complemented by a comprehensive study of metamorphism within the Purcell Anticlinorium and how it relates to that of the Kootenay Arc. Both of these studies will be augmented by thermochronological studies focused on Ar/Ar cooling ages in biotite, muscovite and hornblende. This three-step approach will enhance the understanding of the deformational, metamorphic and cooling/exhumation history the Purcell Anticlinorium and Kootenay Arc.

Fieldwork and Preliminary Observations

A ten-week field season was undertaken during the summer of 2017. The primary goal was to obtain a suite of biotite- and hornblende-bearing rocks that will provide the basis for metamorphic and thermochronological studies across the Purcell Anticlinorium (Figure 3a). Throughout the Purcell Anticlinorium, biotite occurs within pelitic beds of the Aldridge Formation and the interlayered Moyie Sills, and, along its western flank, within metasedimentary rocks

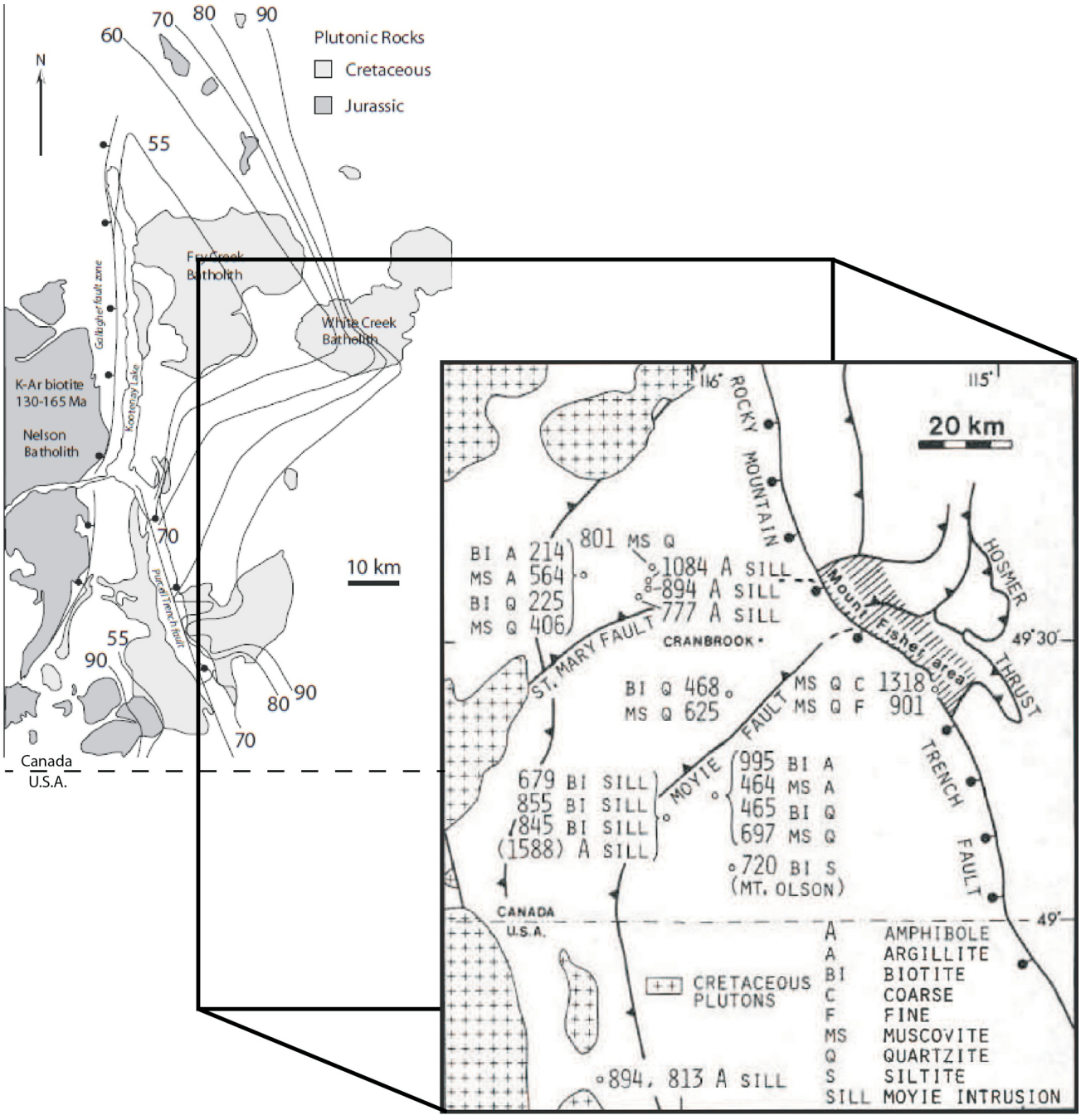

Figure 2. (Left) Potassium-argon cooling ages in biotite (from Archibald et al., 1984); contour interval 10 m. **(Right)** Potassium-argon cooling ages (from McMechan and Price, 1982). Location of figures shown by black outline on Figure 1.

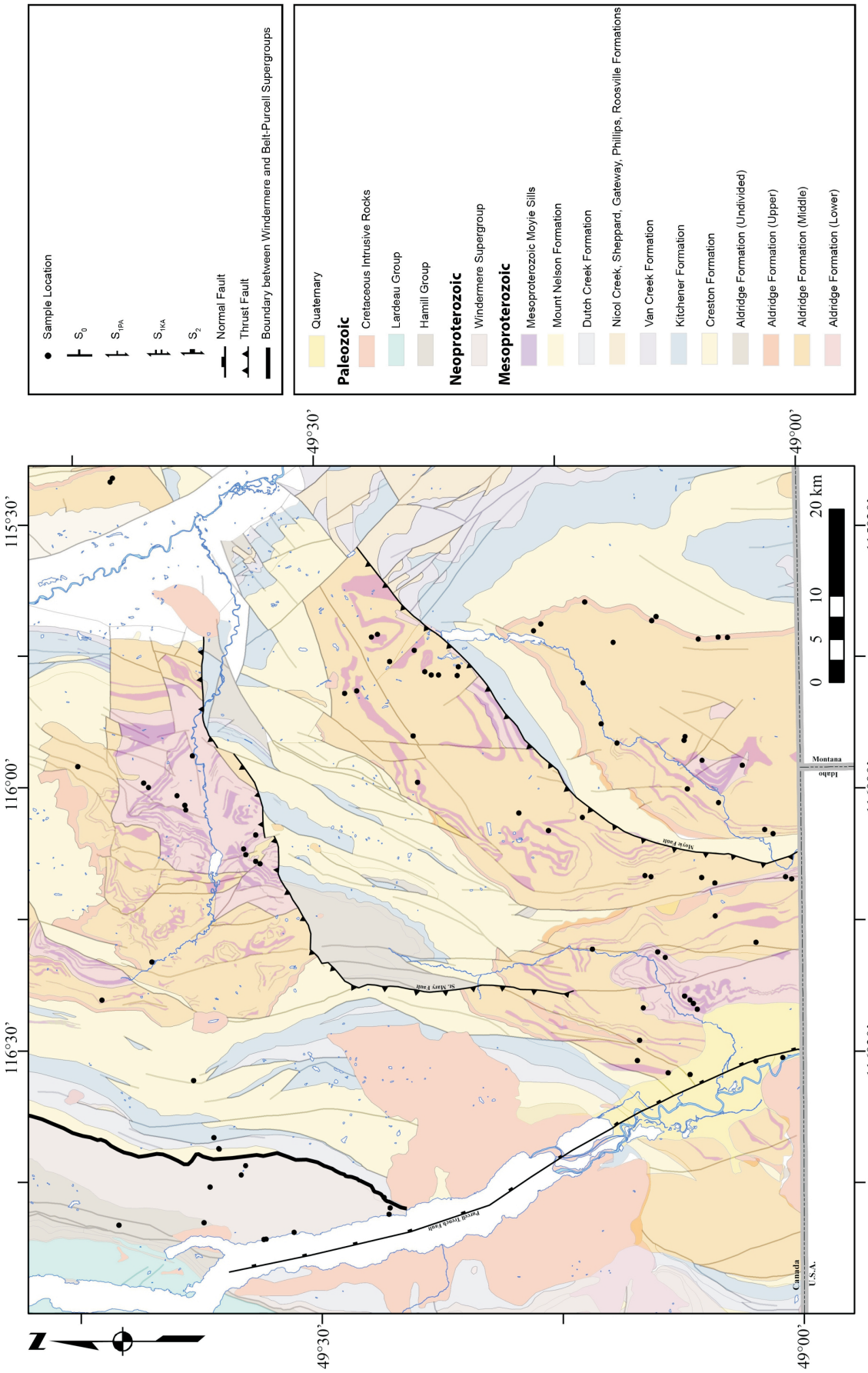

Figure 3. Sample locations in the study area (geology after Höy et al., 1995).

of the Windermere Supergroup. These rocks were targeted during sampling, as biotite-bearing rocks are essential for future metamorphic and thermochronological analysis. Measurements of bedding, foliation(s), lineation(s) and folding were collected to identify changes in structural style between the Purcell Anticlinorium and the Kootenay Arc, complementing the results of metamorphic and thermochronological studies.

Rocks of the lower, middle and upper Aldridge Formation occur as thick, planar-bedded, turbiditic deposits that range from sandy to silty in composition. These strata consist predominantly of massive sandy units, ranging from 0.5–1 m in thickness, with thinner (5–10 cm) silty interbeds (Figure 4a). The Moyie Sills occur mainly in lower and middle Aldridge rocks and are typically massive, with common preservation of ophitic igneous texture (Figure 4b). These units are typically on the order of 6–10 m thick.

Map patterns and structural observations of bedding from within the central part of the field area indicate broad large-scale folding, likely associated with the anticlinal structure formed during Cordilleran orogenesis (Figure 5). The development of an S_1 penetrative slaty cleavage is present throughout the pelitic portions of the Aldridge Formation. This cleavage is referred to as S_{1PA}. In the field, it was observed that the dip of S_{1PA} consistently falls within a range of 15–30º from that of S_0 (bedding; Figures 4c, 6).

Within the Kootenay Arc, the dominant rock fabrics developed (S_1 and S_2) are attributed to two deformation events, D_1 and D_2, respectively. Within the central part of the arc, an S_1 schistosity is axial planar to F_1 folds developed during D_1, a Middle Jurassic metamorphic event responsible for low-grade, regional metamorphism (Moynihan and Pattison, 2013). Moynihan and Pattison (2013) described a second phase of deformation within the Kootenay Arc that is attributed to Early Cretaceous D_2 deformation and is responsible for the development of F_2 folds. An S_2 schistosity that is axial planar to F_2 folds steepens eastward from within the central Kootenay Arc toward the Purcell Anticlinorium (Moynihan and Pattison, 2013). These are Mesozoic fabrics related to the structural and metamorphic evolution of the Kootenay Arc that, in this discussion, will be referred to as S_{1KA} and S_{2KA}.

One of the aims of this project is to understand the nature of overprinting of Proterozoic Belt-Purcell structures by the Mesozoic structures documented above as the Purcell Anticlinorium transitions into the Kootenay Arc. An east to west transect through the northern part of the field area was made possible via the Gray Creek Road, which connects the towns of Crawford Bay and Kimberley, BC. This transect allows for an examination of the change in the structural style of rocks from the core of the Purcell Anticlinorium to the Kootenay Arc. Along this transect, there is a westward transition in structural style. The eastern portion of the transect exposes rocks with a Purcell Anticlinorium–type S_{1PA} fabric. Westward, however, it seems as though the dominant fabric is more Kootenay Arc–type S_{1KA} and S_{2KA}. S_{1KA} and S_{2KA} are the dominant fabrics in rocks exposed along the western part of the Grey Creek Road and are developed in rocks of the Windermere and Belt-Purcell supergroups. Within the rocks that were observed, S_{1KA} is difficult to define but generally dips fairly steeply (65–85º) and was affected by later folding responsible for the development of S_{2KA}. The S_{2KA} fabric depicted in Figures 4d–f is a spaced cleavage that is axial planar to the folding of S_{1KA}. Kootenay Arc–type fabrics in this region of the Purcell Anticlinorium are not stratigraphically restricted, implying overprinting of Kootenay Arc–type fabrics in Mesoproterozoic Belt-Purcell rocks of the Purcell Anticlinorium.

Evidence of metamorphic grade in rocks of the Aldridge Formation is restricted to the pelitic interbeds, which have a bulk composition that allows for the growth of index minerals. Biotite porphyroblasts, ranging from 0.1 to 0.3 mm in size, occur in a matrix of predominantly quartz and mica, indicating that peak metamorphic conditions in these rocks did not exceed those of the biotite zone. Garnet from rocks on Mount Olson occurs as 2–4 mm porphyroblasts accompanied by elongate hornblende porphyroblasts that are similar in size. Based on preliminary petrographic observation, the matrix of garnet- and hornblende-bearing rocks is similar to that of more 'typical' biotite-bearing rocks. The Moyie Sills show no detectable variation in metamorphic grade across the Purcell Anticlinorium. These rocks contain combinations of plagioclase, hornblende, actinolite, chlorite, biotite and epidote. This information, which is based on preliminary petrographic work, indicates metamorphic conditions that fall broadly within the lower-amphibolite facies in the Purcell Anticlinorium. West of the Purcell Trench fault, however, Moyie Sills contain amphibolite-facies assemblages (Webster and Pattison, 2017).

Future Work

The next phases of this project will include a more in-depth analysis of the structural and metamorphic characteristics of the Purcell Anticlinorium–Kootenay Arc transition, augmented by thermochronological analysis.

Stereonet analysis will complement the mapped structural variation, allowing for identification of the interplay between structures of the Purcell Anticlinorium and the Kootenay Arc. A follow-up field season during the summer of 2018 will focus more carefully on structural variation in the northwest corner of the field area, where Kootenay Arc–type structures were identified this year.

The metamorphic portion of the study requires a multifaceted approach, involving 1) petrographic work to identify

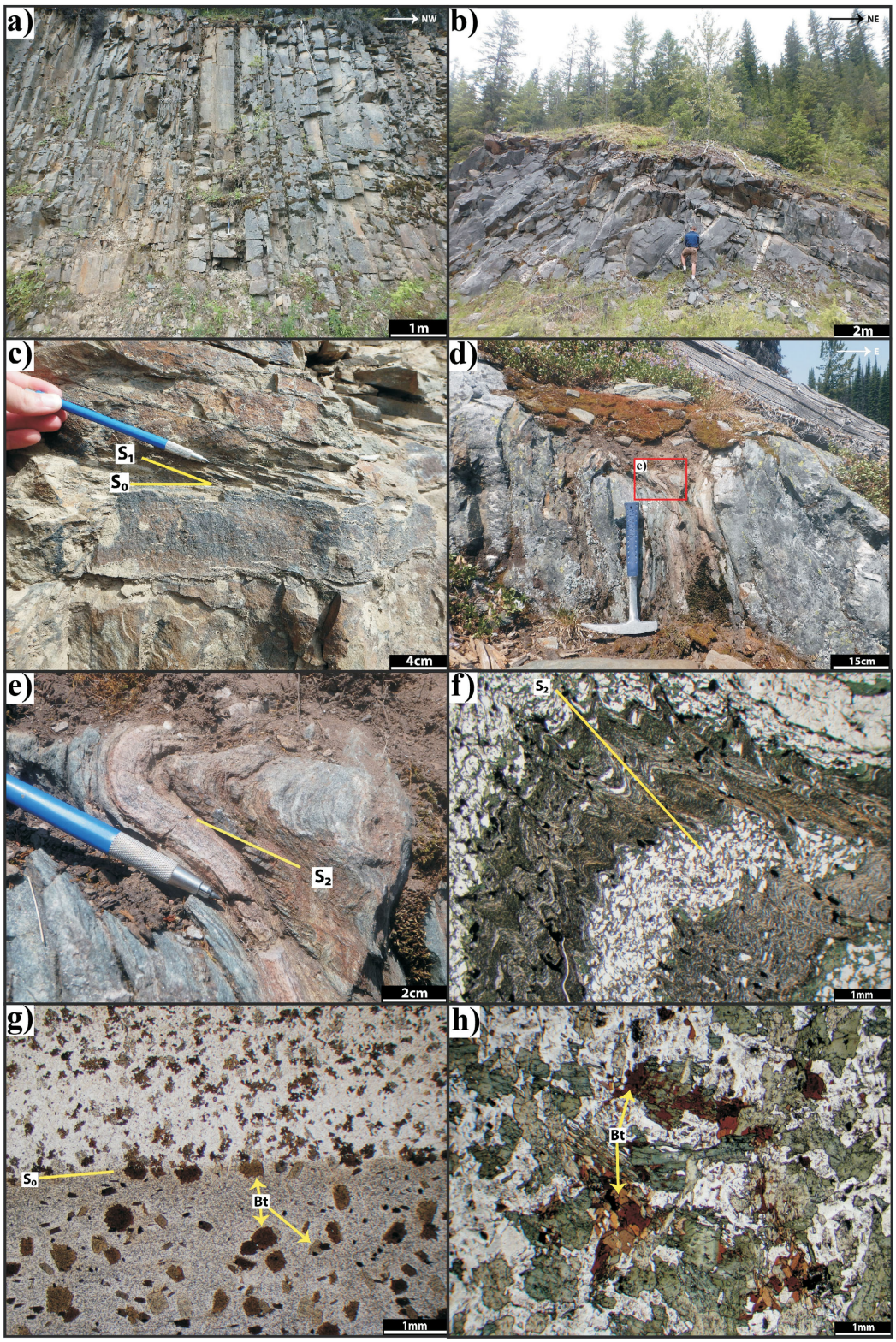

Figure 4. Photos and photomicrographs of representative units, structures and mineralogy in the study area: **a)** exposure of the Aldridge Formation from within the core of the Purcell Anticlinorium near Kitchener, BC; **b)** outcrop of a Moyie Sill as it appears within the core of the Purcell Anticlinorium near Creston, BC; **c)** S_1 cleavage developed within the pelitic interbeds of the Aldridge Formation near Yahk, BC; **d)** fold in rocks of the Windermere Supergroup along the western side of the Gray Creek transect; **e)** close-up of fold shown in part 4d, with an axial-planar S_2 cleavage; **f)** photomicrograph of small-scale fold and S_2 cleavage from the same locality as Figure 2d and e; **g)** photomicrograph of biotite-bearing rock of the Aldridge Formation from Mt. Olson, near Yahk, BC; **h)** photomicrograph of biotite in a Moyie Sill near St. Mary Lake.

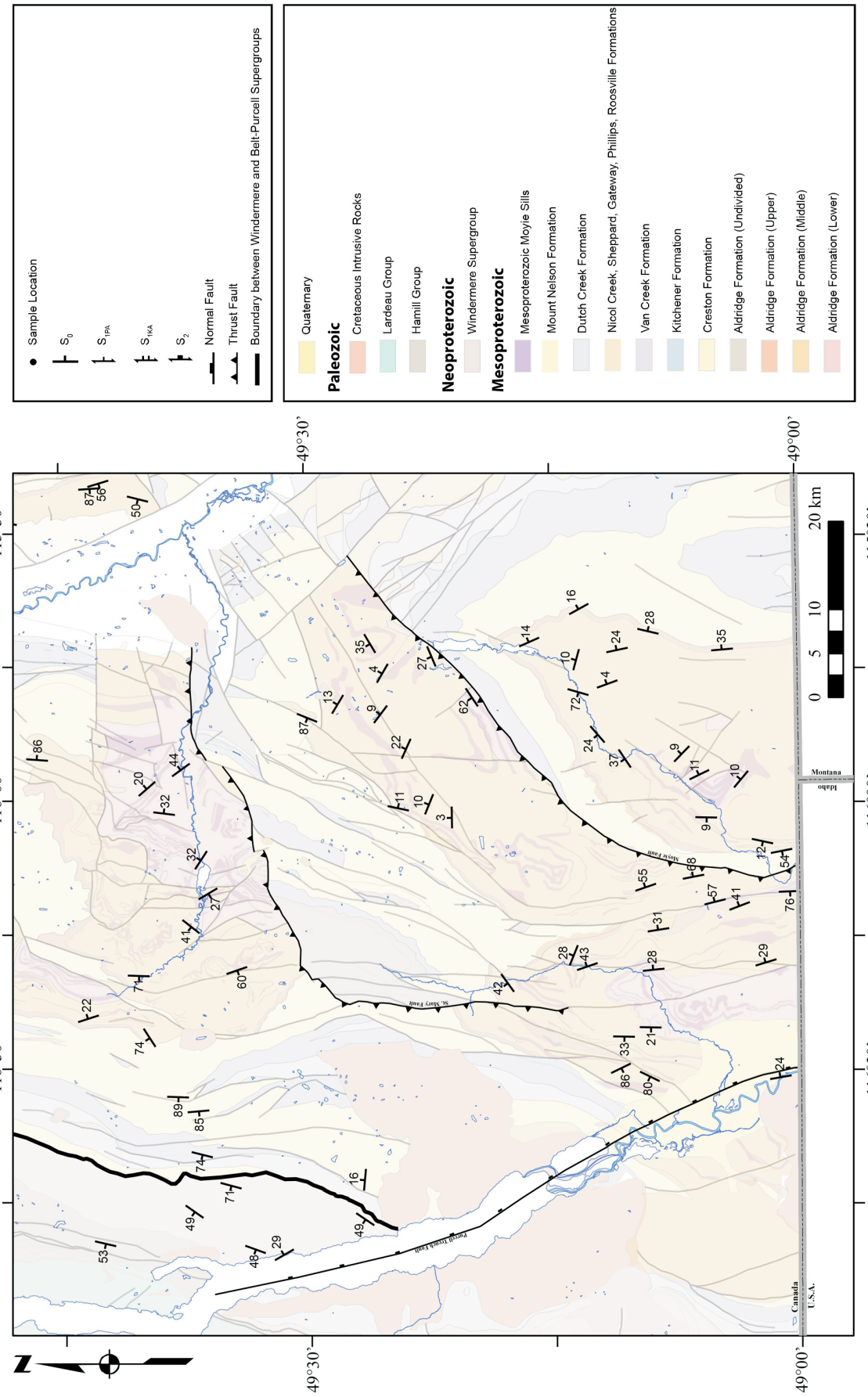

Figure 5. Bedding (S_0) orientations measured during the field season (geology after Höy et al., 1995).

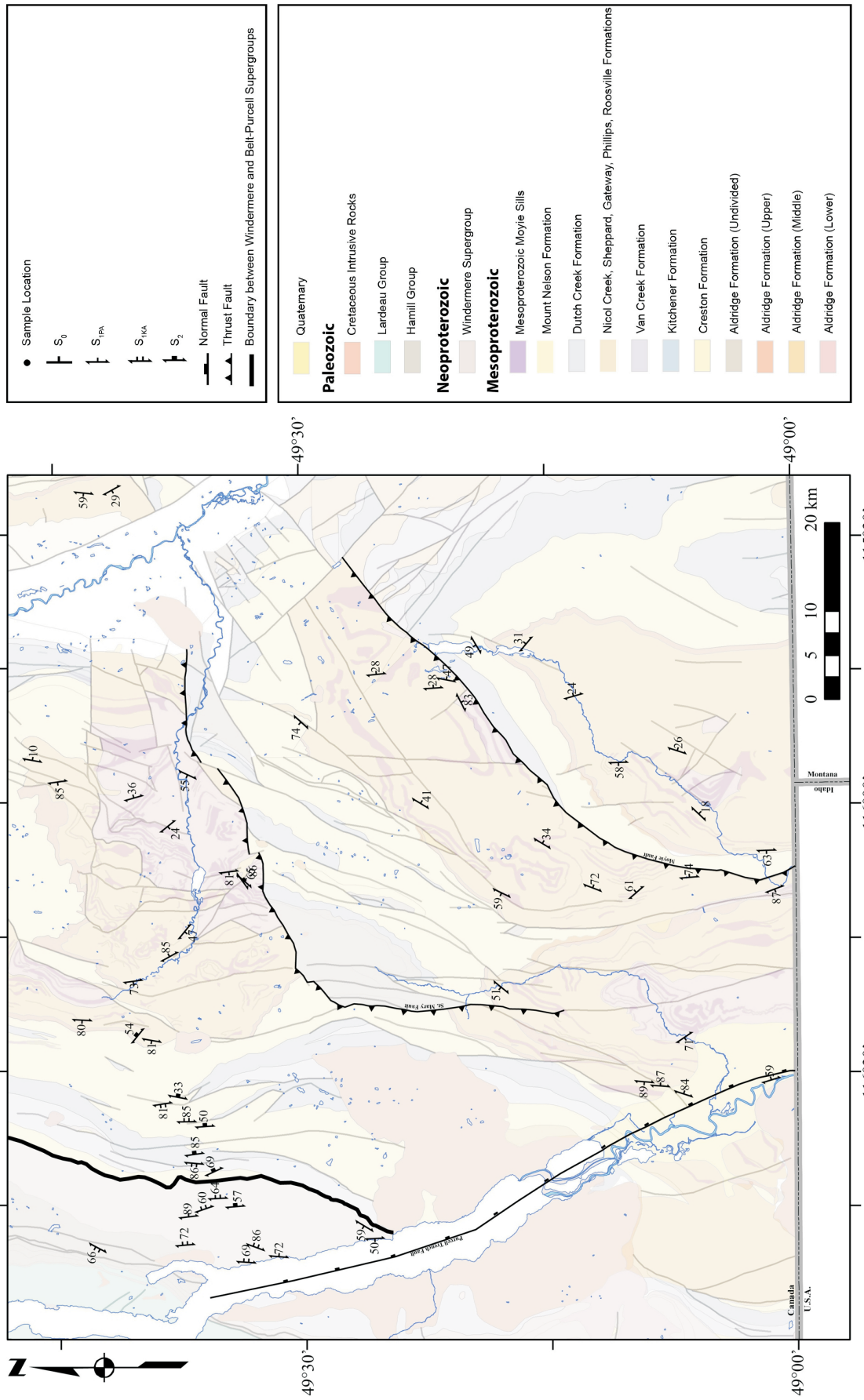

Figure 6. Fabrics S_{1PA} (one tick on symbol), S_{1KA} (two ticks on symbol) and S_{2KA} (thick tick on symbol) measured during the field season (geology after Höy et al., 1995).

mineral assemblages and microstructures that will bear on the variation in grade and timing of metamorphism, especially in the interface between the Purcell Anticlinorium and the Kootenay Arc; 2) microprobe work and X-ray mapping to constrain compositional variations in minerals; and 3) computer-based phase-equilibrium modelling for estimating metamorphic pressure and temperature conditions. Extensive studies of metamorphism within the Kootenay Arc by Moynihan and Pattison (2013) and Webster and Pattison (2017) will serve as the basis for comparison with results from this study. This comparison will aid in elucidating the nature of the metamorphic interface between the two tectonic domains.

Previous thermochronology work in both the Purcell Anticlinorium and the Kootenay Arc has assessed the cooling ages of muscovite, biotite and hornblende using both the K-Ar and Ar/Ar techniques. This study will also focus on the Ar/Ar ages of hornblende, muscovite and biotite east of the Purcell Trench fault, within the Purcell Anticlinorium. Thermochronological studies will focus primarily on biotite, which is present in both pelitic rocks of the Aldridge Formation and the gabbroic Moyie Sills. Figure 4g and 4h show examples of the appearance of biotite within the Aldridge Formation and Moyie Sills, respectively. Mineral separation for thermochronological work will take place during the fall of 2017 at the University of Calgary. Analytical work will take place in 2018 at the University of Manitoba under the guidance of A. Camacho. Biotite and muscovite cooling ages will be compiled on a map that can be compared with that for the Kootenay Arc in Figure 2. Variation in the metamorphic, structural and cooling history of these rocks will provide information on the nature of the tectonic interface between, and exhumation history of, the Purcell Anticlinorium and the Kootenay Arc.

The Purcell Anticlinorium and Kootenay Arc are both host to numerous mineral deposits that reflect the region's diverse geological history. An enhanced understanding of the structural, metamorphic and cooling history of the area will help to place further constraints on the genesis of these deposits. A deeper understanding of the nature of mineral diversity within the region will help to inform mineral exploration in the future.

Acknowledgments

The authors thank Geoscience BC for their support of this study. This work is funded by a Natural Sciences and Engineering Research Council of Canada (NSERC) Discovery Grant to D. Pattison. A special thanks goes to C. Padget, J. Forshaw and M. Lazzarotto for constructive reviews of this manuscript.

References

Archibald, D.A., Glover, J.K., Price, R.A., Farrar, E. and Carmichael, D.M. (1983): Geochronology and tectonic implications of magmatism and metamorphism, southern Kootenay Arc and neighbouring regions, southeastern British Columbia, part I: Jurassic to mid-Cretaceous; Canadian Journal of Earth Sciences, v. 20, p. 1891–1913.

Archibald, D.A., Krough, T.E., Armstrong, R.L. and Farrar, E. (1984): Geochronology and tectonic implications of magmatism and metamorphism, southern Kootenay Arc and neighbouring regions, southeastern British Columbia, part II: Mid-Cretaceous to Eocene; Canadian Journal of Earth Sciences, v. 21, p. 567–583.

Bond, G.C., Christie-Blick, N., Kominz, M.A. and Devlin, W.J. (1985): An early Cambrian rift to post-rift transition in the Cordillera of western North America; Nature, v. 315, p. 742–746.

Colpron, M., Logan, J.L. and Mortensen, J.K. (2002): U-Pb zircon age constraint for late Neoproterozoic rifting and initiation of the lower Paleozoic passive margin of western Laurentia; Canadian Journal of Earth Sciences, v. 39, p. 133–143.

Harrison, J.E. (1972): Precambrian Belt basin of northwestern United States: its geometry, sedimentation and copper occurrences; Geological Society of America Bulletin, v. 83, p. 1215–1240.

Höy, T. (1989): The age, chemistry and tectonic setting of the Middle Proterozoic Moyie sills, Purcell Supergroup, southeastern British Columbia; Canadian Journal of Earth Sciences, v. 26, p. 2305–2317.

Höy, T., Price, R.A., Legun, A., Grant, B. and Brown, D. (1995): Purcell Supergroup, southwestern British Columbia (NTS 82G, F, E; 82J/SW, 82K/SE); BC Ministry of Energy, Mines and Petroleum Resources, BC Geological Survey, Geoscience Map 1995-1, scale 1:250 000.

Hunt, G. (1962): Time of Purcell eruption in southeastern British Columbia and southwestern Alberta; Bulletin of Canadian Petroleum Geology, v. 10, p. 438–442.

Klepacki, D.W. (1985): Stratigraphy and structural geology of the Goat Range area, southeastern British Columbia; Ph.D. thesis, Massachusetts Institute of Technology, Cambridge, Massachusetts 268 p.

Leclair, A.D. (1982): Preliminary results on the stratigraphy, structure, and metamorphism of central Kootenay Arc rocks, southeastern British Columbia; *in* Current Research, Part A, Geological Survey of Canada, Paper 82-1A, p. 45–49.

Leclair, A.D., Parrish, R.R. and Archibald, D.A. (1993): Evidence for Cretaceous deformation in the Kootenay Arc based on U-Pb and $^{40}Ar/^{39}Ar$ dating, southeastern British Columbia; *in* Current Research, Part A, Geological Survey of Canada, Paper 93-1A, p. 207–220.

Leech, G.B. (1962): Metamorphism and granitic intrusions of Precambrian age in southeastern British Columbia; Geological Survey of Canada, Paper 62-13, 11 p.

McFarlane, C.R.M. (2015): A geochronological framework for sedimentation and Mesoproterozoic tectonomagmatic activity in lower Belt-Purcell rocks exposed west of Kimberley, British Columbia; Canadian Journal of Earth Sciences, v. 52, p. 444–465. doi:10.1139/cjes-2014-0215

McFarlane, C.R.M. and Pattison, D.R.M. (2000): Geology of the Matthew Creek metamorphic zone, southeast British Co-

lumbia: a window into Middle Proterozoic metamorphism in the Purcell Basin; Canadian Journal of Earth Sciences, v. 37, p. 1073–1092. doi:10.1139/e00-018

McMechan, M.E. and Price, R.A. (1982): Superimposed low-grade metamorphism in the Mount Fisher area, southeastern British Columbia – implications for the East Kootenay orogeny; Canadian Journal of Earth Sciences, v. 19, p. 476–489.

Moynihan, D.P. and Pattison, D.R.M. 2013: Barrovian metamorphism in the central Kootenay Arc, British Columbia: petrology and isograd geometry; Canadian Journal of Earth Sciences, v. 50, p. 769–794. doi:10.1139/cjes-2012-0083

Pattison, D.R.M. and Seitz, J.D. (2012): Stabilization of garnet in metamorphosed altered turbidites near the St. Eugene lead-zinc deposit, southeastern British Columbia: equilibrium and kinetic controls; Lithos, v. 134–135, p. 221–235. doi:10.1016/j.lithos.2011.12.007

Price, R.A. (1964): The Precambrian Purcell system in the Rocky Mountains of southern Alberta and British Columbia; Bulletin of Canadian Petroleum Geology, v. 12, p. 399–426.

Read, P.B., Woodsworth, G.J., Greenwood, H.J., Ghent, E.D. and Evenchick, C.A. (1991): Metamorphic map of the Canadian Cordillera; Geological Survey of Canada, Map 1714A, scale 1:2 000 000.

Warren, M.J. (1997): Crustal extension and subsequent crustal thickening along the Cordilleran rifted margin of ancestral North America, western Purcell Mountains, southeastern British Columbia; Ph.D. thesis, Queen's University, Kingston, Ontario, 477 p.

Webster, E.R. and Pattison, D. (2017): Spatially overlapping episodes of deformation, metamorphism, and magmatism in the southern Omineca belt, southeastern British Columbia; Canadian Journal of Earth Sciences, v. 0, no. ja. doi:10.1139/cjes-2017-0036.

Wheeler, J.O. and McFeely, P. (1991): Tectonic assemblage map of the Canadian Cordillera and adjacent parts of the United States of America; Geological Survey of Canada, Map 1712A, scale 1:2 000 000. doi:10.4095/133549

Responses of the Soil Microbial Community to Weathering of Ore Minerals

R.L Simister, Department of Microbiology and Immunology, and Mineral Deposits Research Unit (MDRU), Department of Earth, Ocean and Atmospheric Sciences, The University of British Columbia, Vancouver, BC

P.A. Winterburn, Mineral Deposits Research Unit (MDRU), Department of Earth, Ocean and Atmospheric Sciences, The University of British Columbia, Vancouver, BC

S.A. Crowe, Departments of Microbiology and Immunology, and Earth, Ocean and Atmospheric Sciences, The University of British Columbia, Vancouver, BC, sean.crowe@ubc.ca (corresponding author)

Simister, R.L., Winterburn, P.A. and Crowe, S.A. (2018): Responses of the soil microbial community to weathering of ore minerals; *in* Geoscience BC Summary of Activities 2017: Minerals and Mining, Geoscience BC, Report 2018-1, p. 57–68.

Introduction

As global population grows and modernizes, demand for mineral resources is expanding (Kesler, 2007). At the same time, existing orebodies are being exhausted, while the frequency of new discoveries of exposed or partially exposed deposits diminishes. Demand for mineral resources must therefore be met through the discovery and development of buried or concealed mineral deposits. Although mineral resource extraction supported the core of the Canadian economy for over a century—currently contributing $56 billion to Canada's GDP and providing 19% of its goods exports (The Mining Association of Canada, 2017)—its ability to do so relies on continued discovery of mineral deposits that may be concealed by overburden. Finding these mineral deposits beneath exotic overburden consisting of glacial and preglacial sediments remains a fundamental and widespread challenge to mineral exploration in Canada (Anderson et al., 2012; Ferbey et al., 2014).

New and innovative techniques that complement, enhance or even surpass traditional techniques to define the surface expression of buried ore mineralization could minimize the cost of exploration and help in targeting drilling activities (Kelley et al., 2006). Several recent studies in British Columbia (BC) have demonstrated the potential for new surface geochemical techniques to lead to the discovery of concealed orebodies. These include indicator minerals (Plouffe et al., 2013a, b), soil partial leach and selective extraction geochemistry on multiple soil horizons (Van Geffen et al., 2009; Bissig and Riquelme, 2010; Heberlein and Samson, 2010), halogen element detection (e.g., Heberlein et al., 2017), till geochemistry (Cook et al., 1995) and biogeochemistry (Dunn, 1986; Reid and Hill, 2010). Each geochemical technique and media type has both strengths and weaknesses in identifying buried mineralization:

- Indicator minerals (e.g., Plouffe et al., 2013a; Plouffe and Ferbey, 2016) and biogeochemistry (e.g., Dunn et al., 2015; Jackaman and Sacco, 2016) have demonstrated success in targeting at a regional reconnaissance scale, but additional tools are still required to define final drill targets.
- Surface geochemical techniques (e.g., soil and till) for near-source detection have not reached a level of robustness to generate high-confidence drill targets. Specifically, geochemical signatures generated from orientation surveys over known mineral deposits are noisy (i.e., poor resolution of anomalies against background; Stanley, 2003), show poor precision and have element patterns that are often difficult to reconcile with mineral-deposit chemistry and expected element mobility (Heberlein and Samson, 2010).
- Unfortunately for mineral explorers, published research has led to marketing of a range of competitive commercial analytical methodologies loosely grouped as 'selective or partial extraction techniques', many of which are proprietary to specific companies. The interpretation of the data is often ambiguous, especially if it is undertaken without consideration of the heterogeneity of the sampled mineralogy, organic-matter character, element dispersion and host (Cameron et al., 2004; Anand et al., 2016).
- Organic geochemical techniques for direct detection of deposits are dominated by the proprietary Spatiotemporal Geochemical Hydrocarbons (SGH®) method. As with the selective extractions, application of the SGH® technique is dominated by the junior exploration industry. The major exploration companies generally do not apply the technique due to concerns with robustness, repeatability of survey results and lack of a demonstrable link between the compounds analyzed and the mineralization at depth (Noble et al., 2013). There is effectively no fundamental understanding of how and where the hydrocarbon signatures are generated.

This publication is also available, free of charge, as colour digital files in Adobe Acrobat® PDF format from the Geoscience BC website: http://www.geosciencebc.com/s/SummaryofActivities.asp.

The lack of fundamental mechanistic understanding of these techniques beyond their broadest concepts has led to inappropriate application by the mineral exploration industry with minimal return on investment. The failure of the commercial techniques to repeat the performance shown in orientation surveys over known mineralization has, in large part, resulted in their abandonment by major exploration companies. Despite these issues, there is sufficient empirical evidence to indicate causative links between mineralization beneath transported cover and the presence of geochemical gradients in the surface environment (Hamilton, 1998; Smee, 1998; Kelley et al., 2006; Nordstrom, 2011). Although much less explored, biological anomalies may be more robust indicators of buried mineralization (Kelley et al., 2006; Leslie et al. 2013), and such anomalies may be detectable through low-cost, high-throughput geobiological[1] surveys.

Microbial-Community Fingerprinting as a Mineral Exploration Tool

Micro-organisms kinetically enhance and exploit thermodynamically favourable geochemical reactions, including the dissolution and formation of diverse minerals, to support their metabolism and growth in nearly every low-temperature geological setting (Newman and Banfield, 2002; Falkowski et al., 2008). They are acutely sensitive, often rapidly responding to the dynamics of chemical and physical gradients in the environment. Subtle changes in mineral bioavailability, for example, can be reflected in dramatic shifts in composition and activity of the microbial community (Newman and Banfield, 2002; Fierer, 2017). This can be seen at the global scale as marine phytoplankton communities respond to traces of iron in seawater, a process that can be viewed as chlorophyll plumes via remote sensing (O'Reilly et al., 1998; Fuhrman et al., 2008). Application of modern sequencing technologies allows high-throughput profiling of the taxonomic diversity and metabolic potential of soil microbial communities across subtle, and often poorly resolved, geochemical gradients.

Microbial-community profiles thus have a strong potential to resolve chemical and physical differences in sample suites that are not readily discernible through conventional geochemical and geophysical surveys. In residual terrains, for example, where chemical gradients are high, bacterial population changes have been clearly demonstrated (e.g., Southam and Saunders, 2005; Reith and Rogers, 2008). Even outdated techniques with low throughput and resolution, such as Denaturing Gradient Gel Electrophoresis (DGGE), that can produce a crude microbial-community "fingerprint" (Wakelin et al., 2012) reveal changes in bacterial communities in soils over buried volcanogenic massive-sulphide (VMS) deposits. The advent of high-throughput next-generation sequencing (NGS) platforms during the last decade has transformed our capacity to interrogate the molecular fingerprints of microbial communities (Binladen et al., 2007; Shokralla et al., 2012; Zhou et al., 2015). Application of NGS technologies thus allows profiling of the taxonomic diversity and metabolic potential of soil microbial communities across defined survey areas. Given that each soil sample comprises thousands of microbial taxa, each containing hundreds to thousands of genes (Fierer, 2017), the statistical power of this approach to identify anomalies is unprecedented. A schematic diagram of such an approach is illustrated in Figure 1.

To enhance the ability to recognize microbial fingerprints in the surface environment related to buried mineralization, a laboratory experiment has been conducted in which background soils were either amended with the copper-bearing mineral chalcopyrite or doped with copper as copper sulphate ($CuSO_4$). These soils were then incubated to test the response of the microbial community to the presence of copper amendments. Some organisms have evolved distinct extracellular acquisition and internal storage strategies to target elements that are specifically required for enzymatic or metabolic processes (Liermann et al., 2007), and the requirement for copper in some microbial species has been well documented in controlled studies (Knapp et al., 2007; Fru et al., 2011; Balasubramanian et al., 2012; Kenney and Rosenzweig, 2012). Since both chalcopyrite weathering in soils and soil microbial turnover are appreciable over timescales of several weeks, these experiments are traceable in the laboratory (Whitman et al., 1998; Kimball et al., 2010). The composition of the soil microbial community has been analyzed at initial, intermediate and end time-points, allowing identification of members of the soil microbial community that respond to the presence of ore minerals. These first bench-scale results will facilitate more detailed and controlled tests, in the future, for the presence or abundance of specific community members and their metabolic capacity in relation to buried mineral deposits.

Methodology

Soil and Ore Amendment

An archived soil sample from close to the Deerhorn porphyry, located 70 km northeast of Williams Lake in central BC, was retrieved (sample number 282140 of Rich, 2016). This sample is considered as representative of background because it has insignificant base-metal contents. The sample was collected from the upper B horizon under aseptic conditions and screened to –6 mm in the field prior to storage at ambient temperatures in double-sealed zip-lock bags. The sample was digested using a multi-acid digestion

[1] *Geobiology is the interdisciplinary science dealing with the interaction between organisms and ecosystems and their physical environment (Oxford University Press, 2017).*

and the digestate analyzed by inductively coupled plasma–mass spectrometry (ICP-MS) to determine that the soil contains 6 ppm Cu, 1 ppm As and 0.32 ppm Mo. The soil was not dried prior to the start of the experiment. Soil was dispensed aseptically into sterile containers for each treatment, with amendment concentrations chosen to represent either concentrations of copper that are routinely detected in geochemical surveys over buried mineral deposits (ambient or '(Am)') or very high levels of copper that might be expected in highly anomalous soils (high or '(Hi)'). The amendments were as follows: 1) 'Hi-ore' soil was amended with chalcopyrite ore at 600 ppm Cu; 2) 'Am-ore' soil was amended with chalcopyrite ore at 200 ppm Cu; 3) 'Hi-Cu' soil was amended with copper in the form of $CuSO_4$ (dissolved in Milli-Q®-filtered water) to 600 ppm Cu; and 4) 'Am-Cu' soil was amended with copper in the form of $CuSO_4$ to 200 ppm Cu. Soil was sampled at T = 0, T = 1 (2 weeks) and T = 2 (5 weeks).

DNA Extraction

Microbial-community DNA was extracted from samples using a MO BIO Laboratories Inc. PowerMax® Soil DNA Isolation Kit; as per manufacturer's instructions, approximately 0.25 g of soil was used. Resulting DNA was stored at –20°C. The quality and quantity of genomic DNA were measured on a ThermoFisher Scientific NanoDrop® ND-1000 spectrophotometer and by using Invitrogen™ PicoGreen™ (Quant-iT™ dsDNA Assay Kit) dye.

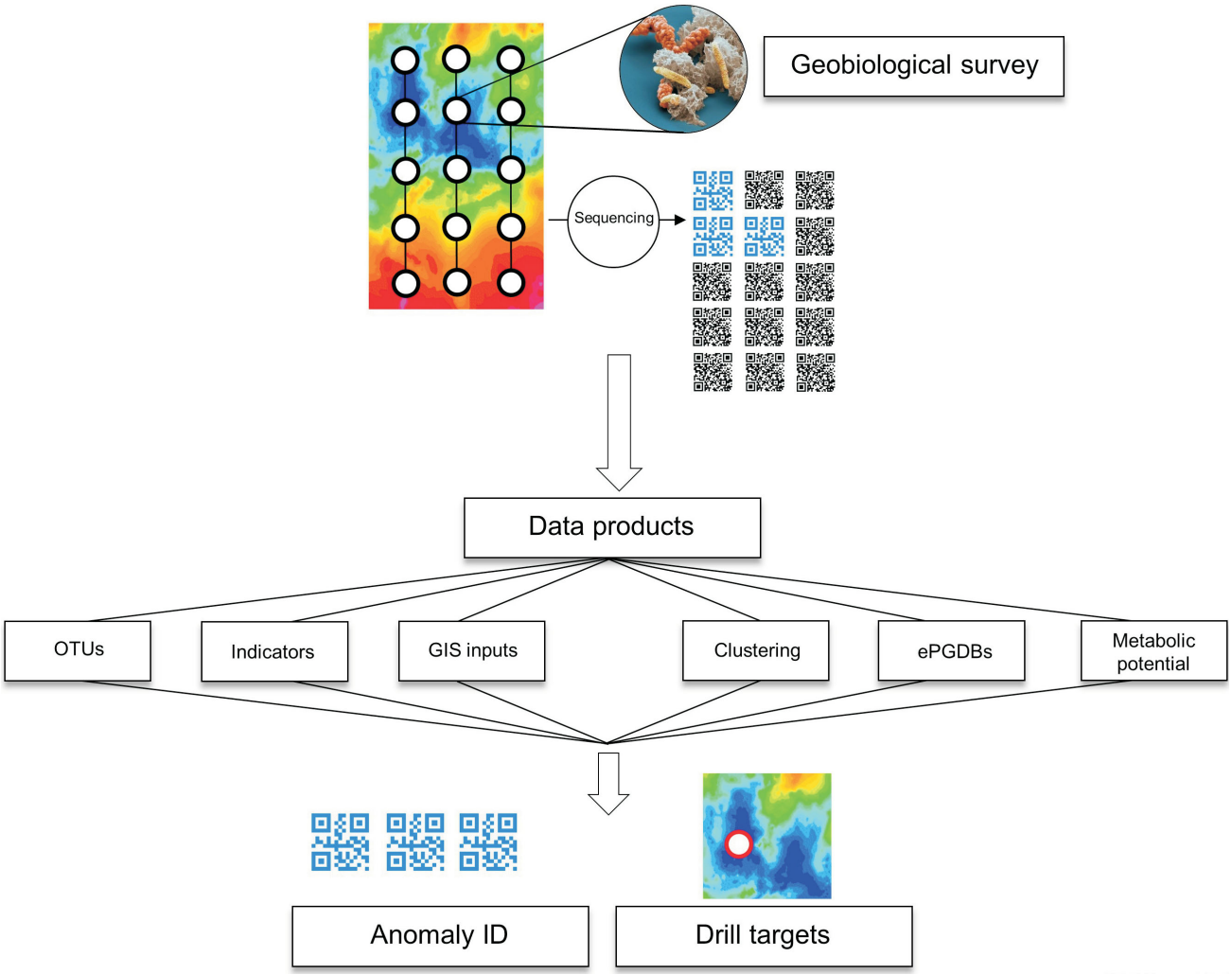

Figure 1. Schematic diagram of microbial fingerprinting applied to mineral deposit exploration. DNA is extracted and purified from soil samples taken in geobiological surveys and then sequenced to 1) generate iTag libraries of the 16S rRNA gene for community fingerprinting analysis, and 2) generate metagenomes to mechanistically link anomalous microbial communities to underlying differences in coded metabolic potential. These anomalies, reflected by hundreds to thousands of microbial species, will form unique fingerprints or barcodes that are characteristic of proximity to buried mineral resources. These barcodes will be formatted into data products such as deposit-scale exploration maps that chart microbial fingerprints (operational taxonomic units [OTUs], indicator and clustering analysis) and anomalies/ePDGBs (environmental pathway genome databases) specifically linked to mineral deposits.

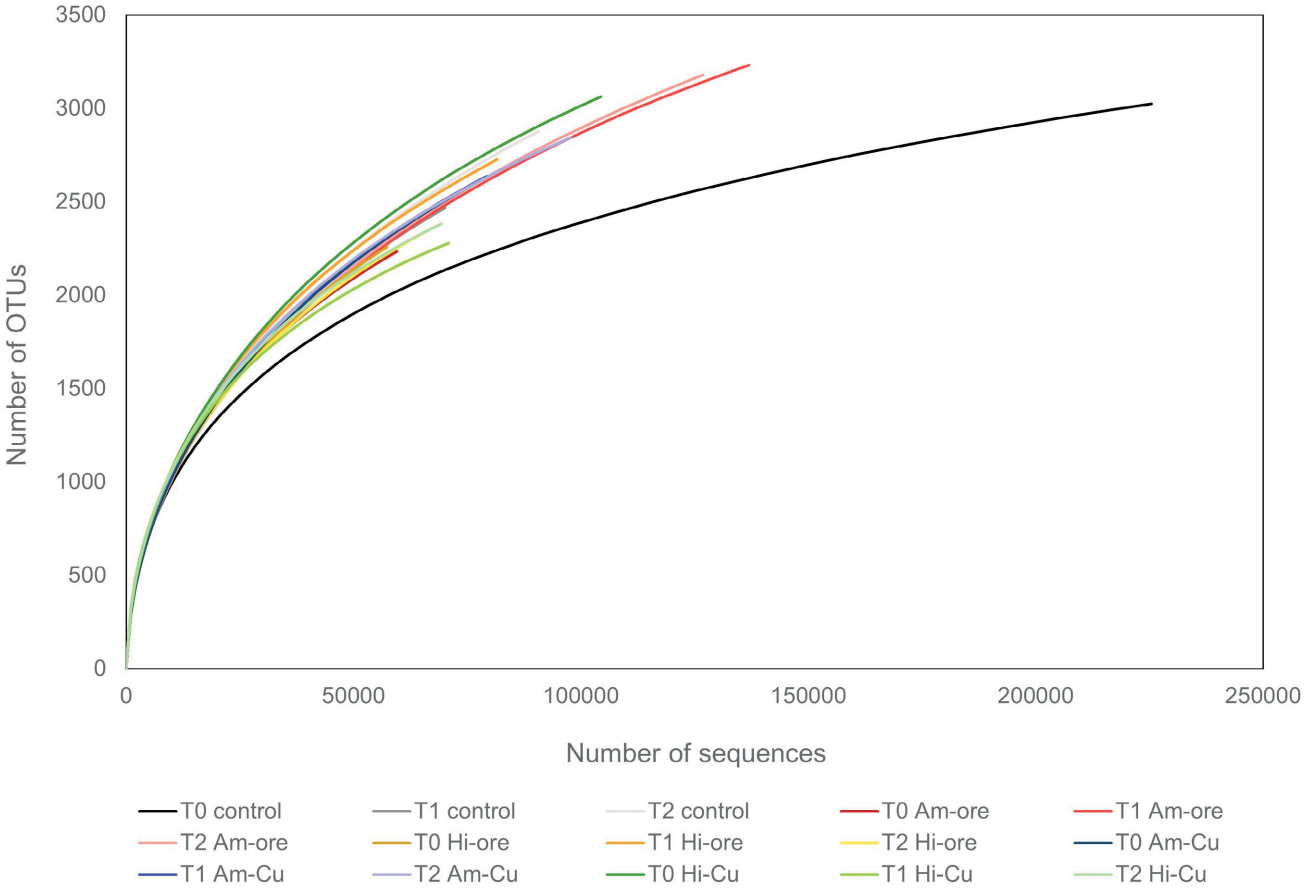

Figure 2. Bacterial diversity of samples. Rarefaction curves are based on operational taxonomic units (OTUs) at 97% sequence similarity.

Small Subunit Ribosomal RNA (SSU rRNA) Gene Amplification and iTag Sequencing

Bacterial and archaeal 16S rRNA gene fragments from the extracted genomic DNA were amplified using primers 515f and 806r (Apprill et al., 2015). Sample preparation for amplicon sequencing was performed as described by Kozich et al. (2013). In brief, the aforementioned 16S rRNA gene-targeting primers, complete with Illumina adapter, an 8-nucleotide index sequence, a 10-nucleotide pad sequence, a 2-nucleotide linker and the gene-specific primer were used in equimolar concentrations together with Deoxynucleotide triphosphate (dNTPs), Polymerase chain reaction (PCR) buffer, $MgSo_4$, 2U/µL ThermoFisher high-fidelity platinum Taq DNA polymerase and PCR-certified water to a final volume of 50 µL. PCR amplification was performed with an initial denaturing step of 95°C for 2 min, followed by 30 cycles of denaturation (95°C for 20 s), annealing (55°C for 15 s) and elongation (72°C for 5 min), with a final elongation step at 72°C for 10 min. Equimolar concentrations of amplicons were pooled into a single library. The amplicon library was analyzed on an Agilent Bioanalyzer using the High-Sensitivity DS DNA Assay to determine approximate library fragment size, and to verify library integrity. Library pools were diluted to 4 nM and denatured into single strands using fresh 0.2 N NaOH, as recommended by Illumina. The final library was loaded at a concentration of 8 pM, with an additional PhiX spike-in of 5–20%. Sequencing was conducted on the MiSeq platform at the Sequencing + Bioinformatics Consortium, The University of British Columbia, Vancouver, BC (The University of British Columbia, 2017).

Informatics

Sequences were processed using mothur (Schloss et al., 2009, Kozich et al., 2013). Briefly, sequences were removed from the analysis if they contained ambiguous characters, had homopolymers longer than 8 base pairs and did not align to a reference alignment of the correct sequencing region. Unique sequences, and their frequency in each sample, were identified and then a pre-clustering algorithm was used to further de-noise sequences within each sample (Schloss et al., 2011). Unique sequences were identified and aligned against a SILVA alignment (mothur Project, 2017a). Sequences were chimera-checked using VSEARCH (Rognes et al., 2016) and reads were then clustered into 97% operational taxonomic units (OTUs) based on uncorrected pairwise distance matrices. OTUs were classified

using the SILVA reference taxonomy database (release 128; mothur Project, 2017b).

Results and Discussion

Soil is one of the most complex and diverse microbial habitats, with merely 1 g containing up to 10^{10} cells and 10^4 bacterial species (Roesch et al., 2007; Torsvik and Øvreås, 2002). The current study's approach relies on the ability to capture this diversity through next-generation sequencing technologies. In microbiology, the assessment of diversity often involves calculation of species richness (number of species present in a sample; Magurran, 2013). The most common approach is to assign 16S rRNA sequences into operational taxonomic units (OTUs) and represent these as rarefaction curves, which plot the cumulative number of OTUs captured as a function of sampling effort, and therefore indicate the OTU richness in a given set of samples. Other common methods include nonparametric analysis, such as Chao1, which estimates the overall sample diversity (also known as alpha diversity; Hughes et al., 2001). The current study extracted microbial-community DNA from the soils amended with either chalcopyrite ore or copper, and sequenced the 16S rRNA gene. Analysis of theses sequences reveals that the number of observed OTUs (hereafter referred to as species) is 2265 ±105 (range 1993–2380), with an alpha diversity (Chao1 index) of 3438 ±327 (range 2808–3791; Table 1), indicating that the sequencing coverage was sufficient to capture 65% of the microbial-community diversity. These levels of diversity are well in line with diversity commonly observed in soils (Thompson et al., 2017). These measurements dispel dogma that extremely high diversity in soil microbial communities renders them intractable to molecular-based microbial-community analysis. Rarefaction analysis revealed that resampling of the observed OTUs approaches asymptotic values (Figure 2), confirming adequate coverage for diversity estimation. There was no pronounced difference in species richness (i.e., the number of species in a given sample) over time, due to amendment with chalcopyrite ore or copper. The study's first measurements demonstrate that soil diversity can be captured through next-generation sequencing technologies, which bodes well for the approach of imparting enormous statistical power to community profiles as anomaly indicators.

Table 1. Overview of the species estimates and diversity metrics obtained per sample after quality filtering. Sample names explained in 'Soil and Ore Amendment' section. Abbreviation: OTU, operational taxonomic unit.

Sample	No. of sequences	No. of OTUs	Chao1
T0 control	57319	1993	2808
T2 control	57319	2272	3567
T3 control	57319	2380	3791
T0 Am-ore	57319	2203	3181
T2 Am-ore	57319	2277	3700
T3 Am-ore	57319	2287	3787
T0 Hi-ore	57319	2257	3364
T2 Hi-ore	57319	2369	3677
T3 Hi-ore	57319	2219	3229
T0 Am-Cu	57319	2306	3610
T2 Am-Cu	57319	2315	3606
T3 Am-Cu	57319	2317	3547
T0 Hi-Cu	57319	2418	3732
T2 Hi-Cu	57319	2129	2854
T3 Hi-Cu	57319	2229	3113

The number of reads per microbial phylum was normalized to total read number for a given sample and expressed as a percentage of the total reads from that sample (Figure 3). Most microbial-community members belong to the Proteobacteria (24–37%), Acidobacteria (13–32%) and Verrucomicrobia (11–21%) phyla (Figure 3). The relative proportions are consistent with previous studies on soil ecosystems (Choi et al., 2016; Kaiser et al., 2016). This high-level taxonomic analysis reveals strong similarities across all samples, thus giving confidence that the analyses are not overwhelmed by intersample variability arising because of the very high levels of microbial diversity and chemical and physical heterogeneity commonly found in soils. The similarity across the samples, however, suggests that discrimination between background and anomalous soils may be more sensitive with analyses at the genus or species level rather than at the phylum level. Nevertheless, when plotted relative to the unamended (control) samples, subtle changes in community composition through time can be detected even at the phylum level (Figure 4). This high-level sensitivity bodes well for application to exploration.

Differences between copper-amended and chalcopyrite ore–amended soils included a higher abundance of Chloroflexi in copper-treated soils at T_1 and T_2 (Figure 4A). The Archaeal phylum Thaumarchaeota increased in abundance relative to the control in samples amended with high levels of chalcopyrite ore (Hi-Ore) and copper (Hi-Cu; Figure 4B). The other phylum that increased over time in response to soil amendments was the Firmicutes (Figure 4C). All amendments elicited a decrease in the relative abundance of Acidobacteria, Ignavibacteria and Bacteroidetes (except for soils treated with ambient levels of chalcopyrite ore [Am-ore]) compared to control soil over time (Figure 4D–F). Relationships between treatment type (chalcopyrite ore or copper) and time point (T = 0, 1, 2) were evaluated through hierarchical-clustering analysis (Figure 5A). All control samples clustered tightly, confirming similar microbial-community compositions. Treated samples grouped apart from controls, indicating that chalcopyrite ore and copper amendments changed the composition of the microbial community and that this change was easily resolvable through standard hierarchical-clustering analysis. Hierarchal clustering separated chalcopyrite ore– and copper-treated samples, indicating that it may be possible to

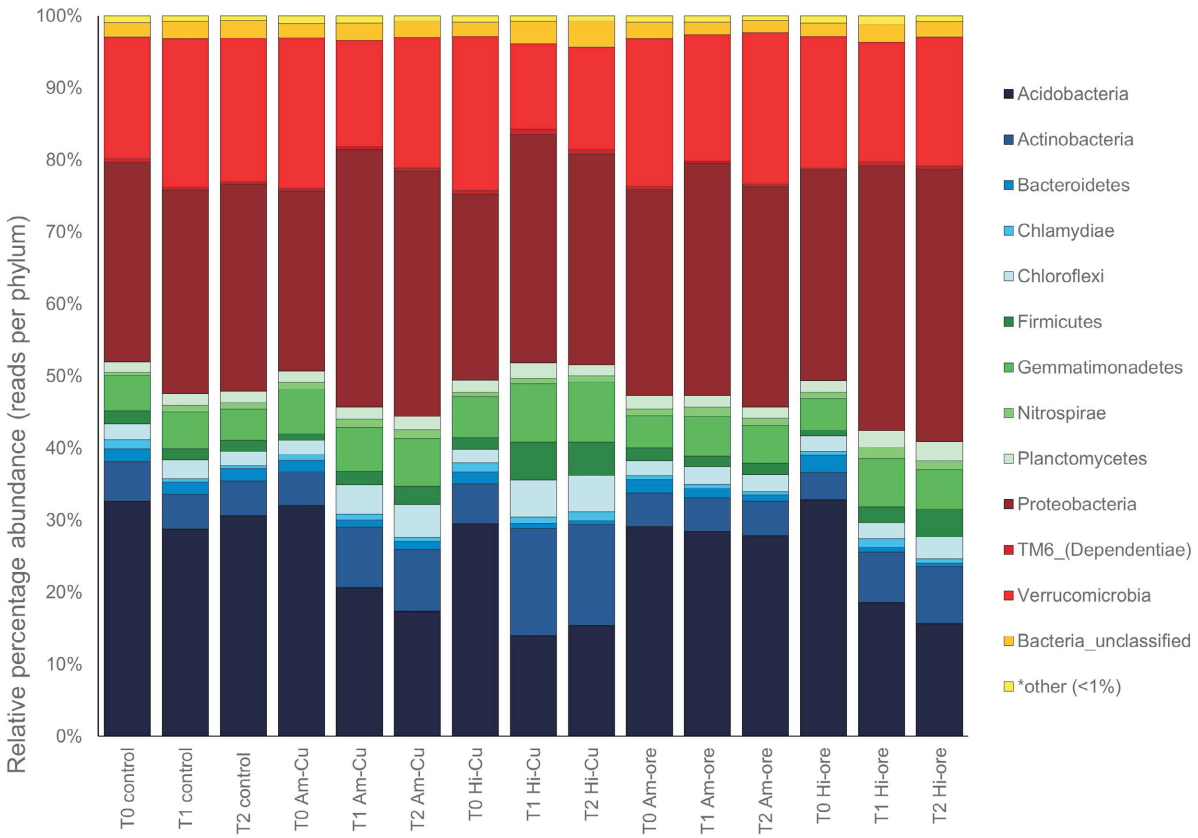

Figure 3. Distribution of 16S rRNA reads per phylum for each sample. The number of reads per phylum is calculated as a percentage of the total reads for each sample. The '*other' grouping represents summed phyla that individually contributed <0.4% of the total number of reads per sample.

determine microbial-community response to individual metals.

A number of species were appreciably enriched or depleted in response to chalcopyrite ore or copper amendment, so the relative abundance of individual species normalized to the relative abundance of the same species in the controls was plotted versus time (examples shown in Figure 5B). The species that increased in response to chalcopyrite ore and copper amendment relative to controls included *Rhodanobacteria* sp. (Koh et al., 2015), SC-I-84 sp. (Huaidong et al., 2017) and *Acidimicrobiales* sp. (Figure 5B; Hallberg et al., 2006). These species have frequently been found in relatively high abundances in materials recovered from acidic waters, sulphidic mine wastes and other mine-related environments, as well as acidic biofilms (Hallberg et al., 2006; Stackebrandt, 2014; Koh et al., 2015; Huaidong et al., 2017), anecdotally suggesting a link between the ecology of these species and the concentration of metals in their habitat. In addition to the broader community-level responses revealed through hierarchical clustering analyses, the data from this study thus imply that certain species in soil microbial communities may be useful as indicators of exposure to ore components.

Conclusions and Future Directions

This study investigated the use of soil microbial-community fingerprinting with modern DNA sequencing technologies to detect changes in soil microbial communities in response to varying levels of exposure to chalcopyrite ore and copper. It was found that soil microbial communities can be coherently sampled such that there is little variability between samples. Exposure of soil microbial communities to ore constituents elicits a response detectable on laboratory time scales of several weeks. These responses are readily resolved through standard statistical analyses, and the specific species that exhibited the strongest responses have known affinities for environments rich in heavy metals. The strong microbial responses observed are encouraging signs for the use of microbial-community fingerprinting in mineral deposit exploration. Further experiments are currently being conducted and work is ongoing to translate the approach to a real-world exploration setting. With the cooperation and permission of Consolidated Woodjam Copper Corporation, the authors have collected a suite of 150 soil samples over known copper-gold porphyry mineralization (the Deerhorn deposit) in central BC, which has

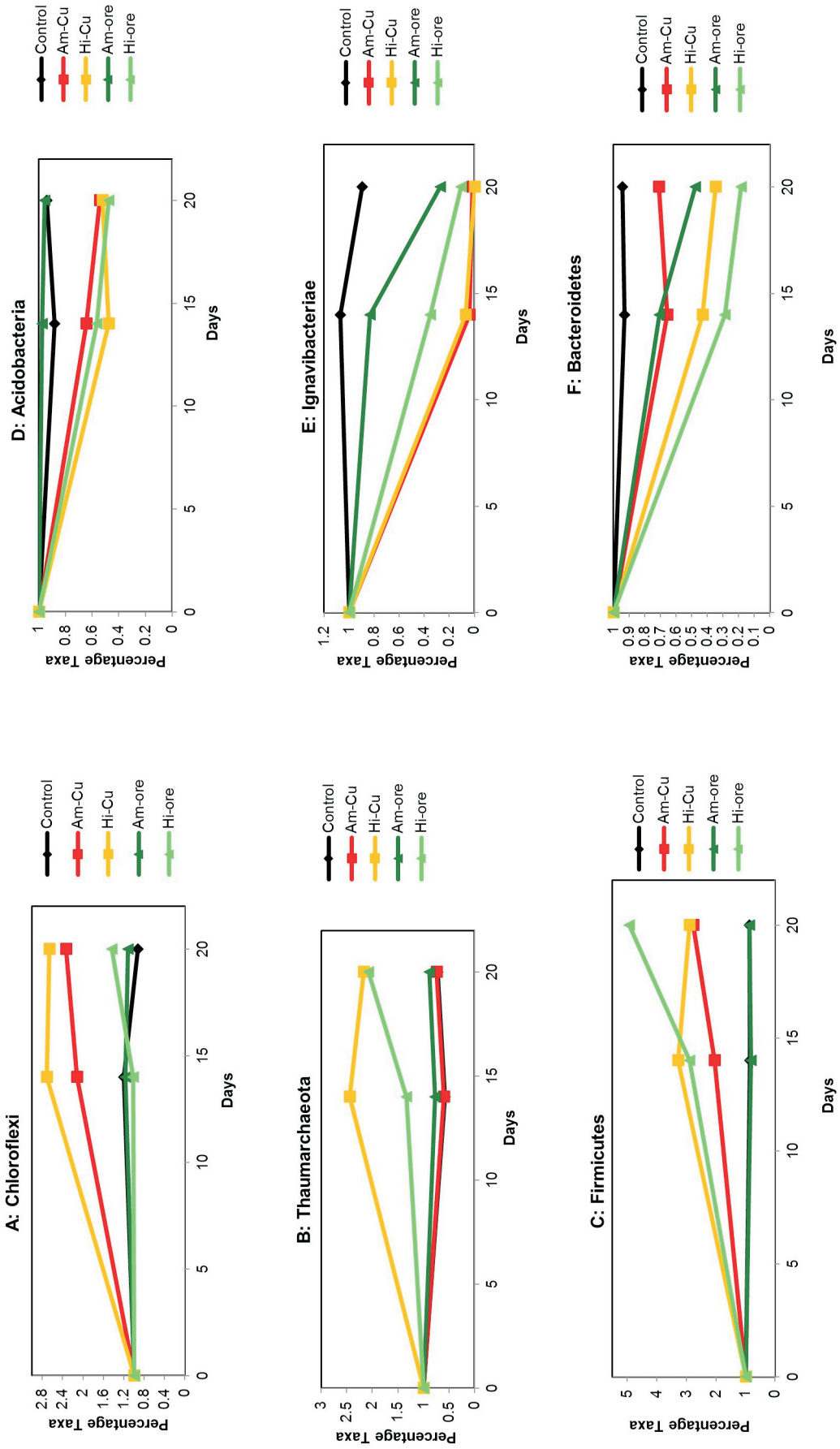

Figure 4. Examples of changes in phylum abundance over time for each sample/treatment. The number of reads per phylum is calculated as a percentage of the total reads for each sample.

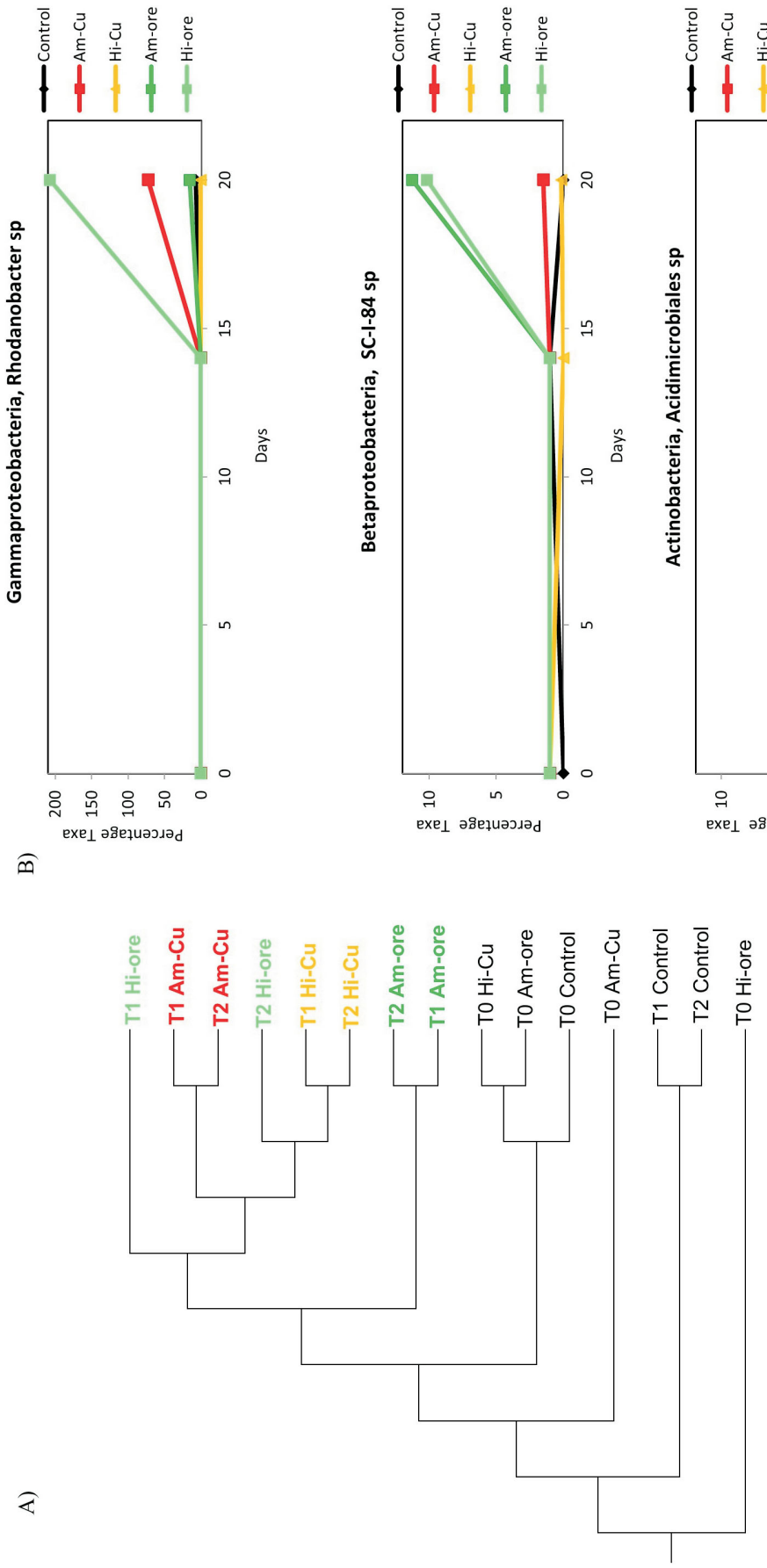

Figure 5. A) Hierarchical relationships among samples based on Euclidean distance of 16S-OTU abundances. The hierarchical relationships between samples were obtained using the unweighted pair group method with arithmetic mean (UPGMA) clustering algorithm. Node labels indicate the sample/treatment. **B)** Examples of operational taxonomic unit (OTU) 'species level' changes across treatments, over time.

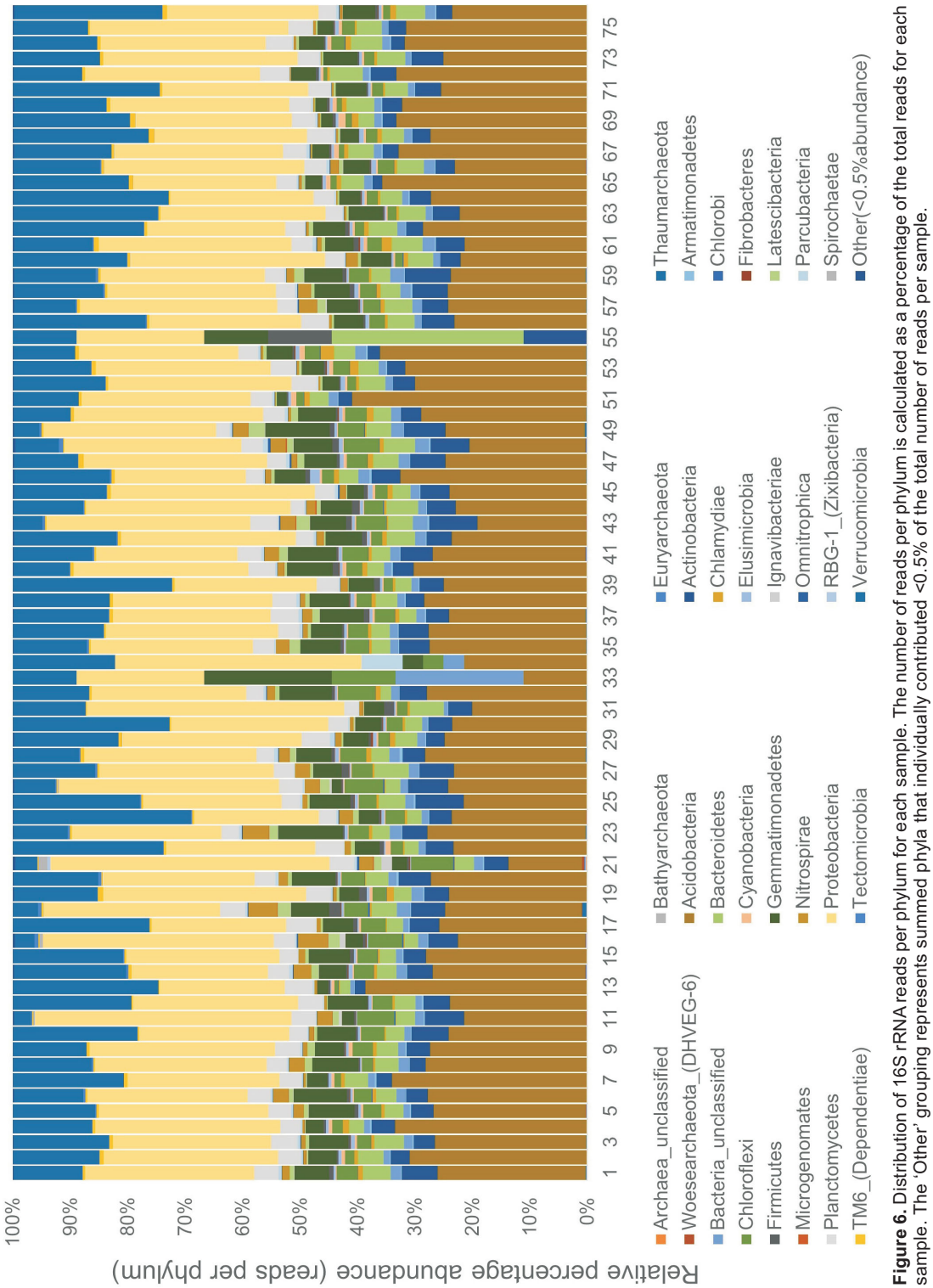

Figure 6. Distribution of 16S rRNA reads per phylum for each sample. The number of reads per phylum is calculated as a percentage of the total reads for each sample. The 'Other' grouping represents summed phyla that individually contributed <0.5% of the total number of reads per sample.

extensive geological, pedological, geochemical and geophysical metadata (Rich, 2016). Genomic DNA from nearly half of the soils collected has been extracted and tag sequencing of the 16S rRNA completed.

The first analyses of these data reveal strong similarities across the entire sample set, lending confidence to the ability to consistently sample microbial communities from the same horizon to yield a dataset from which robust comparisons can be made (Figure 6). Ongoing work includes conducting statistical analyses (hierarchical clustering and indicator-species analysis) to resolve possible patterns in the microbial-community fingerprints that could point to buried mineralization.

Acknowledgments

The authors thank S. Rich for sample collection, and P. Kenward and D. Fowle for peer review of this paper. Funding was provided by Geoscience BC.

References

Anand, R.R., Aspandiar, M.F. and Noble, R.R. (2016): A review of metal transfer mechanisms through transported cover with emphasis on the vadose zone within the Australian regolith; Ore Geology Reviews, v. 73, p. 394–416.

Anderson, R., Plouffe, A., Ferbey, T. and Dunn, C. (2012): The search for surficial expressions of buried Cordilleran porphyry deposits: background and progress in a new Targeted Geoscience Initiative 4 activity in the southern Canadian Cordillera, British Columbia; Geological Survey of Canada, Current Research (online) 2012-7. doi:10.4095/290295

Apprill, A., McNally, S., Parsons, R. and Weber, L. (2015): Minor revision to V4 region SSU rRNA 806R gene primer greatly increases detection of SAR11 bacterioplankton; Aquatic Microbial Ecology, v. 75, no. 2, p. 129–137. doi:10.3354/ame01753

Balasubramanian, R., Smith, S.M., Rawat, S., Yatsunyk, L.A., Stemmler, T.L. and Rosenzweig, A.C. (2012): Oxidation of methane by a biological dicopper centre; Nature, v. 465, no. 7294, p. 115–131.

Bissig, T. and Riquelme, R. (2010): Andean uplift and climate evolution in the southern Atacama Desert deduced from geomorphology and supergene alunite-group minerals; Earth and Planetary Science Letters, v. 299, p. 447–457.

Binladen, J., Gilbert, M.T.P., Bollback, J.P., Panitz, F., Bendixen, C., Nielsen, R. and Willerslev, E. (2007): The use of coded PCR primers enables high-throughput sequencing of multiple homolog amplification products by 454 parallel sequencing; PloS one, e197. doi:10.1371/journal.pone.0000197

Cameron, E.M., Hamilton, S.M., Leybourne, M.I., Hall, G.E.M. and McClenaghan, M.B. (2004): Finding deeply buried deposits using geochemistry; Geochemistry: Exploration, Environment, Analysis, v. 4, p. 7–32.

Choi, J., Yang, F., Stepanauskas, R., Cardenas, E., Garoutte, A., Williams, R., Flater, J., Tiedje, J.M., Hofmockel, K.S. and Gelder, B. (2016): Strategies to improve reference databases for soil microbiomes; The ISME Journal, v. 11, p. 829–834, URL <https://www.nature.com/articles/ismej2016168> [November 2017].

Cook, S.J., Levson, V.M., Giles, T.R. and Jackaman, W. (1995): A comparison of regional lake sediment and till geochemistry surveys: a case study from the Fawnie Creek area, central British Columbia; Exploration and Mining Geology, v. 4, no. 2, p. 93–101.

Dunn, C.E. (1986): Biogeochemistry as an aid to exploration for gold, platinum and palladium in the northern forests of Saskatchewan, Canada; Journal of Geochemical Exploration, v. 25, p. 21–40.

Dunn, C.E., Thompson, R.I., Hetherington R., Cornelius, M. and Ringrose, C.R. (2015): From tree tops to massive sulphides in the Mable Lake area, British Columbia, Canada; Geochemistry: Exploration, Environment, Analysis, v. 15, p. 138–149.

Falkowski, P.G., Fenchel, T. and Delong, E.F. (2008): The microbial engines that drive Earth's biogeochemical cycles; Science, v. 320, no. 5879, p. 1034–1039.

Ferbey, T., Anderson, R.G. and Plouffe, A. (2014): An integrated approach to search for buried porphyry-style mineralization in central British Columbia using geochemistry and mineralogy: a TGI-4 project; Geological Survey of Canada, Current Research (online) 2014-2, 15 p. doi:10.4095/293130

Fierer, N. (2017): Embracing the unknown: disentangling the complexities of the soil microbiome; Nature Reviews Microbiology, v. 15, p. 579–590.

Fru, E.C., Gray, N.D., McCann, C., Baptista, J.D., Christgen, B., Talbot, H.M., Ghazouani, A., Dennison, C. and Graham, D.W. (2011): Effects of copper mineralogy and methanobactin on cell growth and sMMO activity in *Methylosinus trichosporium* OB3b; Biogeosciences, v. 8, no. 10, p. 2887–2894.

Fuhrman, J.A., Steele, J.A., Hewson, I., Schwalbach, M.S., Brown, M.V., Green, J.L. and Brown, J.H. (2008): A latitudinal diversity gradient in planktonic marine bacteria; Proceedings of the National Academy of Sciences, v. 105, p. 7774–7778.

Hallberg, K.B., Coupland, K., Kimura, S. and Johnson, D.B. (2006): Macroscopic streamer growths in acidic, metal-rich mine waters in North Wales consist of novel and remarkably simple bacterial communities; Applied and Environmental Microbiology, v. 72, p. 2022–2030.

Hamilton, S. (1998): Electrochemical mass-transport in overburden: a new model to account for the formation of selective leach geochemical anomalies in glacial terrain; Journal of Geochemical Exploration, v. 63, p. 155–172.

Heberlein, D.R. and Samson, H. (2010): An assessment of soil geochemical methods for detecting copper-gold porphyry mineralization through Quaternary glaciofluvial sediments at the Kwanika central zone, north-central British Columbia; Geoscience BC, Report, 2010-3, 89 p., URL <http://www.geosciencebc.com/s/2010-003.asp> [November 2017].

Heberlein, D.R., Dunn, C.E. and Rice, S. (2017): Halogens and other volatile compounds in surface sample media as indicators of mineralization, part 1: Lara VMS deposit, Vancouver Island, BC (NTS 092B13); Geoscience BC, Report 2017-11, 50 p., URL <http://www.geosciencebc.com/s/2016-007.asp> [November 2017].

Huaidong, H., Waichin, L., Riqing, Y. and Zhihong, Y. (2017): Illumina-based analysis of bulk and rhizosphere soil bacte-

rial communities in paddy fields under mixed heavy metal contamination; Pedosphere, v. 27, p. 569–578.

Hughes, J.B., Hellmann, J.J., Ricketts, T.H. and Bohannan, B.J. (2001): Counting the uncountable: statistical approaches to estimating microbial diversity; Applied and Environmental Microbiology, v. 67, no. 10, p. 4399–4406.

Jackaman, W. and Sacco. D.A. (2016): Reconnaissance biogeochemical survey using spruce-tops in the West Road (Blackwater) River Area, Fraser Plateau, British Columbia; Geoscience BC, Report 2016-5, 7 p., URL <http://www.geosciencebc.com/s/Report2016-05.asp> [November 2017].

Leslie, K., van Geffen, P.W., MacFarlane, B., Oates, C.J., Kyser, T.K. and Fowle, D.A. (2013): Biogeochemical indicators of buried mineralization under cover, Talbot VMS Cu-Zn prospect, Manitoba;. Applied Geochemistry, v. 37, p. 190-202.

Kaiser, K., Wemheuer, B., Korolkow, V., Wemheuer, F., Nacke, H., Schöning, I., Schrumpf, M. and Daniel, R. (2016): Driving forces of soil bacterial community structure, diversity, and function in temperate grasslands and forests; Nature Scientific Reports, v. 6, article 33696. doi:10.1038/srep33696

Kelley, D.L., Kelley, K.D., Coker, W.B., Caughlin, B. and Doherty, M.E. (2006): Beyond the obvious limits of ore deposits: the use of mineralogical, geochemical, and biological features for the remote detection of mineralization; Economic Geology, v. 101, p. 729–752.

Kenney, G.E. and Rosenzweig, A.C. (2012): Chemistry and biology of the copper chelator methanobactin; ACS Chemical Biology, v. 7, no. 2, p. 260–268.

Kesler, S.E. (2007): Mineral supply and demand into the 21st century; *in* Proceedings for a Workshop on Deposit Modeling, Mineral Resource Assessment, and Their Role in Sustainable Development, J.A. Briskey and K.J. Schulz (ed.), United States Geological Survey, Circular 1294, p. 55–62.

Kimball, B.E., Rimstidt, J.D. and Brantley, S.L. (2010): Chalcopyrite dissolution rate laws; Applied Geochemistry, v. 25, p. 972–983.

Knapp, C.W., Fowle, D.A., Kulczycki, E., Roberts, J.A. and Graham, D.W. (2007): Methane monooxygenase gene expression mediated by methanobactin in the presence of mineral copper sources; Proceedings of the National Academy of Sciences of the United States of America, v. 104, no. 29, p. 12040–12045.

Koh, H.-W., Hong, H., Min, U.-G., Kang, M.-S., Kim, S.-G., Na, J.-G., Rhee, S.-K. and Park, S.-J. (2015): *Rhodanobacter aciditrophus* sp. nov., an acidophilic bacterium isolated from mine wastewater; International Journal of Systematic and Evolutionary Microbiology, v. 65, p. 4574–4579.

Kozich, J.J., Westcott, S.L., Baxter, N.T., Highlander, S.K. and Schloss, P.D. (2013): Development of a dual-index sequencing strategy and curation pipeline for analyzing amplicon sequence data on the MiSeq Illumina sequencing platform; Applied and Environmental Microbiology, v. 79, p. 5112–5120.

Liermann, L.J., Hausrath, E.M., Anbar, A.D., and Brantley, S.L. (2007): Assimilatory and dissimilatory processes of microorganisms affecting metals in the environment; Journal of Analytical Atomic Spectrometry, v. 22, p. 867–877.

Magurran, A.E. (2013): Measuring Biological Diversity; John Wiley & Sons.

mothur Project (2017a): Silva reference alignment; mothur Project, URL <http://www.mothur.org/wiki/Silva_reference_alignment> [November 2017].

mothur Project (2017b): Silva reference files; mothur Project, URL <http://www.mothur.org/wiki/Silva_reference_files> [November 2017].

Newman, D.K. and Banfield, J.F. (2002): Geomicrobiology: how molecular-scale interactions underpin biogeochemical systems; Science, v. 296, p. 1071–1077.

Noble, R., Lintern, M., Townley, B., Anand, R., Gray, D. and Reid, N. (2013): Metal migration at the North Miitel Ni sulphide deposit in the southern Yilgarn Craton: part 3, gas and overview; Geochemistry: Exploration, Environment, Analysis, v. 13, p. 99–113.

Nordstrom, D.K. (2011): Hydrogeochemical processes governing the origin, transport and fate of major and trace elements from mine wastes and mineralized rock to surface waters; Applied Geochemistry, v. 26, p. 1777–1791.

O'Reilly, J.E., Maritorena, S., Mitchell, B.G., Siegel, D.A., Carder, K.L., Garver, S.A., Kahru, M. and McClain, C. (1998): Ocean color chlorophyll algorithms for SeaWiFS; Journal of Geophysical Research: Oceans, v. 103, p. 24937–24953.

Oxford University Press (2017): Oxford English Dictionary Online; Oxford University Press, URL <https://en.oxforddictionaries.com/definition/geobiology> [November 2017].

Plouffe, A. and Ferbey, T. (2016): Till geochemistry, mineralogy, and textural data near four Cu porphyry deposits in British Columbia; Geological Survey of Canada, Open File 8038 and BC Ministry of Energy, Mines and Petroleum Resources, BC Geological Survey, GeoFile 2016-10, 44 p.

Plouffe, A., Ferbey, T., Anderson, R., Hashmi, S. and Ward, B. (2013a): New TGI-4 till geochemistry and mineralogy results near the Highland Valley, Gibraltar, and Mount Polley mines, and Woodjam District: an aid to search for buried porphyry deposits; Geological Survey of Canada, Open File 7473, 58 p. doi:10.4095/292907

Plouffe, A., Ferbey, T., Anderson, R., Hashmi, S., Ward, B. and Sacco, D. (2013b): The use of till geochemistry and mineralogy to explore for buried porphyry deposits in the Cordillera—preliminary results from a TGI-4 intrusion-related ore systems project; Geological Survey of Canada, Open File 7367, poster.

Reid, N. and Hill, S. (2010): Biogeochemical sampling for mineral exploration in arid terrains: Tanami Gold Province, Australia; Journal of Geochemical Exploration, v. 104, p. 105–117.

Reith, F. and Rogers, S. (2008): Assessment of bacterial communities in auriferous and non-auriferous soils using genetic and functional fingerprinting; Geomicrobiology Journal, v. 25, p. 203–215.

Rich, S.D. (2016): Geochemical mapping of porphyry deposits and associated alteration through transported overburden; M.Sc. thesis, Department of Geological Sciences, The University of British Columbia, 494 p., URL <http://hdl.handle.net/2429/58704> [November 2017].

Roesch, L.F., Fulthorpe, R.R., Riva, A., Casella, G., Hadwin, A.K.M., Kent, A.D., Daroub, S.H., Camargo, F.A.O., Farmerie, W.G. and Triplett, E.W. (2007): Pyrosequencing enumerates and contrasts soil microbial diversity; The ISME Journal, v. 1, no. 4, p. 283–290.

Rognes, T., Flouri, T., Nichols, B., Quince, C. and Mahé, F. (2016): VSEARCH: a versatile open source tool for metagenomics; PeerJ, v. 4, e2584.

Schloss, P.D., Gevers, D. and Westcott, S.L. (2011): Reducing the effects of PCR amplification and sequencing artifacts on 16S rRNA-based studies; PloS one, v. 6, e27310.

Schloss, P.D., Westcott, S.L., Ryabin, T., Hall, J.R., Hartmann, M., Hollister, E.B., Lesniewski, R.A., Oakley, B.B., Parks, D.H. and Robinson, C.J. (2009): Introducing mothur: open-source, platform-independent, community-supported software for describing and comparing microbial communities; Applied and Environmental Microbiology, v. 75, p. 7537–7541.

Shokralla, S., Spall, J.L., Gibson, J.F. and Hajibabaei, M. (2012): Next-generation sequencing technologies for environmental DNA research; Molecular Ecology, v. 21, p. 1794–1805.

Smee, B.W. (1998): A new theory to explain the formation of soil geochemical responses over deeply covered gold mineralization in arid environments; Journal of Geochemical Exploration, v. 61, p. 149–172.

Southam, G. and Saunders, J.A. (2005): The geomicrobiology of ore deposits; Economic Geology, v. 100, p. 1067–1084.

Stackebrandt, E. (2014): The Family Acidimicrobiaceae: The Prokaryotes; Springer, p. 5–12.

Stanley, C. (2003): Statistical evaluation of anomaly recognition performance; Geochemistry: Exploration, Environment, Analysis, v. 3, p. 3–12.

The Mining Association of Canada (2017): Mining facts; The Mining Association of Canada, URL <http://mining.ca/resources/mining-facts> [November 2017].

The University of British Columbia (2017): Sequencing + Bioinformatics Consortium; The University of British Columbia, URL <https://sequencing.ubc.ca/> [November 2017].

Thompson, L.R., Sanders, J.G., McDonald, D., Amir, A., Ladau, J., Locey, K. J., Prill, R.J., Tripathi, A., Gibbons, S.M., Ackermann, G., Navas-Molina, J.A., Janssen, F., Kopylova, E., Vázquez-Baeza, Y., González, A., Morton, J.T., Mirarab, S., Xu, Z.Z., Jiang, L., Haroon, M.F., Kanbar, J., Zhu, Q., Song, S.J., Kosciolek, T., Bokulich, N.A., Lefler, J., Brislawn, C.J., Humphrey, G., Owens, S.M., Hampton-Marcell, J., Berg-Lyons, D., McKenzie, V., Fierer, N., Fuhrman, J.A., Clauset, A., Stevens, R.L., Shade, A., Pollard, K.S., Goodwin, K.D., Jansson, J.K., Gilbert, J.A., Knight, R. and the Earth Microbiome Project Consortium (2017): A communal catalogue reveals Earth's multiscale microbial diversity; Nature, article 24621, URL <https://www.nature.com/articles/nature24621> [November 2017].

Torsvik, V. and Øvreås, L. (2002): Microbial diversity and function in soil: from genes to ecosystems; Current Opinion in Microbiology, v. 5, no. 3, p. 240–245.

Van Geffen, P.W., Kyser, T.K., Oates, C.J., and Ihlenfeld, C. (2009): Numerical evaluation of partial digestions for soil analysis, Talbot VMS Cu-Zn prospect, Manitoba, Canada; *in* Proceedings of the 24th International Applied Geochemistry Symposium, June 1–4, 2009, Fredericton, NB, D.R. Lentz, K.G. Thorne and K-L. Beal (ed.), p. 597.

Wakelin, S., Anand, R.R., Macfarlane, C., Reith, F., Noble, R. and Rogers, S. (2012): Assessing microbiological surface expression over an overburden-covered VMS deposit; Journal of Geochemical Exploration, v. 112, p. 262–271.

Whitman, W.B., Coleman, D.C. and Wiebe, W.J. (1998): Prokaryotes: the unseen majority; Proceedings of the National Academy of Sciences, v. 95, p. 6578–6583.

Zhou, J., He, Z., Yang, Y., Deng, Y., Tringe, S.G. and Alvarez-Cohen, L. (2015): High-throughput metagenomic technologies for complex microbial community analysis: open and closed formats; MBio, v. 6, e02288–02214.

Producing Clean Coal from Western Canadian Coalfields using the Water-Based Roben Jig Process

M.L. Mackay, Trillium Geoscience Ltd., mmackay@trilliumgeoscience.com

R.L. Leeder, Leeder Consulting Inc., Calgary, AB

L. Giroux, CanmetENERGY, Natural Resources Canada, Ottawa, ON

H. Dexter, GWIL Industries–Birtley Coal & Minerals Testing Division, Calgary, AB

M. Holuszko, The University of British Columbia, Vancouver, BC

J. Halko, Teck Coal Ltd., Calgary, AB

C. Howey, Calgary, AB

D. Thomas, CWA Engineers, Vancouver, BC

Mackay, M.L., Leeder, R.L., Giroux, L., Dexter, H., Holuszko, M., Halko, J., Howey, C. and Thomas, D. (2018): Producing clean coal from western Canadian coalfields using the water-based Roben Jig process; *in* Geoscience BC Summary of Activities 2017: Minerals and Mining, Geoscience BC, Report 2018-1, p. 69–86.

Introduction

In British Columbia (BC), the occurrence of coal is well known and relatively predictable. Several known thermal coalfields exist, as well as two major metallurgical coalfields, the Kootenay and Peace River coalfields (BC Geological Survey, 1992). The challenge isn't in 'finding' the coal, it is in evaluating the coal as a resource for various applications during the exploration stage.

During the exploration phase of coal-mine development, the evaluation of metallurgical coal for resulting coke quality is often determined using small-mass (2–15 kg) samples collected from drillcores. Drilling is the least expensive method of obtaining representative coal-seam samples when compared to developing test pits or adits. If a larger bulk sample is required, it is sometimes possible to use several 6-inch drill-program cores. However, depending on the thickness of the seam, even this may be cost prohibitive, as a large number of drillholes would need to be used to collect the required large coal mass (i.e., several tonnes). This latter amount would need to be collected to conduct pilot-scale carbonization test work for evaluating its coking potential.

Coal samples from the exploration phase are prepared by screening and washing the coal for further quality testing. The float-and-sink procedure used in coal-washability studies is the process where ash/mineral matter is removed from the coal. The coarser coal is processed using mixtures of organic liquids (i.e., white spirit, perchloroethylene (PCE) and methylene bromide) in this procedure, while the finest fraction is cleaned by a process called froth flotation. During the float-and-sink process, the coal sample is separated at relative densities (specific gravity, sg)—white spirit/PCE for 1.4 sg, PCE for 1.6 sg and PCE/methylene bromide for 1.8 sg—that produce clean-coal samples at different ash contents typical of what would be produced in a commercial coal-washing plant.

Project economics are based on the results of the float-and-sink testing, including information on the yield of clean coal as well as the quality of the cleaned coal and resulting coke quality. The coking characteristics for a metallurgical-coal deposit are mandatory in evaluating project economics (i.e., expected price for the clean coal). It is critical to ensure that coal/coking properties are correctly assessed from drillcore samples in order to properly evaluate project economics.

Background

For years, the primary concern in the handling and use of organic liquids, such as perchloroethylene (PCE), was the safety risk associated with human exposure. Perchloroethylene is a known carcinogen, posing a safety hazard for laboratory operators, and therefore must be handled carefully. Figure 1 shows a laboratory technician working in a specially designed fume hood wearing personal protective equipment, including a respirator mask.

A number of investigations and ensuing observations about how PCE may impact coal-sample coking quality have also been identified and noted. Campbell (2010) at ALS Coal Technology (Riverview, Australia) found that organic liq-

This publication is also available, free of charge, as colour digital files in Adobe Acrobat® PDF format from the Geoscience BC website: http://www.geosciencebc.com/s/SummaryofActivities.asp.

Figure 1. Operator working with organic liquids in a specially designed fume hood.

uids could interfere with the properties of interest for a coal producer or end user. Iveson and Galvin (2010) comprehensively examined the effects of organic liquids on coking properties of coal in an Australian Coal Association Research Program project and subsequently published their findings (Iveson and Galvin, 2012). They concluded that PCE had, on one hand, a negative effect on the coking properties of lower rank and lower fluidity coking coals but, on the other hand, a negligible or possibly even a small positive effect on the coke reactivity index (CRI) and coke strength after reaction (CSR) of cokes resulting from coals with relatively good initial coking properties. The latter observation pertaining to a positive impact of PCE on coke quality had been reported earlier by DuBroff et al. (1985) at Inland Steel (East Chicago, Indiana). Their patent outlined a process for improving the quality of some metallurgical coke, produced from coals with high inert content that had produced coke of lower-than-expected stability when compared to the coal rank. They studied several medium-volatile bituminous coal samples that had been soaked and agitated in a PCE bath prior to carbonization. For some of the coals, the resultant coke showed improved stability index, increased hardness index, decreased reactivity and increased tumble strength. It was also found that the carbonization time was decreased. The hypothesis was that the PCE reacted with certain macerals in the coal, producing a "solvent induced reaction product" residue on the coal particles that was highly reactive. In some cases, this reaction product was thought to 'increase' the reactives:inerts ratio at the coal-particle surfaces (DuBroff et al., 1985).

Contrary to what the Inland Steel patent outlines, Iveson and Galvin found that the negative effect of PCE treatment/exposure was shown to be more significant when coal had high inertinite content (>40%). These coals produced lower strength coke as a result of being exposed to PCE. In fact, for coals with high inertinite content, CRI was increased (an adverse effect) by an average of 15% and CSR values decreased by an average of 25% (also an adverse effect) when the coal had been exposed to PCE prior to coking. This effect was more pronounced after the coal had aged for more than 16 weeks (oxidized). The explanation proposed by Iveson and Galvin was that the high porosity of inertinite, namely semifusinite and fusinite, enabled greater access of PCE to the interior of the coal particles (Iveson and Galvin, 2012).

The evidence that organic liquids, as discussed previously, affect the coking properties of low-fluidity Australian coals implies that western Canadian coals, known to have moderate fluidity levels, could be affected in a similar way. Many Canadian geologists have also found that cleaned coal samples from drillcore often had lower caking/coking properties than bulk or production coal samples. Based on these observations, the Canadian Carbonization Research Association (CCRA) undertook a program to investigate the impact of organic solvents used in float-and-sink procedures on the coal and coke properties of a western Canadian coal sample with higher inertinite content (Holuszko et al., 2017).

This study looked at the effects of perchloroethylene on coal rheology and coke quality. It was found that an 80% decrease in Gieseler maximum fluidity occurred in the perchloroethylene-treated coal immediately following treatment, when compared to the control sample. The coke resulting from the treated sample showed a 16-point decrease in CSR when compared to the control sample. These two coal- and coke-quality parameters (i.e., Gieseler maximum fluidity and CSR) are key when evaluating coal resources and reserves. The ramifications of using the wrong numbers for the above-mentioned parameters when determining product characteristics for sale are severe and could result in project abandonment or false overvaluing of the property.

After the initial study outlined above, the CCRA also completed an exploratory study that examined an alternative to organic liquids when processing coal. A jig (Roben Jig, previously called 'Boner Jig') was used to clean coal using only water, and the resulting coal- and coke-quality characteristics were compared to coal that was processed using the traditional organic-chemical washing process. It was found that clean-coal product could be produced that was similar to that generated using the organic liquids. It is believed that, due to the coal type used in this phase study, the perchloroethylene had no negative effect on the coal-rheology and coke-strength parameters. Although this study has not yet been published, its findings are important because it demonstrates that the Roben Jig can be used to produce clean-coal composites similar in all aspects to those produced by traditional float-and-sink methods. The coal used in this work was a relatively 'easy to clean' coal, in that the particles high in mineral matter could be easily separated

from the coal. However, as not all coals wash as easily, it is important to test the Roben Jig on a wide variety of coal types.

Objectives

The objective of this project was to verify that the Roben Jig can be used commercially to wash a broad range of coal types to ultimately produce representative clean-coal composites for coal and coke analysis. This is beneficial to the coal industry for the following reasons:

- It would eliminate the potential negative effects of perchloroethylene and other organic liquids on coal- and coke-quality parameters.
- It would reduce the exposure of lab technicians/operators to carcinogenic organic liquids.

Experimental Methodology

Four coal types (coals A, B, C, D) from British Columbia were tested in this project. One sample originated from a northeastern BC coalfield and the other three originated from southeastern BC coalfields (Figure 2). All samples were collected in an undiluted, raw state from active mining faces.

Upon receipt of the coal samples at the GWIL Industries–Birtley Coal & Minerals Testing Laboratory (Calgary, AB), staff removed the coal from the sealed drums and left it to air-dry overnight. As-received and air-dried weights were reported. The coal was then screened through a 12.5 mm sieve and the oversize was hand-knapped to pass. All coal was sized at –12.5 mm. The entire sample was then split into two size fractions: –12.5 × 0.25 mm and –0.25 mm. The coarse size fraction (–12.5 × 0.25 mm) was then split into two samples. One sample was washed in organic liquids and the other was washed using the Roben Jig. The –0.25 mm coal was treated in the same way and was cleaned using the ASTM D5114-90(2010)[1] froth flotation of coal method.

Float-and-Sink and Jigging Methods

This project evaluated clean-coal products resulting from two washing methods: traditional 'float-and-sink' using organic liquids, and separation using the Roben (previously referred to as 'Boner') Jig. The specific gravity of a coal particle is dependent on the mineral-matter content and maceral composition. Coal particles containing the lowest mineral-matter content will float when separated in a 1.30 sg liquid, whereas those with the highest mineral-matter content are separated at 1.80 sg.

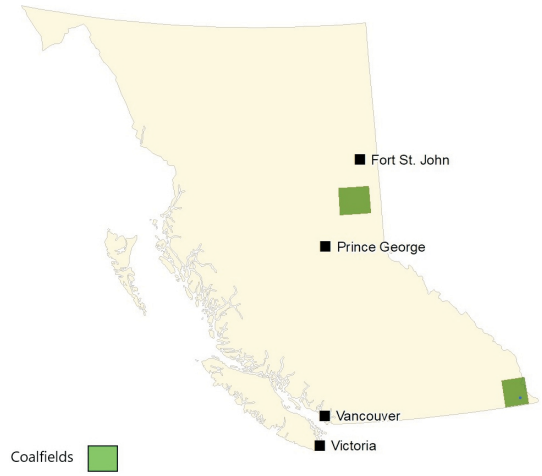

Figure 2. Locations of the coalfields in northeastern and southeastern British Columbia from which the coal samples used in this project originated.

The ASTM D4371-06(2012) float-and-sink method was used in this project. This technique fractionates coal and mineral-matter particles based on particle density by allowing particles to settle in organic-liquid mixtures with a known specific gravity. Mixtures of white spirits, perchloroethylene and methylene bromide are used to produce various media densities ranging from 1.30 to 1.80 sg (Figure 3).

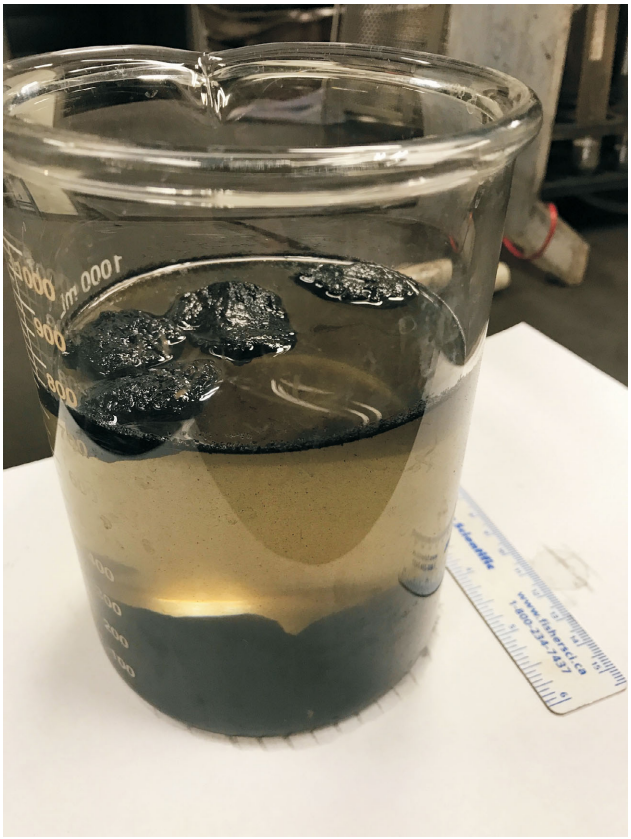

Figure 3. Coal particles floating in perchloroethylene (PCE, 1.6 sg).

[1] *References to the relevant ASTM methods can be found at the end of the 'References' section.*

The Roben Jig is a device that allows the separation of coal particles based on density to occur as the coal is jigged up and down in a column of water (Figure 4). Although a published standard (ASTM, ISO, Australian Standards) does not exist for the use of the Roben Jig, the procedure described here was developed by the inventor. Approximately 15 kg of –12.5 × 0.25 mm coal and tracers (glass marbles) of a known specific gravity (2.70) were added to the jig tube with a 0.25 mm screen at the bottom. This mesh base allows water to enter during the jig downstroke, as well as allowing particle sorting during the jig upstroke. This tube, with coal added, was gently lowered into the jig vessel. Water level was adjusted so that it was approximately 100 mm above the level of the coal. The Jig tube was attached to the pneumatic jigging mechanism. Once turned on, this mechanism moved the jig tube up and down. The downstroke was rapid to suspend particles individually, whereas the upstroke was slower to allow the particles to sort according to density. The jigging time was 15 minutes. When the jig cycle was complete, the coal sample was presumed to have been sorted into a density-continuum column: heaviest material (discard) at the bottom grading to lightest (best) coal at the top.

After jigging was completed, the jigging tube was lifted from the jig vessel, thus allowing the water to drain from the coal. A sample pusher was inserted in the jig tube and pressed to allow more water to drain. The entire tube was then inverted to allow the coal to be pushed upward. Once the jig tube was inverted and the screen removed, the marbles were visible, as they had the heaviest specific gravity. This was evidence that the jigging was successful. A tray was attached to the top of the tube and the sample pusher was rotated, causing the coal to be pushed above the jig tube and allowing the operator to scrape off the layer (Figure 5). The layer was carefully scraped into the apparent relative density (ARD) basket. Note that, because the jig tube was inverted after jigging, the first fraction collected was the highest density (heaviest or highest ash content). The thickness of the layers was dictated by the size distribution of the coal and by how many fractions one expected to remove from the sorted column. As the wet ARDs were calculated immediately, the depth of the layers could be increased or decreased to obtain a range of ARDs and subsequent range of ash contents.

Each wet coal layer was weighed and air dried, and a dry ARD calculated. Samples were then prepared for laboratory testing. Similar ARDs were added together before preparation, or tested first to confirm ash results. The calculated ARD is an average for that layer.

Each coal sample was washed using both the jig method and the organic liquids method, thus yielding two clean-coal composites per coal type. Each of these samples was analyzed at the GWIL Industries–Birtley Coal & Minerals

Figure 4. Roben Jig equipment used in this study.

Figure 5. Inverted Roben Jig with coal slice ready to be removed.

Testing Laboratory for yield (percent), proximate analysis, free swelling index (FSI), specific gravity (sg), total sulphur, Hardgrove Grindability Index (HGI), calorific value (kcal/kg), mercury, ultimate analysis, mineral analyses of the ash, phosphorus in coal (percent, calculated), Gieseler maximum fluidity, Ruhr dilatation, ash fusion (oxidizing and reducing), chlorine, fluorine, alkali extraction–light transmittance test, Sapozhnikov X and Y indices, and caking index (G). Petrographic analysis of the coal was carried out at both CanmetENERGY (Ottawa, ON) and David E. Pearson & Associates Ltd. (Victoria, BC).

Carbonization

The clean-coal composites for coals A–D (~20 kg each) generated by the float-and-sink washing with organic liquids and the Roben Jig washing with water were received at CanmetENERGY in Ottawa between May 12 and June 29, 2017. Upon receipt, the composite samples were air-dried in the open air of the laboratory for 12 hours, homogenized and screened through a nest of sieves, ranging from + 6.35 mm down to –0.5 mm, for measuring the size distribution and for preparing the charges for coking in CanmetENERGY's 12 kg capacity carbonization sole-heated oven, as per ASTM D2014-97(2010), to measure the level of expansion/contraction.

The following section provides a description of the features and operating conditions for carbonization of coal in the sole-heated oven at CanmetENERGY, including the preparation of coke samples from coals A–D for CSR evaluation, following a procedure developed at CanmetENERGY (MacPhee et al., 2013). Figure 6 presents a schematic diagram of a sole-heated oven and Figure 7 a photo of the sole-heated oven used in this project.

Sole-Heated Oven (ASTM D2014-97(2010))

A 12 kg quantity of coal (75–100% –3.35 mm or –6 mesh) was divided equally and each half-charge loaded into a chamber approximately 280 mm in width, length and depth of a double-chambered oven. A weighted piston applied a constant force corresponding to a pressure of 15.2 kPa (2.2 psi) to the top of the coalbed (thickness in the 76–90 mm range), which was heated from below according to a prescribed temperature program. The sole temperature was raised from 554 to 950°C at a heating rate of 0.9–1°C/min during the test. The movement of the load was continuously monitored during the test, which was complete when the temperature at the top of the coalbed reached 500°C (normally after a period of 6–7 hours). The measured expansion or contraction of the sample was converted to a reference base of 833 kg/m^3 (52 lbs./cu. ft.) and 2% moisture.

After carbonization, semi-coke was removed from the sole-heated oven and reheated. This treatment heated the semi-coke to 1100°C in nitrogen gas to complete the annealing of the coke.

Cokes from the sole-heated oven were assessed for apparent specific gravity (ASG) and hot-strength properties, including CSR and CRI following the ASTM D5341 / D5341M-14 standard, and analyzed for proximate (moisture, ash, volatile matter, fixed carbon), sulphur and carbon forms/textures using an optical microscope.

The ASG of coke is defined as the ratio of the mass of a volume of dry coke to the mass of an equal volume of water. Coke ASG varies with the rank and ash content of the coal carbonized, the bulk density of the coal charge in the oven, the carbonization temperature and the coking time (Price and Gransden, 1987). In this project, the ASG values of cokes were determined following a method developed at CanmetENERGY and related to the ASTM D167-93(2004) and ISO 1014:1985 standards.

According to ASTM D5341 / D5341M-14, the CRI is the percent weight loss of the coke sample after reaction in CO_2 at 1100°C for 2 hours. The cooled, reacted coke was then

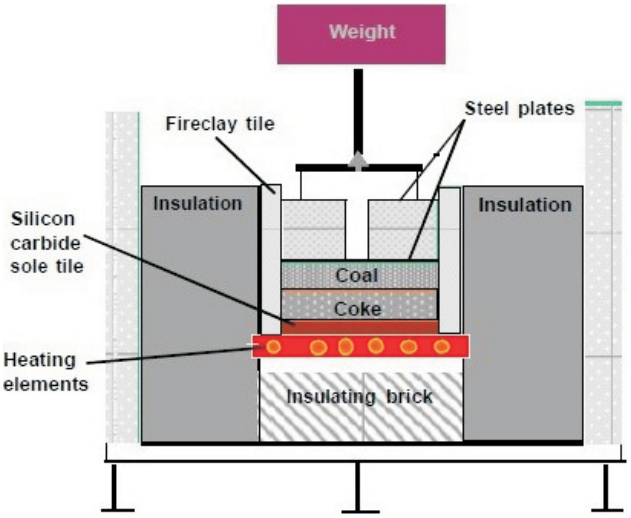

Figure 6. Schematic diagram of the CanmetENERGY sole-heated oven.

Figure 7. CanmetENERGY sole-heated oven (12 kg capacity) used in this study.

tumbled in an I-drum for 600 revolutions at 20 rpm. The cumulative percent of +9.5 mm coke after tumbling is denoted as the CSR.

Microscopic analysis of the textures was also performed on the sole-heated cokes to measure the carbon forms. This technique is extremely useful for understanding the behaviour of coal during coking and for interpreting pressure-generation and coke-quality results.

Carbon-form analysis in this project was carried out using a combination of the US Steel method (Gray and DeVanney, 1986) and the CanmetENERGY method, which is based on work carried out by H. Marsh in 1978-1981 and published in the book *Introduction to Carbon Science* (Edwards et al., 1989). A single point count is made for each measured field of view. For each field, the stage is rotated in order to determine the carbon form of highest possible rank. Normally, 500 point counts are performed on a sample. Each carbon form is derived from an assumed parent coal V-type. From the coke-texture analysis, one can determine the effective coal reflectance (%Ro).

Results

Coal and coke analytical results were analyzed to determine the following:

- Was the Roben Jig capable of producing a clean-coal composite similar to that of organic liquids for use in coal and coke evaluation?
- Did perchloroethylene have any impacts on coal rheology, coke strength and coke size?
- Was there misplaced material (higher ash particles contaminating lower ash/specific gravity slices) in the jig-produced sample, and at what specific gravity fraction did the misplaced material occur?
- Did the misplaced material affect coal and coke quality?

Roben Jig Versus Float-and-Sink Clean-Coal Quality

For all samples tested, the Roben Jig was successful in creating a clean-coal sample similar to that of the float-and-sink method but with better rheology.

Table 1 shows the comparison of some basic coal-quality parameters between the clean coals produced by the jig and the float-and-sink (FS) methods. Most of the clean-coal quality characteristics of the samples produced from both methods compared very closely. Values for ash, volatile matter, fixed carbon, sulphur, free swelling index, calorific value, fluorine, mercury and specific gravity, as well as most Hardgrove Grindability Index values, matched well, thus proving that the jig was useful in creating comparable clean-coal samples. One unexpected result was the increase in Hardgrove Grindability Index in the float-and-sink coal samples compared to the jig-washed sample. Potential causes for this result will be researched at a later date.

For all coal types, the dilatation and fluidity were lower in the float-and-sink–washed samples than in the jig-washed samples. This was expected and was due to the perchloroethylene suppressing the rheology of the coal. The jig was successful in providing a more accurate measurement of the dilatation and fluidity of these samples. Only small differences were seen in the caking index (G) and the Sapozhnikov X and Y indices.

Fluidity refers to coal's plasticity during carbonization, where it changes from a solid material to a fluid (plastic) state and then to a fused porous solid (coke) during cooling. High fluidity is beneficial in the coke-making process. Dilatation determines the swelling properties of coal when heated under standard conditions. The caking index (G) is determined through a laboratory test that measures the caking capacity of a sample of coal to ascertain how well it binds or fuses together. A higher G index indicates greater caking capacity. The Sapozhnikov Y index is a measure of the maximum thickness of the plastic mass when the coal is heated to the peak temperature and before it resolidifies. This measure is similar to the free swelling index and the level of Gieseler maximum fluidity.

As expected, chlorine levels were highly elevated in all float-and-sink coal samples due to residual perchloroethylene remaining on the coal surface and within pore spaces.

Coal petrography is a microscopic technique used to determine a coal's degree of coalification and amount and category of macerals. These macerals can be categorized as reactives or inerts. Reactive macerals are those that burn readily during combustion and those that become plastic during carbonization in the coke oven. Inert macerals are those that are not reactive. The mean max vitrinite reflectance and the amounts of vitrinite, semifusinite, total reactives and total inerts were very comparable between the samples prepared using the jig and the float-and-sink method.

When comparing the clean-coal quality characteristics, it is apparent that the Roben Jig was able to provide a representative clean-coal sample with more realistic values of chlorine, fluidity and dilatation than the float-and-sink–washed sample. It is also evident that exposure to perchloroethylene caused a decrease in fluidity and dilatation in all four coal samples.

Clean-Coal Carbonization

For coals A–D, the percentage of the coal that was <3.35 mm ranged between 77% for coal C and 88% for coal B (Table 2). This indicates that coal B and coal C are the finest and coarsest coals, respectively, of the four coals tested.

Table 1. Clean-coal quality parameters (air-dried basis) for coal types A, B, C and D.

Clean-coal quality parameter (air-dried basis)	Coal A		Coal B		Coal C		Coal D	
	FS	JIG	FS	JIG	FS	JIG	FS	JIG
Moisture (%)	0.99	0.97	2.15	0.56	0.50	0.26	1.05	0.90
Ash (%)	5.74	5.88	8.54	9.70	8.42	8.35	10.95	10.85
Volatile matter (%)	31.76	31.95	23.19	23.52	24.41	24.96	22.14	22.35
Fixed carbon (%)	61.51	61.20	66.12	66.22	66.67	66.43	65.86	65.90
Sulphur (%)	0.46	0.51	0.41	0.42	0.55	0.56	0.30	0.31
Free swelling index	8.5	8.5	7.75	7.5	8.5	8.5	3.5	4.5
Calorific value (cal/g)	7955	7971	7750	7763	7874	7864	7496	7487
Chlorine (ppm)	3906	271	21450	949	733	472	4600	962
Fluorine (ppm)	224	225	118	115	92	134	93	93
Mercury (ppb)	32	24	38	31	86	85	53	55
Hardgrove grindability index	87	82	147	118	81	80	79	78
Specific gravity (sg)	1.30	1.31	1.37	1.36	1.35	1.34	1.39	1.37
Max fluidity (ddpm)	1647	1972	57	257	405	488	2	4
Ruhr dilatation:								
% contraction	24	27	24	21	23	25	20	16
% dilatation	111	139	3	33	93	103	-	-
% total dilatation	135	166	27	54	116	128	-	-
% SD 2.5	120	154	2	29	86	96	-	-
Caking index (G)	96	98	78	82	93	92	35	46
Sapozhnikov Y index	17.0	17.5	14.5	15.0	18.5	18.0	6.5	7.0
Petrography:								
Vitrinite reflectance (mean max)	0.94	0.94	1.22	1.23	1.20	1.21	1.17	1.17
Maceral analysis:								
Vitrinite (%)	68.7	64	38	46.3	60.6	62.9	41.3	43.4
Semifusinite (%)	9.7	12	24.1	18	13.9	12.8	21.6	20.9
Total reactives (%)	84.4	82.8	62.9	65.1	75.3	76.1	63.5	65.1
Inerts:								
Semifusinite (%)	9.7	12	24.1	18	13.9	12.8	21.6	20.9
Total inerts (%)	15.6	17.2	37.1	34.9	24.7	23.9	36.5	34.9

Abbreviation: ddpm, dial divisions per minute

Table 2. Size distribution in the sole-heated oven charges, and reference contraction values obtained from the sole-heated oven coke tests, for coals A–D.

Description	Units	Coal A		Coal B		Coal C		Coal D	
		Float-sink	Jig	Float-sink	Jig	Float-sink	Jig	Float-sink	Jig
Index		26152	26153	26164	26165	26209	26210	26240	26241
Coal pulverization, sole-heated oven charge:									
Sieve analysis, cumulative									
6.30 mm	%	4.62	4.15	3.77	4.02	12.74	8.40	8.26	8.54
3.35 mm	%	19.41	17.93	10.77	12.26	25.24	20.90	22.90	20.24
1.70 mm	%	36.12	34.85	20.96	24.37	42.24	38.09	39.05	36.71
0.85 mm	%	52.39	52.87	32.45	39.02	58.72	56.65	53.20	54.07
0.50 mm	%	63.49	65.07	41.39	50.20	69.20	68.76	62.64	66.07
Passing 3.35 mm	%	80.59	82.07	89.23	87.74	74.76	79.10	77.10	79.76
Sole-heated oven:									
Test date		25-May-17	26-May-17	01-Jun-17	02-Jun-17	28-Jun-17	29-Jun-17	20-Jul-17	19-Jul-17
Expansion/contraction value (%)		-20.8	-20.5	-22.3	-17.9	-6.6	-9.4	-19.8	-17.2

Contraction levels ranged from –21 for coal A to approximately –8 for coal C. In actuality, coals A, B and D exhibited very similar contraction, in the range –18 to –21. The type of washing medium, namely float-and-sink and Roben Jig, did not influence the level of contraction for the individual coals as it remained essentially unchanged.

The low volatile-matter content remaining in the cokes, 0.65–1.08%, provides clear evidence that the coals were essentially fully carbonized by a combination of coking in the sole-heated oven and heat-treatment of the resulting semi-coke to 1100°C under N_2 to complete the annealing of the coke. Figure 8 shows coke made by carbonizing coal C, washed via float-and-sink, in the sole-heated oven and after annealing to 1100°C. The coke reveals a number of cracks/fissures, which develop as the result of contraction due to loss of volatile matter as the semi-coke is heated above resolidification (Jenkins et al., 2010). In a sole-heated oven, fissures propagate from the bottom of the oven toward the top as coking progresses.

Figure 8. Coke made by carbonizing coal C, cleaned using the float-and-sink method, in the sole-heated oven.

The apparent specific gravity (ASG) of coke ranged between 1.01 (coals A and C) and 1.15 (coal D). As stated earlier, the rank and ash content of the carbonized coal dictates the coke ASG. The low ash content in coal A (5.8%) generates the coke with the lowest ASG coke, whereas the high ash content in coal D (10.9%) leads to the coke with the highest ASG.

As shown in Figure 9, the CSR values for coals A, C and D washed using the traditional float-and-sink method were

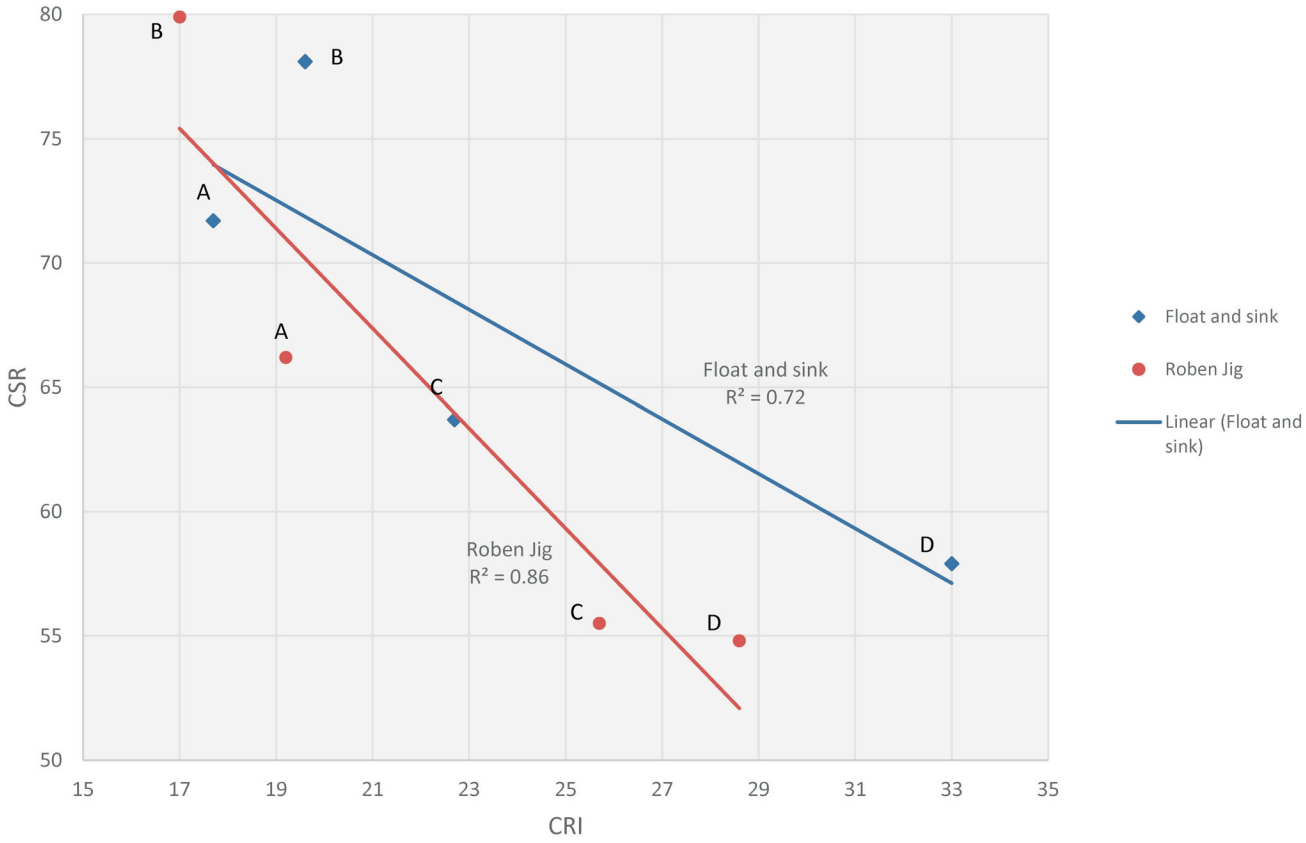

Figure 9. Plots of coke strength after reaction (CSR) versus coke reactivity index (CRI) for coals A–D.

higher than the values for these same coals washed using the water-based Roben Jig. Coal B, on the other hand, has a slightly higher CSR value when washed using the Roben Jig, compared to float-and-sink method. The CSR values for the four coals examined are in the order B > A > C > D. The high CSR and low CRI results for coal B appear to be dictated by its low ash basicity index of 0.049.

The most common classification of coal is based on rank, which refers to the degree of coalification that has occurred. The rank of a coal is determined primarily by the depth of burial and temperature to which the coal was subjected over time. Examination of carbon forms in coke, after a coal is transformed into a coke, provide a true measure of the degree of coalification, or rank, of the coal, which is its effective coking rank (Roeff). Results for coke textures/carbon forms (C forms) are given in Table 3. A close examination of the data indicates that the washing medium does not influence the development of textures during coal to coke transformation for coals A–D. In fact, the fractions of reactive and inert textures in the cokes are found to be similar for coals washed by the traditional float-and-sink method with organic liquids and by the Roben Jig using water. This is also supported by the fact that the 'effective' coking rank (Roeff) for the individual coals washed in the two media are very similar, except perhaps for coal C, which shows slightly stronger C forms and an Roeff value of 1.37 for jig washing compared to 1.32 for float-and-sink washing. It is quite revealing and interesting to note that the effective coking ranks of coals A–D, based on carbon forms measured in the cokes, are appreciably higher than the ranks determined from coal petrography (Ro). These Roeff and Ro values are 1.14 versus 0.94 for coal A, 1.42 versus 1.20 for coal B, 1.32 versus 1.21 for coal C, and 1.27

Table 3. Coke analytical data for cokes produced from coals A–D, including chemistry (proximate and sulphur), coke strength after reaction (CSR) and coke reactivity index (CRI), and coke textures/carbon forms.

Description	Unit	Coal A		Coal B		Coal C		Coal D	
		Float-sink	Jig	Float-sink	Jig	Float-sink	Jig	Float-sink	Jig
Index		26152	26153	26164	26165	26209	26210	26240	26241
Coke analyses:									
Proximate analysis (db)									
Ash	%	7.88	8.10	10.89	10.90	10.55	10.40	13.81	13.55
Volatile matter	%	0.71	1.08	0.70	0.86	0.65	0.69	1.07	0.81
Fixed carbon	%	91.41	90.82	88.40	88.24	88.80	88.90	85.12	85.64
Sulphur	%	0.38	0.41	0.30	0.31	0.46	0.45	0.24	0.26
Coke properties:									
Apparent specific gravity		1.051	1.009	1.085	1.096	1.018	1.005	1.157	1.145
Coke Strength after reaction (CSR)		71.7	66.2	78.1	79.9	63.7	55.5	57.9	54.8
Coke reactivity index (CRI)		17.7	19.2	19.6	17.0	22.7	25.7	33.0	28.6
Coke textural analysis:									
Reactive textures									
Isotropic	%	0.8	1.4	1.6	0.7	1.3	1.2	1.9	1.4
Very fine mosaic	%	1.2	2.4	0.0	0.0	0.6	0.2	0.5	1.3
Fine mosaic	%	13.3	12.2	0.0	0.3	1.0	0.8	1.3	1.4
Medium mosaic	%	58.8	57.7	2.5	3.1	23.4	13.1	20.5	21.7
Coarse mosaic	%	2.8	1.3	2.6	3.1	8.2	4.1	10.0	6.0
Elongated fine flow	%	6.9	12.8	6.6	4.5	29.3	24.7	8.4	7.2
Elongated medium flow	%	0.4	0.4	50.3	52.1	14.9	30.0	8.0	13.3
Elongated coarse flow	%	0.0	0.0	5.1	3.5	0.7	1.9	2.2	2.6
Domain flat flow	%	0.0	0.0	0.2	0.0	0.1	0.3	0.3	0.6
Domain undulating	%	0.0	0.0	0.8	0.3	0.9	0.1	0.7	1.2
Domain ribbon	%	0.0	0.0	0.0	0.0	0.3	0.0	0.5	0.0
Inert textures									
Fusinite	%	0.2	0.5	1.7	0.8	1.1	1.2	1.3	1.9
Semifusinite	%	15.4	11.1	26.7	31.2	17.5	21.3	43.4	39.8
Unidentifed inerts	%	0.2	0.1	1.9	0.4	0.5	0.9	0.9	1.0
Altered vitrinite	%	0.0	0.0	0.0	0.0	0.2	0.1	0.1	0.6
Total mosaic	%	76.9	75.0	6.7	7.2	34.5	19.4	34.2	31.8
Total flows	%	7.3	13.2	62.0	60.1	44.9	56.6	18.6	23.1
Total domains	%	0.0	0.0	1.0	0.3	1.3	0.4	1.5	1.8
Total coke inerts	%	15.8	11.7	30.3	32.4	19.3	23.5	45.7	43.3
Coke mosaic size index		2.11	2.14	3.07	3.01	2.72	2.85	2.66	2.65
Estimated Ro of coal	%	1.13	1.14	1.42	1.42	1.32	1.37	1.27	1.27

versus 1.17 for coal D. This finding indicates that coals A–D actually produce stronger C forms than would be expected based on coal petrography v-type measurements.

The coke mosaic size index (CMSI) values for the coals washed in the two media are also very similar. CMSI is a mathematical method to summarize the carbon-form analysis (Coin, 1982). The higher the CMSI, the higher the rank based on carbon forms measured. In the present study, the CMSI values of the four coals are in the order B > C > D > A.

The CSR values of three of the four coals washed in the two types of media revealed that the float-and-sink method gives a slightly better result than the water-based jig method. It was also found that the washing medium (organic versus inorganic) does not influence the development of textures during the coal to coke transformation for the four coals. Also, coking rank based on carbon forms measured in the cokes is appreciably higher for each coal than rank determined from coal petrography, indicating that these coals produce stronger C forms than expected based on coal petrography v-type measurements.

Washability

Coal A

Figure 10 provides clean-coal curves produced from the float-and-sink procedure and the jig procedure for coal A. Figures 11 and 12 provide correlations between density of separation and cumulative ash, and density of separation and cumulative yield, respectively, for clean coal from tests using the two procedures.

The Jig was able to produce a low-ash clean-coal sample (below 5% ash) but at a much lower yield than the float-and-sink method. While it was easy to obtain a coal concentrate at 2% ash with a 47% yield using the float-and-sink procedure, the jig was only able to provide a concentrate with double the ash content (3.87% ash) at a 37% yield. The Roben Jig always provided products with higher ash content compared to a similar density of separation for the float-and-sink method. The greatest disparities were observed in clean-coal products below 10% ash (Figure 10). This coal seems to be somewhat easy to wash.

Coal B

It was difficult to obtain lower than 10% ash product using the jig procedure since the ash did not vary much within the first five relative density slices (Figures 13 and 14). When comparing the densities of the floats, the Jig clean coal resulted in higher ash values compared to the same density floats in the float-and-sink procedure (Figure 14 and 15). This coal seemed to be easy to wash (by float-and-sink); however, compared to coal A, it provided lower yields at 5% and 10% ash.

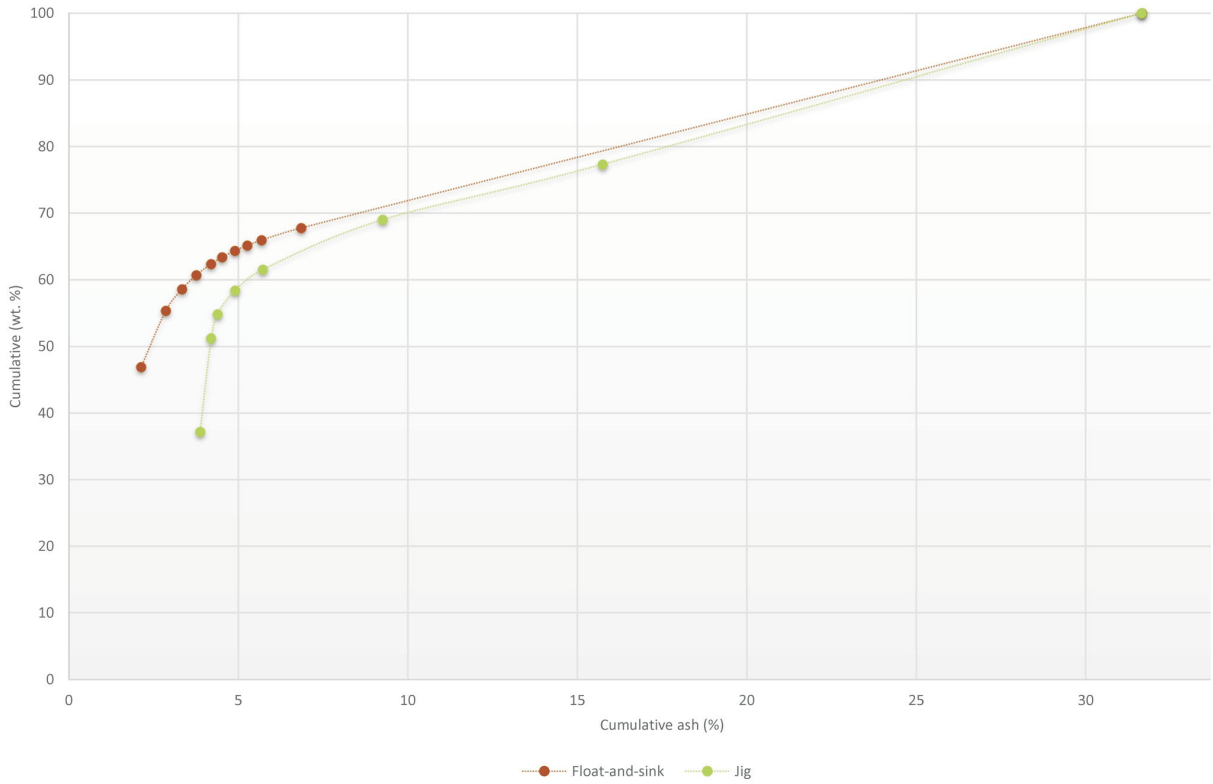

Figure 10. Clean-coal curve for coal A washed by the float-and-sink and jig procedures.

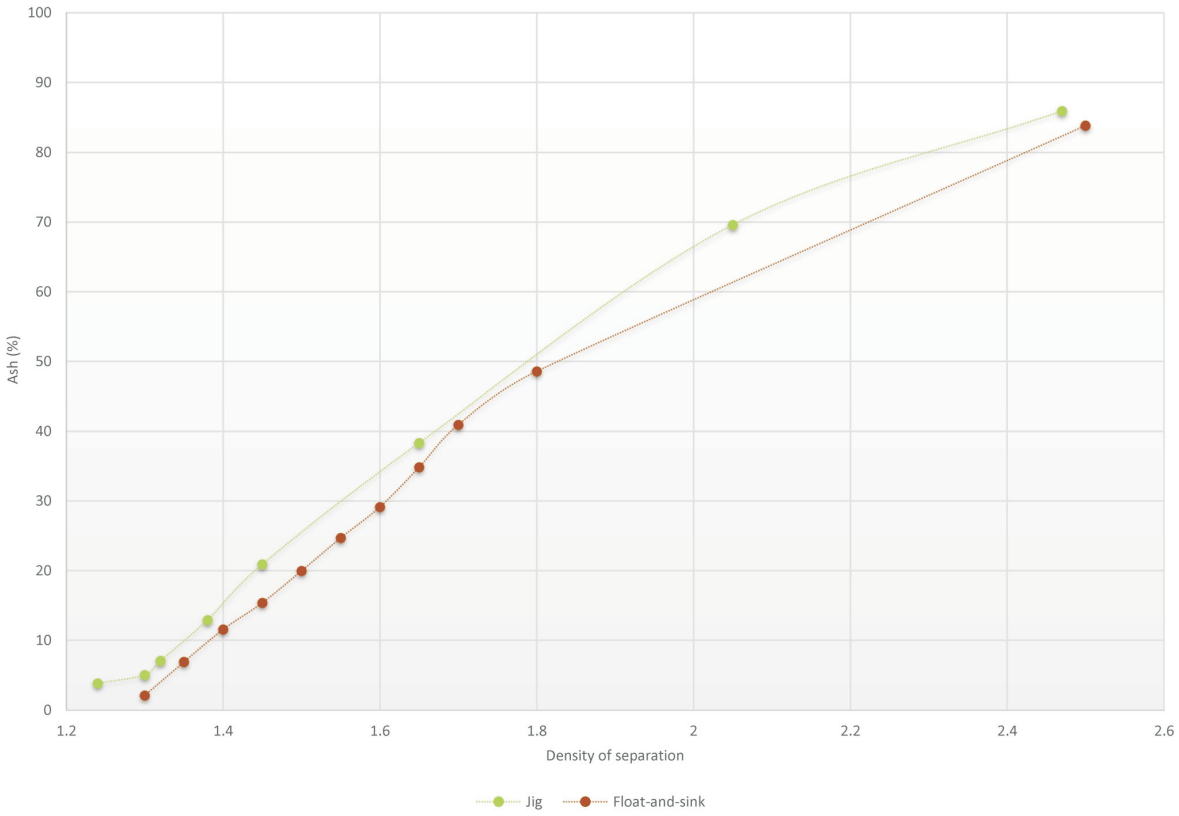

Figure 11. Density of separation (specific gravity and apparent relative density) versus ash in density fractions for coal A washed by the float-and-sink and jig procedures.

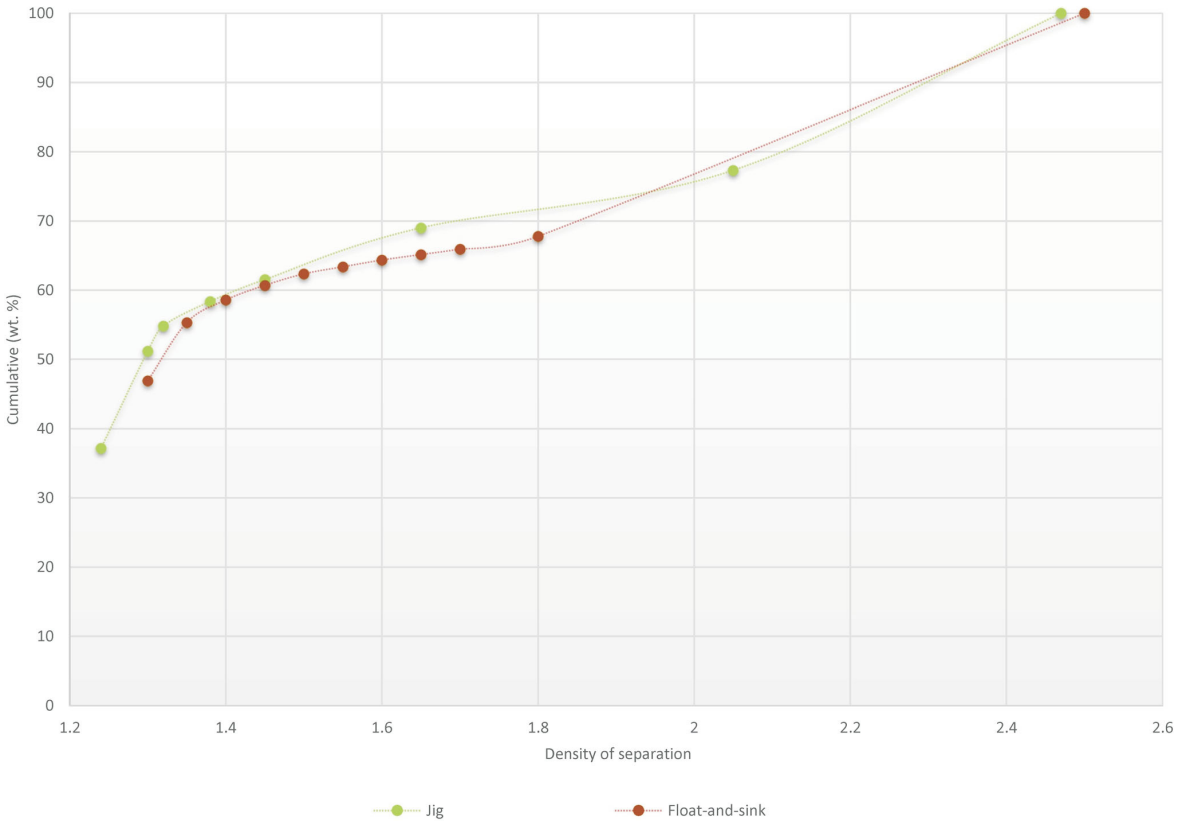

Figure 12. Density of separation versus cumulative yield of clean coal washed by the float-and-sink and jig procedures.

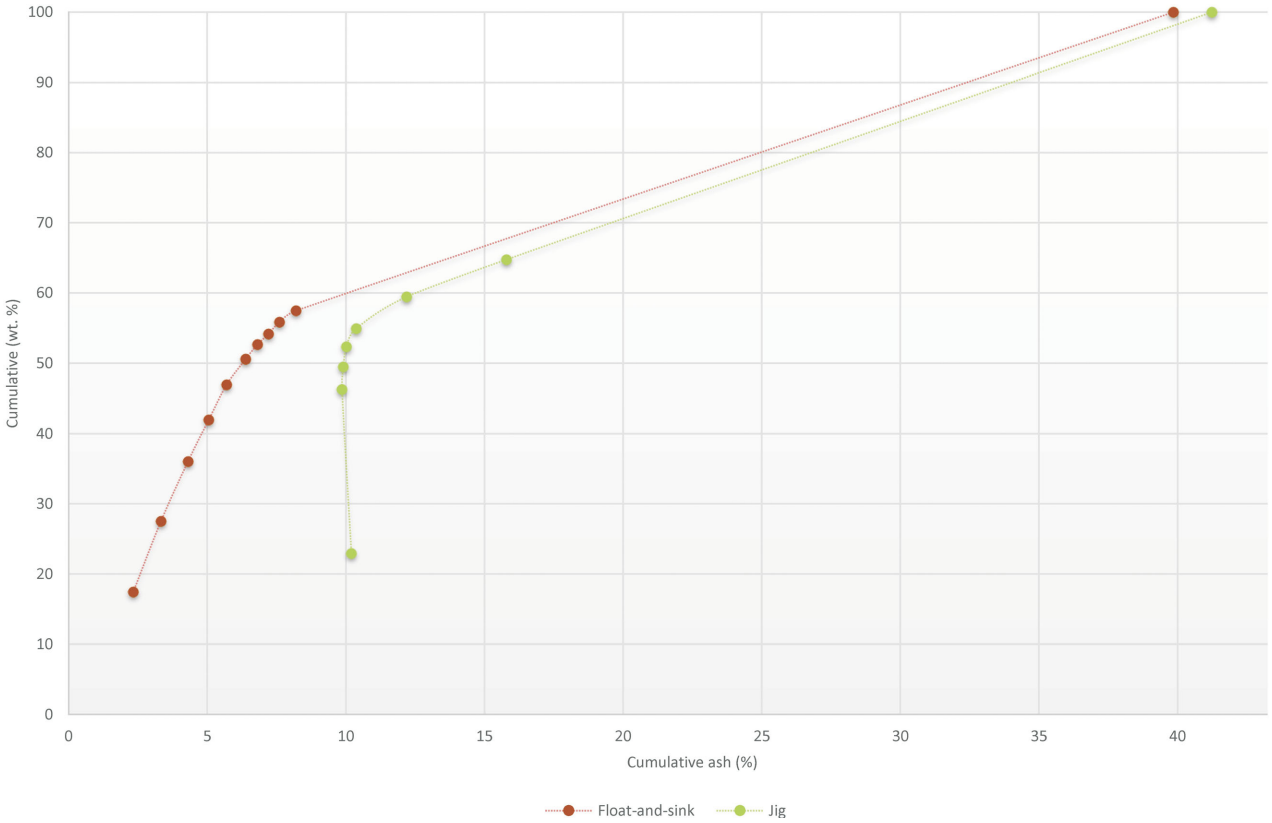

Figure 13. Clean-coal curve for coal B washed by the float-and-sink and jig procedures.

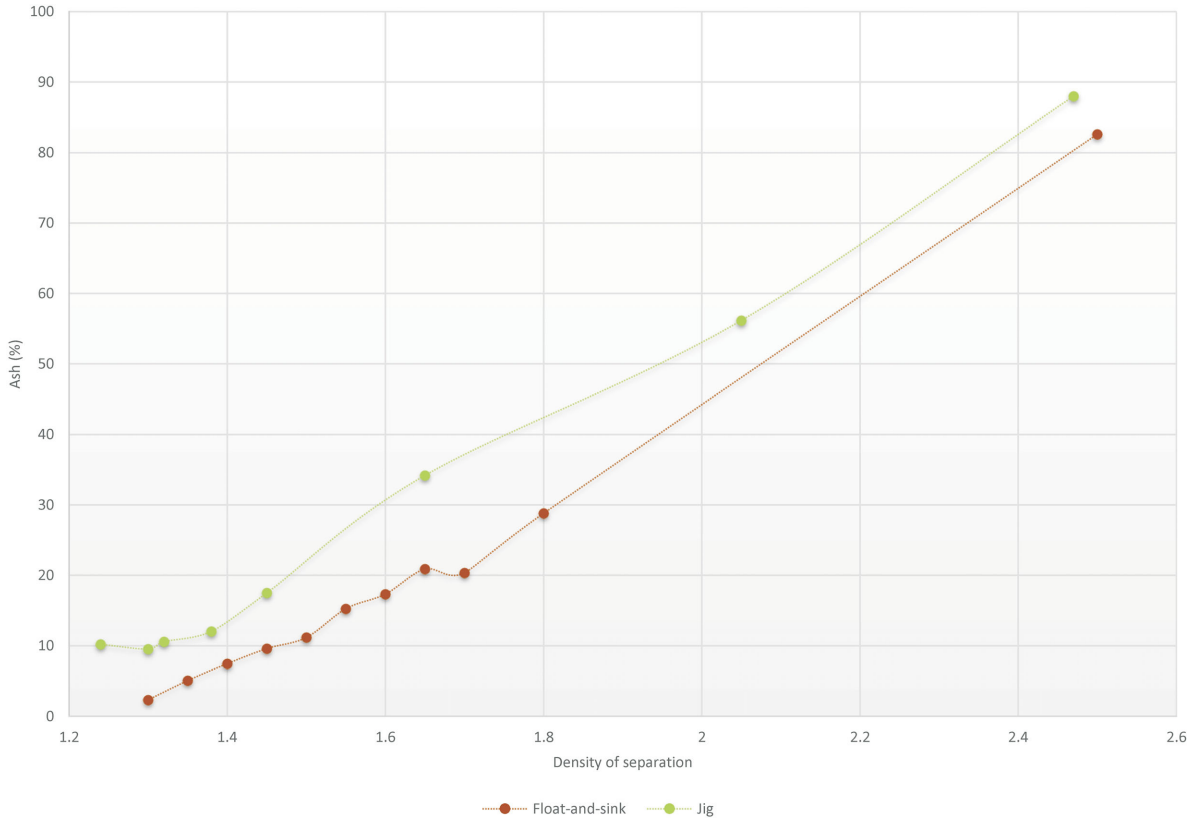

Figure 14. Density of separation (specific gravity and apparent relative density) versus ash in density fractions for coal B washed by the float-and-sink and jig procedures.

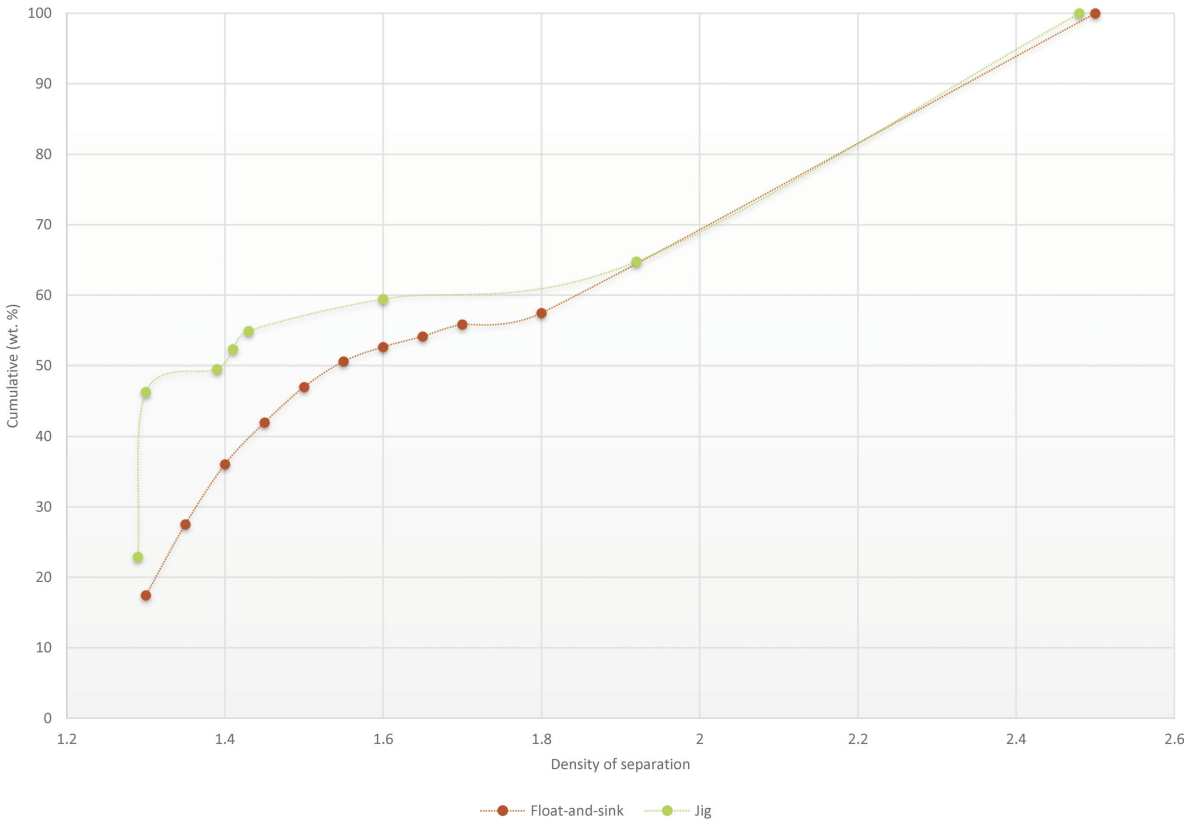

Figure 15. Density of separation versus cumulative yield of clean coal washed by the float-and-sink and jig procedures.

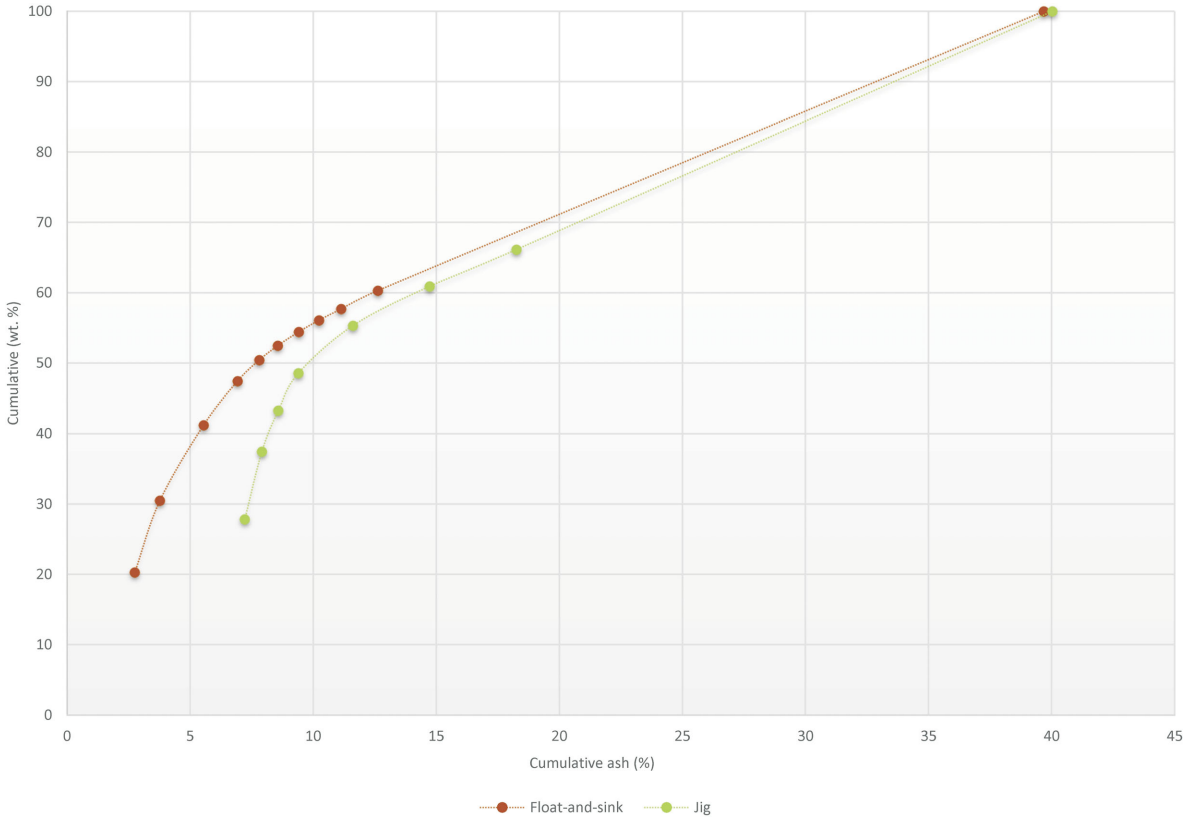

Figure 16. Clean-coal curve for coal C washed by the float-and-sink and jig procedures.

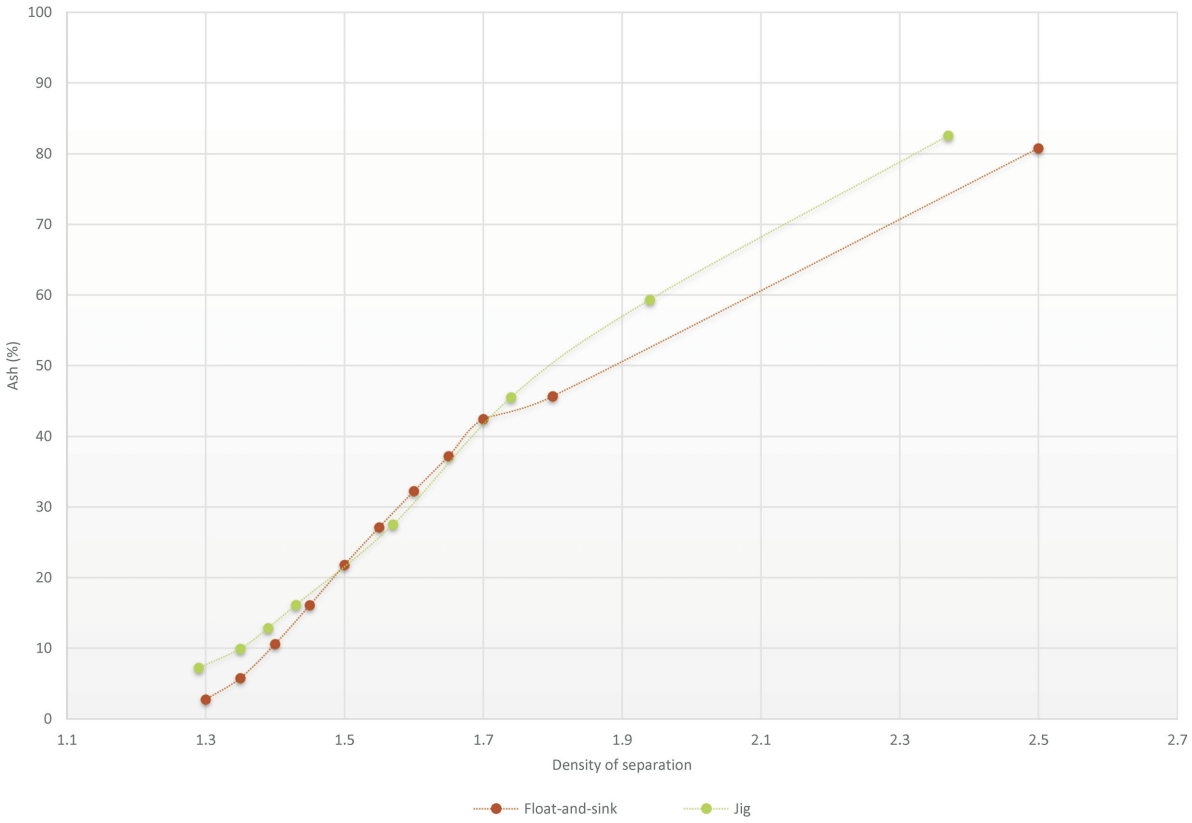

Figure 17. Density of separation (specific gravity and apparent relative density) versus ash in density fractions for coal C washed by the float-and-sink and jig procedures.

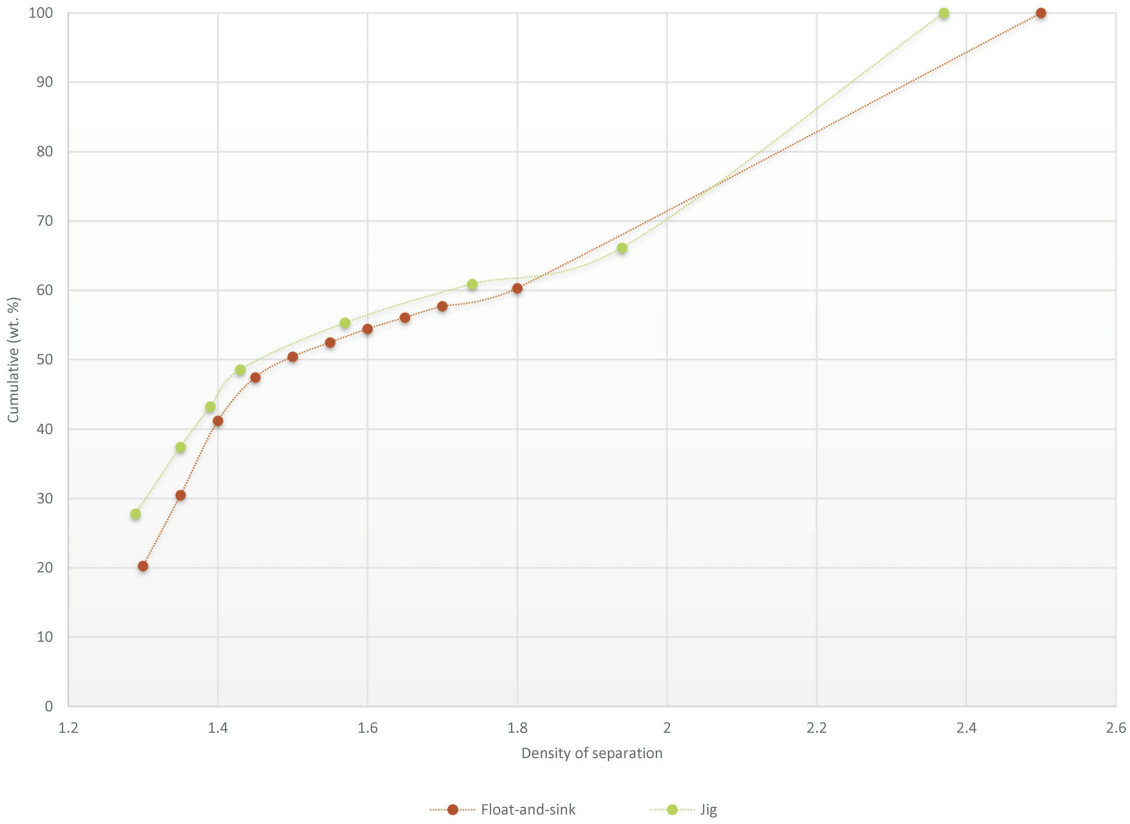

Figure 18. Density of separation versus cumulative yield of clean coal washed by the float-and-sink and jig procedures.

Coal C

Clean-coal curves produced from the float-and-sink and jig procedures for coal C are compared in Figure 16. Figures 17 and 18 provide correlations between density of separation and cumulative ash, and density of separation and cumulative yield, respectively, of clean coal from tests using the two procedures.

Using jig procedure, it was not possible to obtain lower than 5% ash content at the same yield of clean-coal product as from the float-and-sink procedure. However, like coals A and B, yield of product with 10% ash was comparable to that obtained from the float-and-sink procedure. Yield of clean coal was higher with higher ash at every density cut. This coal was more difficult to wash than coals A and B, based on the washability assessment and the much lower yields at 5% and 10% ash content.

Coal D

Clean-coal curves produced from the float-and-sink and jig procedures for coal D are compared in Figure 19. Figures 20 and 21 provide correlations between density of separation and cumulative ash, and density of separation and cumulative yield, respectively, of clean coal from tests using the two procedures.

Coal D exhibited the greatest differences between coal products produced from the jig procedure and the float-and-sink procedure, even at higher than 10% ash products. It seems that it was not possible to obtain coal with lower than 8.87% ash. This sample seems to be difficult to wash, since even the float-and-sink procedure failed to produce a high yield of low-ash coal.

Each of the coal samples tested exhibited different washability characteristics when assessed using the standard float-and-sink procedure. Coal A was the easiest to wash, followed by coals B and C, and coal D was the most difficult to wash. The float-and-sink procedure reflects ideal conditions for gravity separation, and coal D could be deemed the most difficult to wash by gravity methods.

The Roben Jig was used in this study to produce a clean-coal concentrate comparable in quality to that produced by the float-and-sink procedure. In general, it was possible to obtain similar yields of clean-coal product with 10% ash from coals A, B and C using both procedures. However, it was not easy to obtain lower ash products (i.e., less than 5% ash) with the jig procedure either at all or at a yield comparable to that of the float-and-sink procedure. Coal D was deemed to be difficult to wash by the float-and-sink procedure and showed the greatest variability in the results obtained from the two washing procedures.

Since the jig procedure segregates particles by size and density, the stratification of feed containing coal particles

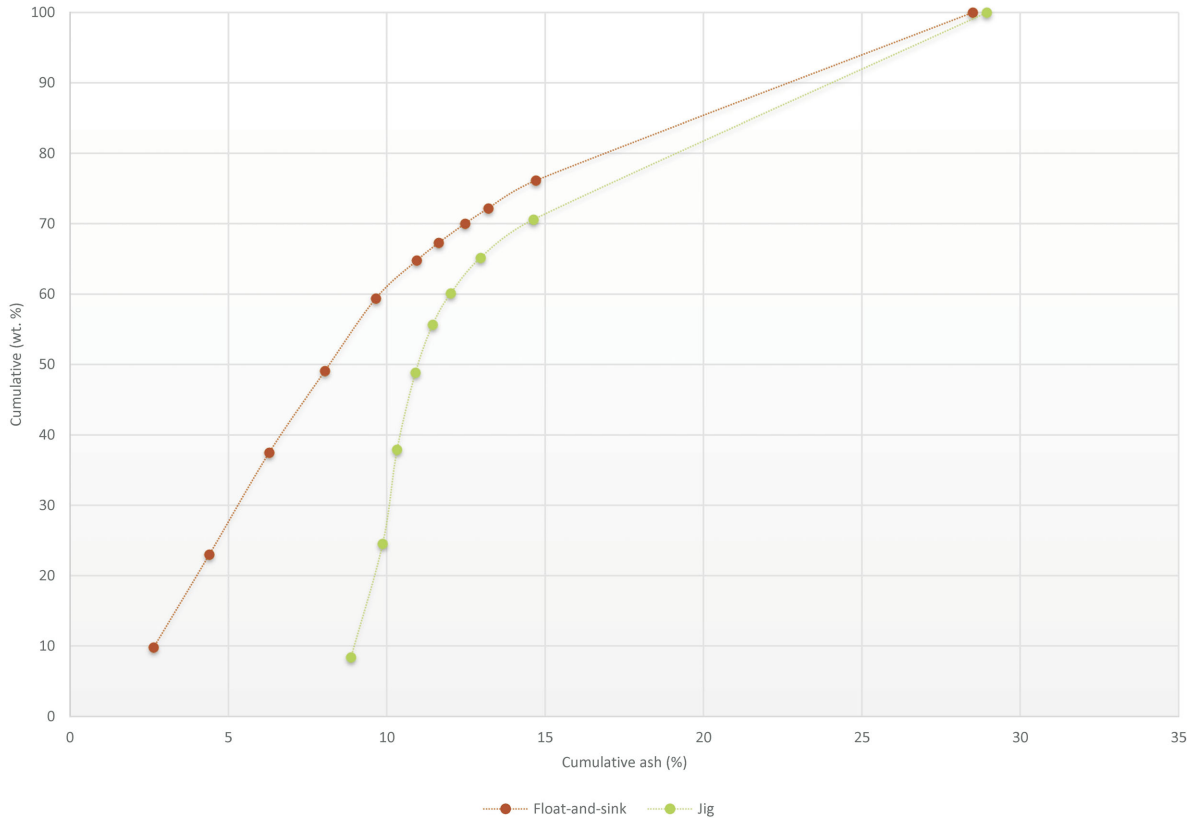

Figure 19. Clean-coal curve for coal D washed by the float-and-sink and jig procedures.

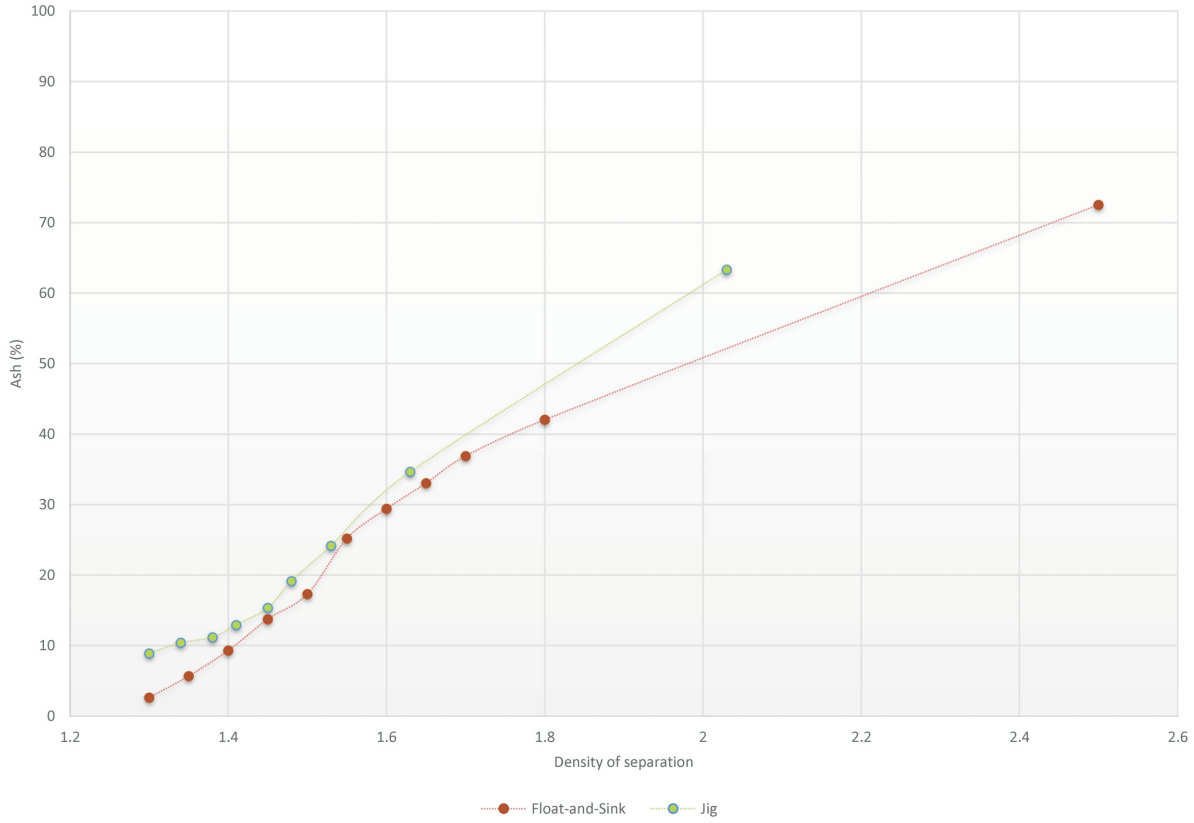

Figure 20. Density of separation (specific gravity and apparent relative density) versus ash in density fractions for coal D washed by the float-and-sink and jig procedures.

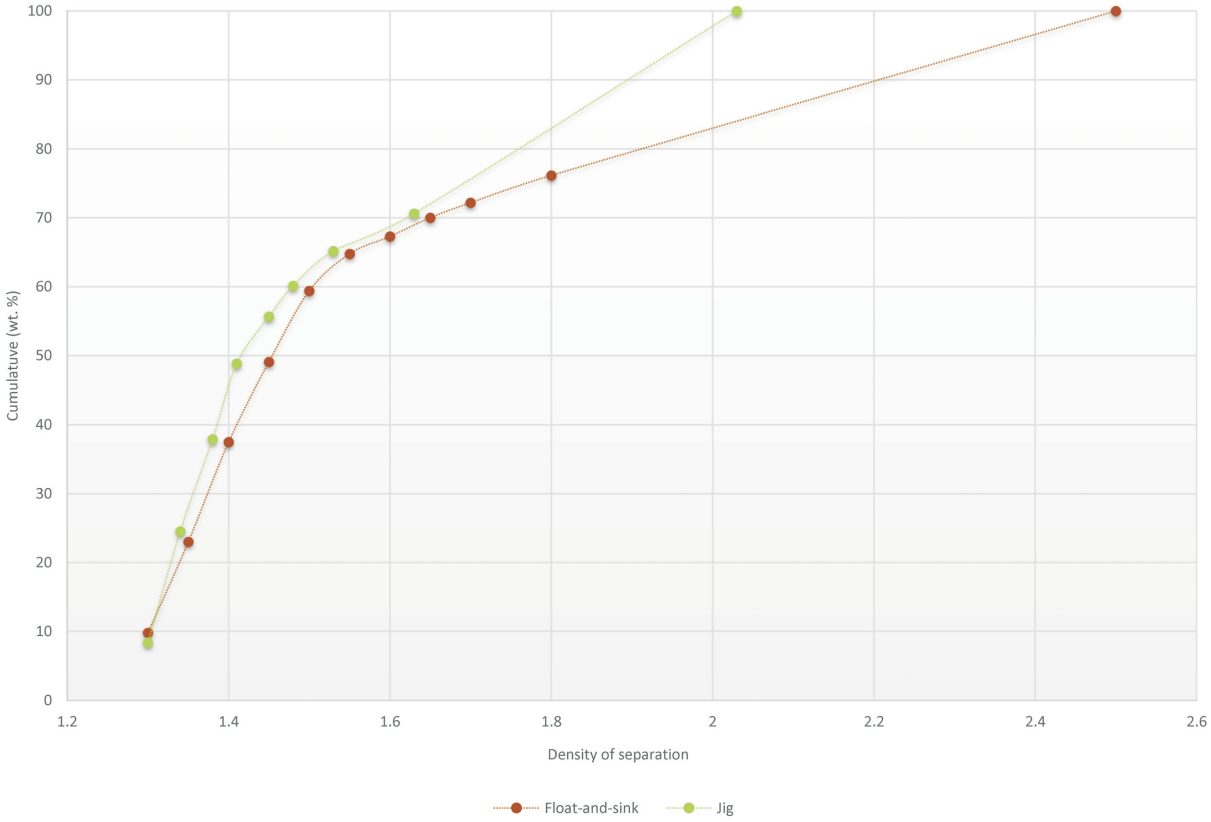

Figure 21. Density of separation versus cumulative yield of clean coal washed by the float-and-sink and jig procedures.

of intermediate density (middling matter) would pose the greatest challenge for the preparation of a clean-coal sample of similar quality by this method. Also, liberated mineral matter could be entrained within the layers of segregated clean coal and increase the ash and yield within each density cut. Even though coals A, B and C had similar washability patterns as determined by the float-and-sink procedure, they showed different trends when washed on the jig, which could indicate that such mineral-matter characteristics as liberation, clay content and content of fine coal could contribute to these outcomes. This aspect needs to be researched further to delineate the effects of possible clay entrainment and/or misplacement of middling matter during the jigging process.

Conclusion

The Canadian coal industry needs a reliable method of washing small-scale metallurgical coal samples where the exposure of both the coal sample and the laboratory technicians to perchloroethylene and other toxic organic liquids can be eliminated. This study evaluated the use of the Roben Jig in satisfying these requirements.

When comparing the clean-coal quality characteristics, it is apparent that the water-based Roben Jig was able to produce a clean-coal sample that had more realistic values of chlorine, fluidity and dilatation than the sample produced by the float-and-sink procedure. It is also evident that the exposure of the coal to perchloroethylene (in the float-and-sink process) caused a decrease in fluidity and dilatation in all four coal samples.

Coke resulting from three of the four coals was evaluated for coke strength after reaction (CSR), which revealed that the float-and-sink clean coal gave a slightly better result than the water-based jig method. It was also found that the washing medium (perchloroethylene or water) did not influence the development of textures during the coal to coke transformation for coals A–D. Also, the coking ranks, based on carbon forms measured in the cokes from all four coals, are appreciably higher than those determined from coal petrography, indicating that these coals produce stronger carbon forms than would be expected based on coal petrography v-type measurements.

Because of the jigging action and subsequent known movement of particles, there was a possibility that coal particles would be misplaced (i.e., fall within a layer of differing specific gravity). Previous work, using 'easy to wash' coal, showed that the Roben Jig worked well to produce representative clean coal samples. Even though coals A, B and C had similar washability patterns from the float-and-sink procedure, they showed different trends when washed in the Roben Jig, which could indicate that such mineral-matter characteristics as liberation, clay content and content of fine coal could contribute to these outcomes. Since the clean-coal quality characteristics were very similar for the samples produced by the two washing methods, it is possible that, if there is misplaced material, it is not significantly affecting the coal quality. This phase of research involving the Roben Jig is nearing its conclusion and will be wrapped up by November 2017. More test work needs to be done on identifying and characterizing any misplaced material that may occur, as well as 'fine tuning' the methodology of the jig procedure.

Acknowledgments

The project members thank the peer reviewer, M. Allen of Norwest Corporation. They also thank Geoscience BC, the Canadian Carbonization Research Association, Teck Resources Ltd. and GWIL Industries–Birtley Coal & Minerals Testing Division for their financial and in-kind contributions that made this project possible.

References

BC Geological Survey (1992). British Columbia coal quality catalog; BC Ministry of Energy, Mines and Petroleum Resources, BC Geological Survey, Information Circular 1992-20, 52 p., URL <http://www.empr.gov.bc.ca/Mining/Geoscience/PublicationsCatalogue/InformationCirculars/Documents/IC1992-20_Coal.pdf> [November 2017].

Campbell, M. (2010): Options for sink/float analysis – economic and technical review; *in* Proceedings of 37th Symposium on the Geology of the Sydney Basin, Pokolbin, Australia, May 2010.

Coin, C.D.A. (1982): Microtextural assessment of metallurgical coke; BHP Central Research Laboratory, unpublished report CRL/TC/41.

DuBroff, W., Kaegi, D.D., Knoerzer, J.J. and Spearin, E.Y. (1985): Solvent pretreatment of coal to improve coke strength; United States Patent and Trademark Office, patent number 4528069, URL <http://patft.uspto.gov/netacgi/nph-Parser?Sect1=PTO2&Sect2=HITOFF&p=1&u=%2Fnetahtml%2FPTO%2Fsearch-bool.html&r=3&f=G&l=50&co1=AND&d=PTXT&s1=4528069&OS=4528069&RS=4528069> [November 2017].

Edwards, A.S., Marsh, H. and Menendez, R. (1989): Introduction to Carbon Science; Butterworth & Co. (Publishers) Ltd., 348 p., URL <http://www.sciencedirect.com/science/book/9780408038379> [November 2017].

Gray, R.J. and DeVanney, K.F. (1986): Coke carbon forms: microscopic classification and industrial applications; International Journal of Coal Geology, v. 6, p. 277–297.

Holuszko, M.E., Leeder, R., Mackay, M., Giroux, L., MacPhee, J.A., Ng, K.W. and Dexter, H. (2017): Effects of organic liquids on coking properties of a higher-inert western Canadian coal; Fuel Processing Technology, v. 155, p. 225–231.

Iveson, S. and Galvin, K.P. (2010): Influence of organic liquids on coal carbonisation properties; Australian Coal Association Research Program (ACARP), Brisbane, Australia, Project C17051.

Iveson, S. and Galvin, K.P. (2012): The effect of perchloroethylene on coking properties; Fuel, v. 95, p. 504–513.

Jenkins, D.R., Mahoney, M.R. and Keating, J.C. (2010): Fissure formation in coke. 1: The mechanism of fissuring; Fuel, v. 89, no. 7, p. 1654–1662.

MacPhee, J.A., Giroux, L., Ng, K.W., Todoschuk, T., Conejeros, M. and Kolijn, C. (2013): Small-scale determination of metallurgical coke; Fuel, v. 114, p. 229–234. doi:10.1016/j.fuel.2012.08.036

Price, J.T. and Gransden, J.F. (1987): Metallurgical coals in Canada: resources, research, and utilization; Energy, Mines and Resources Canada, CANMET Report 87-2E.

ASTM and ISO Standard Methods

ASTM D167-93(2004): Standard test method for apparent and true specific gravity and porosity of lump coke; ASTM International, West Conshohocken, PA, 2004, URL <http://www.astm.org/cgi-bin/resolver.cgi?D167-93(2004)> [November 2017].

ASTM D2014-97(2010): Standard test method for expansion or contraction of coal by the sole-heated oven; ASTM International, West Conshohocken, PA, 2010, URL <http://www.astm.org/cgi-bin/resolver.cgi?D2014-97(2010)> [November 2017].

ASTM D4371-06(2012): Standard test method for determining the washability characteristics of coal; ASTM International, West Conshohocken, PA, 2012, URL <http://www.astm.org/cgi-bin/resolver.cgi?D4371-06(2012)> [November 2017].

ASTM D5114-90(2010): Standard test method for laboratory froth flotation of coal in a mechanical cell; ASTM International, West Conshohocken, PA, 2010, URL <http://www.astm.org/cgi-bin/resolver.cgi?D5114-90(2010)> [November 2017].

ASTM D5341 / D5341M-14: Standard test method for measuring coke reactivity index (CRI) and coke strength after reaction (CSR); ASTM International, West Conshohocken, PA, 2014, URL <http://www.astm.org/cgi-bin/resolver.cgi?D5341D5341M-14> [November 2017].

ISO 1014:1985: Coke – determination of true relative density, apparent relative density and porosity; International Organization for Standardization, Geneva, Switzerland, URL <https://www.iso.org/standard/5483.html> [November 2017].

Occurrence of Rare-Earth Elements in Selected British Columbian Coal Deposits and their Derivative Products

V. Kumar, The University of British Columbia, Vancouver, BC, vinothkumar@alumni.ubc.ca

A. Kumar, The University of British Columbia, Vancouver, BC

M.E. Holuszko, The University of British Columbia, Vancouver, BC

Kumar, V., Kumar, A. and Holuszko, M.E. (2018): Occurrence of rare-earth elements in selected British Columbian coal deposits and their derivative products; *in* Geoscience BC Summary of Activities 2017: Minerals and Mining, Geoscience BC, Report 2018-1, p. 87–100.

Introduction

Coal, an organic sedimentary rock, is reported to contain 86 elements, including 74 trace elements identified using modern analytical techniques (Tang and Huang, 2002). The presence of trace elements in coal is attributed to prevailing conditions in the coal swamp as well as geological activities and atmospheric inputs that would have occurred from time to time during coal deposit formation (Swaine, 1990). Some of the genetic controls that are responsible for the enrichment of trace elements include the source rock, the environment, and the presence of hydrothermal fluid, groundwater and volcanic ash (Dai et al., 2012). Coal with enriched concentrations of valuable trace elements is referred to as metalliferous or mineralized coal (Seredin and Finkleman, 2008). Even though there is no commercial process, metals such as Al, Au, Pt-group metals, V and Zn have been recovered from coal and its byproducts (Bratskaya et al., 2009; Sahoo et al., 2016). Enriched concentrations of rare-earth elements (REE) in coal were first documented in Russian Far East deposits during the early 1990s (Seredin, 1996) and enriched concentrations of REE in coal deposits have been discovered around the world (Birk and White, 1991; Hower et al., 1999; Seredin, 2004; Dai et al., 2007, 2008).

With the emergence of new clean-energy and defense-related technologies, the consumption of REE has increased rapidly (Tse, 2011). For example, it is projected that the demand for Dy will increase by as much as 2600% by 2025 (Chakhmouradian, 2014). In addition, traditional rare-earth ore deposits are depleting quickly and are projected to meet the demand for only the next 15–20 years (Seredin and Dai, 2012). Based on supply and demand, REE are classified as 'critical elements' by the United States and the European Union due to their importance in clean energy and defense applications (United States Department of Energy, 2010; European Commission, 2017). The United States National Energy Technology Laboratory (NETL) has identified coal deposits as a potential source of REE and has conducted a prospective analysis of coal deposits using the United States Geological Survey coal database, which contains data on the concentration of REE across the United States coalfields. Furthermore, the United States Department of Energy has provided US$10 million in funding to research projects that demonstrate the techno-economic feasibility of domestic REE separation technologies from coal and/or its byproducts containing a minimum of 300 ppm total REE and concentrating the REE to a level greater than or equal to 2% (by weight) in processed streams (National Energy Technology Limited, 2016).

Even though the literature indicates the presence of REE in some Canadian coal deposits, especially in British Columbia (BC) coalfields, there has been no effort to properly quantify and characterize these deposits and no analysis of extraction techniques (Birk and White, 1991; Goodarzi et al., 2009). The purpose of this ongoing research is to characterize and quantify the REE and their mode of occurrence in BC coal deposits and coal processing products, and to study the possible extraction of these elements. This paper shows the preliminary results from studies conducted on coal samples originating from coal deposits in southeastern BC.

Background

According to the International Union of Pure and Applied Chemistry (IUPAC), REE are a group of 17 elements in the periodic table, including 15 lanthanides and 2 chemically similar transition metals: Sc and Y. Based on supply and demand, these elements are classified into three categories (Seredin and Dai, 2012):

- critical: Nd, Eu, Tb, Dy, Y and Er
- uncritical: La, Sm, Pr and Gd
- excessive: Ce, Ho, Tm, Yb and Lu

Using the atomic number, REE are classified as heavy REE (HREE) and light REE (LREE), with elements from Tb to Lu and Y belonging to the former group and La to Gd and Sc belonging to the latter group (Dai et al., 2008; Moldoveanu et al., 2013; Zhang et al., 2015).

This publication is also available, free of charge, as colour digital files in Adobe Acrobat® PDF format from the Geoscience BC website: http://www.geosciencebc.com/s/SummaryofActivities.asp.

More than 200 minerals have been identified as containing REE, but the traditional commercial sources of rare-earth elements are (O'Driscoll, 1991)

- bastnaesite, a fluorocarbonate mineral;
- monazite, a LREE phosphate;
- xenotime, a Y-rich phosphate;
- apatite, a Ca fluorophosphate and
- ion-adsorbed clays, an aluminosilicate mineral.

The grade for REE is defined by the content of their oxides (such as lanthanum oxide, La_2O_3) in the deposit. The cut-off grade for a traditional rare-earth resource is approximately 1.5 to 2.0% rare-earth oxide (REO) except for ion-adsorbed clays, for which it is approximately 0.06 to 0.15% REO (Zhang et al., 2015). As noted earlier, the traditional commercial sources are fast depleting and with the increasing demand of REE, the discovery of coal deposits with enriched concentrations of REE have gained special attention in recent years.

Abundance of REE in Coal

Table 1 lists the average concentration of REE in coal from different countries such as the United States, China, the Democratic People's Republic of Korea and Turkey in comparison with average values for the upper continental crust, black shale and world coal on a whole coal basis. The average REE concentration in world coal on a whole coal basis is 68 ppm (Ketris et al., 2009), which is 2.6 times lower than REE in the upper continental crust (179 ppm; Taylor and McClennan, 1985), and the average black shale values are 182 ppm (Ketris et al., 2009). Approximately 80% of the total REE concentration in coal is LREE (Zhang et al., 2015). The average concentration of REE in Chinese coal varies between 101 and 138 ppm (Dai et al., 2008; Zhang et al., 2015), which is 1.5–2 times greater than the world's average. Similar results were observed for Turkish coal (Karayigit et al., 2000; Zhang et al., 2015). The average REE concentration of coal in the United States and the Democratic People's Republic of Korea is close to the world's average. The average REE concentration in world coal on an ash basis is 404 ppm (Seredin and Dai, 2012); however, coal with enriched concentrations of REE on a coal ash basis have been found in coalfields such as in the Sydney Coal Basin, Nova Scotia (72–483 ppm), the coalfields in the Russian Far East (300–1000 ppm) and the Central Appalachian Basin Fire Clay coal bed in the United States (500–4000 ppm; Birk and White, 1991; Seredin, 1996; Hower et al., 1999). The anomalies of REE in coal and distribution patterns are discussed in detail elsewhere (Dai et al., 2016).

Some of the enriched coal (0.68–2.03% REO) have comparable rare-earth concentrations to traditional commercial rare-earth deposits and these coal ashes can be viewed as a potential source for these metals (Seredin and Dai, 2012).

Mode of Occurrence of REE in Coal

Enriched concentrations of REE in coal can be formed under different geological conditions during the entire coal deposit formation process and by various ore-forming processes (Seredin and Finkelman, 2008; Dai et al., 2016). Table 2 shows the four genetic types of REE enrichment in coal: terrigenous, tuffaceous, infiltrational and hydrothermal.

Rare-earth elements can be associated with both organic (Eskenazy, 1987; Seredin, 1996; Wang et al., 2008) and inorganic matter in coal (Eskenazy, 1987; Birk and White, 1991; Seredin, 1996; Hower et al., 1999; Dai et al., 2008), although REE associated with organic matter are considerably less abundant (Eskenazy, 1987; Birk and White, 1991; Seredin, 1996; Zheng et al., 2007). The organic association of the REE in coal is demonstrated by the strong correlation of HREE with organically fixed trace elements like Ge, W and Be and high concentrations of HREE with low-ash coal (Eskenazy, 1982; Eskenazy, 1987; Querol et al., 1995; Seredin, 1996). Trace elements in coal may be associated with organic matter such as carboxylic acid (-COOH), phenolic hydroxyl (-OH), mercapto (-SH) and amino (=NH) groups (Swaine, 1990). Sorption experiments on REE with xylain and humic acid suggested that in the cation exchange process, ions such as Na^+, K^+, Ca^+ and Mg^{2+}, which are bound to COOH and OH^- groups, might have been replaced by REE ions (Eskenazy, 1999).

The mechanism of the organic matter association of REE can also be sorption during coagulation with humic and fulvic acids, as well as the formation of organometallic complexes (Yershov, 1961; Birk and White, 1991; Wang et al., 2008).

On the other hand, the inorganic matter association of REE in coal can be shown by the strong correlation of REE with ash content. In this case, REE minerals are included in accessory minerals, resistate minerals or clay minerals (Eskenazy, 1987; Birk and White, 1991; Zheng et al., 2007). In addition, REE in the Fire Clay coal deposit in the United States have been found to be authigenic in origin (Hower et al., 1999). Finding the percentage of organic and inorganic REE in a coal deposit is essential because it plays a significant role in developing extraction options (Zhang et al., 2015). The present study examines the concentration of REE in coal and their mode of occurrence in select coalfields in BC.

Materials and Methods

An approximately 300 kg run-of-mine sample from five seams were collected at two coal mines in the East Kootenay coalfields, BC. Figure 1 shows the location of East Kootenay coalfields and coal mines. The representative samples were obtained for testing following the stan-

Table 1. Concentration of rare-earth elements (REE; whole coal basis, in ppm) in coal from different countries in comparison with REE contents in coal worldwide, the upper continental crust and black shale. Abbreviations: HREE, heavy rare-earth elements; LREE, light rare-earth elements; ND, no data.

Location of coal	La	Ce	Pr	Nd	Sm	Eu	Gd	Tb	Dy	Y	Ho	Er	Tm	Yb	Lu	Sc	REE	LREE	HREE
Upper continental crust[1]	30	64	7.1	26	4.5	0.88	3.8	0.64	3.5	22	0.8	2.3	0.33	2.2	0.32	11	179	147	32
Black shale[2]	28	58	4.2	33	5.4	1.2	4.7	0.75	3	26	0.52	1.9	0.4	2.8	0.4	12	182	147	36
World[2,7]	11	23	3.5	12	2	0.47	2.7	0.32	2.1	8.4	0.54	0.93	0.31	1	0.2	3.9	72	59	14
United States[3]	12	21	2.4	9.5	1.7	0.4	1.8	0.3	1.9	8.5	0.35	1	0.15	0.95	0.14	ND	62	49	13
China[4]	26	49	5.5	22	4.3	0.9	3.7	0.7	3.1	18	0.7	1.9	0.27	2.1	0.3	ND	138	111	27
China[5]	18	35	3.8	15	3	0.5	3.4	0.52	3.1	9	0.73	2.1	0.34	2	0.32	4	101	83	18
Turkey[5]	21.12	39.24	4.71	16.85	3.18	0.76	3	0.45	2.42	12.76	0.47	1.37	0.21	1.35	0.21	7.92	116	97	19
Democratic People's Republic of Korea[6]	14.5	27.2	2.9	11.1	2.3	0.5	1.4	0.3	2	7.2	0.4	1.1	0.3	1	ND	4.9	77	65	12

[1]From Taylor and McLennan (1985); [2]from Ketris and Yudovich (2009); [3]from Finkelman (1993); [4]from Dai et al. (2008); [5]from Karayigit et al. (2000), Zhang et al. (2015); [6]from Hu et al. (2006); [7]from Seredin and Finkelman (2008)

Table 2. Genetic types of rare-earth element enrichment in coal (Seredin and Finkelman, 2008; Seredin and Dai, 2012).

Genetic type	Mode of rare earth element input	Coalification stage
Terrigenous	Surface waters	Peat-bog stage
Tuffaceous	Leaching of acid and falling alkaline volcanic ash	Peat-bog stage
Infiltrational	Meteoric groundwater	Epigenetic (lignite, sub-bituminous, bituminous-anthracite)
Hydrothermal	Thermal mineral water and deep fluids	Any stage

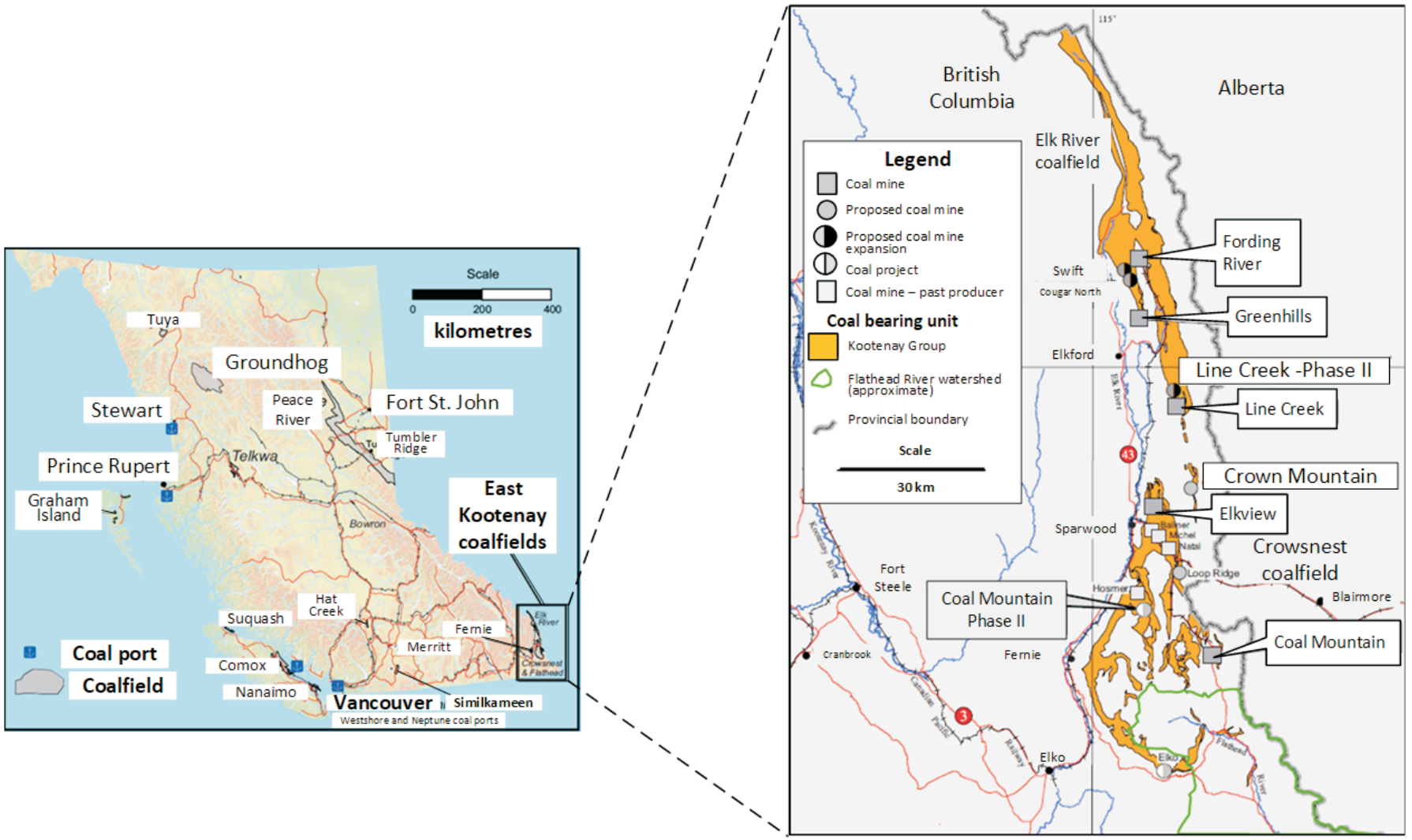

Figure 1. Location of East Kootenay coalfields and coal mines in the southeastern British Columbia (adapted from the BC Ministry of Energy, Mines and Petroleum Resources, 2015, 2016).

dard test procedure ASTM D2013/D2013M-12(2012)[1]. Proximate analysis was conducted on the representative samples in duplicates using the standard methods ASTM D3173/D3173M–17(2017), ASTM D3174–12(2012), ASTM D3175–17(2017) and ASTM D3172–13(2013).

Release Analysis Test

The release analysis test is a technique that is considered to produce an ideal separation curve for the flotation response of any coal. In the release analysis test, as initially outlined by Dell (1964), a flotation test is performed in two stages. In the first stage, coal is floated to achieve maximum recovery, whereas in the second stage, all products from the previous stage are separated into different concentrate products with varying grades and yields. Because products from the release test will have fractions consisting of clean coal (low mineral matter) to tailings (liberated mineral matter) with incremental ash percent, studying REE concentration in these products helps increase understanding of the nature of REE association (organic or inorganic) in the studied samples. For the first stage of release analysis test, a 250 g sample passing 500 µm was mixed with 1800 mL of tap water in a laboratory-scale 2 L Denver flotation cell and conditioned for 5 minutes at 1200 rpm. Then, the coal slurry was subjected to flotation reagents using 50 g/t methyl isobutyl carbinol (MIBC) and 200 g/t kerosene and conditioned for 14 minutes followed by another 50 g/t of frother addition and conditioning for 1 minute. Using an aeration rate of 4–5 L/min of air, concentrate was collected until the froth was barren; if required, extra collector and frother were added to ensure the maximum recovery. In the second stage, concentrate was fractionated into different products using variable impeller speed and aeration rates.

Agglomeration Test

Efficiency of very fine coal recovery from conventional flotation is usually poor (Sastri et al., 1988). The presence of ultrafine slimes or clays also increases the difficulties of processing fine coal, which is ultimately disposed into tailings ponds (Laskowski, 2001). In coal agglomeration, fine coal particles are mixed with the oil under intense agitation, which preferentially covers only fine coal particles and facilitates aggregation of these particles into clusters called agglomerates. Because there is no lower particle size limit for agglomeration, it can be used to recover very fine coals from tailings ponds (Mehrotra et al., 1983).

The presence of REE in agglomerated coal products were also studied in this project. If successful, this agglomeration process may encourage cleaning tailings as a value-added product with REE recovery from the tailings ponds.

In this study, pure diesel was used as a reagent for agglomeration. Reagent concentrations varying from 8 to 20% (by weight) were used for agglomerating a fine coal slurry containing 12% (by weight) coal (sample S3) with a P_{80} (80% of particles finer than the size) of 250 µm. In each test, 500 ml of a 12% coal slurry was conditioned in a high-speed blender at 12 000 rpm for 2 minutes. The reagent (diesel) of required concentration was added and mixing continued for an additional 150 seconds before the mixture was poured onto the sieves to obtain three size fractions: >500 µm (concentrate), <500 µm to >210 µm (middling) and <210 µm (tailings). These products were dried and used for the chemical analysis.

Chemical Analysis of REE and Characterization

For total REE quantification, feed and test product samples (0.2 g) were added to lithium metaborate and lithium tetraborate flux and mixed thoroughly. The samples were then fused in a furnace at 1025°C. Finally, resulting melts were cooled and digested in an acid mixture containing nitric, hydrochloric and hydrofluoric acids. The digested solutions were then analyzed by inductively coupled plasma–mass spectrometry (ICP-MS). The analytical results were corrected for inter-elemental spectral interference. This analysis was conducted by ALS Geochemistry (Vancouver, BC). In this study, REE in coal are expressed as follows: whole coal basis (REE concentration in the coal sample) and ash basis (REE concentration in the ash of the coal sample).

Additional sample characterization was conducted using FEI Quanta 650 ESEM (environmental scanning electron microscope) equipped with scanning energy microscopy with energy dispersive X-ray spectroscopy (SEM-EDX).

Results and Discussion

Results of the as-determined proximate analysis of the samples are shown in Table 3. According to ASTM D388-17(2017), all the feed coal samples (samples S1–S5) are classified as medium volatile bituminous coal. Flotation release analysis tests provided an estimate of ideal separation achievable for the given coal. Samples used for the release tests showed excellent performance with the clean concentrate containing less than 10% ash while recovering 85% of the combustible material. In the case of the agglomeration test, results indicated that selectivity was not possible with a similar amount of ash in the concentrate (S10), middling (S11) and tailings (S12), which can be observed in the Table 3. All five coal samples along with the flotation and agglomeration products and their respective ashes were analyzed for the REE content and the results are shown in Table 4. Table 5 shows the calculated REE values on a whole coal basis.

[1]*References to the relevant ASTM methods can be found at the end of the 'References' section.*

Table 3. Proximate analysis of the five British Columbia feed coal samples and flotation and agglomeration products (as-determined basis)

Sample ID	Sample name	Moisture (%)	Volatile matter (%)	Ash (%)	Fixed carbon (%)
S1	Feed sample	2.97	21.01	15.93	60.09
S2	Feed sample	1.49	18.5	18.44	61.57
S3	Feed sample	2.19	16.42	39.63	41.76
S4	Feed sample	2.81	23.27	16.93	56.99
S5	Feed sample	1.13	22.26	20.21	56.4
S6	Flotation concentrate	0.99	20.74	6.39	71.88
S7	Flotation tailings	0.9	19.72	18.64	60.74
S8	Flotation concentrate	0.94	20.79	10.82	67.45
S9	Flotation tailings	0.96	19.79	67.01	12.24
S10	Agglomeration concentrate	1.33	23.67	19.45	55.55
S11	Agglomeration middling	1.03	21.83	19.81	57.33
S12	Agglomeration tailings	1.16	21.22	22.56	55.06

The REE content in the samples varied from approximately 240 ppm to 570 ppm (Table 4), and Ce, La, Nd and Y accounted for 80% of the total REE. Among the five feed samples, sample 1 had the highest REE content (~350 ppm) and sample 3 had the lowest content (~270 ppm). Also, among the treated samples, the REE content in flotation concentrate (~569 ppm) is more than the tailings (~340 ppm) and the similar trend was observed for the agglomeration product (~315 ppm) compared to its tailings (~258 ppm). Furthermore, mass balance showed that 60 to 80% of total REE by weight in the coal is present in the tailings and middling streams.

Preliminary Economic Evaluation of BC Coal as Raw Materials for REE

Based on the rare-earth oxide (REO) content, a coal seam with a thickness greater than 5 m may be considered as a potential source of REE if the minimum REO content is above 800–900 ppm in the coal ash formed from combustion (Seredin and Dai, 2012). Assuming a valence state of +2 for Ce and +3 for the remaining REE, REO content for the samples were calculated. Also, using the ash data from Table 3, REE content on a whole coal basis were determined. Total REO and REE (whole coal basis) values are given in Table 6. The REO concentrations in the samples (Table 6) do not meet the cut-off grade as described by Seredin and Dai (2012), but they still represent a significant resource potential. As mentioned earlier, the coal seams in the United States with REE content of more than 300 ppm are still considered as a potential source for developing the extraction process (National Energy Technology Laboratory, 2016). This shows that BC coal deposits are prospective REE sources depending on the advancement in the extraction practices that could be applied for recovery.

One of the important trends observed in this study is that the product with a low ash content has higher REE concentration on an ash basis but lower concentration on a whole coal basis (Table 6), which might be due to organic dilution. It implies that a significant portion of REE are associated with ash components in the samples studied. When organic matter in coal is oxidized during the ashing process, REE associated with the organic matter of the coal reports to the ash, thus increasing the REE content of the ash. These associations can be organic REE compounds or microdispersed REE minerals. Further studies, including sequential extraction and sodium hydroxide extraction of REE from the coal, are necessary to assess the percentage of organic association in the samples.

The outlook coefficient is another factor that can be used to assess the quality of the REE concentration in the coal seam, which can be defined as the ratio between the relative amounts of critical REE in the sample to the relative amounts of excessive REE in the sample (Seredin and Dai, 2012). It can be calculated as

$$C_{outl} = \frac{\dfrac{Sum\ concentrations\ of\ Nd, Eu, Tb, Dy, Er\ and\ Y}{Total\ REE\ concentration}}{\dfrac{Sum\ concentrations\ of\ Ce, Ho, Tm, Yb\ and\ Lu}{Total\ REE\ concentration}}$$

where Coutl is the outlook coefficient. A higher value for this index represents a higher market value of REE in the coal seam because the concentration of critical REE increases with the index, allowing for the REE in coal as a potential source for industrial purposes. The Coutl for world coal is 0.64 (Ketris et al., 2009; Zhang et al., 2015). The calculated values of Coutl for the five coal samples are given in Table 7. The Coutl values for the BC coal samples are near to or more than 1, implying that critical REE concentration is significant and accounts for more than 35% of the total REE. This provides further evidence for BC coal deposits to be potential sources for REE. The correlation between the outlook coefficient and REE content is believed to be an indicator of organic REE; otherwise, the dominant carrier of REE is authigenic minerals (Seredin, 1996;

Table 4. Rare-earth element (REE) content of the five British Columbia feed coal samples and flotation and agglomeration products (ash basis, in ppm).

Sample ID	Sample name	Ce	Dy	Er	Eu	Gd	Ho	La	Lu	Nd	Pr	Sm	Tb	Tm	Y	Yb	REE* (ash basis)
S1	Feed sample	114	9.82	5.93	2.69	10.5	2.04	57.6	0.92	55.2	14.15	13	1.62	0.92	55.6	5.73	349.72
S2	Feed sample	101	8.4	5.13	2.6	8.66	1.79	53.1	0.76	45.4	12.25	9.77	1.73	0.8	58.8	4.81	315
S3	Feed sample	91.3	6.6	4.2	1.7	7.04	1.45	48.5	0.65	41.5	11.15	8.62	1.09	0.6	41.5	3.91	269.81
S4	Feed sample	97.2	7.1	4.66	2.33	7.71	1.55	55	0.66	44.5	11.85	8.92	1.54	0.69	53.6	4.39	301.7
S5	Feed sample	101	9.02	5.47	2.52	8.76	1.9	53.5	0.86	46.8	12.25	10.35	1.74	0.8	59.7	5.2	319.87
S6	Flotation concentrate	184.5	15.95	9.88	4.05	16.05	3.38	97.1	1.65	85.5	22.7	17.95	2.67	1.51	96.3	9.8	568.99
S7	Flotation tailings	110.5	9.67	5.91	2.51	9.48	1.95	57.9	0.94	52.3	13.4	11.15	1.58	0.87	56.7	5.39	340.25
S8	Flotation concentrate	140.5	12.95	7.82	3.24	12.65	2.63	73.7	1.59	66.3	17.4	14.55	2.09	1.18	76.7	7.72	441.02
S9	Flotation tailings	82.5	5.75	3.66	1.61	6.31	1.19	43.6	0.57	37.8	10.1	8.07	0.99	0.53	35.3	3.31	241.29
S10	Agglomeration concentrate	100.5	8.75	5.32	2.51	9	1.83	52.7	0.84	46.3	12.15	10.6	1.62	0.8	56.6	5.19	314.71
S11	Agglomeration middling	95.5	8.15	5	2.25	8.39	1.69	50.9	0.81	44	11.75	9.35	1.53	0.76	53.4	4.91	298.39
S12	Agglomeration tailings	84.2	6.32	3.92	2.07	6.88	1.32	45.7	0.59	38.4	10.15	7.87	1.43	0.57	44.8	3.6	257.82

*REE = Ce + Dy + Er + Eu + Gd + Ho + La + Lu + Nd + Pr + Sm + Tb + Tm + Y + Yb + Sc** + Pm***

**ICP-MS analysis was not done for Sc.

***Pm is extremely rare and generally considered not to exist in nature (Resende and Morais, 2010).

Table 5. Rare-earth element (REE) content of the five British Columbia feed coal samples and flotation and agglomeration products (whole coal basis, in ppm).

Sample ID	Sample name	Ce	Dy	Er	Eu	Gd	Ho	La	Lu	Nd	Pr	Sm	Tb	Tm	Y	Yb	REE* (whole coal basis)
S1	Feed sample	18.16	1.56	0.94	0.43	1.67	0.33	9.18	0.15	8.80	2.25	2.07	0.26	0.15	8.86	0.91	55.72
S2	Feed sample	18.62	1.55	0.95	0.48	1.60	0.33	9.79	0.14	8.37	2.26	1.80	0.32	0.15	10.84	0.89	58.08
S3	Feed sample	36.19	2.62	1.66	0.67	2.79	0.57	19.22	0.26	16.45	4.42	3.42	0.43	0.24	16.45	1.55	106.94
S4	Feed sample	16.46	1.20	0.79	0.39	1.31	0.26	9.31	0.11	7.53	2.01	1.51	0.26	0.12	9.07	0.74	51.08
S5	Feed sample	20.42	1.82	1.11	0.51	1.77	0.38	10.81	0.17	9.46	2.48	2.09	0.35	0.16	12.07	1.05	64.66
S6	Flotation concentrate	11.80	1.02	0.63	0.26	1.03	0.22	6.21	0.11	5.47	1.45	1.15	0.17	0.10	6.16	0.63	36.38
S7	Flotation tailings	20.59	1.80	1.10	0.47	1.77	0.36	10.79	0.18	9.75	2.50	2.08	0.29	0.16	10.57	1.00	63.41
S8	Flotation concentrate	15.20	1.40	0.85	0.35	1.37	0.28	7.97	0.17	7.17	1.88	1.57	0.23	0.13	8.30	0.83	47.70
S9	Flotation tailings	55.28	3.85	2.45	1.08	4.23	0.80	29.22	0.38	25.33	6.77	5.41	0.66	0.36	23.66	2.22	161.69
S10	Agglomeration concentrate	19.55	1.70	1.03	0.49	1.75	0.36	10.25	0.16	9.01	2.36	2.06	0.32	0.16	11.01	1.01	61.22
S11	Agglomeration middling	18.92	1.61	0.99	0.45	1.66	0.33	10.08	0.16	8.72	2.33	1.85	0.30	0.15	10.58	0.97	59.12
S12	Agglomeration tailings	19.00	1.43	0.88	0.47	1.55	0.30	10.31	0.13	8.66	2.29	1.78	0.32	0.13	10.11	0.81	58.17

*REE = Ce + Dy + Er + Eu + Gd + Ho + La + Lu + Nd + Pr + Sm + Tb + Tm + Y + Yb + Sc** + Pm***

Table 6. Rare-earth oxide (REO) content and rare-earth element (REE; whole coal and ash basis) content for British Columbia coal samples and flotation and agglomeration products (in ppm).

Sample ID	Sample name	REE (ash basis)	REE (whole coal basis)	Total REO
S1	Feed sample	349.72	55.72	420.88
S2	Feed sample	315	58.08	379.93
S3	Feed sample	269.81	106.94	324.88
S4	Feed sample	301.7	51.08	363.72
S5	Feed sample	319.87	64.66	385.67
S6	Flotation concentrate	568.99	36.38	685.34
S7	Flotation tailings	340.25	63.41	409.75
S8	Flotation concentrate	441.02	47.7	531.2
S9	Flotation tailings	241.29	161.69	290.42
S10	Agglomeration concentrate	314.71	61.22	379.3
S11	Agglomeration middling	298.39	59.12	359.64
S12	Agglomeration tailings	257.82	58.17	310.77

Table 7. Outlook coefficient (C_{outl}) for British Columbia coal samples and flotation and agglomeration products. Abbreviation: REE, rare-earth elements.

Sample ID	Sample name	C_{outl}	Critical REE (ppm)
S1	Feed sample	1.06	130.86
S2	Feed sample	1.12	122.06
S3	Feed sample	0.99	96.59
S4	Feed sample	1.09	113.73
S5	Feed sample	1.14	125.25
S6	Flotation concentrate	1.07	214.35
S7	Flotation tailings	1.08	128.67
S8	Flotation concentrate	1.1	169.1
S9	Flotation tailings	0.97	85.11
S10	Agglomeration concentrate	1.11	121.1
S11	Agglomeration middling	1.1	114.33
S12	Agglomeration tailings	1.07	96.94

Hower et al., 1999) and there is no correlation observed for the BC coal samples that implies the REE may originate from authigenic minerals.

Correlation Analysis

Table 8 shows the correlation coefficients of REE (ash basis) with other elements (ash basis) and ash in the coal samples. Table 9 shows the correlation coefficients for REE (whole coal basis) with other elements (whole coal basis). A strong correlation between ash and REE content calculated on a whole coal basis is observed (r = +0.95 to +0.99), indicating the presence of REE mineral phases in the coal samples. One such rare-earth mineral in these types of metalliferous coal is zircon, which can originate from volcanic ash or authigenic minerals and can be identified by the enrichment of Hf, Th, U, Y and HREE (Finkelman, 1981; Seredin, 2004). A compelling correlation between Hf, Th, U, Y and other REE implies that zircon is one of the source minerals of REE and an indication of volcanic ash input of REE into these coal samples. Elemental analysis results using ICP-MS proved the presence of zircon in the samples. Also, volcanic ash is believed to be source for the tonsteins in the Mist Mountain Formation, which further validates the inference made in this study (Grieve, 1993).

Weak negative correlation between ash and REE content on an ash basis (r = –0.58 to –0.78), however, highlights that a small portion of REE in the samples are associated with coal organic matter due to the organic affinity of certain REE with humic acid. A similar trend has been identified in the Sydney Coal Basin, Nova Scotia (Birk and White, 1991), which further supports the inferences made in this study. The presence of a strong correlation between REE and W, which is believed to be organically fixed in coal, is additional evidence for the presence of organically associated REE in the coal.

Figure 2 shows a similar pattern between REE content normalized to upper continental crust values for all the feed and product samples. This may indicate the REE in the ash material in the organic matrix, partings, roof and floor ma-

Table 8. Correlation coefficients of rare-earth elements (REE; ash basis) with other elements in British Columbia coal samples.

Correlation	Ash	REE (ash basis)	Ga	Hf	Nb	Ta	Th	U	V	W	Zr	Ce	Dy	Er	Eu	Gd	Ho	La	Lu	Nd	Pr	Sm	Tb	Tm	Y	Yb
Ash	1																									
REE (ash basis)	–0.63	1																								
Ga	–0.62	0.99	1																							
Hf	–0.63	0.99	0.99	1																						
Nb	–0.53	0.92	0.93	0.93	1																					
Ta	–0.31	0.85	0.84	0.8	0.75	1																				
Th	–0.63	0.95	0.95	0.97	0.93	0.68	1																			
U	–0.58	0.94	0.95	0.97	0.96	0.69	0.98	1																		
V	–0.4	0.71	0.74	0.74	0.93	0.52	0.79	0.85	1																	
W	–0.58	0.89	0.91	0.86	0.86	0.8	0.82	0.86	0.69	1																
Zr	–0.62	0.99	0.99	1	0.94	0.8	0.97	0.97	0.76	0.87	1															
Ce	–0.59	1	0.99	0.99	0.92	0.87	0.94	0.94	0.72	0.9	0.99	1														
Dy	–0.66	0.99	0.97	0.97	0.85	0.83	0.94	0.91	0.61	0.87	0.97	0.98	1													
Er	–0.65	0.99	0.98	0.98	0.88	0.84	0.95	0.93	0.66	0.89	0.98	0.99	1	1												
Eu	–0.76	0.97	0.96	0.96	0.86	0.75	0.93	0.9	0.65	0.86	0.95	0.95	0.97	0.97	1											
Gd	–0.65	0.99	0.98	0.98	0.86	0.85	0.93	0.9	0.62	0.87	0.97	0.99	0.99	1	0.97	1										
Ho	0.66	0.99	0.98	0.98	0.87	0.82	0.95	0.92	0.64	0.87	0.98	0.99	1	1	0.97	1	1									
La	0.6	0.99	1	0.99	0.95	0.85	0.95	0.96	0.77	0.9	0.99	1	0.97	0.98	0.95	0.97	0.98	1								
Lu	–0.59	0.95	0.93	0.94	0.82	0.8	0.91	0.89	0.6	0.83	0.94	0.95	0.97	0.97	0.92	0.96	0.96	0.94	1							
Nd	–0.59	1	0.99	0.98	0.9	0.89	0.93	0.92	0.68	0.9	0.98	1	0.98	0.99	0.95	0.99	0.99	0.99	0.95	1						
Pr	–0.58	1	0.99	0.98	0.92	0.88	0.94	0.93	0.71	0.89	0.99	1	0.98	0.99	0.95	0.99	0.99	0.99	0.95	1	1					
Sm	–0.6	0.98	0.96	0.95	0.83	0.89	0.89	0.86	0.57	0.86	0.94	0.98	0.98	0.98	0.95	0.99	0.98	0.95	0.95	0.99	0.98	1				
Tb	–0.78	0.94	0.94	0.95	0.86	0.67	0.94	0.91	0.67	0.85	0.95	0.92	0.94	0.94	0.99	0.94	0.95	0.93	0.89	0.91	0.92	0.9	1			
Tm	–0.66	0.99	0.98	0.98	0.87	0.83	0.94	0.92	0.64	0.87	0.98	0.99	1	1	0.98	1	1	0.98	0.96	0.99	0.99	0.98	0.95	1		
Y	–0.74	0.97	0.97	0.98	0.9	0.71	0.97	0.95	0.71	0.86	0.98	0.96	0.97	0.97	0.99	0.96	0.98	0.96	0.93	0.95	0.95	0.93	0.99	0.98	1	
Yb	–0.65	0.99	0.98	0.98	0.88	0.82	0.95	0.93	0.65	0.87	0.98	0.99	1	1	0.97	1	1	0.98	0.97	0.99	0.99	0.98	0.95	1	0.98	1

Table 9. Correlation coefficients of rare-earth elements (REE; whole coal basis) with other elements in the British Columbia coal samples.

Correlation	Ash	REE (whole coal basis)	Ga	Hf	Nb	Ta	Th	U	V	W	Zr	Ce	Dy	Er	Eu	Gd	Ho	La	Lu	Nd	Pr	Sm	Tb	Tm	Y	Yb
Ash	1																									
REE (whole coal basis)	0.993	1																								
Ga	0.997	1	1																							
Hf	0.952	0.98	0.97	1																						
Nb	0.969	0.97	0.97	0.95	1																					
Ta	0.799	0.84	0.83	0.81	0.82	1																				
Th	0.992	0.99	0.99	0.98	0.98	0.78	1																			
U	0.988	0.99	0.99	0.98	0.98	0.78	1	1																		
V	0.93	0.92	0.93	0.9	0.98	0.73	0.94	0.95	1																	
W	0.97	0.97	0.97	0.91	0.94	0.83	0.96	0.96	0.9	1																
Zr	0.904	0.94	0.93	0.99	0.93	0.79	0.94	0.95	0.89	0.86	1															
Ce	0.992	1	1	0.98	0.98	0.85	0.99	0.99	0.93	0.97	0.94	1														
Dy	0.973	0.99	0.98	0.98	0.95	0.84	0.98	0.98	0.88	0.95	0.95	0.99	1													
Er	0.98	1	0.99	0.98	0.96	0.84	0.99	0.98	0.9	0.96	0.95	0.99	1	1												
Eu	0.99	0.99	0.99	0.95	0.95	0.8	0.99	0.98	0.89	0.96	0.9	0.98	0.98	0.98	1											
Gd	0.986	1	0.99	0.98	0.96	0.85	0.99	0.98	0.9	0.96	0.94	1	1	1	0.99	1										
Ho	0.976	0.99	0.99	0.99	0.95	0.82	0.99	0.98	0.89	0.95	0.96	0.99	1	1	0.98	1	1									
La	0.994	1	1	0.97	0.98	0.84	0.99	0.99	0.94	0.97	0.94	1	0.98	0.99	0.98	0.99	0.99	1								
Lu	0.947	0.97	0.97	0.97	0.93	0.86	0.96	0.96	0.86	0.93	0.95	0.97	0.99	0.99	0.95	0.98	0.98	0.97	1							
Nd	0.99	1	1	0.97	0.97	0.86	0.99	0.99	0.92	0.97	0.94	1	0.99	1	0.98	1	0.99	1	0.98	1						
Pr	0.991	1	1	0.98	0.97	0.85	0.99	0.99	0.93	0.97	0.94	1	0.99	0.99	0.98	1	0.99	1	0.97	1	1					
Sm	0.982	1	0.99	0.97	0.95	0.87	0.98	0.97	0.89	0.96	0.93	0.99	0.99	1	0.98	1	0.99	0.99	0.98	1	1	1				
Tb	0.985	0.98	0.98	0.94	0.94	0.74	0.98	0.97	0.89	0.95	0.89	0.97	0.97	0.97	0.99	0.97	0.97	0.97	0.93	0.97	0.97	0.97	1			
Tm	0.977	0.99	0.99	0.98	0.95	0.85	0.98	0.98	0.89	0.95	0.95	0.99	1	1	0.98	1	1	0.99	0.98	0.99	0.99	1	0.97	1		
Y	0.987	0.99	0.99	0.97	0.96	0.76	1	0.99	0.91	0.95	0.94	0.99	0.99	0.99	0.99	0.99	0.99	0.99	0.96	0.98	0.99	0.98	0.99	0.99	1	
Yb	0.974	0.99	0.99	0.98	0.95	0.84	0.99	0.98	0.89	0.95	0.96	0.99	1	1	0.98	1	1	0.99	0.99	0.99	0.99	0.99	0.96	1	0.99	1

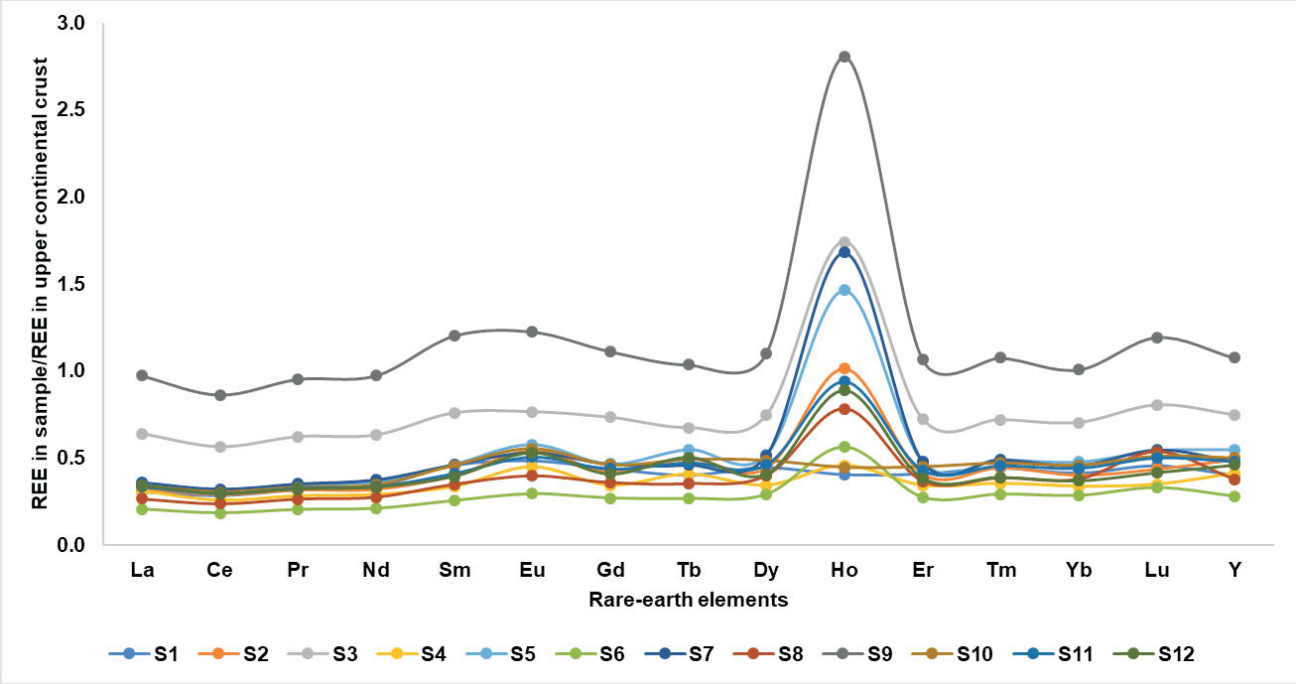

Figure 2. Upper continental crust–normalized rare-earth element (REE) content in British Columbia coal samples.

terial have the same source. The REE sites in the samples were identified using SEM-EDX.

Figure 3 shows grains that contain REE in the sample S3. Based on the elements found using SEM-EDX, it can be inferred that some of the REE are associated with aluminosilicate minerals, which may be clay, although further analysis is required. In addition, REE strongly correlate with U ($r > +0.86$ on ash basis; $r > +0.96$ on whole coal basis) and Th ($r > +0.89$ on ash basis; $r > +0.98$ on whole coal basis). This suggests that one of the REE mineral phases could be monazite.

Conclusions

Five coal samples from BC coal deposits were tested for the presence of REE and it was found that total REE concentration on an ash basis varied from 240 to 570 ppm. It was inferred from the data that REE in the coal samples are associated with both the organic and inorganic portions of the coal constituents. The highest concentration was reported in the flotation product with low ash content, indicating that some of the REE are associated with the organic matter of the coal. Additionally, correlation analysis showed a significant amount of organic matter associated with REE is due to the organic affinity of REE with humic acid. Total REE concentration versus the outlook coefficient did not, however, show any pattern suggesting the presence of authigenic REE minerals either. Rare-earth element content normalized to the upper continental crust indicated a similar source for all the samples and one of the possible REE sources identified as volcanic ash. The SEM-EDX and chemical analysis data suggested that minerals that contain REE in the coal samples could be monazite and zircon and some of the REE could also be associated with aluminosilicate minerals. Further studies will include sequential extraction, X-ray diffraction analysis and detailed SEM-EDX, required to estimate the quantity of REE associated

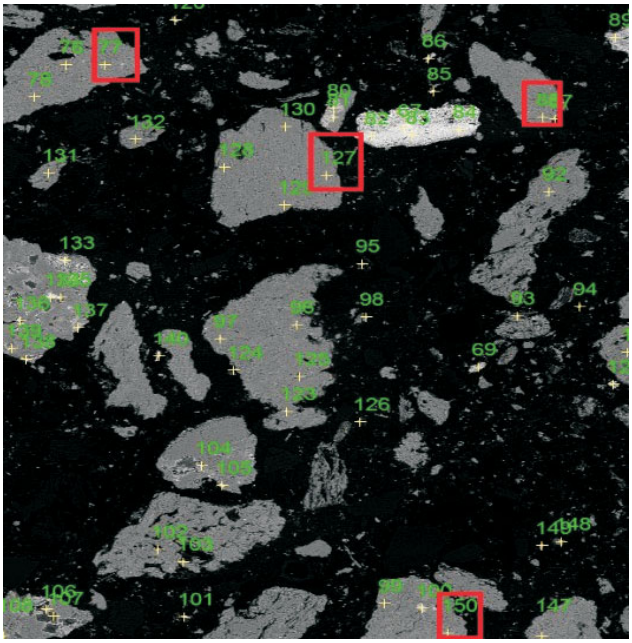

Figure 3. Rare-earth element (REE) sites in sample S3 (200 times magnification); the elements observed in the highlighted grains are as follows: spot 77: Dy, Gd, K, O, P, Si, Y; spot 88**:** Dy, Fe, K, O, P, Si, Ti; spot 127: Al, Ba, Ca, Ce, Fe, K, O, P, Si, Ti; spot 150: Al, Ce, K, O, P, Si.

with organic matter and inorganic matter of the coal samples.

With the development of extraction techniques for REE in coal, these elements will be extracted as byproducts of coal mining, which strengthens the brownfield operations by increasing profitability and possible green credits as these REE are used in the clean energy technologies. In case of the greenfield operations, the possibility of extracting REE from coal will increase the competitiveness of the deposits and its feasibility for actual mining and extraction.

Acknowledgments

The authors gratefully acknowledge the Geoscience BC scholarship. The authors also thank M. Mastalerz, Indiana University and M. Mackay for their valuable comments and suggestions to improve this manuscript.

References

BC Ministry of Energy, Mines and Petroleum Resources (2015): The East Kootenay coalfields; BC Ministry of Energy, Mines and Petroleum Resources, BC Geological Survey, Information Circular 2015-10, 1 p., URL <http://www.empr.gov.bc.ca/Mining/Geoscience/Publications Catalogue/InformationCirculars/Documents/IC2015-10.pdf> [September 2017].

BC Ministry of Energy, Mines and Petroleum Resources (2016): British Columbia coal industry overview 2015; BC Ministry of Energy, Mines and Petroleum Resources, BC Geological Survey, Information Circular 2016-2, 14 p., URL <http://www.empr.gov.bc.ca/Mining/Geoscience/PublicationsCatalogue/InformationCirculars/Documents/IC2016-2%20coal.pdf> [September 2017].

Birk, D. and White, J.C. (1991): Rare earth elements in bituminous coals and underclays of the Sydney basin, Nova Scotia: element sites, distribution, mineralogy; International Journal of Coal Geology, v. 19, p. 219–251, doi:10.1016/0166-5162(91)90022-B

Bratskaya, S.Y., Volk, A.S., Ivanov, V.V., Ustinov, A.Y., Barinov, N.N. and Avramenko, V.A. (2009): A new approach to precious metals recovery from brown coals: correlation of recovery efficacy with the mechanism of metal–humic interactions; Geochimica et Cosmochimica Acta, v. 73, no. 11, p. 3301–3310.

Chakhmouradian, A. (2014): Evidence presented to standing committee on natural resources; House of Commons, February 25, 2014, 26 p., URL <http://www.parl.gc.ca/HousePublications/Publication.aspx?DocId=6437615&Language=E&Mode=1&Parl=41&Ses=2> [September 2017].

Dai, S., Graham, I.T. and Ward, C.R. (2016): A review of anomalous rare earth elements and yttrium in coal; International Journal of Coal Geology, v. 159, p. 82–95.

Dai, S., Li, D., Chou, C., Zhao, L., Zhang, Y., Ren, D., Ma, Y. and Sun, Y. (2008): Mineralogy and geochemistry of boehmite-rich coals: new insights from the Haerwusu surface mine, Jungar coalfield, Inner Mongolia, China; International Journal of Coal Geology, v. 74, p. 185–202.

Dai, S., Ren, D., Chou, C., Finkelman, R., Seredin, V. and Zhou, Y. (2012): Geochemistry of trace elements in Chinese coals: a review of abundances, genetic types, impacts on human health, and industrial utilization; International Journal of Coal Geology, v. 94, p. 3–21.

Dai, S., Zhou, Y., Ren, D., Wang, X., Li, D. and Zhao, L. (2007): Geochemistry and mineralogy of the late Permian coals from the Songzao coalfield, Chongqing, southwestern China; Science in China, Series D, Earth Sciences, v. 50, p. 678–688.

Dell, C.C. (1964): An improved release analysis procedure for determining coal washability; Journal of the Institute of Fuel, v. 37, p. 149–150.

Eskenazy, G.M. (1982): The geochemistry of tungsten in Bulgarian coals; International Journal of Coal Geology, v. 2, p. 99–111.

Eskenazy, G.M. (1987): Rare earth elements in a sampled coal from the Pirin deposit, Bulgaria; International Journal of Coal Geology, v. 7, p. 301–314.

Eskenazy, G.M. (1999): Aspects of the geochemistry of rare earth elements in coal: an experimental approach; International Journal of Coal Geology, v. 38, p. 285–295.

European Commission (2017): Study on the review of the list of critical raw materials; 92 p., URL <https://publications.europa.eu/en/publication-detail/-/publication/08fdab5f-9766-11e7-b92d-01aa75ed71a1/language-en> [September 2017].

Finkelman, R.B. (1981): Modes of occurrence of trace elements in coal; United States Geological Survey, No. 81-99, 30 p., URL <https://pubs.usgs.gov/of/1981/0099/report.pdf> [September 2017].

Finkelman, R.B. (1993): Organic geochemistry principles and applications; *in* Organic Geochemistry Trace and Minor Elements in Coal, M.H. Engel and S.A. Macko (ed.), Springer Science+Business Media, New York, New York, p. 593–604.

Goodarzi, N.N., Goodarzi, F., Grieve, D.A., Sanei, H. and Gentzis, T. (2009): Geochemistry of coals from the Elk Valley coalfield, British Columbia, Canada; International Journal of Coal Geology, v. 77, p. 246–259.

Grieve, D.A. (1993): Geology and rank distribution of the Elk Valley coalfield, southeastern BC (82G/15, 82J/2, 6, 7, 10, 11); BC Ministry of Energy, Mines and Petroleum Resources, BC Geological Survey, Bulletin 82, 188 p., URL <http://www.empr.gov.bc.ca/Mining/Geoscience/PublicationsCatalogue/BulletinInformation/BulletinsAfter1940/Documents/Bull82.pdf> [September 2017].

Hower, J.C., Ruppert, L.F. and Eble, C.F. (1999): Lanthanide, yttrium, and zirconium anomalies in the Fire Clay coal bed, eastern Kentucky; International Journal of Coal Geology, v. 39, p. 141–153.

Hu, J., Zheng, B., Finkelman, R.B., Wang, B., Wang, M., Li, S. and Wu, D. (2006): Concentration and distribution of sixty-one elements in coals from DPR Korea; Fuel, v. 85, p. 679–688.

Karayigit, A.I., Gayer, R.A., Querol, X. and Onacak, T. (2000): Contents of major and trace elements in feed coals from Turkish coal-fired power plants; International Journal of Coal Geology, v. 44, p. 169–184.

Ketris, M.P. and Yudovich, Y.E. (2009): Estimations of clarkes for carbonaceous bioliths: world averages for trace element contents in black shales and coals; International Journal of Coal Geology, v. 78, p. 135–148.

Laskowski, J.S. (2001): Coal Flotation and Fine Coal Utilization (1st Edition); Elsevier, Amsterdam, The Netherlands, 368 p.

Mehrotra, V.P., Sastry, K.V.S. and Morey, B.W. (1983): Review of oil agglomeration techniques for processing of fine coals; International Journal of Mineral Processing, v. 11, p. 175–201.

Moldoveanu, G. and Papangelakis, V. (2013): Recovery of rare earth elements adsorbed on clay minerals: II. leaching with ammonium sulfate; Hydrometallurgy, v. 117–118, p. 71–78, doi:10.1016/j.hydromet.2012.02.007

National Energy Technology Laboratory (2016): Rare earth elements program, 2016 project portfolio; National Energy Technology Laboratory, 19 p., URL <https://www.netl.doe.gov/File%20Library/Research/Coal/Rare%20Earth% 20Elements/REE-Project-Portfolio-2016.pdf> [September 2017].

O'Driscoll, M. (1991): An overview of rare earth minerals supply and applications; Materials Science Forum, v. 70–72, p. 409–420. doi:10.4028/www.scientific.net/MSF.70-72.409

Querol, X., Fernández-Turiel, J. and López-Soler, A. (1995): Trace elements in coal and their behaviour during combustion in a large power station; Fuel, v. 74, p. 331–343.

Resende, L.V. and Morais, C.A. (2010): Study of the recovery of rare earth elements from computer monitor scraps – leaching experiments; Minerals Engineering, v. 23, p. 277–280.

Sahoo, P.K., Kim, K., Powell, M.A. and Equeenuddin, S.M. (2016): Recovery of metals and other beneficial products from coal fly ash: a sustainable approach for fly ash management; International Journal of Coal Science and Technology, v. 3, p. 267–283.

Sastri, S.R.S., Reddy, P.S.R., Bhattacharyya, K.K., Kumar, S.G. and Narasimhan, K.S. (1988): Recovery of coal fines using column flotation; Minerals Engineering, v. 1, p. 359–363.

Seredin, V.V. (1996): Rare earth element-bearing coals from the Russian Far East deposits; International Journal of Coal Geology, v. 30, p. 101–129, doi:10.1016/0166-5162(95)00039-9

Seredin, V.V. (2004): Metalliferous coals: formation conditions and outlooks for development; Coal Resources of Russia, v. 6, p. 452–519.

Seredin, V. and Dai, S. (2012): Coal deposits as potential alternative sources for lanthanides and yttrium; International Journal of Coal Geology, v. 94, p. 67–93.

Seredin, V.V. and Finkelman, R.B. (2008): Metalliferous coals: a review of the main genetic and geochemical types; International Journal of Coal Geology, v. 76, p. 253–289.

Swaine, D.J. (1990): Trace Elements in Coal; Butterworth, London, United Kingdom, 278 p.

Tang, X.Y. and Huang, W.H. (2002): Trace elements in coal and significance of the research; Coal Geology of China, v. 14 (Suppl.), p. 1–4 [in Chinese with English abstract].

Taylor, S.R. and McLennan, S.M. (1985): The Continental Crust: Its Composition and Evolution: An Examination of the Geochemical Record Preserved in Sedimentary Rocks; Blackwell Science, Oxford, United Kingdom, 312 p.

Tse, P.K. (2011): China's rare-earth industry: United States Geological Survey, Open-File Report 2011-1042, 11 p., URL <https://pubs.usgs.gov/of/2011/1042/of2011-1042.pdf> [September 2017].

United States Department of Energy (2010): Critical materials strategy; United States Department of Energy, 190 p., URL <https://energy.gov/sites/prod/files/DOE_CMS2011_FINAL _Full.pdf> [September 2017].

Wang, C., Wang, W., Qin, Y., Sang, S., Zhu, Y. and Weiss, D.J. (2008): Geochemistry of rare earth elements in a marine influenced coal and its organic solvent extracts from the Antaibao mining district, Shanxi, China; International Journal of Coal Geology, v. 76, p. 309–317.

Yershov, V.M. (1961): Rare earth elements in the coals of the Kizelovskii coal basin; Geochemistry, v. 3, p. 306–308.

Zhang, W., Rezaee, M., Bhagavatula, A., Li, Y., Groppo, J. and Honaker, R. (2015): A review of the occurrence and promising recovery methods of rare earth elements from coal and coal by-products; International Journal of Coal Preparation and Utilization, v. 35, p. 295–330.

Zheng, L., Liu, G., Chou, C., Qi, C. and Zhang, Y. (2007): Geochemistry of rare earth elements in Permian coals from the Huaibei coalfield, China; Journal of Asian Earth Sciences, v. 31, p. 167–176.

ASTM Standard Methods

ASTM D388-17(2017): Standard classification of coals by rank; ASTM International, West Conshohocken, Pennsylvania, 2017, URL <https://www.astm.org/Standards/D388.htm> [November 2017].

ASTM D2013/D2013M-12(2012): Standard practice for preparing coal samples for analysis; ASTM International, West Conshohocken, Pennsylvania, 2012, URL <https://www.astm.org/Standards/D2013.htm> [November 2017].

ASTM D3172-13(2013): Standard practice for proximate analysis of coal and coke; ASTM International, West Conshohocken, Pennsylvania, 2013, URL <https://www.astm.org/Standards/D3172.htm> [November 2017].

ASTM D3173/D3173M-17a(2017): Standard test method for moisture in the analysis Sample of coal and coke; ASTM International, West Conshohocken, Pennsylvania, 2017, URL <https://www.astm.org/Standards/D3173.htm> [November 2017].

ASTM D3174-12(2012): Standard test method for ash in the analysis sample of coal and coke from coal; ASTM International, West Conshohocken, Pennsylvania, 2012, URL <https://www.astm.org/Standards/D3174.htm> [November 2017].

ASTM D3175-17(2017): Standard test method for volatile matter in the analysis sample of coal and coke; ASTM International, West Conshohocken, Pennsylvania, 2017, URL <https://www.astm.org/Standards/D3175.htm> [November 2017].

Geochemistry of Selenium in the Residual from Biologically Treated Mine-Impacted Waters

L.M. Volden, Department of Earth Sciences, Simon Fraser University, Burnaby, BC, laura_volden@sfu.ca

D. Kirste, Department of Earth Sciences, Simon Fraser University, Burnaby, BC

R.A. Gordon, Department of Physics, Simon Fraser University, Burnaby, BC

M. Bianchin, Amec Foster Wheeler, Burnaby, BC

Volden, L.M., Kirste, D., Gordon, R.A. and Bianchin, M. (2018): Geochemistry of selenium in the residual from biologically treated mine-impacted waters; *in* Geoscience BC Summary of Activities 2017: Minerals and Mining, Geoscience BC, Report 2018-1, p. 101–108.

Introduction

Although selenium (Se) is an essential element for human, animal and vegetation health, an over- or underabundance may cause adverse health effects and ecological problems. Due to the onset of industrialization, Se has become a contaminant of concern in many parts of the world, including North America. It is naturally occurring in many environments and can become mobile under the right chemical conditions, potentially affecting aquatic habitats and drinking-water sources. While Se occurs naturally at elevated concentrations in sediments, soils and rocks, many anthropogenic activities have been shown to facilitate its mobility. Mining, agriculture and nuclear-power generation have all been demonstrated to increase the potential for mobilizing Se into both groundwater and surface water (Chapman et al., 2010). Of particular importance to British Columbia (BC), elevated Se concentrations in the environment as a result of mining practices have been documented in both Canada and the United States.

Once Se reaches the aquatic environment, it can quickly attain high concentrations due to rapid bioaccumulation within food chains (Lemly, 2004). Selenium in high concentrations can be fatal and, even in lower doses, has the potential to negatively affect human health and reproduction in fish, birds, amphibians and reptiles (Chapman et al., 2010). For example, larval deformities in northern pike were attributed by Muscatello et al. (2006) to exposure to Se in mining effluent from a uranium operation in Saskatchewan. Holm et al. (2003) described harmful impacts of elevated Se from active coal mining on wild rainbow trout and brook trout. Moreover, Se deficiencies can result in humans experiencing growth retardation and impaired bone metabolism (Kang et al., 2013).

This publication is also available, free of charge, as colour digital files in Adobe Acrobat® PDF format from the Geoscience BC website: http://www.geosciencebc.com/s/SummaryofActivities.asp.

Selenium mobility is directly related to the redox state, which controls the speciation in aqueous solution; the sorption properties of the coinciding solid state; and the stability of Se minerals (White and Dubrovsky, 1994). In general, the more oxidizing the environment is, the more mobile Se can be, with the solid-state species of Se occurring under reducing conditions (White et al., 1991). A significant control on Se mobility is the tendency for the element to adsorb onto mineral surfaces. The extent of adsorption is largely dependent on pH, redox conditions and adsorption-site density, with either a decrease in pH or the presence of mildly oxidizing conditions causing a higher rate of Se adsorption (Balistrieri and Chao, 1990). In the aqueous phase, Se species consist of selenate (Se VI) and selenite (Se IV). Selenite adsorbs much more strongly than selenate, with the presence of each species dependent upon the redox conditions of the system (Neal and Sposito, 1989). The reduction and oxidation of Se can occur in the absence of microbes, but the reaction rates are often faster when microbially mediated (Dowdle and Oremland, 1998).

Although the release of Se from industrial wastes to natural waterways and associated impacts are documented (Muscatello et al., 2006; Chapman et al., 2010), technology exists to actively remove Se from industrial effluents. Suspended-growth biological wastewater-treatment systems are currently being used as a way to remove Se from contaminated waters (Lenz et al., 2008; Jain et al., 2015). While wastewater treatment has been proven effective in removing Se from the water, it produces a sludge residual with high concentrations of Se that requires disposal or tertiary treatment. Due to the recent emergence of this technology, there has been little research into the potential for Se to remobilize from a biologically fixed state (i.e., in sludge), and the risks associated with landfilling of this material are not understood.

The purpose of this research is to determine the Se speciation within the solid-phase fraction of the residual produced from biological wastewater treatment, and to advance the understanding of mobilization mechanisms

within this residual. By addressing both aspects, it will be possible to determine the conditions under which the risk of remobilization is elevated and precisely which Se species are the most vulnerable. Understanding the geochemistry of Se mobility and transport is essential to the development of strategies for mitigating the negative effects of Se in the environment.

The specific objectives of this research are to

- characterize the occurrence of Se in the solid phase of the sludge/residual, specifically the oxidation state(s);
- gain an understanding of the mobility controls on Se within the residual by conducting a suite of aqueous geochemical batch experiments; and
- relate the solid-phase fraction of Se to the results of the batch experiments, to learn if preferential species mobilization occurs under different oxidation pathways when multiple species are present in the residual.

Methods

Bulk Characterization

Residual samples were collected from a suspended-growth biological treatment system for mine-impacted waters and were submitted to ALS Laboratories in Vancouver, BC for analysis of 35 elements (Ag, Al, As, B, Ba, Be, Bi, Ca, Cd, Co, Cr, Cu, Fe, Ga, Hg, K, La, Mg, Mn, Mo, Na, Ni, P, Pb, S, Sb, Sc, Sr, Th, Ti, Tl, U, V, W, Zn) by aqua-regia digestion and for Se content by four-acid digestion. Organic content was estimated by measuring S as SO_4 using a carbonate-leach analysis, and S as S_2 and C concentrations by LECO combustion analysis. By having a bulk chemical characterization of the residual, more detailed characterization methods could be further refined in order to optimize the characterization process. Figure 1 is a photo of the residual sample.

Figure 1. Residual from biological treatment of mine-impacted waters, showing evidence of Fe oxidation on the edges.

Sequential-Extraction Procedures

Sequential-extraction procedures (SEP) were carried out in order to determine which Se species were present in the residual and their relative abundances. The method used was based on a study by Wright et al. (2003), who compared two different methods of sequential extraction for Se in soils and sediments. The method identified as most relevant was originally developed by Zhang and Moore (1996); it was then modified for this study by adding a step to target acid-volatile sulphide compounds, which was identified by Chao and Sanzolone (1989) to also remove selenide compounds. The need for the selenide step was motivated by a study by Lenz et al. (2008) that used X-ray absorption near-edge structure (XANES) analysis to critically evaluate the accuracy of the sequential-extraction procedure and found that elemental Se was overestimated due to the concurrent mobilization of selenide with the intended mobilization of elemental Se.

Residual samples were stored in resealable plastic bags at 4°C until analysis to limit microbial activity. All reagents used were analytical grade and, due to the oxidation sensitivity of the residual, all solutions used were prepared in 1 L polyethylene bottles under an N_2 atmosphere and bubbled with N_2 gas for 10 minutes to ensure that all oxygen was removed from solution. All sample preparation and handling was conducted under N_2 atmosphere to prevent oxidation of the residual. Six replicates of each sample were prepared by placing 6 g of residual in separate 50 mL centrifuge tubes. Following each extraction step, the solid fraction from one replicate was set aside and preserved for solid-state characterization. After each step, the samples were centrifuged at 10 000 rpm for 10 minutes and the supernatant decanted to a 50 mL test tube. Following this, the samples were diluted with 10 mL of de-ionized water, stirred for 5 minutes and centrifuged a second time. The second supernatant was combined with the first in the 50 mL test tube. The supernatant was then filtered using a 0.45 µm syringe filter, diluted with 2% nitric acid to reach a 1 in 10 dilution factor and stored at 4°C until analysis. Table 1 provides a summary of the five steps used and the Se species targeted by each step.

Table 1. Reagents used and targeted Se species for each of the fractions in the sequential-extraction procedure.

Fraction	Concentration	Reagent	Targeted Se species
F1	0.25 M	KCl	Selenate
F2	0.1 M	K_2HPO_4	Selenite
F3	4 M	HCl	Selenide
F4	0.25 M	Na_2SO_3	Elemental Se
F5	5%	NaOCl	Organoselenium

Fraction F1: 0.25 M KCl was added to each 6 g sample at a 1 in 8 solid:solution ratio and the sample stirred with a glass rod for 2 minutes, capped, placed on the shaker bench at 300 rpm for 5 minutes and left at room temperature for 2 hours.

Fraction F2: 0.1 M K_2HPO_4 was added to each 6 g sample at a 1 in 8 solid:solution ratio and the sample adjusted to a pH of 8 using 6 M HCl, stirred with a glass rod for 2 minutes, placed on the shaker bench at 300 rpm for 5 minutes and left at room temperature for 2 hours.

Fraction F3: 4 M HCl was added to each sample at a 1 in 8 solid:solution ratio and the sample placed on the shaker bench at 300 rpm for 5 minutes and then in a hot-water bath at 95°C for 45 minutes. Due to the presence of iron sulphides in the residual, considerable volatilization of sulphur gas was observed after the addition of HCl. Because of this, stirring was not required and the 50 mL centrifuge tubes were capped immediately following the addition of the reagent.

Fraction F4: 0.25 M Na_2SO_3 was added to each sample at a 1 in 8 solid:solution ratio and the sample adjusted to a pH of 7 using 6 M HCl, stirred with a glass rod for 2 minutes and placed on the shaker bench at 300 rpm for 4 hours.

Fraction F5: 4% NaOCl was added to each sample at a 1 in 20 solid:solution ratio and the sample stirred with a glass rod for 2 minutes and placed in a hot-water bath for 1 hour. Zhang and Moore (1996) originally used a 1 in 4 solid:solution ratio for this step, but not all of the organoselenium was thought to have mobilized after a trial run of this method. Consequently, the solid:solution ratio was decreased in this study so more reactant was available.

Following the SEP, the supernatant was analyzed for Se and 41 additional elements (Li, Be, Al, Sc, Ti, V, Cr, Mn, Fe, Co, Ni, Cu, Zn, As, Rb, Sr, Zr, Ag, Cd, Sn, Sb, Cs, Ba, La, Ce, Pr, Sm, Eu, Gd, Tb, Dy, Ho, Er, Tm, Yb, Lu, Hg, Tl, Pb, Th and U) using inductively coupled plasma–mass spectrometry (ICP-MS) in the 4D Laboratories at Simon Fraser University.

Batch Experiments

Geochemical batch experiments were conducted on the residual (RES) and four Se standards (Na_2SeO_3, SeS_2, Se_0 and ZnSe) to evaluate Se oxidation. The RES and SeS_2 experiments were conducted simultaneously for 64 and 46 days, respectively. The experiments for the remaining standards were conducted approximately 10 weeks later for a total of 25 days. Batches were sampled on a 2 or 3 day interval for the first 2 weeks and then approximately every 4 days for the remainder of the experiments.

Three oxidants were used (O_2, Fe^{3+} and NO_3^-) to simulate mildly oxidizing or highly oxidizing conditions. For each of the redox conditions, the pH was either left at the natural pH of the solution or controlled with HCl at pH 2.5. Table 2 provides a summary of the redox and pH conditions simulated for each sample. Iron III and nitrate solutions were prepared in an N_2 atmosphere and then bubbled with N_2 gas for 10 minutes to ensure the intended oxidant was isolated

Table 2. Summary of the samples subjected to batch experiments, the oxidant type and concentration associated with each one, and the corresponding pH of each batch reactor.

Sample	Oxidant	Concentration	pH
RES	O_2	Open to atm.	Natural
RES	O_2	Open to atm.	2.5
RES	O_2	Closed to atm.	Natural
RES	O_2	Closed to atm.	2.5
RES	$NaNO_3$	1.0 mmol	Natural
RES	$NaNO_3$	1.0 mmol	2.5
RES	$NaNO_3$	100 mmol	Natural
RES	$NaNO_3$	100 mmol	2.5
RES	$FeCl_3$	0.1 mmol	Natural
RES	$FeCl_3$	0.1 mmol	2.5
RES	$FeCl_3$	10 mmol	Natural
RES	$FeCl_3$	10 mmol	2.5
SeS_2	O_2	Open to atm.	Natural
SeS_2	O_2	Open to atm.	2.5
SeS_2	O_2	Closed to atm.	Natural
SeS_2	O_2	Closed to atm.	2.5
SeS_2	$NaNO_3$	1.0 mmol	Natural
SeS_2	$NaNO_3$	1.0 mmol	2.5
SeS_2	$NaNO_3$	100 mmol	Natural
SeS_2	$NaNO_3$	100 mmol	2.5
SeS_2	$FeCl_3$	0.1 mmol	Natural
SeS_2	$FeCl_3$	0.1 mmol	2.5
SeS_2	$FeCl_3$	10 mmol	Natural
SeS_2	$FeCl_3$	10 mmol	2.5
Na_2SeO_3	O_2	Closed to atm.	Natural
Na_2SeO_3	O_2	Closed to atm.	2.5
Na_2SeO_3	$NaNO_3$	1.0 mmol	Natural
Na_2SeO_3	$NaNO_3$	1.0 mmol	2.5
Na_2SeO_3	$FeCl_3$	0.1 mmol	Natural
Na_2SeO_3	$FeCl_3$	0.1 mmol	2.5
Se^0	O_2	Closed to atm.	Natural
Se^0	O_2	Closed to atm.	2.5
Se^0	$NaNO_3$	1.0 mmol	Natural
Se^0	$NaNO_3$	1.0 mmol	2.5
Se^0	$FeCl_3$	0.1 mmol	Natural
Se^0	$FeCl_3$	0.1 mmol	2.5
ZnSe	O_2	Closed to atm.	Natural
ZnSe	O_2	Closed to atm.	2.5
ZnSe	$NaNO_3$	1.0 mmol	Natural
ZnSe	$NaNO_3$	1.0 mmol	2.5
ZnSe	$FeCl_3$	0.1 mmol	Natural
ZnSe	$FeCl_3$	0.1 mmol	2.5

Abbreviations: 'Closed to atm.', closed to atmosphere; 'Open to atm.', open to atmosphere; 'RES', residual.

in solution. For the oxygen experiments, de-ionized water was used and either left open to the atmosphere to simulate highly oxidizing conditions or sealed to limit the oxygen available and simulate mildly oxidizing conditions. $FeCl_3$ was used to prepare 0.1 mmol (mildly oxidizing) and 10 mmol (highly oxidizing) iron solutions, and $NaNO_3$ was used to prepare 1.0 mmol (mildly oxidizing) and 100 mmol (highly oxidizing) nitrate solutions. All chemicals used were analytical grade. Following the first round of experiments, the highest Se mobilization was observed under mildly oxidizing conditions; therefore, only the lower concentration of the two oxidants was used for the remaining experiments.

Residual samples were prepared by freezing with liquid nitrogen and grinding to approximately 10 µm. Each batch reactor was prepared using a 500 mL resealable polyethylene bottle. The batch reactors can be seen in Figure 2. A 1:10 solid:solution ratio was prepared by adding 30 g of sample to 300 g of oxidizing solution. For the Se standards, the weight used was calculated to equal the molarity of Se present in 30 g of the residual, and 300 g of oxidizing solution was used to ensure the same Se:solution ratio. The batch reactors were left at room temperature for the duration of the experiment and hand shaken after each sampling event.

Figure 2. Selection of batch reactors used to evaluate Se oxidation.

Table 3. Summary of the residual samples analyzed using X-ray absorption near edge structure (XANES) analysis at the Canadian Light Source and the Advanced Photon Source, their associated valence state and the corresponding experiments.

Light source	Sample name	Experiment description
CLS	RES 2_1	Starting residual sample
CLS	RES 2_2	Starting residual sample - duplicate
CLS	RES 2_3	Starting residual sample - duplicate
CLS	O2-O	O_2 oxidant - open to atmosphere
CLS	O2-O 2.5	O_2 oxidant - open to atmosphere with pH at 2.5
CLS	O2-C	O_2 oxidant - closed to atmosphere
CLS	O2-C 2.5	O_2 oxidant - closed to atmosphere with pH at 2.5
CLS	NO3 1.0	NO_3 oxidant using 1.0 mmol $NaNO_3$
CLS	NO3 1.0 2.5	NO_3 oxidant using 1.0 mmol $NaNO_3$ with pH at 2.5
CLS	NO3 100	NO_3 oxidant using 100 mmol $NaNO_3$
CLS	NO3 100 2.5	NO_3 oxidant using 100 mmol $NaNO_3$ with pH at 2.5
CLS	Fe 0.1	Fe oxidant using 0.1 mmol FeCl
CLS	Fe 0.1 2.5	Fe oxidant using 0.1 mmol FeCl with pH at 2.5
CLS	Fe 10	Fe oxidant using 10 mmol FeCl
CLS	Fe 10 2.5	Fe oxidant using 10 mmol FeCl with pH at 2.5
APS	RES 2	Starting residual sample
APS	RES 2_B	Starting residual sample - duplicate
APS	RES 3	Starting residual sample - duplicate
APS	F1	Residual following Fraction 1 of the SEP (targets selenate)
APS	F2	Residual following Fraction 2 of the SEP (targets selenite)
APS	F3	Residual following Fraction 3 of the SEP (targets selenides)
APS	F4	Residual following Fraction 4 of the SEP (targets elemental)
APS	F5	Residual following Fraction 5 of the SEP (targets organic)

Prior to each sampling event, the pH and the oxidation-reduction potential (ORP) of the solution were measured and recorded. In the controlled pH experiments, HCl was added prior to sampling to adjust the pH to 2.5. The solution was then sampled using a syringe and a 0.45 µm filter. Following this, three separate 1 mL aliquots of the supernatant were transferred to 15 mL test tubes and diluted to a ratio of 1 in 10 with either 2% nitric acid for analysis of cations by inductively coupled plasma–emission spectrometry (ICP-ES) and ICP-MS, or de-ionized water for analysis of anions by ion chromatography. At the end of the experiments, the solid-phase fraction was retained for Se-species characterization.

X-ray Absorption Near Edge Structure

X-ray absorption near edge structure (XANES) analysis was performed at the Canadian Light Source (CLS) in Saskatoon, SK and the Advanced Photon Source (APS) in Chicago, IL to characterize the Se speciation in the residual before and after the batch and SEP experiments. The first run was performed at the CLS and included the starting residual and the samples associated with the batch experiments. The second run was performed at the APS and included samples associated with the SEPs and replicate samples of the starting residual. Table 3 provides a summary of the samples analyzed at each light source and their associated experiments.

In addition to the samples, a series of Se standards was run for the purpose of linear combination fitting. This method fits the known spectra of the standards to the unknown composition of the residual in order to determine the relative amounts of each Se species in the residual. While this method can identify the composition of an unknown sample accurately, it requires that the general composition of the material be known, to account for the major Se species, so that the appropriate standards are selected. Based on the bulk characterization performed, ten Se standards were identified to be of interest and were run at the CLS and the APS. Table 4 provides a summary of these standards.

In both cases, samples were shipped to the light source at a temperature of 4°C and kept at that temperature until analysis to limit biological activity and subsequent sample oxidation. Samples were prepared using Teflon® washers sealed in Kapton® tape, and the standards were prepared by grinding the sample to a fine powder that was spread on and sealed between layers of Kapton tape.

Se K-Edge Data Collection

Canadian Light Source

Bulk Se K-edge XANES spectra were collected on the very sensitive elemental and structural probe employing radiation from a synchrotron (VESPERS) 07B2-1 beamline at the Canadian Light Source. Samples were positioned in front of the X-ray beam at an angle of 45°. The XANES spectra of the samples were collected in fluorescence mode using a four-element silicon drift (SD) Vortex detector. The spectra of the Se standards were collected in both transmission and fluorescence modes. Spectra were collected from ~200 to ~250 eV above the Se K-edge absorption edge (12658 eV), with a step size of 0.5 eV near the edge. The energy range was selected using a silicon (111) double-crystal monochromator, which provided a monochromatic flux of ~10^{10} photons/sec. The beam size was set to 0.8 mm wide and 0.8 mm tall. A Se reference standard was run periodically between samples for beamline energy calibration. Ion chambers were filled with 100% N_2 gas. Samples were initially measured by performing three scans on three separate spots, for a total of nine scans. Due to evidence of beam damage in some samples, a second run was performed with one scan at nine separate spots, for a total of nine scans. Figure 3 provides a schematic representation of the experimental set-up that was used for XANES analysis on the VESPERS beamline.

Advanced Photon Source

Bulk Se K-edge XANES spectra were collected on a bending magnet beamline (9BM) at the Advanced Photon Source. Samples were positioned in front of the X-ray beam at an angle of 45°. XANES spectra of the samples were collected in fluorescence mode using a four-element silicon drift (SD) Vortex detector. The spectra of the Se standards were collected in both transmission and fluorescence modes. Spectra were collected from ~200 to ~250 eV above the Se K-edge absorption edge (12658 eV), with a step size of 0.5 eV near the edge. The energy range was selected using a silicon (111) double-crystal monochromator, which provided a monochromatic flux of ~10^{10} photons/sec. The beam size was set to 0.3 mm wide and 0.3 mm tall. A Se reference standard was run concurrently with samples for beamline energy calibration. Ion chambers were filled with one-third Ar gas and two-thirds N_2 gas. Three layers of

Table 4. Summary of the Se standards analyzed using X-ray absorption near edge structure (XANES) analysis at the Canadian Light Source and the Advanced Photon Source, and their associated valence state.

Standard	Se species
Barium selenate	Se^{6+}
Sodium selenite	Se^{4+}
Elemental Se	Se^{0}
Selenium sulphide	Se^{4+}
Iron selenide	Se^{2-}
Zinc selenide	Se^{2-}
Copper selenide	Se^{2-}
Seleno-DL-cystine	Se^{2-} (organoSe)
Seleno-L-methionine	Se^{2-} (organoSe)
Seleno-cystamine	Se^{2-} (organoSe)

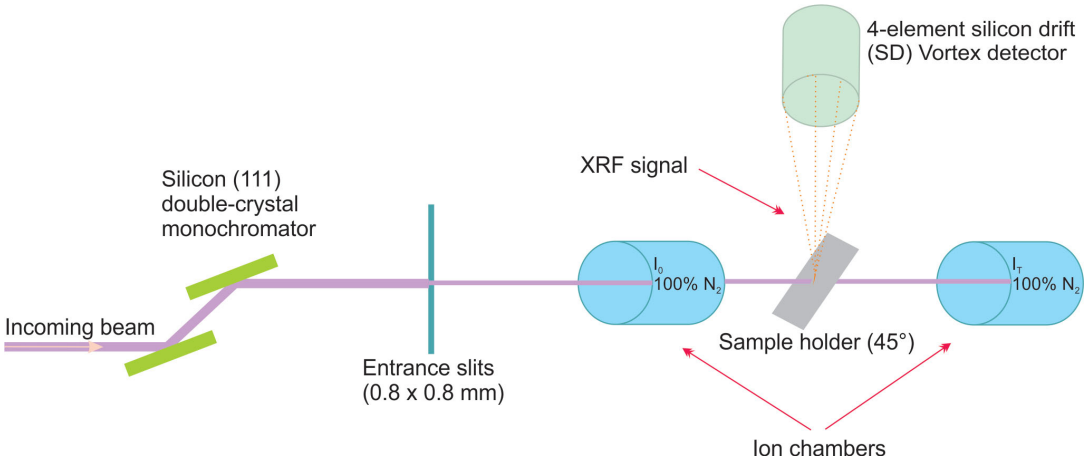

Figure 3. Schematic of the experimental set-up used on the VESPERS beamline at the Canadian Light Source, Saskatoon, SK.

thick aluminum foil were placed over the detector to mitigate detector saturation from high Fe content in the samples. Residual samples were measured by conducting two scans on three separate spots on each sample to avoid beam damage. Figure 4 provides a schematic representation of the experimental set-up that was used for XANES analysis on the 9BM beamline.

Future Work

The experimental portion of this study is complete and analysis of the supernatant from the batch experiments for cations and anions is underway. The data obtained from the XANES work will be analyzed using a technique known as linear combination fitting (LCF), where the spectra from known Se standards will be fitted to the unknown residual samples to determine the relative proportions of each Se species. Modelling of the batch experiments will be done in Geochemists Workbench to determine reaction rates for the oxidation of Se in the residual. Conclusions can then be drawn with regards to which Se species are most vulnerable to mobilization under the specific conditions of the experiments. Once the speciation and mobilization mechanisms are better understood, this information can by used to develop an optimal sludge-management plan to minimize associated potential environmental risks. The increased understanding of Se behaviour can also aid in the development of further remediation technologies and support the decision-making process where risk-based management is optimal.

Acknowledgments

The authors thank the Society of Contaminated Sites Approved Professionals of BC, SRK Consulting, Teck Resources Limited, the Canadian Light Source and funding provided to D. Kirste as part of the Hydrogeochemistry Re-

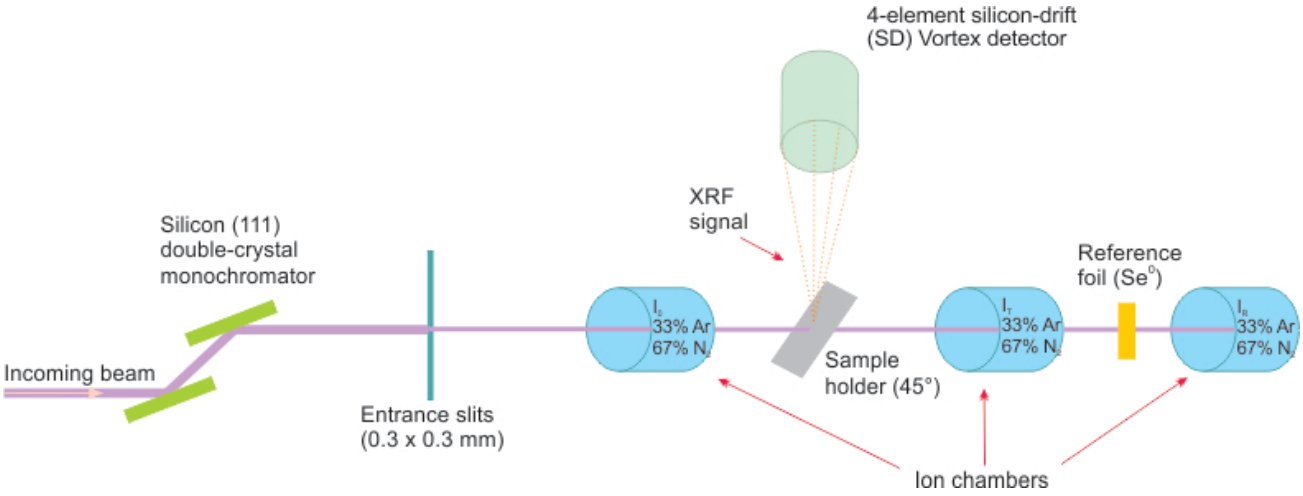

Figure 4. Schematic of the experimental set-up used on the 9BM beamline at the Advanced Photon Source, Chicago, IL.

search Group Project, and Geoscience BC for the funds and resources required to carry out this research.

Use of the Advanced Photon Source, an Office of Science User Facility operated for the United States Department of Energy (DOE) Office of Science by Argonne National Laboratory, was supported by the DOE under Contract No. DE-AC02-06CH11357. The authors extend a special thanks to T. Wu and G. Sterbinsky for their support during the experiments.

Research described in this paper was performed at the Canadian Light Source, which is supported by the Canada Foundation for Innovation, the Natural Sciences and Engineering Research Council of Canada, the University of Saskatchewan, the Government of Saskatchewan, Western Economic Diversification Canada, National Research Council Canada and the Canadian Institutes of Health Research. The authors extend a special thanks to R. Feng and P. Blanchard for their support during the experiments.

The authors also thank J. Ross-Lindeman for helpful comments and early review, which helped to improve and clarify this manuscript and to A. Allen for hours spent in the laboratory assisting with sample analysis and experimental work.

References

Balistrieri, L.S. and Chao, T.T. (1990): Adsorption of selenium by amorphous iron oxyhydroxide and manganese dioxide; Geochimica et Cosmochimica Acta, v. 54, no. 3, p. 739–751. doi:10.1016/0016-7037(90)90369-V

Chao, T.T. and Sanzolone, R.F. (1989): Fractionation of soil selenium by sequential partial dissolution; Soil Science Society of America Journal, v. 53, p. 385–392.

Chapman, P.M., Adams, W.J., Brooks, M.L., Delos, C.G., Luoma, S.M., Maher, W.A., Ohlendorf, H.M., Presser, T.S. and Shaw, D.P., editors (2010): Ecological Assessment of Selenium in the Aquatic Environment; CRS Press, Taylor & Francis Group, Boca Raton, Florida, 368 p.

Dowdle, P.R. and Oremland, R.S. (1998): Microbial oxidation of elemental selenium in soil slurries and bacterial cultures; Environmental Science and Technology, v. 32, no. 23, p. 3749–3755.

Holm, J., Palace, V.P., Wautier, K., Evans, R.E., Baron, C.L., Podemski, C., Siwik, P. and Sterling, G. (2003): An assessment of the development and survival of wild rainbow trout (*Oncorhynchus mykiss*) and brook trout (*Salvelinus fontinalis*) exposed to elevated selenium in an area of active coal mining; *in* The Big Fish Bang: Proceedings of the 26th Annual Larval Fish Conference, H.I. Browman and A.B. Skiftesvik (ed.), Institute of Marine Research.

Jain, R., Seder-Colomina, M., Jordan, N., Dessi, P., Cosmidis, J., van Hullebusch, E.D. and Weiss, S. (2015): Entrapped elemental selenium nanoparticles affect physicochemical properties of selenium fed activated sludge; Journal of Hazardous Materials, v. 295, p. 193–200. doi:10.1016/j.jhazmat.2015.03.043

Kang, M., Ma, B., Bardelli, F., Chen, F., Liu, C., Zheng, Z., Wu, S. and Charlet, L. (2013): Interaction of aqueous Se(IV)/Se(VI) with FeSe/$FeSe_2$: implication to Se redox process; Journal of Hazardous Materials, v. 248–249, p. 20–28.

Lemly, D.A. (2004): Aquatic selenium pollution is a global environmental safety issue; Ecotoxicology and Environmental Safety, v. 59, p. 44–56. doi:10.1016/S0147-6513(03)00095-2

Lenz, M., Van Hullebusch, E.D., Farges, F., Nikitenko, S., Borca, C.N., Grolimund, D. and Lens, P.N.L. (2008): Selenium speciation assessed by X-ray absorption spectroscopy of sequentially extracted anaerobic biofilms; Environmental Science and Technology, v. 42, no. 20, p. 7587–7593. doi:10.1021/es800811q

Muscatello, J.R., Bennett, P.M., Himbeault, K.T., Belknap, A.M. and Janz, D.M. (2006): Larval deformities associated with selenium accumulation in northern pike (*Esox Lucius*) exposed to metal mining effluent; Environmental Science and Technology, v. 40, no. 2, p. 6506–6512.

Neal, R.H. and Sposito, G. (1989): Selenate adsorption on alluvial soils; Soil Science Society of America Journal, v. 53, p. 70. doi:10.2136/sssaj1989.03615995005300010013x

Wen, H. and Carignan, J. (2007): Reviews on atmospheric selenium: emissions, speciation and fate; Atmospheric Environment, v. 41, no. 34, p. 7151–7165. doi:10.1016/j.atmosenv.2007.07.035

White, A.F. and Dubrovsky, N.M. (1994). Chemical oxidation-reduction controls on selenium mobility in groundwater systems; *in* Selenium in the Environment, W.T. Frankenberger, Jr. and S. Benson (ed.), CRC Press, Taylor & Francis Group, Boca Raton, Florida, p. 185–221.

White, A.F., Benson, S.M. Yee, A.W., Wollenberg, H.A. and Flexser, S. (1991): Groundwater contamination at the Kestrson Reservoir, California, part 2: geochemical parameters influencing selenium mobility; Water Resources Research, v. 27, no. 6, p. 1085–1098.

Wright, M.T. and Parker, D.R. (2003): Critical evaluation of the ability of sequential extraction procedures to quantify discrete forms of selenium in sediments and soils; Environmental Science and Technology, v. 37, no. 20, p. 4709–4716.

Zhang, Y. and Moore, J.N. (1996): Selenium fractionation and speciation in a wetland system; Environmental Science and Technology, v. 30, p. 2613–2619.

Carbon Mineralization in Ultramafic Tailings, Central British Columbia: A Prospect for Stabilizing Mine Waste and Reducing Greenhouse Gas Emissions

S.S.S. Vanderzee, Bradshaw Research Initiative for Minerals and Mining, The University of British Columbia, Vancouver, BC, svander@eoas.ubc.ca

I.M. Power, Bradshaw Research Initiative for Minerals and Mining, The University of British Columbia, Vancouver, BC

G.M. Dipple, Bradshaw Research Initiative for Minerals and Mining, The University of British Columbia, Vancouver, BC

P.M.D. Bradshaw, FPX Nickel Corp., Vancouver, BC

Vanderzee, S.S.S., Power, I.M., Dipple, G.M. and Bradshaw, P.M.D. (2018): Carbon mineralization in ultramafic tailings, central British Columbia: a prospect for stabilizing mine waste and reducing greenhouse gas emissions; *in* Geoscience BC Summary of Activities 2017: Minerals and Mining, Geoscience BC, Report 2018-1, p. 109–112.

Introduction

The goal of this research is to assess the prospect of reducing the costs and risks associated with the storage of ultramafic mine tailings by sequestering carbon dioxide (CO_2) through carbon mineralization. Herein, the tailings are physically stabilized by the rapid formation of secondary magnesium-carbonate minerals, which act as cement. The magnesium ions are sourced from minerals found within ultramafic tailings, and once released into water, can react with dissolved CO_2 (specifically HCO_3) to safely sequester the greenhouse gas in mineral form (e.g., $MgCO_3 \cdot 3H_2O$). These cement-forming reactions can be accelerated by exposing the tailings to a CO_2-rich gas (Harrison et al., 2013), such as the flue gases produced by onsite power generators. In addition to the partial pressure of CO_2 within the gas that the tailings are exposed to, the reactivity of the magnesium minerals can also be rate-limiting. The pH dependent dissolution rate of brucite ($Mg(OH)_2$) is several orders of magnitude greater than that of other magnesium minerals that are commonly found within ultramafic tailings (e.g., serpentine and olivine; Power et al., 2013). Therefore the significance of brucite's presence, even in trace amounts, is that it offers a source of quickly dissolving magnesium ions for rapid and inexpensive tailings cementation through carbon mineralization.

In this study, the prospect of stabilizing brucite-bearing ultramafic mine tailings through carbon mineralization is assessed by testing their unconfined compressive strength as a proxy for stability after they have been compacted and exposed to a 10% CO_2 gas while partially saturated with water. The effect of the initial brucite abundance within 'prospective tailings' (i.e., finely ground exploration pulps from the Baptiste nickel deposit in FPX Nickel Corp.'s Decar property, central British Columbia; Britten, 2017) on unconfined compressive strength after exposure to the 10% CO_2 gas stream is studied. The consumption of brucite is used as evidence for the sequestration of CO_2 through carbon mineralization (in future work, the increase in carbon content [wt. % C] will also be used as evidence). It should be noted that in a separate study, it has been demonstrated that brucite-rich zones of the Baptiste nickel deposit can be identified and targeted through geometallurgical analysis (described in Dipple et al., 2002) that projects mineral abundance from whole-rock geochemical data collected during the exploration phase of mining.

Methods

To examine proof of concept, cylinders (5.0 cm in height, 2.5 cm in diameter) of compacted prospective tailings, henceforth referred to simply as tailings, were prepared with brucite abundances that ranged from 0.2 to 10 wt. %. In addition to the five prospective tailings samples, there was one sample from tailings produced by a nickel-iron alloy recovery method that was based on magnetic susceptibility. The mineralogical composition of each starting material is shown in Table 1 and was determined through the Rietveld method using powder X-ray diffraction (XRD) data (Wilson et al., 2009). The cylinders were prepared by placing ~2.5 g of tailings in a hollow cylinder before compacting the material with a piston under a force of ~100 psi, then wetting the newly compacted surface with deionized water, and then repeating the process to form laminates of undersaturated compacted tailings. The pore space in the compacted tailings was saturated to a level of approximately ~50% with deionized water. The compacted tailings were placed in a chamber with continuous flow through of a hydrated 10% CO_2 and 90% N_2 gas at a flow rate of

This publication is also available, free of charge, as colour digital files in Adobe Acrobat® PDF format from the Geoscience BC website: http://www.geosciencebc.com/s/SummaryofActivities.asp.

Table 1. The mineralogical composition of samples from the Baptiste nickel deposit, central British Columbia, which were used as raw materials for producing cemented tailings cylinders. All samples, except D-43, are exploration pulps. Sample D-34 consists of tailings produced by a nickel-iron alloy recovery method that was based on magnetic susceptibility.

Sample ID	Brucite (wt. %)	Magnetite (wt. %)	Olivine (wt. %)	Serpentine (wt. %)	Diopside (wt. %)
1423072	10.1	4.1	3.4	81.8	0.5
1423128	6.8	3.6	8.3	81.3	0
1423127	4.6	2.2	11.6	81.7	0
1423090	1.8	1.8	11	84.6	0.8
1423111	0.2	4.6	3.9	88.9	2.4
D-43	0.9	0	3.1	94.6	1.5

~10 mL/min for three weeks. The chamber volume was ~5 L and 4–8 cylinders were in it at a time. The tailings cylinders were then allowed to dry for several days in open air in the laboratory (pCO_2 = 0.04%) before their porosity and unconfined compressive strength were measured. The total porosity of each sample was calculated from independent measurements of bulk (geometric) and matrix (helium-pycnometery) density (Kennedy et al., 2009), and the unconfined compressive strength tests were conducted with a loading rate of 34 kg/min (75 lb./min) in a uniaxial press. Figure 1 shows a tailings cylinder after failure. Ongoing work includes measuring the carbon content of selected tailings cylinders as a function of distance from the surface by collecting aliquots at intervals along the radius.

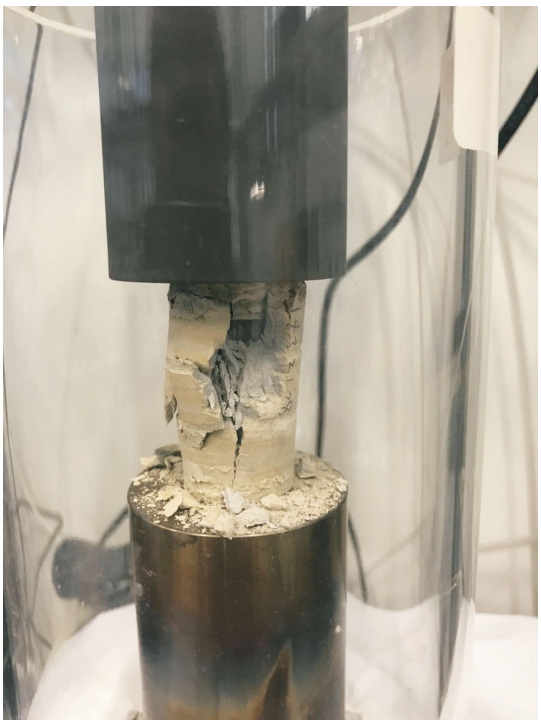

Figure 1. A tailings cylinder after being compressed until failure. The sample was cemented by the formation of secondary magnesium-carbonate minerals after exposure to a 10% CO_2 gas stream for three weeks.

Results and Discussion

From Figure 2 it can be seen that the initial amount of brucite within the tailings had a remarkable influence on the compressive strength of the tailings cylinders after exposure to a 10% CO_2 environment. This is inferred to be due to the transformation of brucite into secondary magnesium-carbonate cement phases. The transformation of brucite, rather than other minerals such as serpentine, is supported by XRD results that show the abundance of brucite significantly decreases after exposure to a 10% CO_2 environment (Figure 3). Samples with relatively low initial brucite content (~0.5 wt. %) yielded unconfined compressive strengths of ~50–100 psi, whereas samples with initial brucite contents of ~5 wt. % had unconfined compressive strengths of ~1000 psi. Interestingly, the sample with highest initial brucite content (10 wt. %) did not yield the highest strength. This is hypothesized to be because CO_2 was consumed by reaction before it was able to fully penetrate to the core of the cylinder; this hypothesis will be tested in the future by assessing the carbon content of the cylinders along their radii. A relationship between total porosity and compressive strength may exist (Figure 2), however, the physical mechanisms of strength development require further investigation.

Conclusions and Future Work

These lab-scale tests have demonstrated that exposing partially saturated and compacted ultramafic tailings to a 10% CO_2 gas stream can effectively stabilize the waste and sequester CO_2 when trace amounts of brucite are initially present. An unconfined compressive strength of up to 1000 psi was achieved with an initial brucite content of ~5 wt. %, and even samples with an initial brucite content of ~0.5 wt. % exhibited unconfined compressive strengths of ~50–100 psi. If this process is utilized at a mine site, the tailings become resistant to liquefaction under stress due to the formation of the magnesium-carbonate cement and development of compressive strength, potentially reducing the risk of a tailings dam failure. Furthermore, these results encourage collaboration between science and engineering to assess alternative and less costly tailings storage facility designs that exploit the ability of brucite-bearing tailings to become self-stabilizing after adequate reaction with CO_2.

Due to the scale of tailings production at mine sites, the reaction between CO_2 and even trace amounts of brucite in the tailings can generate significant greenhouse gas emission offsets. Assuming a large nickel mine produces 10 Mt of tailings per year and has an average brucite content of 2 wt. %, up to 150 000 tonnes of CO_2 can be sequestered per year. To evaluate the prospect of achieving carbon-neutral nickel mining in BC by the reaction of brucite in tailings

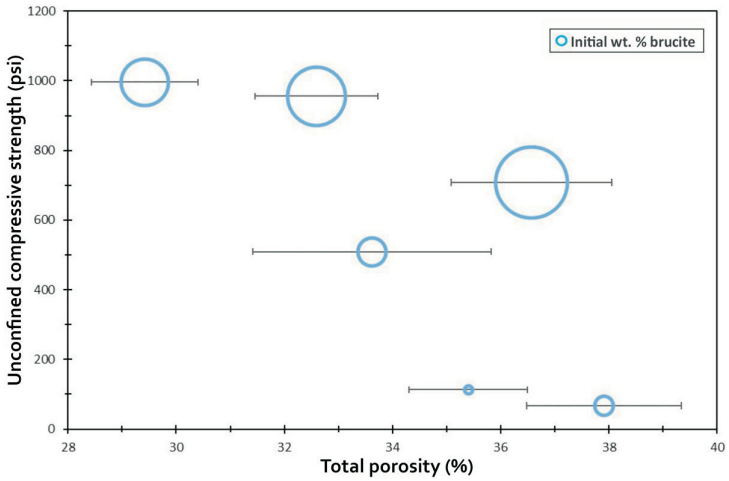

Figure 2. The compressive strength of tailings cylinders after exposure to a 10% CO_2 environment for three weeks. The size of the circle represents the initial brucite content, and the total porosity is the sum of the connected and isolated porosities.

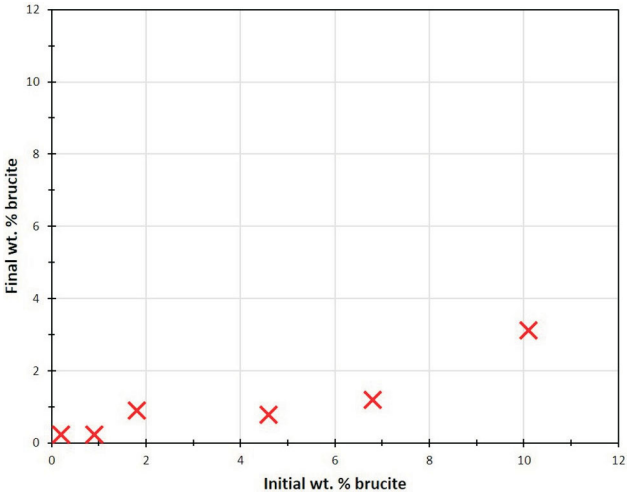

Figure 3. The initial wt. % brucite content of the tailings versus their final wt. % brucite content after being exposed to a 10% CO_2 environment for three weeks. Determined by Rietveld method using X-ray diffraction analysis data.

with CO_2, the CO_2 emission and tailings production data from the Mount Keith nickel mine in Australia can be considered. At this mine, 11 Mt of tailings are produced per year, and 140 000 tonnes of CO_2 are produced per year by mining trucks (accounting for 40% of total mine emissions, with the remainder accounted for by onsite electricity generation from natural gas for ore processing facilities; Wilson et al., 2014). Furthermore, Wilson et al. found that approximately 40 000 tonnes of CO_2 are sequestered per year at Mount Keith due to the 'accidental' reactions between atmospheric CO_2 and brucite found in the mine tailings. The authors also found that brucite was not being fully consumed by reaction with atmospheric CO_2 before being buried by subsequent layers of tailings. If the tailings were allowed to react for a longer period of time, or if they were deposited in thinner layers, then up to 120 000 tonnes of CO_2 could be sequestered just by reaction of brucite with atmospheric CO_2. Therefore, carbon-neutral nickel mining in BC could potentially be achieved if hydroelectricity is used at ore processing facilities and mining truck emissions are offset by fully reacting tailings containing an average of 2 wt. % brucite with CO_2.

Future work will narrow in on the threshold parameters for stabilization and investigate other methods of manufacturing cemented tailings cylinders. Processes of tailings compaction and CO_2 delivery will be assessed to find a procedure that more closely resembles that which could be readily adopted at mine sites. The diffusion rates of CO_2 into the tailings as a function of both brucite content and permeability will be modelled. Imaging and chemical characterization of the magnesium-carbonate cement phases will be conducted through X-ray mapping and electron microprobe analysis to better understand the mechanisms of stabilization. Furthermore, the thermodynamic stability of the cement phases in various environments will be studied through geochemical modelling.

Acknowledgments

In addition to Geoscience BC, FPX Nickel Corp. and Natural Sciences and Engineering Research Council are acknowledged for financial support of this project. The authors thank S. McDougall from the Department of Earth, Ocean and Atmospheric Sciences at The University of British Columbia for reviewing this paper.

References

Britten, R. (2017): Regional metallogeny and genesis of a new deposit type: disseminated awaruite (Ni_3Fe) mineralization hosted in the Cache Creek Terrane; Economic Geology, v. 112, p. 517–550.

Dipple, G.M., Raudsepp, M. and Gordon, M.T. (2002): Assaying wollastonite is skarn; *in* Industrial Minerals in Canada, Canadian Institute of Mining, Metallurgy and Petroleum, Special Volume 53, p. 1–10.

Harrison, A.L., Power, I.M. and Dipple, G.M. (2013): Accelerated carbonation of brucite in mine tailings for carbon sequestration; Environmental Science & Technology, v. 47, issue 1, p. 126–134.

Kennedy, L.A., Russell, J.K. and Nelles, E. (2009): Origins of Mount St. Helens cataclasites: experimental insights; American Mineralogist, v. 94, p. 995–1004.

Power, I.M., Harrison, A.L. and Dipple, G.M. (2013): Carbon mineralization: from natural analogues to engineered systems; Reviews in Mineralogy and Geochemistry, v. 77, p. 305–360.

Wilson, S.A., Dipple, G.M., Power, I.M., Throm, J.M., Anderson, R.G., Raudsepp, M., Gabites, J.E. and Southam, G. (2009): Carbon dioxide fixation within mine wastes of ultramafic-hosted ore deposits: examples from the Clinton Creek and

Cassiar chrysotile deposits, Canada; Economic Geology, v. 104, p. 95–112.

Wilson, S.A., Harrison, L.A., Dipple, G.M., Power, I.M., Barker, S.L.L., Mayer, K.U., Fallon, S.J., Raudsepp, M. and Southam, G. (2014): Offsetting CO_2 emissions by air capture in mine tailings at the Mount Keith nickel mine in western Australia: rates, controls and prospects for carbon neutral mining; International Journal of Greenhouse Gas Control, v. 25, p. 121–140.

1101-750 West Pender Street
Vancouver,BC V6C 2T7

t: 604.662.4147
e: info@geosciencebc.com
w: www.geosciencebc.com